# Dielectrophoretic discrimination of pluripotent myoblast with Raman spectroscopic analysis of the cell plasma membrane for application in Huntington's disease

*Massimo Muratore*


A thesis submitted for the degree of Doctor of Philosophy

***The University of Edinburgh***

March 18, 2014

# Abstract

Myoblasts are muscle derived mesenchymal stem cell progenitors that have great potential for use in regenerative medicine, especially for cardiomyogenesis grafts and intracardiac cell transplantation. To utilise such cells for pre-clinical and clinical applications, and especially for personalized medicine, it is essential to generate a synchronised, homogenous, population of cells that display phenotypic and genotypic homogeneity within a population of cells. This thesis demonstrates that the biomarker-free technique of dielectrophoresis (DEP) can be used to discriminate cells between stages of differentiation in the C2C12 myoblast pluripotent mouse model. Terminally differentiated myotubes were separated from C2C12 myoblasts to better than 96% purity, a result validated by flow cytometry and Western blotting. To determine the extent to which cell membrane capacitance, rather than cell size, determined the DEP response of a cell, C2C12 myoblasts were co-cultured with GFP-expressing fibroblasts of comparable size distributions (mean diameter ~10 μm). A DEP sorting efficiency greater than 98% was achieved for these two cell types, a result concluded to arise from the fibroblasts possessing a larger membrane capacitance than the myoblasts. It is currently assumed that differences in membrane capacitance primarily reflect differences in the extent of folding or surface features of the membrane. However, our finding by Raman spectroscopy that the fibroblast membranes contained a smaller proportion of saturated lipids than those of the myoblasts suggests that the membrane chemistry should also be taken into account.

These high levels of discrimination raised more questions about the cell plasma membrane characteristics that may be responsible for the dielectrophoretic response. This prompted to extend the work to a specific neurodegenerative disease, Huntington's disease. Several studies have been revealing the association between plasma membrane dysregulation and Huntington's disease. In particular the

feasibility to use peripheral fibroblasts cells from donors affected by the disease, as a forecasting model marker for Huntington. Although there are substantial evidences about the indirect effect of the disease on the plasma membrane, a non-invasive technique that can discriminate and characterise a cell sample is not available. Raman spectroscopy with associated statistical multivariate analysis was used to characterise sub-cellular differences in extracted plasma membranes from peripheral fibroblastic cells in order to elucidate the differences between cells affect and non-affected by the disease. The results clearly showed that indeed the plasma membrane carries differences that can be attributed to the presence of the disease making the plasma membrane an amenable and novel biomarker for Huntington's disease

.

# Lay summary

Progenitor's pluripotent cells are stem-like cells that have great potential for use in regenerative medicine. To utilise such cells for pre-clinical and clinical applications, and especially for personalized medicine, it is essential to generate homogenous population of cells that display the same characteristics and high purity.

In this thesis is demonstrated a novel application of a technique called dielectrophoresis (DEP) that can be used to discriminate cells and therefore guarantee purity of a population of cells.

From the results, conclusions arise about the membrane capacitance (stored charges) of the cell plasma membrane (membrane that separates the contents of the cell from outside environment). The plasma membrane characteristics were further analysed by a chemical analytical technique in the form of Raman spectroscopy. This raised more questions about the characteristics of the cell plasma membrane that may be responsible for the DEP response. This prompted to extend the work to other cell types that present dysregulation in their plasma membrane.

This lead to the Raman spectroscopic analysis of cells that present a neurodegenerative disease called Huntington's disease. In this work, it has been shown for the first time that the cell plasma membrane can be a suitable biomarker (an indicator of the physiological state of the cell) in detection of Huntington's disease in peripheral fibroblasts (skin type cells).

# Declaration

I hereby declare that the research reported in this thesis is my own work, produced without the assistance of third parties and without making use of aids other than those specified. The thesis itself has been written by me and the work presented has been conducted in the School of Engineering at the University of Edinburgh from 2009 to 2013. This work has not been submitted for any other degree or professional qualification.

Edinburgh

Massimo Muratore Date 18/03/2014

**To my grandmother Ada and grandfather Ernesto**

Dedicata ai nonni  Ada e Ernesto

# Acknowledgements

I would like to thank Dr. Vlastimil Srsen and Dr Martin Waterfall for the help during my PhD studies and for the time spent with me discussing experiments, techniques and the generous donations in chemicals and reagents. In addition, I would like to thank my supervisor Prof Ron Pethig for the help given me during my PhD.

I am very thankful to my girlfriend Anna for the support and patience over the years. This thesis is dedicated to my family and to the memory of my grandmother Ada and my grandfather Ernesto.

# Table of Contents

# Table of figures

# List of Tables

# Chapter 1 Theoretical basis of Electrostatics

## 1.1 Introduction

In this chapter, the bases of electrostatics are discussed as introduction concepts for the basic of dielecrophoresis DEP.

The chapter is devised in six main sections that describe:

1. Governing laws of Electrostatics
    a. Coulomb's Law.
    b. Gauss's, Poisson's, Laplace's basic equations.
2. Introductions to the concepts of dipole moment, polarisation and dielectric.
3. Details about the types of polarisation.
4. Dispersion and relaxation of dielectrics are elucidated.
5. Complex permittivity in an AC field.
6. The dipole moment model is explained for spherical particles approximating a biological cell.

## 1.2 Governing laws of Electrostatics

### 1.2.1 Coulomb's Law

Consider a charge q at a distance r from another charge Q. If we consider q and Q as static, we can express the force (F) between $Q_1$ and $Q_2$ using Coulomb's Law [1,2]

$$F = \frac{Q_1 Q_2}{4\pi\varepsilon_0 r^2}\hat{r}_{1,2} \qquad \textit{Equation 1-1}$$

with $\varepsilon_0$ as the permittivity[1] of evacuated free space with a value of 8.85 x $10^{-12}$ $\frac{C^2}{Nm^2}$ *or* $\frac{F}{m}$ (N as Newton, C for Coulombs and F for Farads) with $\hat{r}_{1,2}$ as the unit vector between charge $q$ and $Q$ as illustrated in *Figure 1-1a* The force expressed in *Equation 1-1* can be repulsive (as illustrated by *Figure 1-1*) or attractive depending on the sign of the charge of $q$ and $Q$. In addition, the force ($F$) is proportionally related to the $q$ and $Q$ product and inversely related to the squared distance between the two charges.

Considering the case when there are multiple $Q_n$ charges at distance,$\bar{r}_n$, we can calculate the total force ($F_{tot}$) by *Equation 1-2*

$$F_{tot} = F_1 + F_2 + \cdots F_n \qquad \textit{Equation 1-2}$$

If we consider Lorentz Law as[3]

$$F = QE_{(r)} \Rightarrow E_{(r)} = \frac{F}{Q} \qquad \textit{Equation 1-3}$$

[1] Permittivity of a material is defined as the ability to polarise upon the application of an electrical field. The value of $\varepsilon_0$ is related to the speed of light $c$ in a vacuum given by Maxwell as $c = 1/(\varepsilon_0\mu_0)^{1/2}$ in which $\mu_0$ is the magnetic permeability of vacuum.

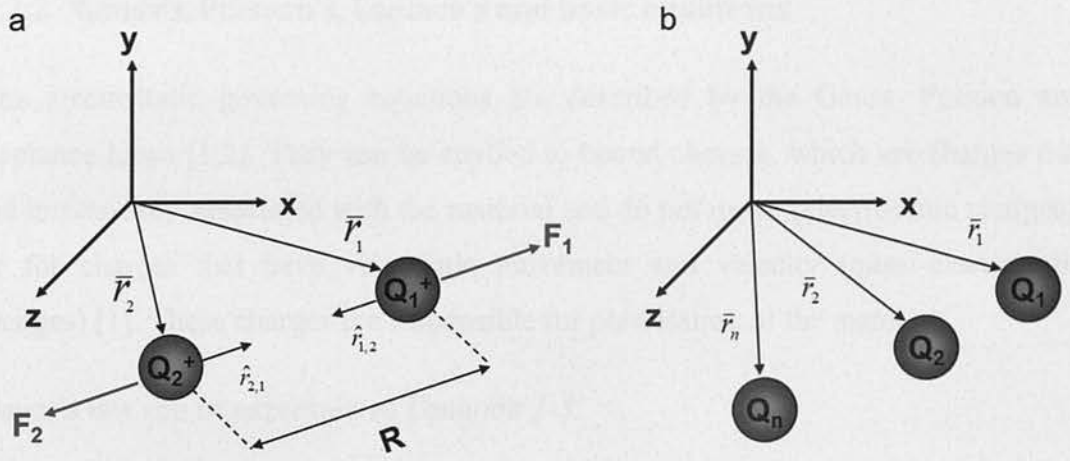


*Figure 1-1Representation of the force $F_1$ and $F_2$ acting on two charges $Q_1$ and $Q_2$ with distance R between them. b) Multiple charges representation for total force calculation.*

This employs the convention that the field $E_{(r)}$, at a point in space, is defined in terms of the electric force that will be exert on a unit test charge at that point. $E_{(r)}$ thus has units of N/C. By substituting *Equation 1-1* into *Equation 1-3* for all the forces generated by $Q_n$ charges we have *Equation 1-4* [3].

$$E(r) = \frac{1}{4\pi\varepsilon_0}\sum_{i=1}^{n}\frac{Q_i}{R_i^2}\hat{r}_i \qquad \textit{Equation 1-4}$$

Here we are considering $E$ as a force on a singular point charge. We can extend the problem to a surface, areas and volumes that contains several charges as a continuous charge distribution. This involves the derivation of *Equation 1-4* to determine charges per unit length/area/surface, which can be found in literature [3].

### 1.2.2 Gauss's, Poisson's, Laplace's and basic equations

The electrostatic governing equations are described by the Gauss, Poisson and Laplance Laws [1,2]. They can be applied to bound charges, which are charges that are intrinsically associated with the material and do not move (electrostatic charges), or for charges that have very little movement and velocity (quasi-electrostatic charges) [1]. These charges are responsible for polarisation of the material.

Gauss's law can be expressed as *Equation 1-5*.

$$\nabla \cdot E = \frac{\rho}{\varepsilon_0} \qquad \textit{Equation 1-5}$$

where ρ is the charge density (number of charges per unit volume) and $\nabla$ is the gradient vector operator acting on the x, y, z coordinates of the field.

$$\nabla^2 \emptyset = -\frac{\rho}{\varepsilon_0} \qquad \textit{Equation 1-6}$$

In the case where the total charge density is equal to zero, *Equation 1-6* is reduced to Laplace's *Equation 1-7*.

$$\nabla^2 \emptyset = 0 \qquad \textit{Equation 1-7}$$

Considering *Equation 1-6* and *Equation 1-7* we can calculate the electric field using $\phi$ by *Equation 1-8*.

$$E \equiv -\nabla \emptyset \qquad \textit{Equation 1-8}$$

$E$ in *Equation 1-8* is used to calculate the dielectrophoretic force $F_{DEP}$.

## 1.3 Dipoles, dielectrics and polarisation

The dipole can be described as a distribution of two charges ($Q_1$ and $Q_2$) with same magnitude but opposite signs at distance d from each other as expressed in *Equation 1-9* [4].

$$p = Qd \qquad \textit{Equation 1-9}$$

where p is the vector dipole moment (at origin pointing in z direction as illustrated in *Figure 1-2a*) expressed in units of Cm. Historically, the magnitude of a dipole moment has been expressed in Debye units (1 D = 3.3E-30 Cm). For a point dipole the potential can be expressed by *Equation 1-10* [4].

$$\emptyset = \frac{p \cdot \hat{r}}{4\pi\varepsilon_m r^2} \rightarrow \emptyset = \frac{|p|cos\theta}{4\pi\epsilon_m r^2} \qquad \textit{Equation 1-10}$$

where $p$ is the point dipole moment, $\varepsilon_m$ is the permittivity of the medium, $\theta$ the polar angle and $r$ the radial position *Figure 1-2a*. The electric field can be expressed [3] so that:

$$E_r = -\frac{2p\,cos\theta}{4\pi\varepsilon_0 r^3} \qquad \textit{Equation 1-11}$$

$$E_\theta = -\frac{p\,sin\theta}{4\pi\varepsilon_0 r^3} \qquad \textit{Equation 1-12}$$

$$E_\emptyset = 0 \qquad \textit{Equation 1-13}$$

so that [3]

$$E = -\frac{|p|}{4\pi\varepsilon_0 r^3}\left(2cos\theta\hat{r} + sin\theta\hat{\theta}\right) \;\; (with\ r \gg d) \qquad \textit{Equation 1-14}$$

This expression is for a point dipole with the field related (see *Figure 1-2b*) to the inverse of $r^3$. For higher numbers of charges that can be represented as a quadrupole or octopole the potential is related to $1/r^4$ and $1/r^5$, respectively. We can now define the average dipole moment ($p_{av}$) related to the molecules present in a material proportional to the field magnitude by *Equation 1-15* [1].

$$p_{av} = \alpha E' \qquad \textit{Equation 1-15}$$

where $\alpha$ is the polarisability as the ability of the material to produce charges at the interface and $E'$ is the localised electric field near the dipole.

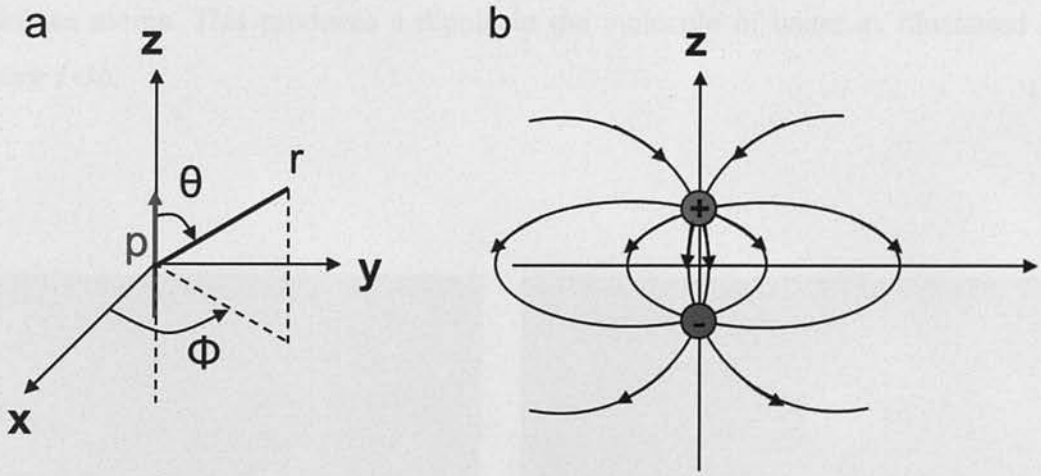


*Figure 1-2 a) electric field representation with p at origin rotated on the z-axis. b) Field dipole lines representation of two charges with opposite sign*

From *Equation 1-15* the dipole moment per unit volume can be define by *Equation 1-16*.

$$P = n\alpha E' \qquad \textit{Equation 1-16}$$

where $n$ is the number of molecules in the unit volume.

The net charge of the material at the surface can be expressed by the charge density $\rho$ in *Equation 1-17* [1,2,4].

$$\rho = -\nabla \cdot p \qquad \textit{Equation 1-17}$$

A material with dielectric properties has charges that polarise when an electric field is applied. The dipoles can be permanent (polar material) or induced (non-polar material). Permanent dipoles are due to the asymmetric distribution of polar bonds in a molecule, as for example in water. In a water molecule the distribution of the electrons from the two hydrogen atoms is shared with oxygen. The oxygen becomes negatively charged with an opposite charge (positive charge) at the centre of the two hydrogen atoms. This produces a dipole in the molecule of water as illustrated in *Figure 1-3b*.

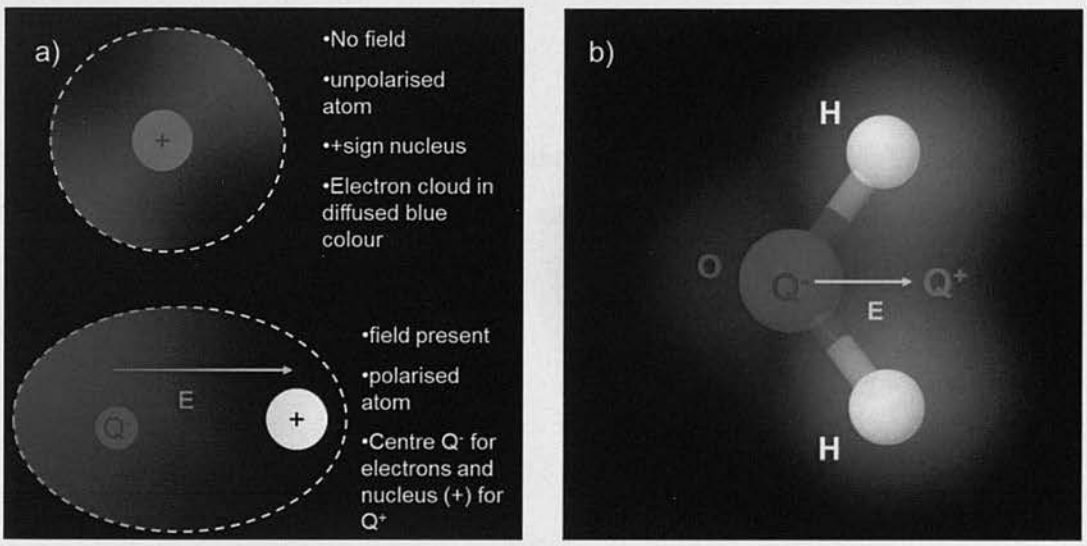


*Figure 1-3 a) Induced dipole representation on a generic atom. b) Permanent dipole of a water molecule.*

*Figure 1.3-2 cont.-The oxygen is the centre of the negative charge $Q^-$ and the centre of the positive charge $Q^+$ is between the two hydrogen atoms. The yellow arrow indicates the dipole moment.*

Induced dipoles arise when an electric field produces slight perturbations of bound charges that have very limited mobility, such as in ionic solids or for electrons and the nucleus in an atom (*Figure 1-3b*). The magnitude of this type of dipole is very small as a single entity, but the overall effect of very large numbers can have a significant effect [2]. If we consider a dielectric material not all the charges will be bound; some will be free to move in the applied electrical field. The resulting electrical current density ($J$) can be expressed by *Equation 1-18* by the amount of charges that pass the area in a second [1]

$$J = \rho v_c \qquad \textit{Equation 1-18}$$

where $\rho$ is the charge density. The velocity $v_c$ of the charge carrier, that can be expressed by *Equation 1-19*.

$$v_c = \mu E \qquad \textit{Equation 1-19}$$

where $\mu$ is the mobility of the charge in the applied electrical field. We can now use Ohm's law to define the term electrical conductivity ($\sigma$) of a material by *Equation 1-20* [1,3].

$$J = \sigma E \qquad \textit{Equation 1-20}$$

## 1.4 Polarisation types

The type of polarisation differs at the atomic level and for a relative macro scale as illustrated in *Figure 1-4*. Each type has a dependency on the frequency of the field [1,2].

1. Atomic level polarisation
    a. Electron and nucleus reorientation in an applied field (electronic polarisation)
    b. When charges move in a material at opposite locations. (atomic polarisation)
2. For relatively macro scale polarisation
    a. There is orientational polarisation for permanent dipole molecules.
    b. Interfacial polarisation (also known as Maxwell-Wagner polarization) in the case of different materials where the charges accumulate at the interface.

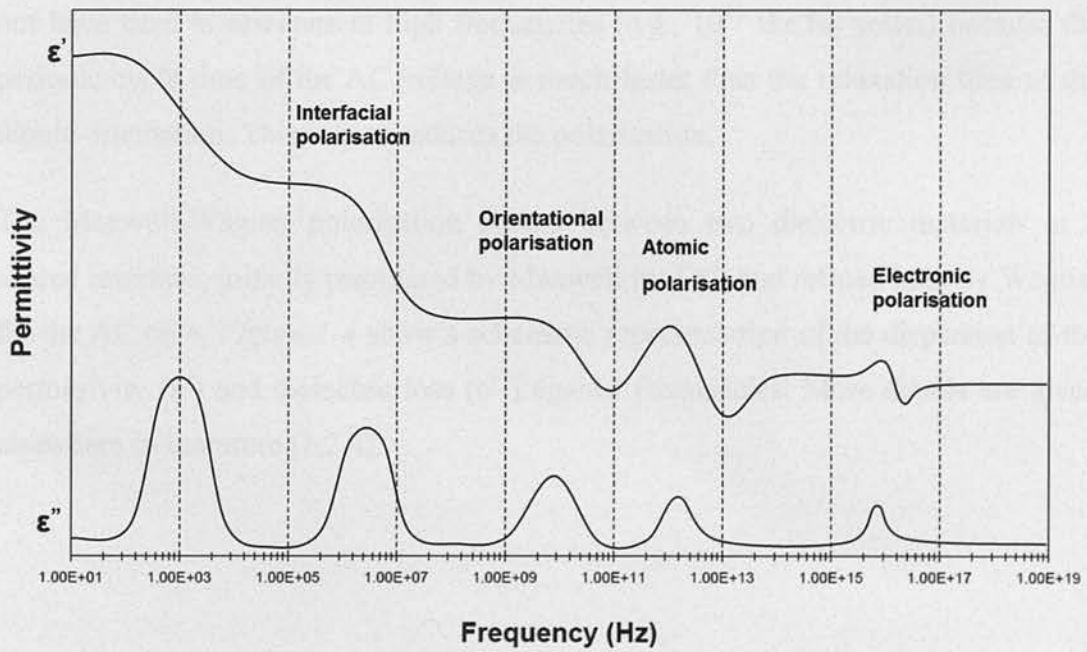


*Figure 1-4Representative plot of the permittivity ($\varepsilon'$) and dielectric loss ($\varepsilon''$) against frequency.*

## 1.5 Dispersion and relaxation in a dielectric

Two types of dispersion mechanisms are presented here:

1. Debye relaxation that happens in the material.
2. Maxwell-Wagner relaxation that is produced at the interface between two different materials.

The Debye relaxation is derived from the fact that the dipole takes time to orientate in the electric field. This means that the orientation of the charges is not instantaneous after the electric field is applied [1,2]. In addition, there is a time delay for the dielectric to depolarise after the electric field is withdrawn. This time delay in polarisation and depolarisation in the material is called the relaxation time [1]. It is also important to mention that the AC frequency of the field plays a role in polarisation due to the fact that at low frequencies the dipole has time to form as the cycles per unit of time alternate relatively slowly. On the contrary, the dipole does not have time to orientate at high frequencies (e.g., $10^{11}$ Hz for water) because the periodic cycle time of the AC voltage is much faster than the relaxation time of the dipole orientation. This in turn reduces the polarisation.

The Maxwell-Wagner polarisation occurs between two dielectric materials at a shared interface, initially postulated by Maxwell for DC, and refined later by Wagner for the AC case. *Figure 1-4* show a schematic representation of the dispersion of the permittivity (ε') and dielectric loss (ε'') against frequencies. More details are given elsewhere in literature [1,2,4].

## 1.6 Complex permittivity in AC Field

As a definition the complex permittivity is the response of the dielectric to a frequency dependent AC field [1]. If a potential is applied for a single frequency a harmonic potential can be expressed using phasor[2] notation [1,4] as:

$$\phi(x,t) = \Re e\left[\tilde{\phi}(x)e^{i\omega t}\right] \qquad \textit{Equation 1-21}$$

with $i = \sqrt{-1}$, x the position vector, $\widetilde{\emptyset}$ as the complex phasor and $\Re e[\cdots]$ as the real part of the complex function. The potential of the electric field can be expressed by

$$E(x,t) = \Re e\left[\tilde{E}(x)e^{i\omega t}\right] \qquad \textit{Equation 1-22}$$

with $\tilde{E} = (-\nabla\widetilde{\emptyset})$ as the phasor. We can re-arrange *Equation 1-5* (Gauss's Law) to give:

$$\nabla \cdot \sigma E = i\omega p_f \;\rightarrow\; \nabla \cdot (\tilde{\varepsilon}E) = 0 \qquad \textit{Equation 1-23}$$

with

$$\tilde{\varepsilon} = \varepsilon_0\varepsilon_r - \; i\frac{\sigma}{\omega} \qquad \textit{Equation 1-24}$$

where $\omega$ is the angular frequency, $\rho_f$ is the free charge density, $\tilde{\varepsilon}$ is complex permittivity, $i$ the imaginary part, $\varepsilon_0$ permittivity of vacuum and $\varepsilon_r$ relative permittivity of the material.

Here it is important to note that the complex permittivity is frequency related, so for high frequencies, approaching $\infty$, the $-i = \frac{\sigma}{\omega}$ term will be close to zero and therefore the permittivity will dominate the equation. The opposite situation it is true when the frequency approaches zero (DC) and therefore the conductivity ($\sigma$) will dominate the equation.

[2] Phasor is a sinusoidal wave with amplitude frequency and phase as a function of time.

## 1.7 Dipole moment of spherical particles

If we consider an homogeneous dielectric spherical particle with radius ($R$) with permittivity ($\varepsilon_p$) in a dielectric homogenous medium with permittivity ($\varepsilon_m$) with a uniform electric field, $\vec{E} = E\hat{z}$ in the z-direction as illustrated in *Figure 1-5*.

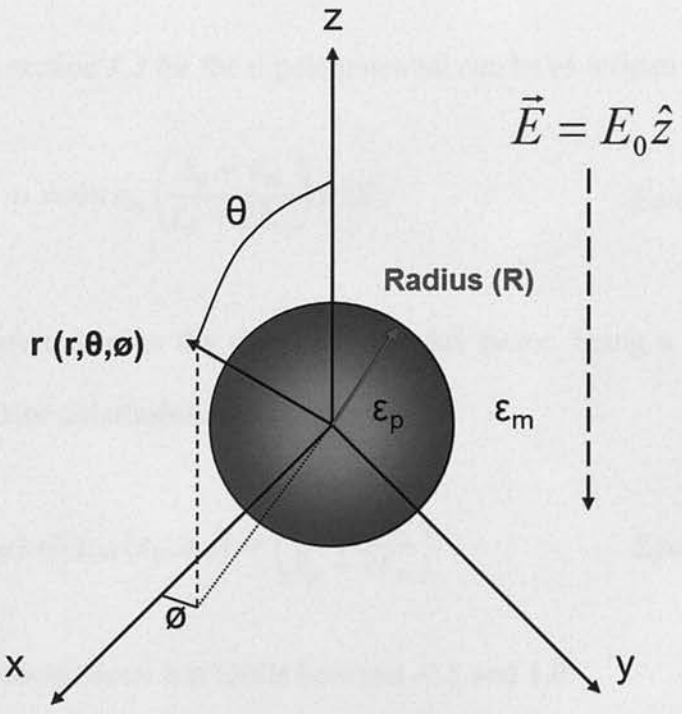


*Figure 1-5 Spherical dielectric particle in a homogenous medium.*

Satisfying Laplance's equation for electrical potential and with $r = R$ the boundary condition, for the particle and medium, using Gauss's law can be written as [4]

$$\phi_m(r = R, \theta) - \phi_p(r = R, \theta) = 0 \Rightarrow \varepsilon_m \frac{\partial \emptyset_p}{\partial r} - \varepsilon_p \frac{\partial \emptyset_m}{\partial r} = 0 \quad \textit{Equation 1-25}$$

The potential ($\phi$) for the boundary between sphere and medium can be expressed as [1]:

$$\phi_m = ER^3\left(\frac{\tilde{\varepsilon}_p - \tilde{\varepsilon}_m}{\tilde{\varepsilon}_p + 2\tilde{\varepsilon}_m}\right)\frac{cos\theta}{r^2} - Er\,cos\theta \qquad \textit{Equation 1-26}$$

$$\phi_p = -\left(\frac{3\tilde{\varepsilon}_m}{\tilde{\varepsilon}_p + 2\tilde{\varepsilon}_m}\right)Er\,cos\theta \qquad \textit{Equation 1-27}$$

*Equation 1-10* in section *1.3* for the dipole potential can be re-written as:

$$p = 4\pi\varepsilon_m\left(\frac{\tilde{\varepsilon}_p - \tilde{\varepsilon}_m}{\tilde{\varepsilon}_p + 2\tilde{\varepsilon}_m}\right)R^3E \qquad \textit{Equation 1-28}$$

with $\left(\frac{\tilde{\varepsilon}_p - \tilde{\varepsilon}_m}{\tilde{\varepsilon}_p + 2\tilde{\varepsilon}_m}\right)$ referred to as the Clausius-Mossotti factor, being a measure of the frequency dependent polarisability of the particle.

$$(f_{CM}) \Rightarrow f_{CM}(\varepsilon_p, \varepsilon_m) = \left(\frac{\tilde{\varepsilon}_p - \tilde{\varepsilon}_m}{\tilde{\varepsilon}_p + 2\tilde{\varepsilon}_m}\right) \qquad \textit{Equation 1-29}$$

The Clausius-Mossotti factor has limits between -0.5 and 1.0.

# Chapter 2 Dielectrophoresis

## 2.1 Introduction

This chapter presents an initial description of electrophoresis (EP), introducing some of the main concepts such as the zeta potential $\zeta$. Basic concepts are then introduced to explain the dielectrophoretic phenomenon with more complex concepts elucidated for biological applications. Initially, a physical dipole is considered with the dipole moment explained. Dielectrophoresis (DEP) for positive and negative DEP is then analysed. Finally, DEP for biological cells is clarified together with its relationship with the cell plasma membrane.

## 2.2 Elecrophoresis (EP)

EP is the induced motion of a particle carrying a net fixed charge when it is suspended in an electrolyte fluid and subjected to an electric field [5,6]. The fixed charges on the particle surface attract counter-charged ions to produce an electrical double layer as shown in *Figure 2-1*. These counter-ions screen the large electrostatic potential of the charged particles from the bulk electrolyte. The number of counter-ions decreases roughly exponentially with distance from the particle surface, until they equal the number required to maintain electrical neutrality of the bulk electrolyte solution. The electric potential reference is taken as zero in the neutral bulk fluid away from the influence of the charged particle. When an electric field is applied, an electric force acts on both the charged particles and also on the counter-ions in the electrical double layer. The particle moves and carries with it some of the laminar fluid layers close to its surface. The hydrodynamic slip plane defines where the moving particle and its bound layers of counter-ions leave behind the bulk fluid.

The ζ potential (zeta potential) is defined as the electric potential at the slip plane [6] as schematically illustrated in *Figure 2-1*.

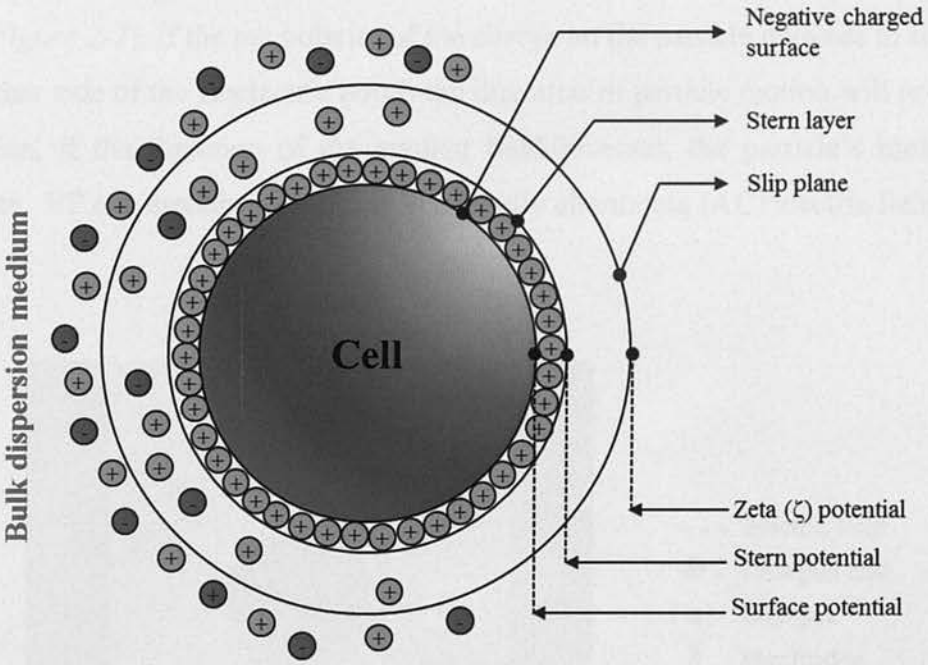


*Figure 2-1 Schematic representation of a negative charged particle in a dispersion medium. The negative particle surface, Stern layer and slip plane are indicated schematically by concentric circles. The zeta potential is located at the hydrodynamic shear surface zone between the inner boundaries and the bulk of the dispersion medium.*

The electrophoretic velocity of the particle will be dependent, after the initial viscous force is overcome, on the viscosity and the ionic concentration of the surrounding medium and zeta potential [5]. So we can define the electrophoretic mobility (*Ue*) using Henry *Equation 2-1*

$$U_e = \frac{2\varepsilon\xi\, f(ka)}{3\eta} \qquad \textit{Equation 2-1}$$

where ε is the permittivity of the medium, $\zeta$ zeta potential, $\eta$ the viscosity of the medium and *f (ka)* is Henry function which is usually approximated for values of 1.5 or 1.0.

The essential feature of EP is that it can only occur for electrically charged particles (see *Figure 2-2*). If the net polarity of the charge on the particle reverses in sign (e.g., on either side of the isoelectric point) the direction of particle motion will reverse. In addition, if the direction of the applied field reverses, the particle's motion will reverse. EP can therefore not occur in a rapidly alternating (AC) electric field.

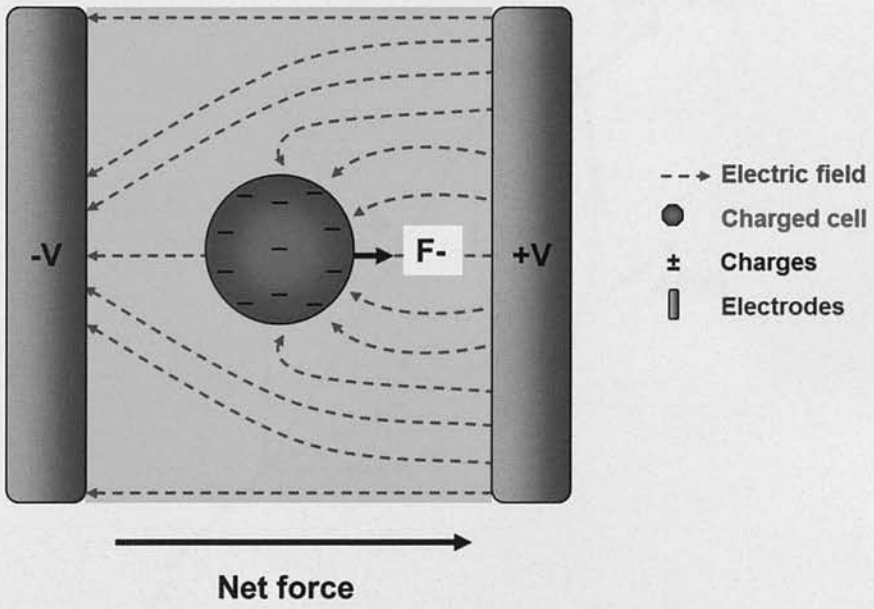


*Figure 2-2 Electrophoresis of a negative charged particle. The particle is negatively charged overall, the net force will move the particle towards the positive electrode (+V) in a uniform electrical field produced by two parallel electrodes.*

## 2.3 Dielectrophoresis

### 2.3.1 Small physical dipole

Revisiting *Equation 1-9* in section *1.3* and the electric potential $\phi$ in *Equation 1-10* we can expand the concepts of electrostatics and consider a dielectric particle in a spatial non-uniform electrical field as shown in *Figure 2-3*. The particle acquires polarisation and a dipole is formed of opposite charges as illustrated in *Figure 2-4*.

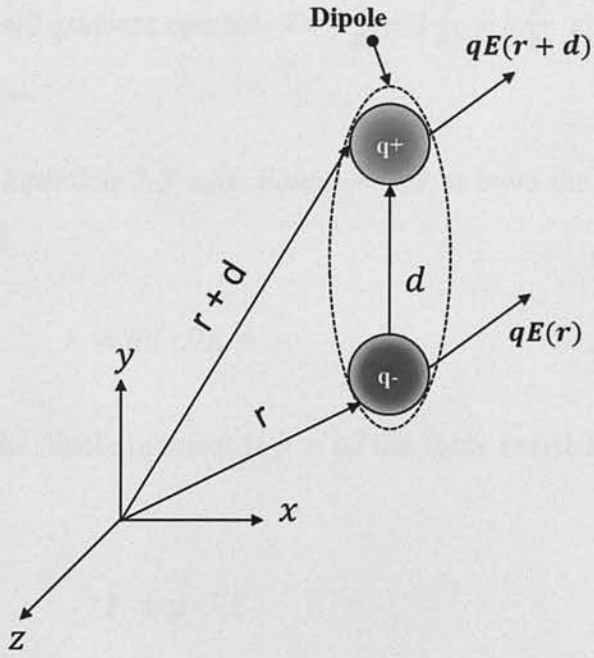


*Figure 2-3 A small dipole with zero net charge in a non-uniform electric field forming a net force on the dipole of p = qd.*

The two charges $q+$ and $q-$ illustrated in *Figure 2-3* experience different values of the electric field $E$ and therefore the net force acting on the dipole can by expressed as [7]:

$$F = qE(r + d) - qE(r) \qquad \textit{Equation 2-2}$$

*Equation 2-2* can be simplified, when d is small compared with the characteristic dimensions of the non-uniform electrical field, using Taylor series expression [8]

$$E(r + d) = E(r) + d \cdot \nabla E(r) + \cdots \frac{d^n}{n!} \cdot \frac{\partial^n E}{\partial x^n} \qquad \textit{Equation 2-3}$$

We will neglect terms $\frac{d^n}{n!} \cdot \frac{\partial^n E}{\partial x^n}$ higher than $n = 2$.

$\nabla E$ is the vector field gradient operator $\nabla = i\frac{\partial}{\partial x} + j\frac{\partial}{\partial y} + k\frac{\partial}{\partial z}$ and $E = -\nabla V$ with V the electric potential.

We can combine *Equation 2-3* with *Equation 2-2* to have the force exerted by the electric field as [4]

$$F = qd \cdot \nabla E + \cdots \qquad \textit{Equation 2-4}$$

Considering that the dipole moment is $p = qd$ the force exerted on the dipole can be expressed as [4]

$$F = p \cdot \nabla E \qquad \textit{Equation 2-5}$$

Equation 2-5 describes the DEP force as the required energy to move a dipole particle from the field $E$ to a region with no field.

### 2.3.2 Effective dipole moment

If we consider a spherical particle, immersed in a dielectric medium, we can produce an equation of the effective dipole moment that gives the same potential outlines of a point dipole as illustrated in *Figure 2-4*

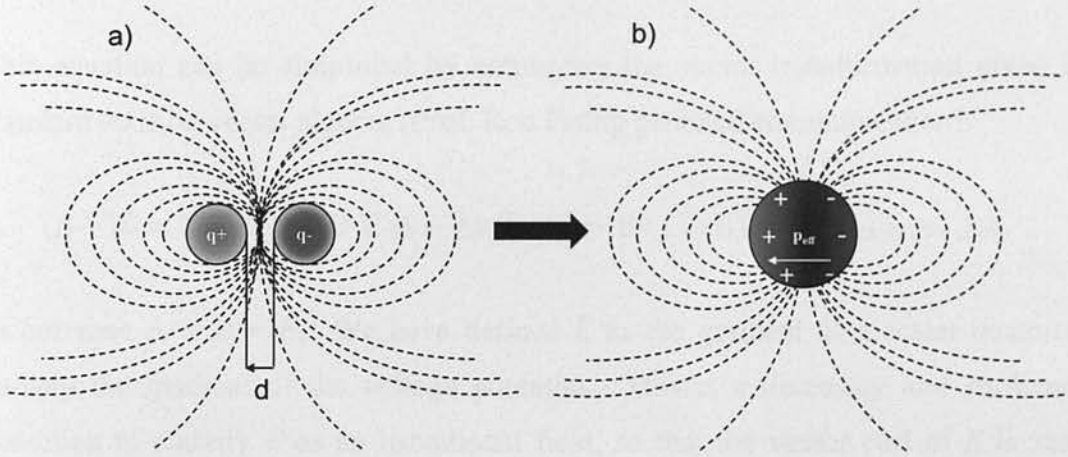


*Figure 2-4 Dipole representations. a) Point dipole of +q and-q charges at distance d apart .b) Equivalent dipole on peff on particle that as results in the same distribution of electric potential lines around the dipole.*

The effective dipole moment of a particle can be expressed as [4]

$$P_{eff} = 4\pi\varepsilon_o\varepsilon_m R^3 f(\varepsilon)E \qquad \textit{Equation 2-6}$$

where $f(\varepsilon)$ is known as the Clausius-Mossotti factor (CM), which represents the effective polarisation of the particle as function of the surrounding medium and particle absolute permittivity[3] as $\varepsilon_m$ and $\varepsilon_p$ respectively.

[3] Absolute permittivity is the product of the relative permittivity ($\varepsilon_r$) and the permittivity in a vacuum $\varepsilon_0 = 8.85\times10^{-12}\frac{C^2}{Nm^2}$

We can use *Equation 2-5* and *Equation 2-6* to give [4]

$$F_{DEP} = 4\pi\varepsilon_m R^3 f(\varepsilon)(E \cdot \nabla)E \qquad \textit{Equation 2-7}$$

The above equation can be re-written as [Prof. Ron Pethig personal communication]:

$$F_{DEP} = 4\pi\varepsilon_0\varepsilon_m R^3 [CM](E \cdot \nabla)E \qquad \textit{Equation 2-8}$$

This equation can be simplified by employing the vector transformation given in standard texts on vector algebra [Prof. Ron Pethig personal communication]:

$$(\mathrm{A}\cdot\nabla)\mathrm{B} = \nabla(\mathrm{A}\cdot\mathrm{B}) - (\mathrm{B}\cdot\nabla)\mathrm{A} - \mathrm{A}\times(\nabla\times\mathrm{B}) - \mathrm{B}\times(\nabla\times\mathrm{B}) \qquad \textit{Equation 2-9}$$

In our case A = B = $E$. We have defined $E$ as the gradient of a scalar quantity, namely the gradient of the voltage potential. This is a necessary and sufficient condition to classify $E$ as an irrotational field, so that the vector curl of $E$ is zero ($\nabla\times E = 0$). The vector transformation of $(E\cdot\nabla)\,E$ thus leads to the identity [Prof. Ron Pethig personal communication]:

$$2(E\cdot\nabla)E = \nabla E^2 \qquad \textit{Equation 2-10}$$

The above equation for the dielectrophoretic force can thus be written as:

$$F_{DEP} = 2\pi\varepsilon_0\varepsilon_m R^3 [CM]\nabla E^2 \qquad \textit{Equation 2-11}$$

Because the field is irrotational the dielectrophoretic force acting on a particle can be written as:

$$F_{DEP} = 2\pi\varepsilon_m R^3 f_{(CM)}\nabla(E \cdot E) = 2\pi\varepsilon_m R^3 f_{(CM)}\nabla E^2 \qquad \textit{Equation 2-12}$$

The previous equation is denoted as the dipole approximation for DEP [8] For more details and refinement of *Equation 2-12* regarding multipoles such as quadrupoles and octopoles can be found elsewhere in the literature [8,9].

By using the Maxwell-Wagner equation to describe the complex permittivity, which is [10]

$$\varepsilon^* = \varepsilon' - i\varepsilon'' \qquad \textit{Equation 2-13}$$

with $\varepsilon'' = \frac{\sigma}{\omega}$

and $\varepsilon'$as the permittivity and σ the conductivity and ω the angular frequency.

The Clausius-Mossotti factor can be defined as [4,11]

$$f_{(CM)} = \frac{\varepsilon_p^* - \varepsilon_m^*}{\varepsilon_p^* + 2\varepsilon_m^*} = \frac{(\varepsilon_p - \varepsilon_m) - \frac{i(\sigma_p - \sigma_m)}{\omega}}{(\varepsilon_p + 2\varepsilon_m) - \frac{i(\sigma_p + 2\sigma_m)}{\omega}} \qquad \textit{Equation 2-14}$$

Considering the two limiting cases as:

1. $\lim_{\omega \to 0} Re[f_{CM}] = \frac{\sigma_p - \sigma_m}{\sigma_p + 2\sigma_m}$
2. $\lim_{\omega \to \infty} Re[f_{CM}] = \frac{\varepsilon_p - \varepsilon_m}{\varepsilon_p + 2\varepsilon_m}$

The first limit gives the magnitude and sign of the Clausius-Mossotti factor as determined by the electrical conductivity at low frequencies. The second, high frequency limit is determined by the permittivity of the particle and medium. *Figure 2-5* shows the CM factor curves for spherical homogenous particles using arbitrary parameters for conductivity and permittivity. When the effective polarisability of the particle is the same as that of the medium, then *Re* $[f_{CM}]$ for *Equation 2-14* is zero.

The transition when the DEP became positive from negative is called the DEP cross over frequency as illustrated in *Figure 2-5*.

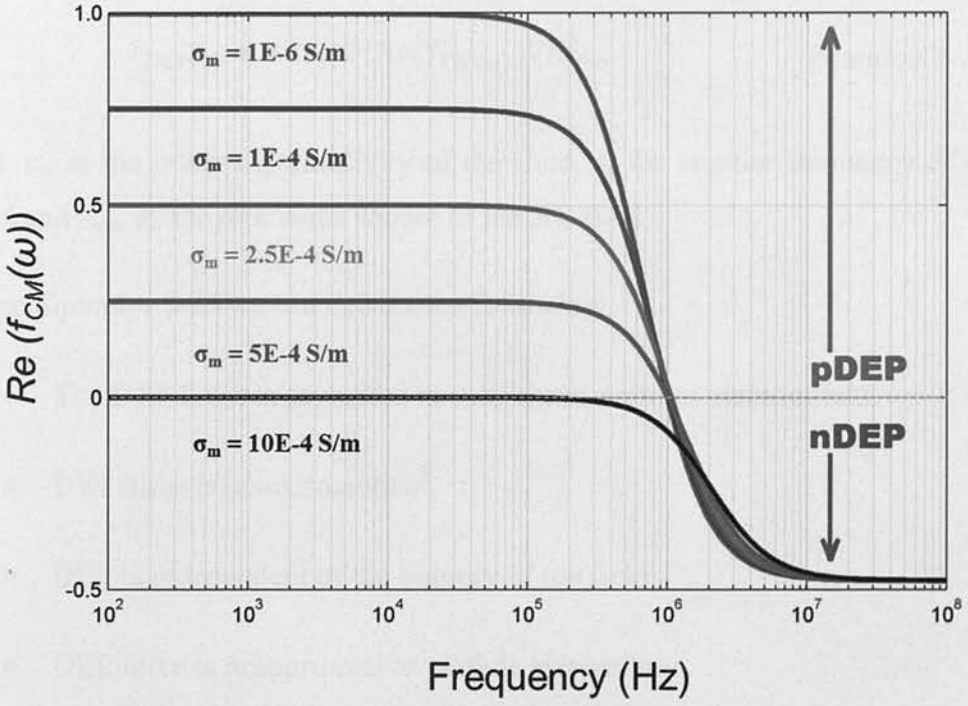


*Figure 2-5 DEP profiles of homogenous particles with arbitrary assigned medium conductivity ($\sigma_m$).The five lines of different colours have different profiles based on the medium conductivity as indicated in the graph. The relative permittivity of the medium was set to 80 (i.e., the value for an aqueous medium) and that of the particle to 3. The graph was produced using MATLAB.*

We can define the time average of the DEP force in complex form of the dipole moment and electric field as [1]

$$F_{DEP(t)} = \frac{1}{2} Re(P_{eff} \cdot E^*) \qquad \textit{Equation 2-15}$$

with $E^*$ indicating the complex conjugate[4] and $P_{eff}$ the complex effective dipole moment.

From the combination of *Equation 2-6* and *Equation 2-12* into *Equation 2-5* we have the DEP force for the time average as:

$$F_{DEP(t)} = 2\pi\varepsilon_m R^3 Re(f_{CM(\omega)})\nabla E_{rms}^2 \qquad \textit{Equation 2-16}$$

with $\varepsilon_m$ as the relative permittivity of the fluid, $\omega$ the angular frequency of the AC field and $E_{rms}$ as the root mean square of the AC field.

From *Equation 2-16* we can deduce the following:

- The DEP force is generated in only a non-uniform electric field.
- DEP force is ponderomotive[5].
- DEP is independent of the polarity of the field.
- DEP force is proportional to particle size/volume.
- The DEP force is dependent on the electrical properties of the medium and particle (permittivity and conductivity of medium and particle).
- The DEP force depends on the Clasusius-Mossotti factor for sign and magnitude ($-0.5 < f_{CM} < 1$)

*Equation 2-16* is useful because it shows that the DEP force is proportional to the particle radius cubed. This equation also shows the favourable scaling properties of DEP such as in a microfluidic device the characteristic length $L$ of the electrode and the applied voltage are proportional to the DEP force as:

[4] Complex conjugate refers to a pair of complex numbers, both having the same real part, with the imaginary parts equal in magnitude but opposite in signs.
[5] A time-averaged nonlinear force acting on the particle in the presence of the field.

$$F_{DEP} \propto \frac{\emptyset^2}{L^3} \qquad \textit{Equation 2-17}$$

From *Equation 2-17* we can see that the DEP force is inversely proportional to characteristic length $L$ of the electrode, so with reduced size of the electrodes the DEP force will increase. Also by reduction of the electrode size, the voltage $V$ can be diminished to produce the same DEP force. This is very important as the voltage can be significantly reduced in micro-devices, avoiding Joule heating effects and/or pH shifts in the surrounding medium.

### 2.3.3 Types of DEP: Positive (pDEP) and negative (nDEP)

When an electric field is applied, a charged particle will move due to Coulombic forces; however, formation of a dipole in a polarisable particle does not guarantee an associated movement through the electric field. If a uniform electric field is present the polarised particle does not experience a net force since both positive and negative halves of the dipole feel the same force in opposite directions (*Figure 2-6* left hand side).

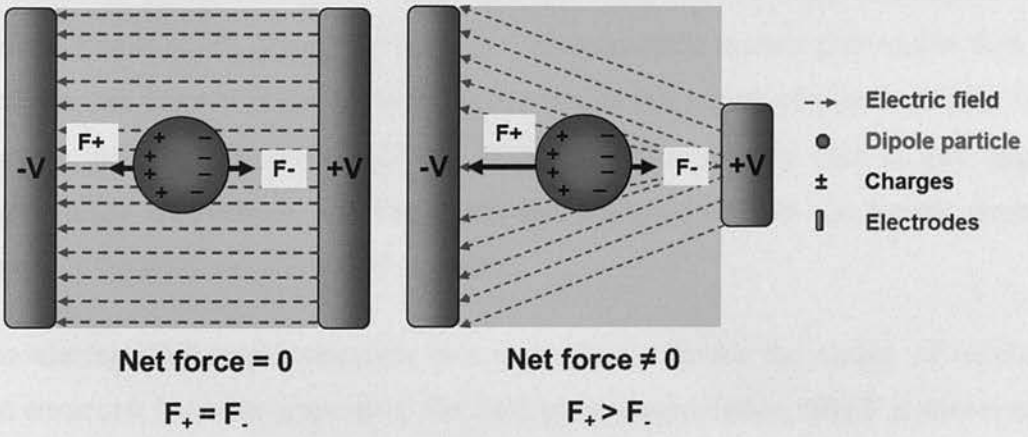


*Figure 2-6 Charged particle in uniform and non-uniform electric fields. Particle in a uniform electric field, it will experience no net force because the magnitudes of the attractive and repulsive forces are the same. On the right the particle is subjected to a non-uniform electric field with the resultant production of a net force responsible in moving the particle.*

However, if we consider a non-uniform electric field each half dipole will experience different forces, this will generate a net force that is commonly called Dielectrophoresis (*Figure 2-6* right hand side). Considering a particle in a suspending electrolyte under the influence of an electrical field, the charges present in the particle and in the electrolytic medium will be distributed at the interface between particle and medium.

This capacity of a material to produce charges at the interface between itself and a surrounding medium is called polarisability (see section *1.4* for more details on polarisation). There are two cases: when the polarisability is higher in the medium (lower in the particle) and when it is higher in the particle (lower in the medium). In the first case the charge number will be higher, so more charges accumulate in the medium side; in the second case, the opposite will be true so the charge number will be higher in the particle and therefore more particle will accumulate inside the particle surface. Both cases lead to a non-uniform distribution of charges density on opposite sides of the particle, which generate a dipole aligned to the electric field.

In a non-uniform electrical field, the particle will experience different forces at its ends due to the polarisability of the particle itself, surrounding medium and the induced dipole as illustrated in *Figure 2-7*. If the particle is more polarisable than the medium, the force will move the particle towards the region of higher electric field strength generating positive DEP (pDEP). When the opposite case is true, higher polarisibility of medium, the force will move the particle in the lowest strength region of the field, negative DEP (nDEP).

Considering DEP implementation in a microfluidic device the ability of repulsion and attraction becomes important. For biological manipulation, nDEP is favoured to reduce any possible physiological harm resulting from exposure to the high field strengths and gradients that occur at electrode edges.

Furthermore the voltage applied should be such as to avoid electroporation (in case of biological cells) and to minimise Joule heating effects [6]. This can be

significantly diminished with AC DEP in comparison to DC DEP where higher voltages are often used [6].

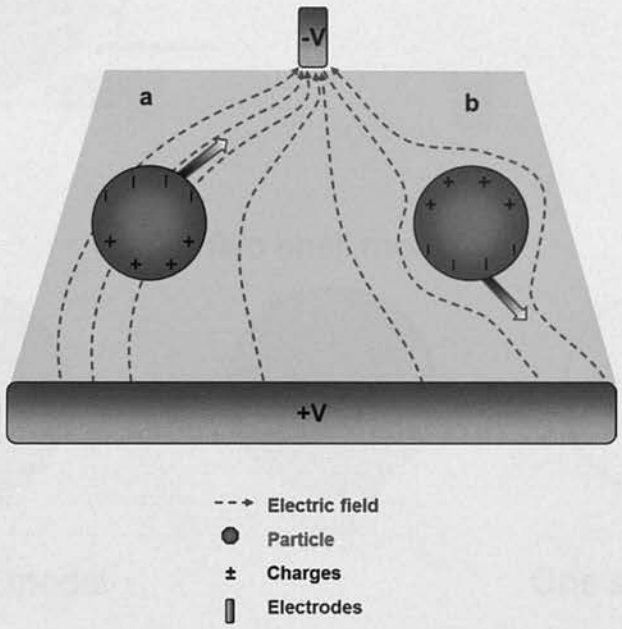


*Figure 2-7 Positive and negative DEP representation. On the left hand side (a) the particle is moved in the highest strength region of electric filed, positive DEP (pDEP). On the right hand side (b), the particle is moved in the lowest strength region of the electric field, negative DEP (nDEP).*

### 2.3.4 DEP on biological cells

Biological cells have more complex structures than homogeneous spherical particles. We can modify the expression of the dipole moment and DEP force to account for this increased complexity of the model in biological cells. The approach commonly used is called the multi-shell model [8,12]. In general, we can describe a mammalian cell as composed of a thin plasma membrane, first shell, a cytoplasmic second shell and a nucleus as a third shell. This has been schematically illustrated in *Figure 2-8*.

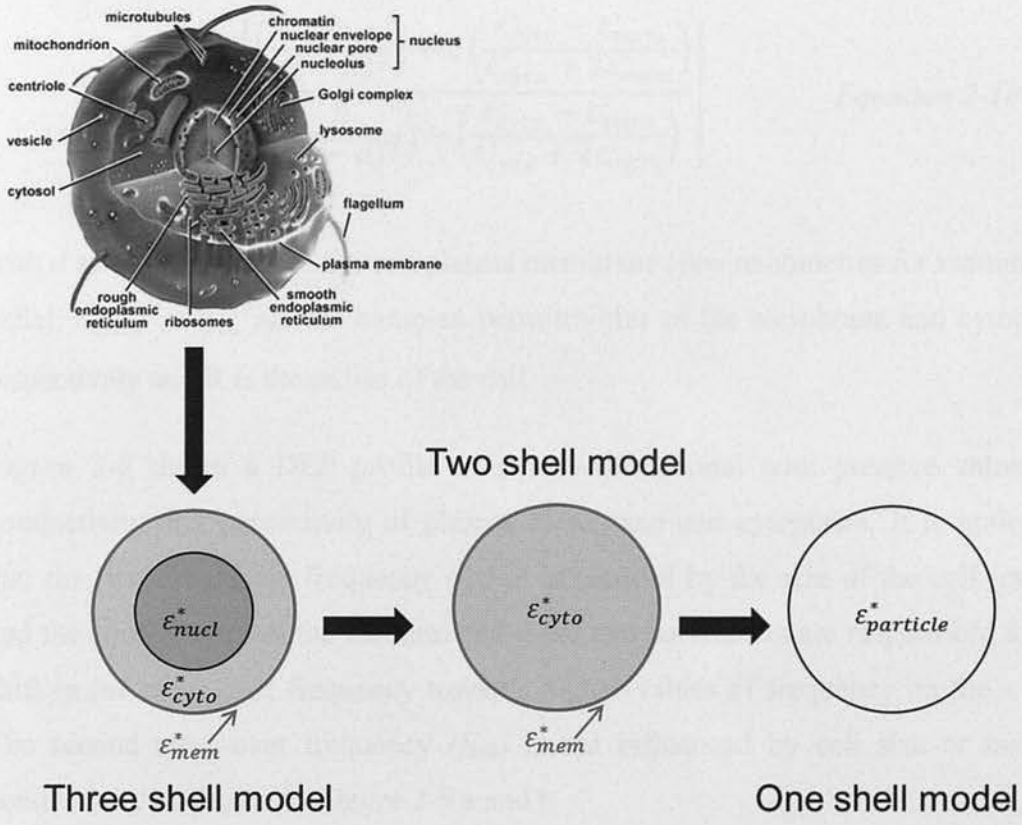


*Figure 2-8 Multishell model simplification of a biological cell structure. Representation of the cell from:* http://2.bp.blogspot.com/_Um_MFFpjTxg/TIikP9jcdPI/AAAAAAAAAtQ/laDFkBKvuXc/s1600/cell.jpg.

Considering that, a mammalian cell has a conductive cytoplasm surrounded by an insulating plasma membrane the Maxwell-Wagner polarisation will be produced at the interfaces of the shells due to differences in dielectric properties of the biological material present. Huang *et al* [13] have produced details about the mathematical model. The *effective* complex permittivity value ($\varepsilon'^*_p$) can be substituted in the Clausius-Mossotti factor instead of ($\varepsilon^*_p$) to have *Equation 2-18* [12]:

$$\varepsilon_p' = \varepsilon_{mem}^* \left[ \frac{\left(\frac{R}{(R-d)^3}\right) + 2\left(\frac{\varepsilon_{cyto}^* - \varepsilon_{mem}^*}{\varepsilon_{cyto}^* + 2\varepsilon_{mem}^*}\right)}{\left(\frac{R}{(R-d)^3}\right) - \left(\frac{\varepsilon_{cyto}^* - \varepsilon_{mem}^*}{\varepsilon_{cyto}^* + 2\varepsilon_{mem}^*}\right)} \right] \qquad \textit{Equation 2-18}$$

with $d$ as the thickness of the cell plasma membrane (few nanometres for mammalian cells), $\varepsilon_{mem}^*$ , $\varepsilon_{cyto}^*$ are the complex permittivities of the membrane and cytoplasm respectively and R is the radius of the cell.

*Figure 2-9* shows a DEP profile of a two-shell model with putative values for conductivity and permittivity of plasma membrane and cytoplasm. It is noticeable that the first cross-over frequency *($f_{xo}$)* is influenced by the size of the cell (radius) and the conductivity of the medium and these two parameters are responsible for the shift in the cross-over frequency towards higher values of frequency on the x axis. The second cross-over frequency *($f_{hxo}$)* is not influenced by cell size or medium conductivity as shown in *Figure 2-9* a and b.

Regarding the first cross-over frequency the plasma membrane of the cell acts as an insulator and so the electrical field will preferentially follow the surrounding electrolyte medium [8] When the frequency is increased (above 1 MHz), the capacitance of the plasma membrane will short circuit the interior of the cells. If the cell interior is more polarisable than the surrounding medium, the electrical field will penetrate the cell membrane and the cell will exhibit positive DEP.

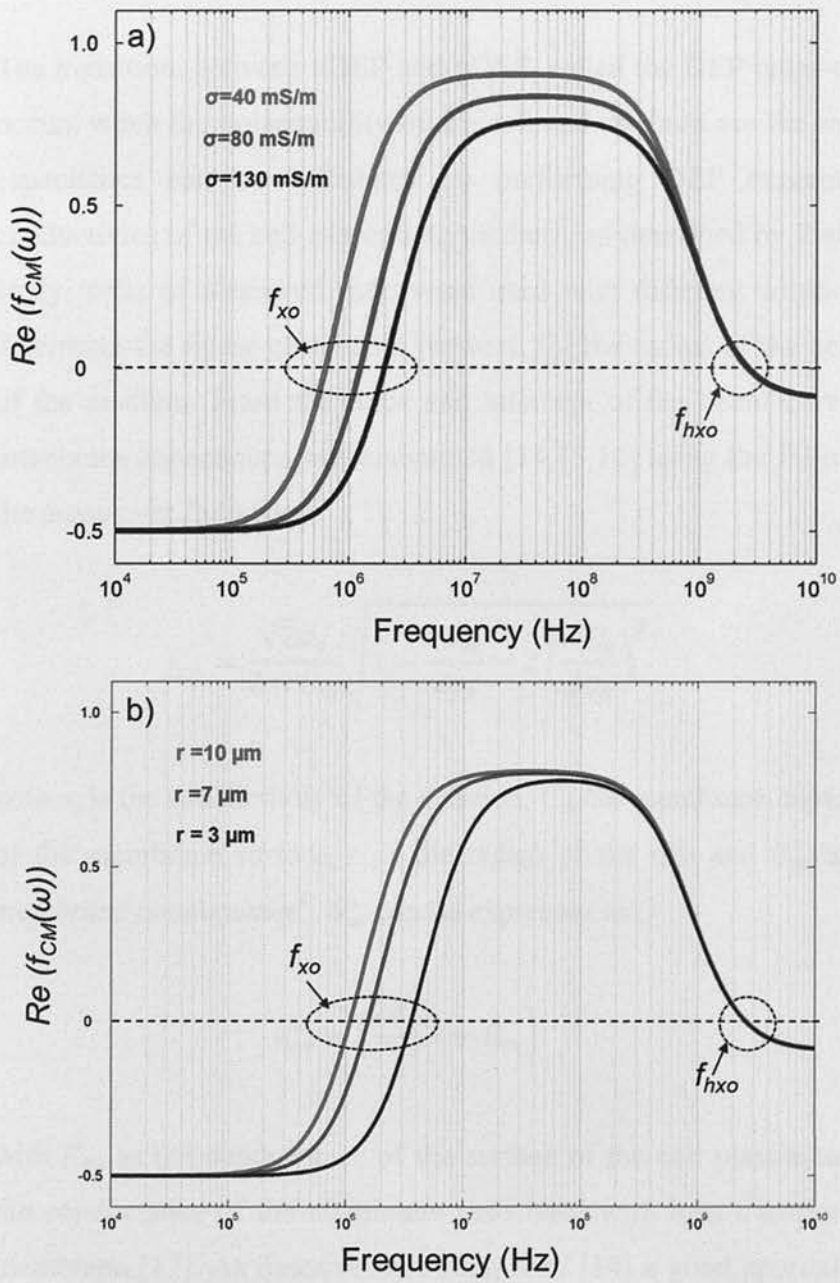


*Figure 2-9 DEP plot for cross-over frequencies with different medium conductivity (a) and cell radius (b).In graph a radius of the cells was keep constant and the conductivity of the medium was changed as indicated by the three curves. In graph b the conductivity of the medium was kept constant and the radius of the cells was changed as indicated by the three curves. Both graphs were produced using MatLab.*

### 2.3.5 Cell plasma membrane capacitance

The transition, between nDEP and pDEP, called the DEP cross-over frequency ($f_{xo}$) occurs when the polarisability of the cell and medium are the same. The membrane capacitance can be calculated by performing DEP experiments for different conductivies of the cell suspending medium, as described by Pethig *et al*[14]. In this study, cells of measured radii were used with different solution conductivities to determine the linear correlation between $f_{pk}$, the radius of the cells and conductivity of the medium. From the slope and intercept of the linear curve, the value for the membrane capacitance was elaborated [14,15,16] using the following expression for the cross-over frequency:

$$f_{xo} = \frac{\sqrt{2}\sigma_s}{2\pi r C_m}\sqrt{1 - \frac{rG_m^*}{2\sigma_s} - 2\left(\frac{rG_m^*}{2\sigma_s}\right)^2} \qquad \textit{Equation 2-19}$$

with $\sigma_s$ is the conductivity of the solution, $C_m$ the membrane capacitance per unit area of the membrane surface, r as the radius of the cell and $G_m^*$ as the *total effective membrane conductance*[6]. $G_m^*$ can be expressed as:

$$G_m^* = \left(\frac{2K_{ms}}{r^2} + G_m\right) \qquad \textit{Equation 2-20}$$

with $K_{ms}$ as the conductance of the surface of the cell plasma membrane and $G_m$ as the conductance of the membrane associated with ions transport across the plasma membrane [17]. As describe by Pethig *et al* [14] a good approximation of *Equation 2-19* can be expressed as:

$$f_{xo} \cdot r = \frac{\sqrt{2}\sigma_s}{2\pi C_m} - \frac{\sqrt{2}G_m^* r}{8\pi C_m} \rightarrow f_{xo} = \frac{\sqrt{2}\sigma_s}{2\pi r C_m} - \frac{\sqrt{2}G_m^*}{8\pi C_m} \qquad \textit{Equation 2-21}$$

[6] Conductance is defined as the ability of a material to carry electrical charge; it is measured in Siemens (S).

In *Equation 2-21* the second term can be neglected for $G_m^* << \frac{4\sigma_s}{r}$ [17] This simplifies *Equation 2-21* to:

$$f_{xo} = \frac{\sqrt{2}\sigma_s}{2\pi r C_m} \qquad \textit{Equation 2-22}$$

Alternatively:

$$C_m = \frac{\sqrt{2}}{2\pi r f_{xo}}\sigma_s \qquad \textit{Equation 2-23}$$

For a completely smooth spherical cell, the cell membrane capacitance can be expressed as:

$$C_m = \frac{\varepsilon_m \varepsilon_o}{d} \qquad \textit{Equation 2-24}$$

with $d$ and $\varepsilon_m$ as the thickness and relative permittivity of the membrane respectively and $\varepsilon_o$ as the permittivity of vacuum. The total capacitance ($C_t$) of the cell is defined as [18]:

$$C_t = 4\pi r^2 C_m \qquad \textit{Equation 2-25}$$

For erythrocytes the values of the plasma membrane capacitance has been extrapolated in several studies as 6–8 mF $m^{-2}$[19,20,21]. The values for $C_m$ have been evaluated in cells presenting projection and other morphological bound extensions on the plasma membrane resulting in higher values [22,23,24]. This demonstrates correlation between the $C_m$ and the overall roughness of the cell plasma membrane and the presence of projection/microvilli. The presence of microvilli is common; with variations in length and number due to cell's environmental conditions and/or cellular adaptations associated with differentiation/function [17,23,25]. Asami used finite element methods for numerical simulation of changes

during osmotic perturbation[7] of the dielectric properties of bound microvilli in the cell plasma membrane. However, it has also been shown that the presence of proteins of different sizes and that perturbations created by proteins-lipids bilayer interactions may play an important role in membrane capacitance [26,27].

[7] Here osmotic perturbation is intended as a disruption of the osmotic equilibrium between the cell internal solvent content and the outside environment.

# Chapter 3 Modelling and simulation

## 3.1 Introduction

In this chapter, the finite element simulation of the microfluidic device for continuous separation of specific mammalian cells is presented. The software used was COMSOL Multiphysics®. Different simulations for some parameters of DEP are presented here in order to simulate possible responses of the cells.

The simulation has been realised on a 3D geometry drawing using AutoCAD® software and it relies on heuristically chosen parameters and characteristics to optimise the computational power. The meshing has been customised to account for the minimum features and to maximise speed of computation for simulation on the most important parts of the main section of the DEP micro channel. Considerations related to fluid, particle/cell size, materials and frequencies have been chosen to maximise simulation, partially modified from the COMSOL library for customisation of this particular study.

The data presented here rely on the results produced by the software, the fluidic mechanic principles are not investigated in detail although some formulas will be presented as a brief reference to the underlining physics.

The DEP chip consists of a main channel with three inlets and three fluid outlets for the introduction and collection of cells from the micro device. In the main channel, there are 60 embedded platinum electrodes at the top and bottom of the channel angled at ~18° degrees to the direction of the fluid flow. These electrodes are grouped in three sets of five that differ in the gaps between the opposite set by 100, 75 and 50 μm distances (*Figure 3-1*) The AC non-uniform electric field is generated

by these electrodes, arranged in a 3D conformation, ensuring the funnelling of the cells of interest into the central outlet using nDEP.

The chip is able to sort cells by making use of hydrodynamic flow of suspending fluid (medium) and the deflection of the cells by the electrode edges (along their entire length), by nDEP. The chip was microfabricated by photolithographic processes commonly used in Micro-Electro-Mechanical-Systems (MEMS). This was mounted on a custom-made holder that contains the hydraulic and electric connections.

The simulation presented is for one prototype used to separate cells. However, variations of this prototype have been manufactured and used. For brevity of this thesis, only the modelling and simulation of one prototype will be presented.

## 3.2 Initial considerations

The final internal height of the DEP chamber was 100μm, although other devices were constructed with heights of 40, 60 and 80μm, respectively, with two different central inlet sizes. The two types mainly used for the sorting were the 80 and 100μm heights. It was noticed that by reduction below 80 μm there was probably clogging of the microchannel resulting in difficulties in the re-collection of cells (this will decrease sorting efficiency when DEP is applied). This was verified by microscopy using fluorescent GFP-fibroblasts recuperated after passing them through the device. Cells were counted by fluorescent microscopy for the GFP-fibroblasts before and after passage in the device without the application of any voltage in order to verify possible cell accumulation in the channel.

The placement of 60 electrodes was conceived to extend the area where the cells were subjected to DEP in order to guarantee separation. However, by simulation analysis a lower number of electrodes may achieve the same results by modulation of the inlet fluid velocity and applied electric field. In addition, the thickness of the

electrodes was considered negligible in the 3D simulation to limit the computational power required.

In the simulation the viscosity and density of the medium was approximated to the parameters of 20% sucrose solution. The density of a cell was approximated at 1110 $kg/m^3$ ($\rho$)[8].

The initial number of cells in solution for DEP sorting was kept constant at around one million/ml. This number density was chosen with the view that ~10% of the cells, on a per ml basis, would be lost due to the procedure of re-suspension in the DEP medium (before the DEP procedure) and again when re-suspended in flow cytometry buffer after DEP sorting. In addition, this cell concentration was assumed to guarantee that at least $10^5$ cells were collected for analysis by flow cytometry in order to have a significant statistical result[9].

Because of the microscale of the DEP chamber, the resulting fluid flow can be assumed to be laminar (i.e., low Reynolds number). This means that diffusion will be the main mechanism (in the absence of a DEP force) for cells to cross between adjacent fluid streamlines. However, cells are macroscopic and their diffusion coefficient is very small [29,30]. In the COMSOL simulations the diffusion coefficients for the cells was set to the lowest permitted value of $10^{-7}$ $m^2/s$. The cell separation system uses nDEP to separate cells from the two outer fluid streams by pushing them across laminar flow streams into the central fluid stream for collection at the central exit fluid port. The COMSOL simulation did not model the full length of the DEP chamber, to include the initial mixing of the three fluid flow streams, but concentrated on a section above the electrodes where laminar flow of a parabolic velocity profile was assumed.

[8] Here the density of the cell was approximated at 1110 $kg/m^3$ although, by using a micro cantilever device, values could be higher [28] K. Park, J. Jang, D. Irimia, J. Sturgis, J. Lee, J.P. Robinson, M. Toner, R. Bashir, 'Living cantilever arrays' for characterization of mass of single live cells in fluids, Lab on a Chip 8 (2008) 1034-1041.

[9] The number of cells collected, mention in the above text, was used as a minimum "rule of thumb" for Flow cytometry in order to have meaningful mathematical analysis of the data.

The simulation used the following parameters: Fluid density of 1000 kg/m$^3$, dynamic viscosity of 0.0015 Pa s, average velocity at the inlets of 330 μm/s, relative permittivity of the fluid of 80.1, solution conductivity of ~120 mS/m, initial concentration of the solute of 1mol/m$^3$ and cell size was set at 6μm radius. Voltage applied varied from 3 to 7 V pk, and CM factor values of -0.5 and -0.25 were used to simulate two levels of nDEP. The boundary conditions at the channel wall were set to fluid non-slip, as is appropriate for laminar flow, and the fluid was assumed to be incompressible.

## 3.3 Simulation

### 3.3.1 Geometry

The micro device is illustrated schematically in *Figure 3-1* where the main features and domain used in simulation are represented. The term "*main channel*" is used to describe the part of the micro device that contains the 60 electrodes. There are three inlet and three outlet fluid ports with specific functions in cell separation. The two outer inlets are responsible for driving the buffer medium and cells into the main channel, with the central inlet delivering only buffer medium. The two exit fluid ports were used to collect the fluid medium and unwanted cell types, whilst collection from the central exit port gave the wanted target cells responding to nDEP. The electrodes were orientated at an 18° angle to the direction of the buffer flowing along the channel and were located at the top and bottom of the chamber in order to generate a vertically orientated non-uniform electric field. Each electrode was of width ~15 μm and spaced 500 μm from the next one, with gaps from the corresponding opposite electrode of 100 μm for the first set of five electrodes nearest the entrance fluid ports, 75 μm for the second set of five and 50μm for the last set of five electrodes near the exit fluid ports[10] ( See *Figure 3-1* for a visual representation)

[10] The set of five electrodes modelled were on one side (top or bottom) of the channel. The 3D geometry of this set consisted of 20 electrodes that differed in opposing gaps of either 100, 75 or 50 μm.

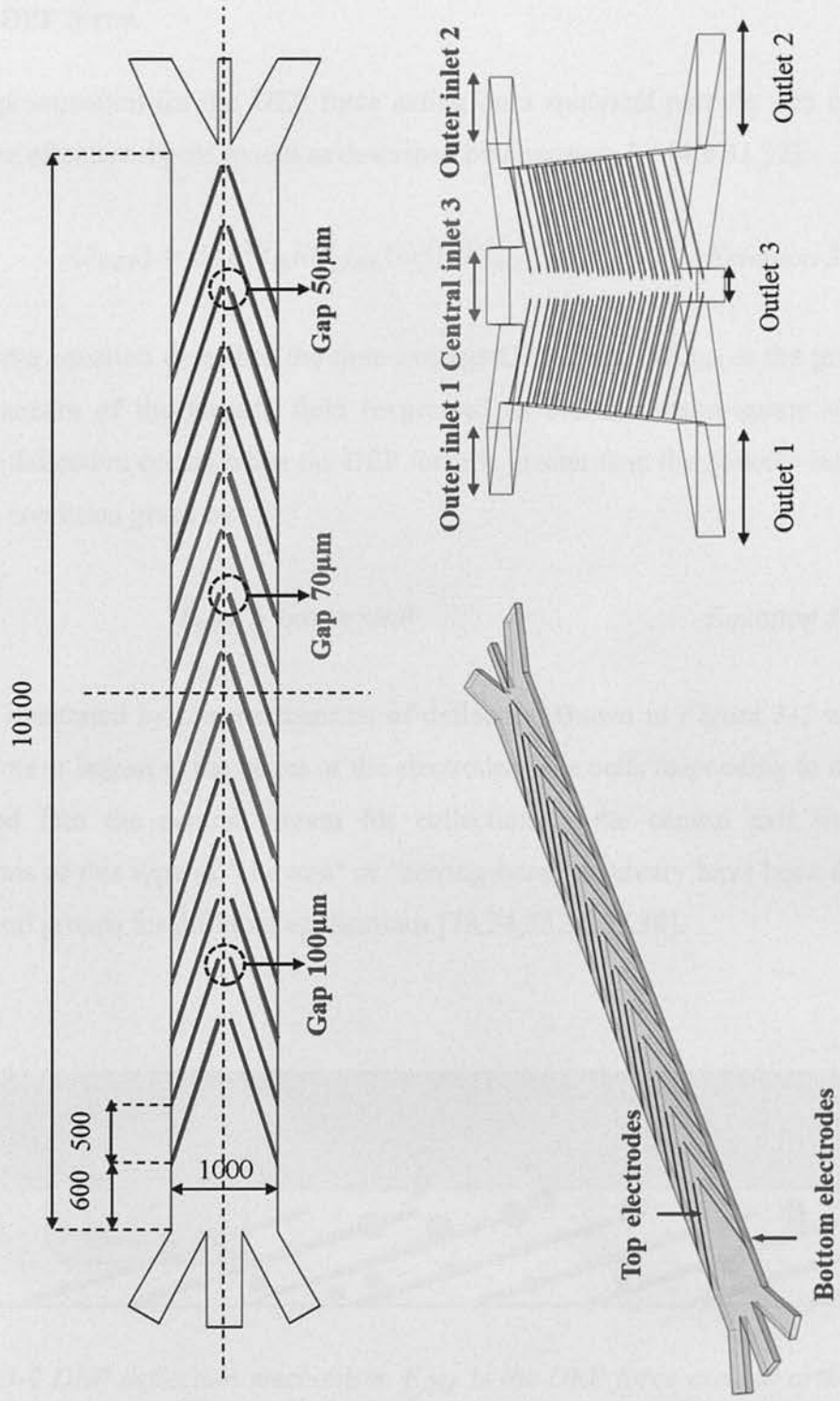


*Figure 3-1 Schematic illustration of the main channel.*

### 3.3.2 DEP force

The approximation for the DEP force acting on a spherical particle was computed using the effective dipole model as described by *Equation 3-1* [4,8,31,32]:

$$\langle F_{DEP} \rangle = 2\pi r^3 \varepsilon_m Re\big(f_{cm}(\omega)\big)\nabla E_{rms}^2 \qquad \textit{Equation 3-1}$$

The above equation describes the time-average DEP force, $\nabla E_{rms}^2$ is the gradient of of the square of the electric field (expressed as the root-mean-square value). A particle deflection occurs when the DEP force is greater than the Stokes viscous drag force, a condition given by:

$$\vec{F}_{DEP} > 6\pi\eta v r sin\theta \qquad \textit{Equation 3-2}$$

This is illustrated by the mechanisms of deflection shown in *Figure 3-2* where the DEP force is largest at the edges of the electrodes. The cells responding to nDEP are deflected into the central stream for collection at the central exit fluid port. Variations of this type of 'chevron' or 'herring-bone' geometry have been described by several groups for different applications [33,34,35,36,37,38].

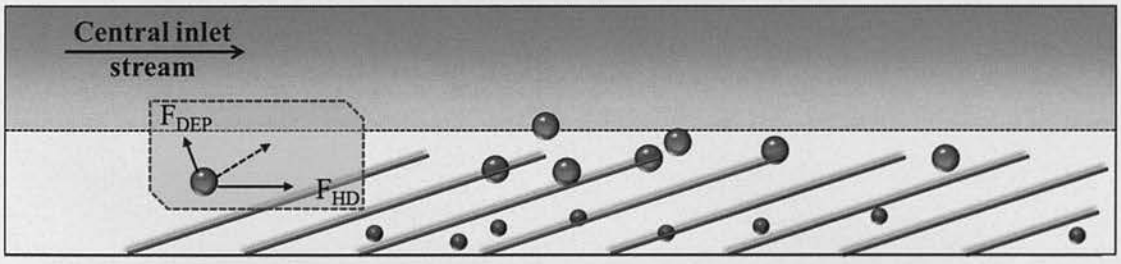


*Figure 3-2 DEP deflection mechanism. $F_{DEP}$ is the DEP force created orthogonally to the electrodes, and $F_{HD}$ is the hydrodynamic viscous drag force that accelerates the particle to the velocity of its laminar flow streamline.*

Illustrated in *Figure 3-3* are the *x* and *y* components of the DEP force values at different heights above the electrode surface, simulated for a CM factor value of -0.25, with an applied voltage of 5Vpk at the electrodes (see *Figure 3-4*) Here the electrodes were simulated with negligible thickness.

In *Figure 3-3* the components of the DEP force (x- along the chamber length, and y- across the chamber width) are shown as a function of height above the electrode plane. The maximum DEP force occurs at an electrode edge and the minimum at the centre mid-line of an electrode's upper surface. The DEP force at a distance of ~1μm from the electrode edge is approximately 43 nN in the vertical direction. *Figure 3-3* show a decrease of the *x* and *y* components of the DEP force with increasing distance from the electrode edge. In *Figure 3-3* the *x* and *y* component of the DEP force is illustrated for distances of 1, 2, 4, 8, 16, 32 and 50 μm from the electrode surface.

*Figure 3-5* illustrates the electric field and DEF force in vertical direction of the main channel. In other words, always cells experience DEP force except in the areas between electrodes (500μm gap) and in the central gap narrowing down from 100 to 50μm. The cross-sections were taken arbitrarily for the purpose of illustration. The DEP force is shown as the cross-section of the electrodes at the three gaps of 100, 75 and 50 μm. The DEP force generated is illustrated in log 10 scale for better visualisation of the data in *Figure 3-5*.

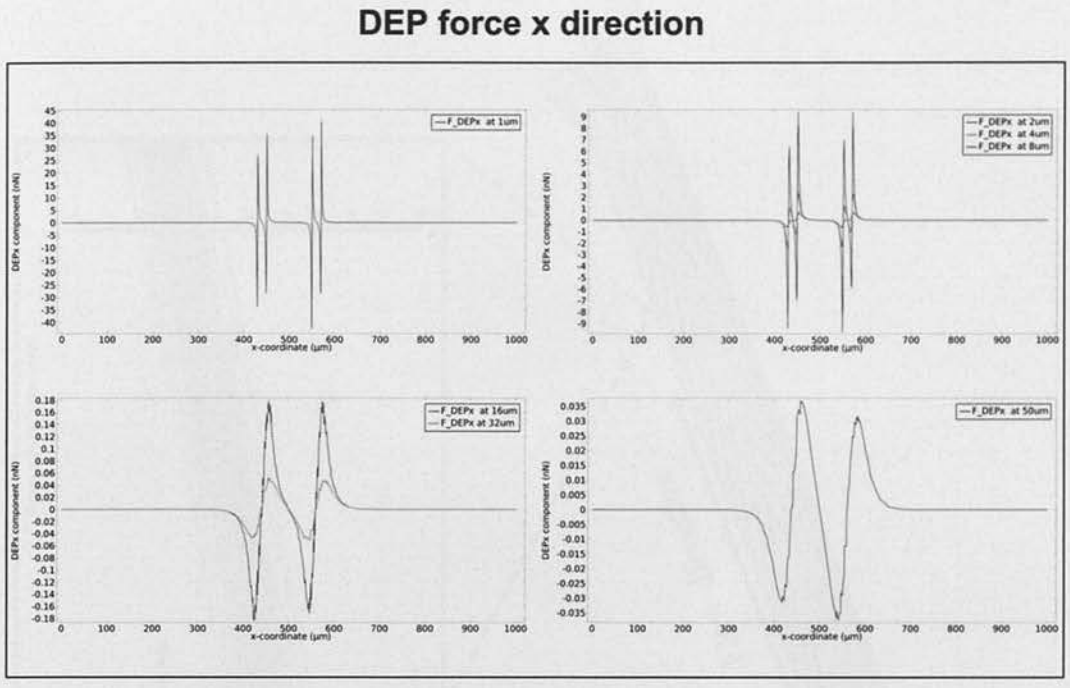


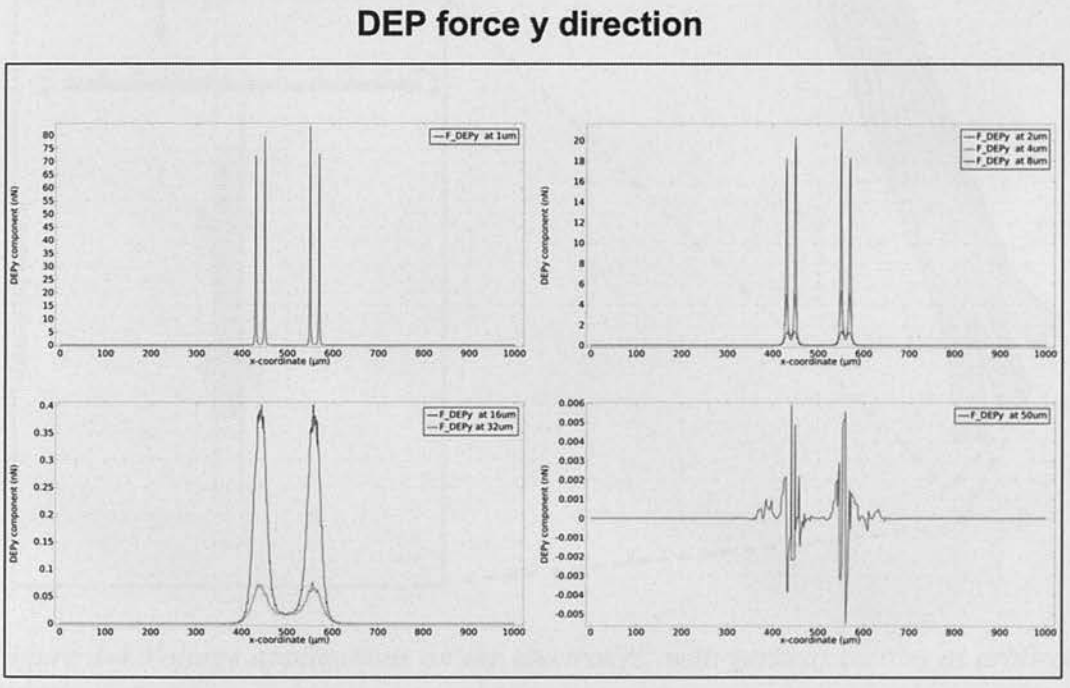


*Figure 3-3 DEP force plots for two electrodes at 100 μm apart. The plots represent the force at different heights in the main channel for this cross-line 1D plots .*

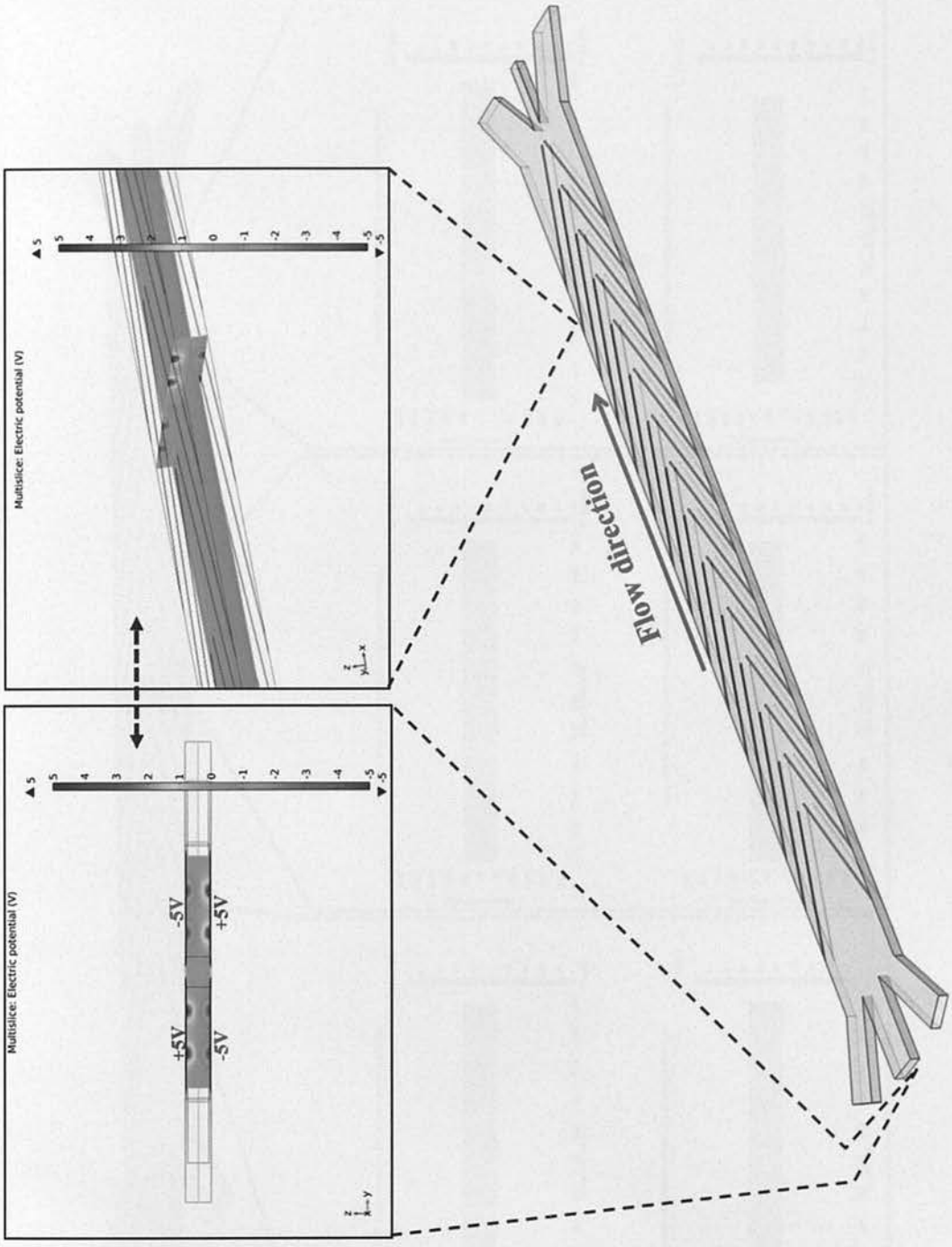


*Figure 3-4 Voltage applications on the electrodes, with vertical section at arbitrary point.*

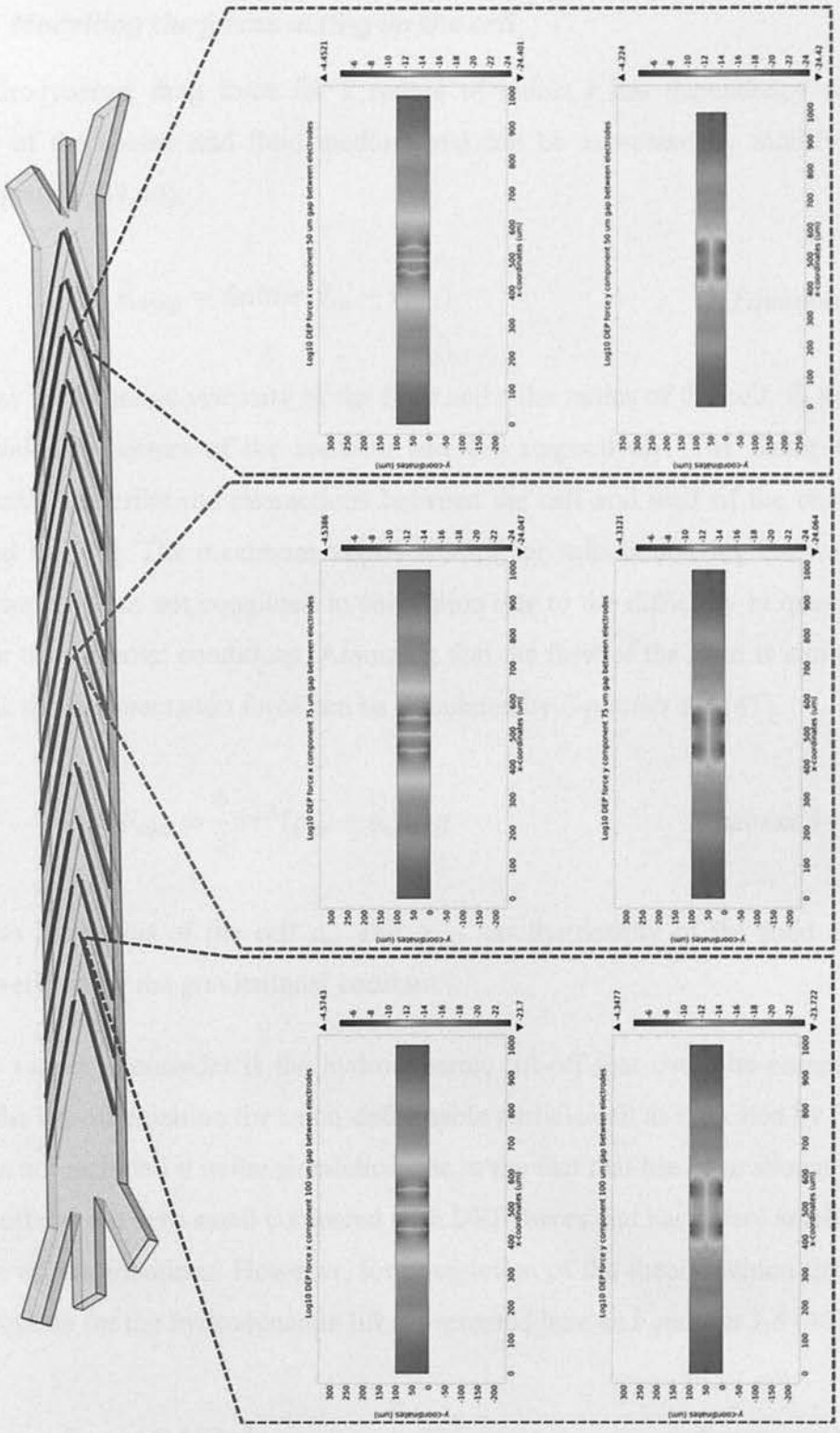


*Figure 3-5 DEP force for the three gaps at 100, 75 and 50 μm. Force is expressed in log 10 scale for x and y directions*

### *3.3.2.1 Modelling the forces acting on the cell*

The hydrodynamic drag force for a sphere of radius $r$ has dependency with the velocity of the sphere and fluid medium and can be expressed by modifying the Stoke equation [39,40]:

$$\vec{F}_{drag} = 6\pi k\eta r(\vec{v}_m - \vec{v}_{cell}) \qquad \textit{Equation 3-3}$$

With $\eta$ as the dynamic viscosity of the fluid and $r$ the radius of the cell, $\vec{v}_m$and $\vec{v}_{cell}$ as the velocity vectors of the medium and cell respectively. The factor $k$ (non-dimensional) describe the interactions between the cell and wall of the channel as described by [39]. The maximum values is ~1.7 for cells contacting the wall [39]. This parameter was not computed in simulation due to the difficulty in quantify the value for the different conditions. Assuming that the flow of the fluid is laminar and parabolic the sedimentation force can be calculated by *Equation 3-4* [41].

$$F_{sed} = \frac{4}{3}\pi r^3(\rho_m - \rho_{cell})g \qquad \textit{Equation 3-4}$$

With $r$ as the radius of the cell $\rho_m$ and $\rho_{cell}$ as the density of the fluid and cell respectively, and $g$ the gravitational constant.

Another aspect to consider is the hydrodynamic lift-off that could be computed by adding the lift-off equation for a non-deformable particle/cell as indicated by [40,42]. This was not included it in the simulation due to the fact that has been shown by [43] that the effects are very small compared with DEP forces and has a very small role in this type of fractionations. However, for completion of the theory behind the model the expression for the hydrodynamic lift is presented here as *Equation 3-5* [40].

$$F_{lift} \approx 0.153r^3\eta\frac{1}{(y-r)}\cdot\frac{dv_m}{d_y}\Big|_{y=0} \qquad \textit{Equation 3-5}$$

With $y - r$ as the distance of a particle from the bottom of the channel.

In order to determine the trajectory of the cells in the main channel the ordinary differential equations are solved for *x(t)* and *y(t)* expressed by:

$$F_x = mv'_x = F_{DEPx} + 6\pi kr\eta[v_m(y) - x(t)] \qquad \textit{Equation 3-6}$$

$$F_y = mv'_y = F_{DEPy} - 6\pi kr\eta\, y(t) - \frac{4}{3}\pi r^3(\rho_{cell} - \rho_m)g \qquad \textit{Equation 3-7}$$

With *x(t)* and *y(t)* for the positions in $x$ and $y$ directions which can be solved numerically from the two above equations. Here both $F_{DEPx}$ and $F_{DEPy}$ are function of the position $x$ and $y$ which are computed by data and mesh points of the software (see figure 33 and 34).

The boundary conditions are described as $v_y=0$ so we assume that the velocity in $y$ direction is zero after collision with top and bottom of the main channel. In addition, the interactions between particles are neglected in the simulation

### *3.3.2.2 Inlets velocities and voltage parameters*

As indicated in *Table 3-1* and *Table 3-2* the parameters analysed for the simulation were the voltage and average velocity of the three inlets (*Table 3-1*) and the CM values (*Table 3-2*). Here the fluid viscosity was set at 0.0015 Pa*s in order to account of the amount of sugar required in the DEP medium (used as fluid buffer for sorting). Sugars were added to equilibrate the osmolarity resembling more closely the value of ~320 mOsm of the DMEM used in culture. The simulation parameters were kept constant as indicated in the initial consideration paragraph of this chapter.

Starting from CM of -0.25 the different conditions are described in *Table 3-1*. The relative simulations for each condition are illustrated in figures from one to 28.

For 7V and 5V all the average velocities tested worked to produce movement of the cells in the central stream (nDEP with CM = -0.25). The only exception is when the central inflow increase to 330μm/s and the two outer inlets drop to ~41 μm/s (figure 22). A possible explanation, considering the simulation results, is that with a ratio of

approximately 1:8 in the velocities of central inlet/outer inlets the cells cannot be pushed to penetrate the central stream flow in the main channel and the simulation indicate no trajectory of the cells. Interestingly, in figure 21 can be seen that with a ratio of 1:4 in velocities between central inlet/outer inlets was enough for the cells to reach the first set of electrodes in order to be moved in the central stream accordingly to simulation results.

At 4V the central inlets inflow need to drop to a ratio 1:16 and 1:32 with the two outer inlets in order to generate enough force to move the cells in the central stream (figure 12, 13, 23 and 24). For velocities above these parameters of inflow, there is not movement in the central stream (figure 8 to 11). As described for the condition at 5V when the central inlet increase to 330μm/s and outer inlets drop to ~41μm/s (ratio 1:8) no cells can enter the main channel (figure 25).

At 3V there is not enough DEP force to produce sorting in all the simulations the nDEP at -0.25 is not enough to purify a population of cells (figure 14 to 19 and 26 to 28).

From these first simulations at -0.25 of CM the main important parameter is principally the voltage applied at the electrodes for values above 5V Pk. However, 4V could be used by fine-tuning the inlets velocity to achieve nDEP as demonstrated by simulations in figures 12, 13, 23 and 24.

Here a very small central inlet velocity, in the ratios of 16:1 or 32:1 with the outer inlets, produces separation (figure 12 and 13). In addition, when the central inlets has higher velocity in the ratios 1:2 and 1:4 with the outer inlets separation is simulated successfully as indicated by figure 23 and 24.

The 4V seems the minimum threshold to achieve separation below this value modification of the inlets velocities do not produce separation with contaminations present at the outlets as illustrated by figure 14 to 19 and 26 to 28.

### *3.3.2.3 CM simulation values*

The parameters described in the previous chapter were kept constant here in these simulations. The velocity inflow was also kept at 330μm/s for all three inlets.

In order to evaluate the effect of the CM on the separation capability of the device simulations of different conditions are illustrated in figure 29, 30, 30, 31 and 32. Figure 29 at CM of zero validate the DEP theory and underline physics. Here no DEP force act on the cells as expected the cells go through the main channel and elute in the two outer outlets.

For positive value CM of 0.25 we have pDEP here the cells are repelled by the electrodes and theoretically should move along with the outer inlet streams of the main channel. This is the case illustrated in figure 30.

With CM of -0.5, the DEP force is maximal for nDEP as illustrate by figure 31. By simulation and as expected the cells are deflected in central stream. Regarding the values of CM of 0.5 there is maximal pDEP and the cells are kept in the two outer streams as illustrated in figure 32.

## 3.4 Simulation parameters table

| Clausius–Mossotti factor of -0.25 | | | | |
|---|---|---|---|---|
| Voltage (V-Pk) | Inflow average velocities (µm/s) | | n° electrodes required x4 | Figure n° |
| | Two outer inlets | One central inlet | | |
| 7V | 330 | 330 | 1 | 1 |
| 5V | 330 | 330 | 14 | 2 |
| 5V | 330 | 165 | 7 | 3 |
| 5V | 330 | 82.5 | 5 | 4 |
| 5V | 330 | 41.25 | 4 | 5 |
| 5V | 330 | 20.625 | 3 | 6 |
| 5V | 330 | 10.3125 | 3 | 7 |
| 4V | 330 | 330 | 0 | 8 |
| 4V | 330 | 165 | 0 | 9 |
| 4V | 330 | 82.5 | 0 | 10 |
| 4V | 330 | 41.25 | 0 | 11 |
| 4V | 330 | 20.625 | 15 | 12 |
| 4V | 330 | 10.3125 | 14 | 13 |
| 3V | 330 | 330 | 0 | 14 |
| 3V | 330 | 165 | 0 | 15 |
| 3V | 330 | 82.5 | 0 | 16 |
| 3V | 330 | 41.25 | 0 | 17 |
| 3V | 330 | 20.625 | 0 | 18 |
| 3V | 330 | 10.3125 | 0 | 19 |
| 5V | 165 | 330 | 3 | 20 |
| 5V | 82.5 | 330 | 1 | 21 |
| 5V | 41.25 | 330 | 0 | 22 |

| Clausius–Mossotti factor of -0.25 continues | | | | |
|---|---|---|---|---|
| **Voltage (V-Pk)** | **Inflow average velocities (µm/s)** | | **n° electrodes required x4** | **Figure n°** |
| | **Two outer inlets** | **One central inlet** | | |
| 4V | 165 | 330 | 14 | 23 |
| 4V | 82.5 | 330 | 6 | 24 |
| 4V | 41.25 | 330 | 0 | 25 |
| 3V | 165 | 330 | 0 | 26 |
| 3V | 82.5 | 330 | 0 | 27 |
| 3V | 41.25 | 330 | 0 | 28 |

*Table 3-1 Simulation parameters for -0.25CM*

| Clausius–Mossotti factor zero (no DEP) | | | | |
|---|---|---|---|---|
| 5V | 330 | 330 | No DEP | 29 |
| **Clausius–Mossotti factor of +0.25 (pDEP)** | | | | |
| 5V | 330 | 330 | Positive DEP | 30 |
| **Clausius–Mossotti factor of -0.5 (max nDEP)** | | | | |
| 5V | 330 | 330 | 14 | 31 |
| **Clausius–Mossotti factor of +0.5 (max nDEP)** | | | | |
| 5V | 330 | 330 | Positive DEP | 32 |

*Table 3-2 Simulation parameters for different CM values.*

## 3.5 Modelling outputs

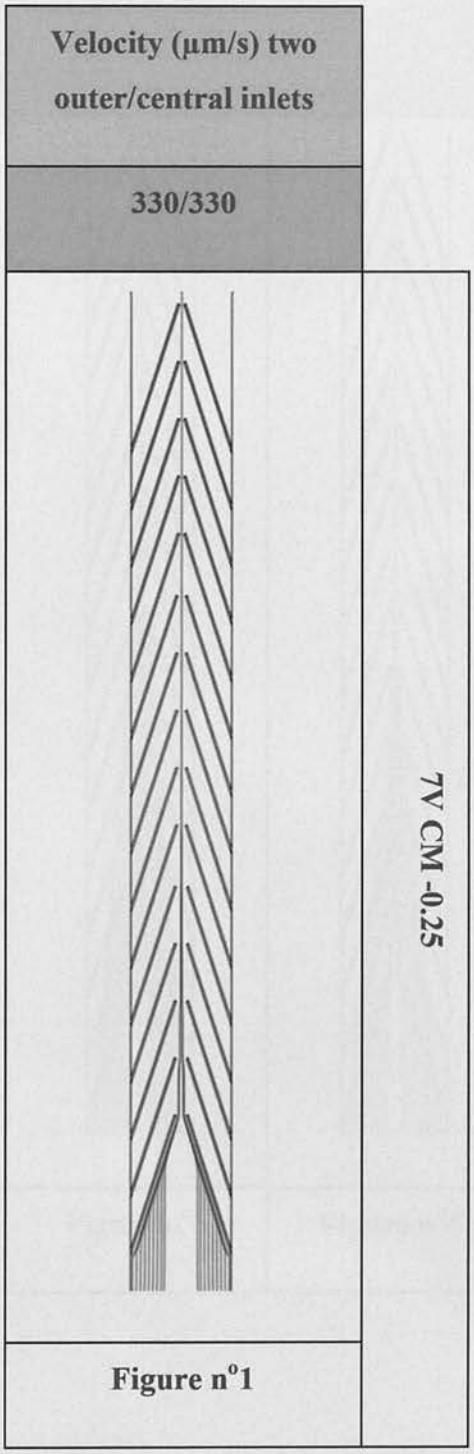


**Figure n°1**

| Velocity (µm/s) two outer/central inlets | | | |
|---|---|---|---|
| 330/330 | 330/165 | 330/82.5 | |
|  |  |  | 5V<br>CM = -0.25 |
| **Figure n°2** | **Figure n°3** | **Figure n°4** | |

| Velocity (µm/s) two outer/central inlets | | | |
|---|---|---|---|
| **330/41.25** | **330/20.625** | **330/10.3125** | |
| 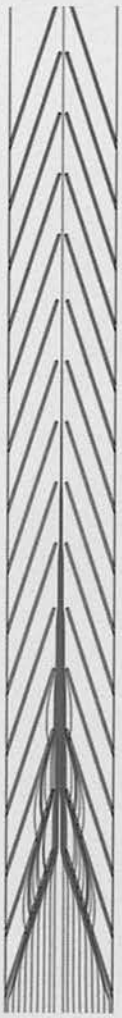 | 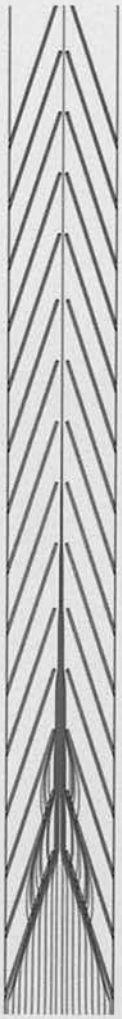 | 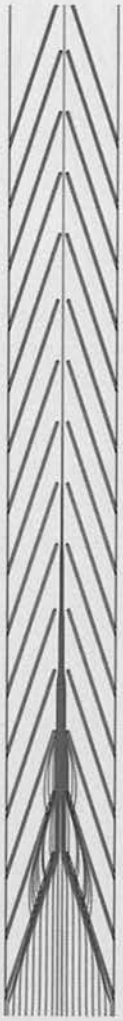 | **5V CM =-0.25** |
| **Figure n°5** | **Figure n°6** | **Figure n°7** | |

| Velocity (µm/s) two outer/central inlets | | | |
|---|---|---|---|
| **165/330** | **82.5/330** | **41.25/330** | |
| 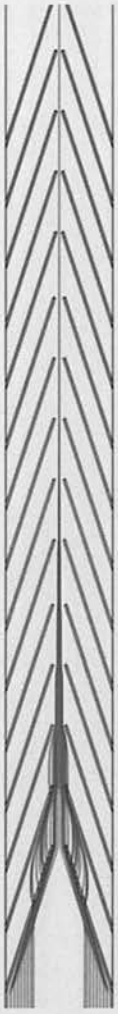 | 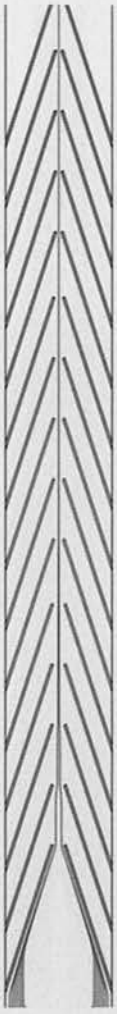 |  | **5V CM =-0.25** |
| **Figure n°20** | **Figure n°21** | **Figure n°22** | |

| Velocity (µm/s) two outer/central inlets | | | |
|---|---|---|---|
| **330/330** | **330/165** | **330/82.5** | |
|  |  |  | **4V CM =-0.25** |
| **Figure n°8** | **Figure n°9** | **Figure n°10** | |

| Velocity (µm/s) two outer/central inlets | | | |
|---|---|---|---|
| **330/41.25** | **330/20.625** | **330/10.3125** | |
|  |  | 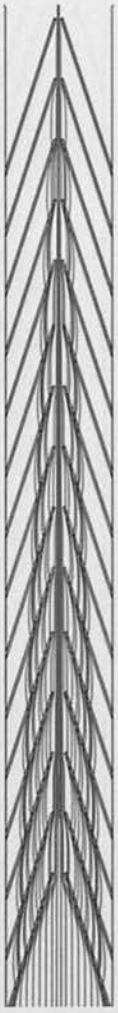 | **4V CM =-0.25** |
| **Figure n°11** | **Figure n°12** | **Figure n°13** | |

| Velocity (µm/s) two outer/central inlets | | | |
|---|---|---|---|
| 165/330 | 82.5/330 | 41.25/330 | 4V<br>CM =-0.25 |
|  | 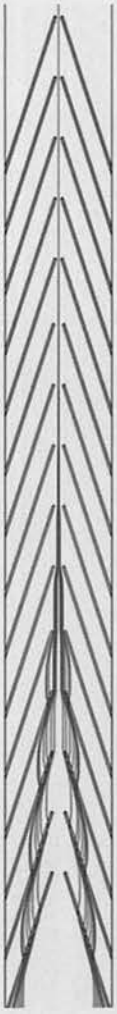 |  | |
| **Figure n°23** | **Figure n°24** | **Figure n°25** | |

| Velocity (µm/s) two outer/central inlets | | | |
|---|---|---|---|
| 330/330 | 330/165 | 330/82.5 | 3V<br>CM =-0.25 |
|  | 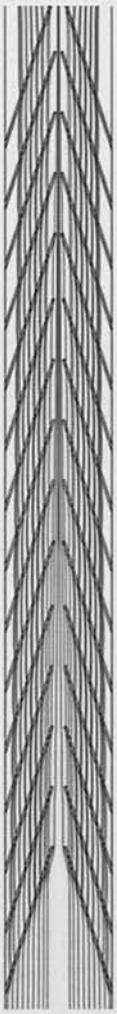 |  | |
| **Figure n°14** | **Figure n°15** | **Figure n°16** | |

| Velocity (µm/s) two outer/central inlets | | | |
|---|---|---|---|
| **330/41.25** | **330/20.625** | **330/10.3125** | |
| 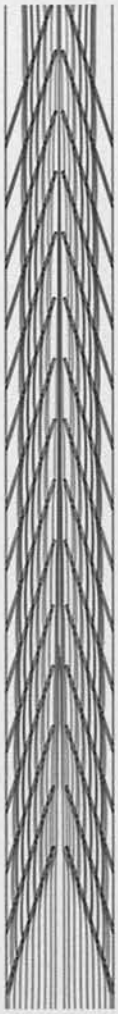 | 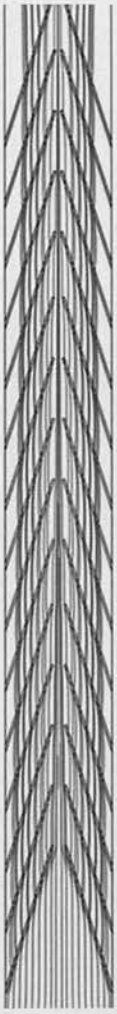 |  | **3V**<br>**CM =-0.25** |
| **Figure n°17** | **Figure n°18** | **Figure n°19** | |

| Velocity (µm/s) two outer/central inlets | | | |
|---|---|---|---|
| **165/330** | **82.5/330** | **41.25/330** | **3V CM =-0.25** |
|  | 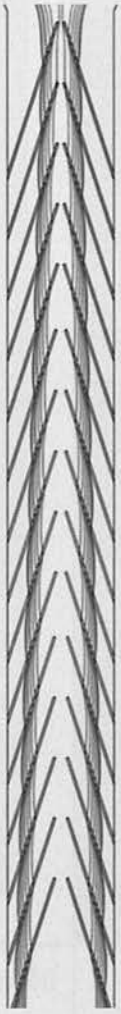 |  | |
| **Figure n°26** | **Figure n°27** | **Figure n°28** | |

| 330/330 | | 330/330 | | 330/330 | | 330/330 | |
|---|---|---|---|---|---|---|---|
|  | 5V CM = 0 |  | 5V CM = +0.25 |  | 5V CM = -0.5 |  | 5V CM = +0.5 |
| **Figure n°29** | | **Figure n°30** | | **Figure n°31** | | **Figure n°32** | |

## 3.6 Meshing samples

| Main Channel meshing | Inlets meshing |
| --- | --- |
| 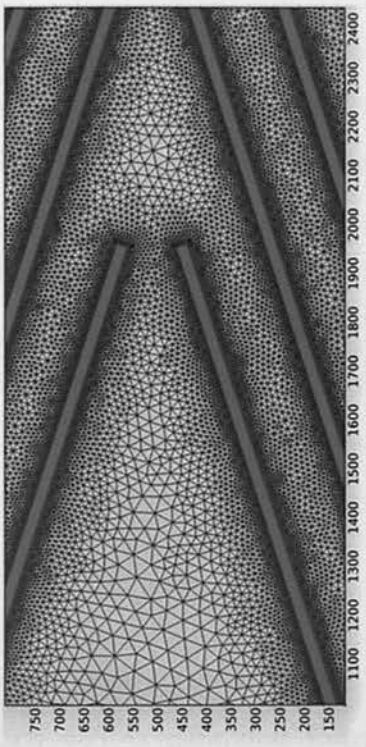 | 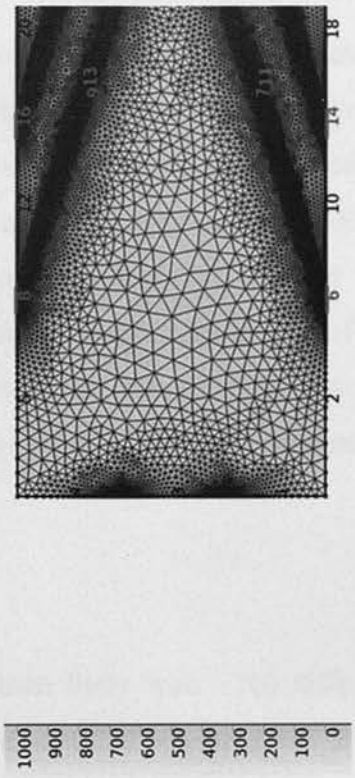 |
| **Figure n°33** | **Figure n°34** |

# Chapter 4 The cell plasma membrane

## 4.1 Introduction

In this chapter, the cell plasma membrane is analysed starting from an overall description in chapter 4.2. Initially, the main components of the plasma membrane are described in the form of the lipids classes and moieties present. Descriptions and chemical illustrations of the main components are reported. Secondly, the initial plasma membrane model of Singer and Nicolson is decribed, together with the new refinements to this original hypothesis. Thirdly, physical properties of the lipids in the plasma membrane are described, focusing on bilayer aggregation/formation. Finally, a briefly explanation of the context of the DEP experiments for cells of similar size/volume is given.

## 4.2 The lipid bilayer

There are approximately $10^{14}$ cells in a human body with ~200 different types of cells [44] Each cell is delimited from the external environment by a physical boundary called the plasma membrane [45]. This membrane regulates the passage of material in and out of the cell, isolates the cell interior content and determines the cell's overall stability [45,46,47]. The plasma membrane is constituted mainly of a double bilayer of lipids with polar head and hydrophobic tails. As shown in *Figure 4-1* transmission electron microscope image of myoblasts (C2C12) were taken by post-fixation with Osmium Tetroxide and Sodium Cacodylate, stained with Uranyl Acetate and Lead Citrate. The main sub-cellular structure, phospholipids, of the plasma membrane is indicated in *Figure 4-1*. In this cell component the van der Waals force between the hydrophobic tails is responsible for the assembly of the bilayer [46,47,48]. Phospholipids are assembled in a double layer sheet-like (two leaflets) conformation which are separated by the hydrophobic tails of ~3-4 nm in thickness [47].

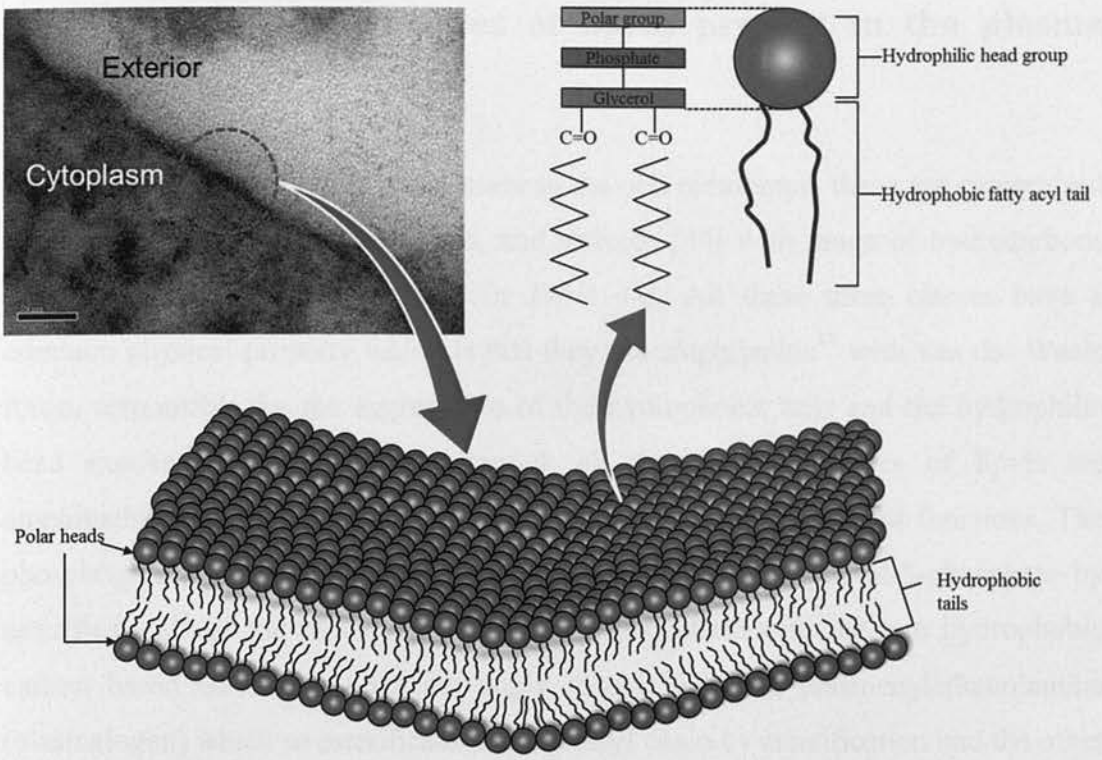


*Figure 4-1 Transmission Electron Microscopic picture of C2C12 myoblasts plasma membrane. Representation of the plasma membrane, the lipid components and related structures are illustrated on the right top side. The left-top image shows a part of the plasma membrane with the interior dark grey (cytoplasm) and exterior light grey (exterior), scale bar 50nm.*

The main functions of the membrane are to constituted a barrier for hydrophilic solutes to cross the membrane and to guarantee overall physical stability of the cell. Proteins present in the membrane are responsible for the passage of water-soluble particles otherwise not possible through the membrane only. The overall membrane bilayer conformation is obtained and preserved by van der Waals and hydrophobic forces between the lipids chains [46,47,48]. Different cells types have different membrane characteristics such as villi and overall shapes [46,47]. For clarity the external bilayer part of the plasma membrane will be defined as exoplasmic (external leaflet exposed to surrounding environment) and an internal cytoplasmic leaflet in contact to the cytoplasm (inside cell).

## 4.3 Classes and sub-classes of lipids present in the plasma membrane

There are three classes of lipids present in the cell membrane, these are categorised as phosphoglycerides, sphingolipids, and steroids [49] with range of hydrocarbons chain lengths (tails) as illustrated in *Table 4-1*. All these three classes have a common physical property which is that they are amphipathic[11] with van der Waals forces responsible for the aggregation of the hydrophobic tails and the hydrophilic head exposed towards water. Although all the three categories of lipids are amphipathic, they present different chemical structures and different functions. The phosphoglycerides are a class of lipids that derive from glycerol-3-phosphate by esterification[12] of the two OH groups of the phosphate with the two hydrophobic carbon based tails. This does not apply to one subclass, plasmenylethanolamine (plasmalogen) which as esterification in one acyl chain by esterification and the other tail by ether bond[13] to glycerol as illustrated in *Table 4-1a*$_3$ This lipid represents 20% of the total phospholipids present in humans, but the exact physiological function has not yet fully clarified [50,51]. Although more studies are emerging about correlations with peroxisome[14] malfunctioning and neurodegenerative diseases such as Alzheimer's [52,53]. Classification of this class is based on chemical moieties in the head group *Table 4-1* (in blue) of the lipid, although other differences are also present in other areas of the chemical structure. The subclasses are phosphatidylserine (PS), phosphatidylethanolamine (PE), plasmenylethanolamine (plasmalogen), phosphatidylcholine (PC), and phosphatidylinositol (PI) as illustrated in chemical structures in *Table 4-1* ($a_{1\text{-}5}$) The acyl tails of this class vary in length (number of carbon bonds see *Table 4-2* ) and saturation (carbon single or double

[11] A molecule that contains structures with characteristics of both polar (water-soluble) and non-polar (non-water soluble) nature.
[12] A chemical reaction between an acid and an alcohol which produces the release of water as by-product.
[13] Ether bond is oxygen attached, in this case, to two C atoms in form of C-O-C. This linkage is between acyl chain and glycerol.
[14] Peroxisome is an organelle thought to be responsible for synthesis of plasmalogens more details are provided in references 52 and 53.

bonds present). The most abundant phosphoglycerides in plasma membrane is phosphatidylcholine [47,49]. The second class of lipids are the sphingolipids that are derived from sphingosine (as illustrated in purple in *Table 4-1* in $b_{1\text{-}3}$), which is composed of a long chain of hydrocarbons attached to amino alcohol (sphingosine amino group). In this subclass the most abundant substructure in membranes is sphingomyelins with amino group terminal phosphocholine as shown in *Table 4-1* $b_1$[54]. However, a second subclass of sphingolipids contains a polar head composed of sugars. These compounds are identified as glycolipids/glycosphingolipids (*Table 4-1* $b_2$ and $b_3$). The basic structure of glycolipids is a glucose molecule attached to the sphingosine backbone as indicate in *Table 4-1* $b_2$. Gangliosides are another type of subclass similar to cerebrosides with added sugar chains linked to sialic acid as indicated in *Table 4-1* $b_3$. These classes of lipids normally associate with themselves, cholesterol, and proteins (glycosyl phosphatidylinositol anchor[15]) to produce aggregates denoted as "*lipids rafts*" one subset of this rafts are define as caveolae [48,54,55,56]. Caveolae are invaginations produced by the caveolins proteins that associate with cholesterol [57,58]. The turnover of this membrane sub-domain is fast between formation and dispersion mainly to the chemical saturation of the acyl groups and hydrogen bonds of the sphingolipids [48,56]. The function of these rafts is not fully understood at the present moment, however it is thought that they are playing an important role for cell signalling and nutrient transport across the plasma membrane of the cell [48,56].

The third class of compounds found in membrane are steroids in the form mainly of cholesterol [48,59]. The basic structure is a four ring hydrocarbons, which is highly hydrophobic alone, but with the presence of a hydroxyl group (OH in blue in *Table 4-1*c makes this compound amphipathic due to the hydroxyl interaction with water. Mammalian plasma membranes are rich in cholesterol [48] but due to its

[15] They are proteins that present covalent bonding to the lipids. The tail of the lipid, which is hydrophobic in nature, is localized in one leaflet of the membrane anchoring the protein to the membrane, although the polypeptide structure of the protein does not penetrate the bilayer.

hydrophobicity cannot create lipid bilayers on its own without other type of lipids present.

| Membrane lipids components | Name/ *Class* |
|---|---|
| 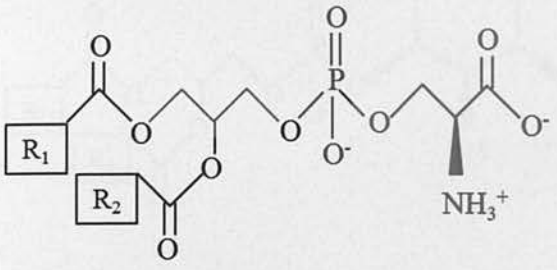 **$a_1$)** | Phosphatidylserine (PS) *Phosphoglycerides* |
| 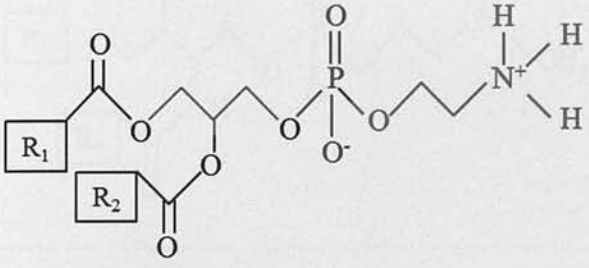 **$a_2$)** | Phosphatidylethanolamine (PE) *Phosphoglycerides* |
| 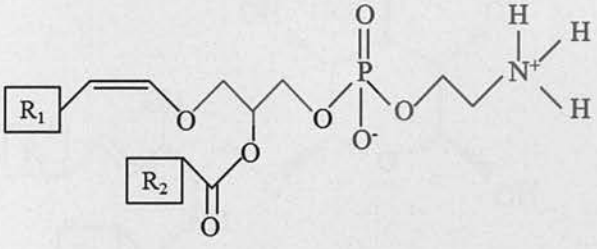 **$a_3$)** | Plasmenylethanolamine (plasmalogen) *Phosphoglycerides* |
| 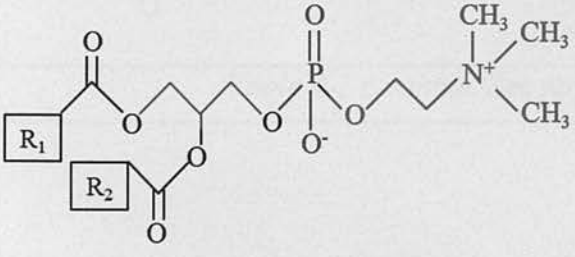 **$a_4$)** | Phosphatidylcholine (PC) *Phosphoglycerides* |

*Table 4-1 see page 67 for legend text*

| Membrane lipids components | Name/ *Class* |
|---|---|
| 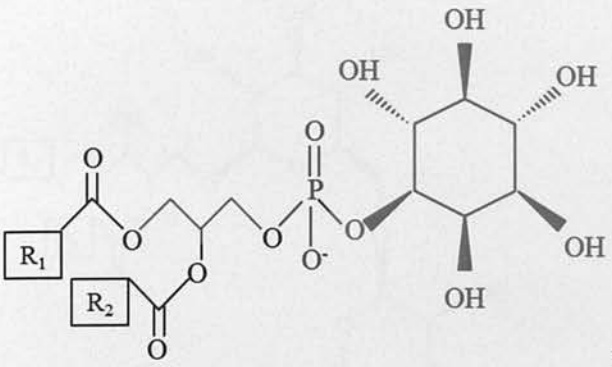 **$a_5$)** | Phosphatidylinositol (PI)<br>*Phosphoglycerides* |
| 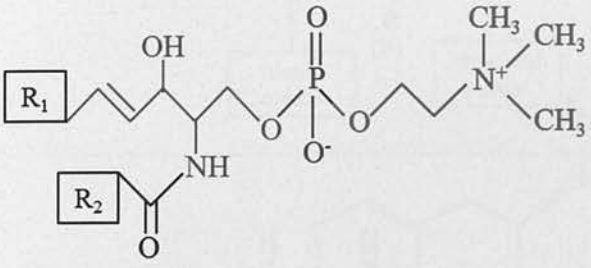 **$b_1$)** | Sphingomyelins (SM)<br>*Sphingolipids* |
| 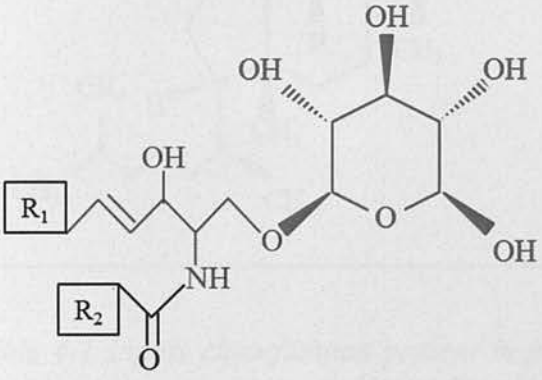 **$b_2$)** | Cerebrosides (Cer)<br>*Sphingolipids/*<br>*GlycoSphingolipids* |

*Table 4-1 continue. See page 67 for legend text*

| Membrane lipids components | Name/ *Class* |
|---|---|
| 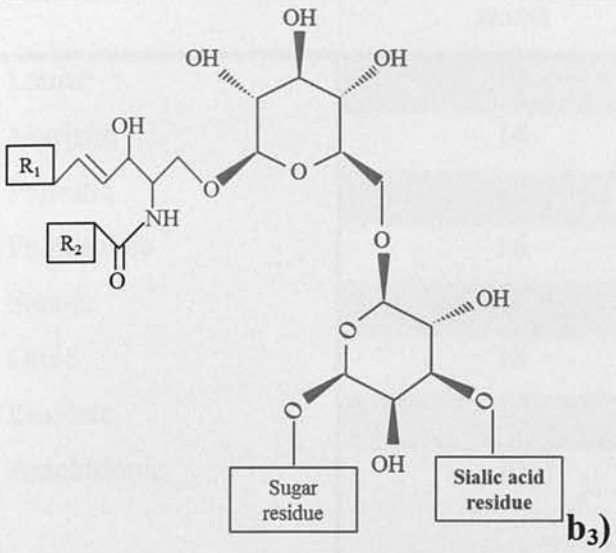 **b3)** | Ganglioside<br>*Sphingolipids/*<br>*GlycoSphingolipids* |
| 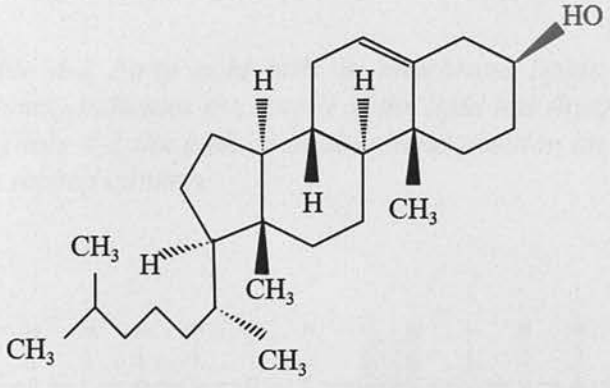 **c)** | Cholesterol<br>*Steroids* |

*Table 4-1 Lipids classification present in plasma membrane (from page 65 to 67). The blue colour structures indicates the polar head of the lipid, the red colour is the phosphate link, and the purple colour indicates a common derivative chemical molecules for the specific class. $R_1$ and $R_2$ signifies the chain of hydrocarbons (tail of the lipid) attached to the glycerol link when present. $a_{1\text{-}5}$ are the subclasses of lipids derived from phosphoglycerides. $b_{1\text{-}3}$ are the subclasses of lipids derived from sphingolipids and c is the cholesterol derived from the steroid class.*

| Name | Number of carbon atoms | Double bond position |
|---|---|---|
| Lauric | 12 | 0 |
| Myristic | 14 | 0 |
| Palmitic | 16 | 0 |
| Palmitoleic | 16 | 9-*cis*[16] see *Figure 4-2* |
| Stearic | 18 | 0 |
| Oleic | 18 | 9-*cis* |
| Linoleic | 18 | 9-*cis*, 12-*cis* |
| Arachidonic | 20 | 9-*cis* , 8-*cis*, 11-*cis* and 14-*cis* |

*Table 4-2 Fatty acid tails in membrane lipids. The carbon atoms number (first column) indicates the length of the lipid tail (hydrocarbon chain as indicated as $R_{1/2}$ in Table 4-1 the kink or double bond position on the fatty acid chain is indicated in the second column.*

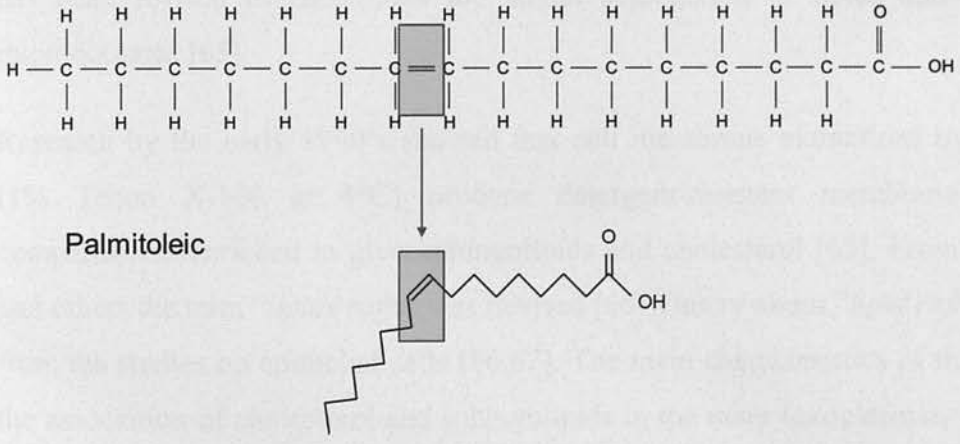


*Figure 4-2 Representation of kink/double bond of palmitoleic acid at 9-cis position of the hydrocarbon chain.*

[16] *Cis* conformation indicates that the two hydrogens atoms of adjacent carbon atom are on the same side of the double bond between carbon atoms.

## 4.4 Cell membrane models and new findings

The "*mosaic fluid model*" has been adopted for a long time since 1972, when it was first proposed by Singer and Nicolson [60]. They first described the organisation of the cell membrane on a molecular scale with the lipid bilayer as a 2D neutral solvent for the embedded proteins, with minor influences of the proteins itself [56]. More recently, new evidences emerged that the lipids, present in membrane, are in several different physical states (phases) and not only as a fluid disordered liquid phase as proposed by Singer and Nicolson [56,61]. These physical phases comprise liquid-order/disorder and gel (semi-frozen state) to enhance the fluidity of the membrane [56,62]. The exact characterisation of the different phases of lipids in complex cellular structures is still difficult to achieve [56].From the Singer and Nicolson model new refinements of the plasma membrane have emerged [63]. The density and location of the proteins, present on the plasma membrane, has been redefined [63]. For example, in human erythrocytes the entire inner and outer leaflets are covered in proteins, with transmembrane helical proteins occupying ~23% of the entire plasma membrane core [63,64]. The structural model proposed by Singer and Nicolson also has been revised to encompass the lateral segregation of lipids and protein in microdomains [63].

Research by the early 1990's showed that cell membrane extractions by detergent (1% Triton X-100 at 4°C) produce detergent-resistant membrane (DRM)[17] compartments enriched in glycosphingolipids and cholesterol [65]. From this result and others the term "*lipids rafts*" was devised [66].Theory about "*lipid raft*" emerged from the studies on epithelial cells [66,67]. The main characteristics of these rafts is the association of cholesterol and sphingolipids in the outer (exoplasmatic) leaflet of the bilayer. The interactions of saturated hydrocarbon chains of the sphingolipids with cholesterol produce a liquid ordered state of the membrane, due to the tight binding of intercalated cholesterol with hydrocarbon tails of the sphingolipids

[17] Many acronyms are used to define DRMs depending on the scientific paper - sometime they are referred as: Detergent Insoluble Glycolipid enriched membrane domain (DIG) or Detergent-Insoluble Membranes (DIMs), lipids rafts and membrane rafts.

[56,68]. The precise characterisation and interaction between leaflets of the plasma membrane has been argued and several studies have produced different models to address the interactions between sphingolipids and cholesterol [61,68,69]. In addition, the size of the rafts has been reported with variations between studies from 50nm [70,71] to smaller size around 20 nm [70,72]. Other forwarded hypotheses concern possible compartmentalization of these structures within limits related to cytoskeletal meshwork[73].

Studies have used different biochemical techniques to validate the existence and elucidate the biochemistry of the rafts [70,71,74,75] and membrane lateral heterogeneity has been accepted[76]. However debate around the lipids raft is still open at the time of this present work [63,77].

Considering the protein contribution to the raft structure, this includes glycosylphosphatidylinositol also known as GPI anchor protein, acylated[18] proteins (Src kinase family), G proteins, Hedgehog and transmembrane proteins (palmitoylated[19]) [78,79,80]. By using chemical manipulation, such as cholesterol depletion (Methyl-β-cyclodextrin), cholesterol inhibition (Lovastatin), the proteins associated with the raft can be dissociated and studied *in vivo* [56].

Another important aspect of the rafts in plasma membranes is that they are distributed in relation to the cell type [56,59]. For example, in fibroblasts this type of structures are found all around the cell's surface when it is considered that 45% of the plasma membrane is made up of sphingolipids [56,66,81]. Sub-domains considered a sub-set of the lipids rafts are caveolae, which could be described as invagination or flask-shaped inclusions of the plasma membrane[57]. These structures are formed by the protein caveolin which tightly binds to cholesterol[57,58].The caveolae have been associated with cell processes such

[18] Proteins with an acyl group attached, which are composed of a carbon atom double bonded to oxygen and organic substituent group (organyl)
[19] Palmitoylated proteins are proteins with an attached fatty acid (palmitic acid)

endocytosis, cholesterol transport, transcytosis[20] and calcium regulation in muscle differentiation [82,83]

## 4.5 Physical properties of the lipids in the plasma membrane and principle of bilayer formation

The lipids comprising the plasma membrane or any other membrane present in the cell are dynamic chemical structures. Considering a two-dimensional plane, thermal forces allow rotation along the axes and lateral diffusion between leaflets of the membrane [84]. Considering that the motions are lateral or rotational, the central core of acyl chains is localised in the hydrophobic region of the bilayer.

The exchange rate of motion of a single lipid is approximately $10^7$ times per second in rotational interchange and the diffusion constant can be in the range of $10^{-8}$ $cm^2/s$ [47,59,84]. This diffusion rate is slower in plasma membrane than in synthesised membranes consisting of only phospholipids, suggesting that interaction of lipids with integral proteins may cause more stable aggregation[59].

Considering the length of the hydrocarbons chains in lipids, we can see a range with distribution around 15 carbon atoms (see *Table 4-2* and *Figure 4-3*) [44]. With shorter chains the bilayer will be not formed and with longer chains the later diffusion is impaired ( bilayer too viscous see *Figure 4-3*) [44].

Long hydrocarbons chains will have aggregative tendency producing a compact structure as in a gel-like state. The opposite with shorter tails will have less van der Waals interaction and so producing a more fluid membrane as illustrated in *Figure 4-3* [44,59]. Another important property is the size of the lipids heads that influence the curvature of the membrane locally [59]. For example phosphatidylcholine with large head group and long tails will produce a cylindrical shape overall (flatter membrane) as oppose to phosphatidylethanolamine with small head group and long

[20] Transcytosis is the cell process responsible for the transport of macromolecules (such insulin and complex sugars) across the cell.

hydrocarbon chains that will produce a cone shape overall. This combination of these two overall shapes can play a role in the formation of blebs, microvilli and other morphological changes of the plasma membrane[59].

Lateral diffusion, in the bilayer, is dependent upon its composition, the hydrocarbons chains (tails) and temperature as illustrated in *Figure 4-3*. Since every $CH_2$ group has a length of around 0.1 nm the overall size of the hydrocarbon chain is ~ 2nm in each leaflet of the bilayer [44,85]. This is equal to a total bilayer thickness of ~ 4-5 nm [44,85]. We need also to consider the presence of cholesterol that can be as much as 17% of the total amount of lipid, as for example in red blood cells [44]. Cholesterol with much larger proteins, embedded in the bilayer, increase the overall thickness of the membrane [44].

As we have previously discussed the plasma membrane is composed of inhomogeneous structures, as the lipid rafts, that determine chemical and spatial difference of the membrane structure [66]. This entails different level of ordering between the hydrocarbons chains with separate mechanical properties to accommodate different type of proteins [44,86].

Using the known values from C-C bond from literature [44,87,88] the volume ($V_{hcc}$ ) of a single saturated (no double bonds present in the chain) hydrocarbon chain is expressed by [44]:

$$V_{hcc} = 27.4 + 26.9(n_C^o)(10^{-3}nm^3) \qquad \textit{Equation 4-1}$$

with $n_C^0$ as the number of carbon atoms with maximal hydrocarbon chain length ($L_{hcc}$) as:

$$L_{hcc} = 0.154 + 0.126(n_C^o)nm \qquad \textit{Equation 4-2}$$

In *Equation 4-1* and *Equation 4-2* increase length of the hydrocarbon chain (more C-C bonds and so more C atoms) will simplify the two equation as:

$$V_{hcc} = 26.9(n_C^o)(10^{-3}nm^3) \qquad \textit{Equation 4-3}$$

*With the constant term neglected*

$$L_{hcc} = 0.126(n_C^o)nm \qquad \textit{Equation 4-4}$$

*With the constant term neglected*

From the simplified expressions, we can derive the effective cross-sectional area $A_{hcc}$ of the hydrocarbon chain by:

$$A_{hcc} = \frac{V_{hcc}}{L_{hcc}} \qquad \textit{Equation 4-5}$$

*Equation 4-5* has been estimated as 0.21 $nm^2$[44] for a single hydrocarbon chain. However, in bilayers the head of the lipid present an area greater than the area of a single hydrocarbon chain. The area has been calculate for many head groups ($A_h$) of phospholipids to be 0.5 $nm^2$[44]. The difference between $A_h$ and $A_{hcc}$ (hydrocarbons chains accounting for kinks due to carbon double bond) needs to be consider in order to efficiently pack the lipids.

Now that the area of the head group and the volume of hydrocarbons chains are determined, the total number of molecules in a given area and volume of a sphere (micelle[21]) with radius R can be calculated.

[21] Micelles are surfactant (amphiphilic lipids) molecules that aggregate in a liquid colloid (solution with even distributed in solution).

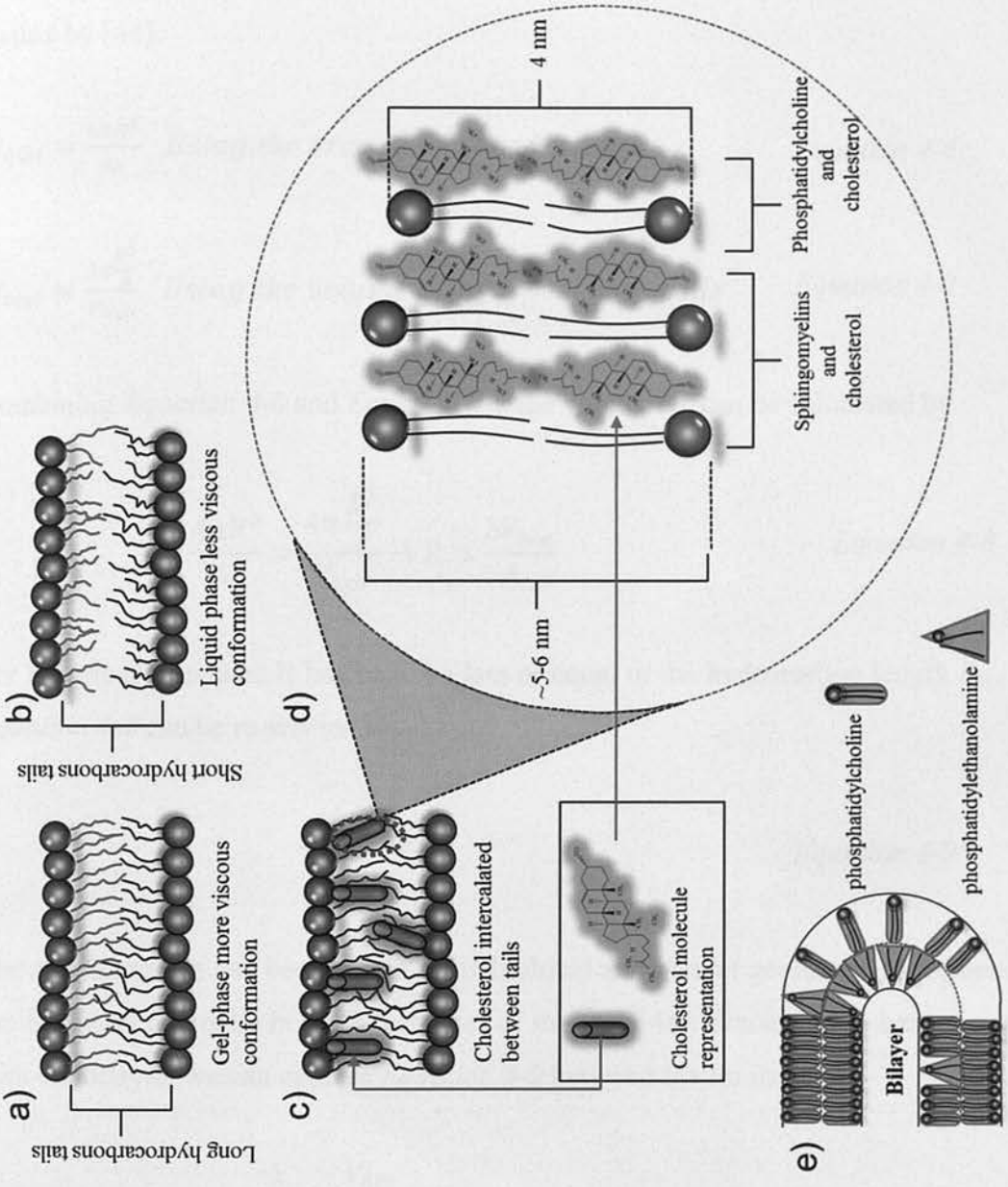


*Figure 4-3 Lipids representation in bilayer membrane. a) The gel-phase state is represented with hydrocarbon tail tightly packed by van der Waals interactions. b) The liquid phase state with shorter hydrocarbon tails in the phospholipids bilayer. c) Intercalated cholesterol gives more stability to the bilayer structure. d) shows more details of the cholesterol position on the phospholipids tails with relative measurements of length between two types of phospholipids (phosphatidylcholine and sphingomyelins) as an example in variation of the membrane thickness. e) Overall shape of two lipids types, which may determine the formation of microvilli and blebs[59]. Note that this is a general representation in order to give a visual reference of the concept described in the chapter.*

We can use either the area of the head group or the volume of the hydrocarbon chains by [44]:

$$N_{mol} = \frac{4\pi R^2}{A_h} \quad Using\ the\ area\ of\ the\ head\ group \qquad \textit{Equation 4-6}$$

$$N_{mol} = \frac{4\pi\frac{R^3}{3}}{V_{hcc}} \quad Using\ the\ volume\ of\ hydrocarbons\ tails \qquad \textit{Equation 4-7}$$

Combining *Equation 4-6* and *Equation 4-7* the value of R can be calculated by

$$\frac{4\pi R^2}{A_h} = \frac{4\pi\frac{R^3}{3}}{V_{hcc}} \rightarrow R = \frac{3V_{hcc}}{A_h} \qquad \textit{Equation 4-8}$$

For spherical structures R has be to be less or equal to the hydrocarbon length $L_{hcc}$ so *Equation 4-8* can be re-written as:

$$\frac{V_{hcc}}{A^h L_{hcc}} \leq \frac{1}{3} \qquad \textit{Equation 4-9}$$

The above process can be repeated for cylindrical and bilayer geometry. More details can be found in Boal's book "Mechanics of the cell"[44]. Since we are here concern with the bilayer, we can express *Equation 4-9* between the limits as:

$$\frac{1}{2} < \frac{V_{hcc}}{A^h L_{hcc}} \leq 1 \qquad \textit{Equation 4-10}$$

For lipids aggregation in the cell membrane the head group will have a cross-sectional area of approximately 0.4 $nm^2$ for phosphatidylethanolamines and 0.5 to 0.7 $nm^2$ for phosphatidylcholines (as visually depicted in *Figure 4-3 e*). Therefore, for a double chain hydrocarbon tail the ratio described in *Equation 4-10* is ~0.8, thus validating the argument that double chain lipids will preferentially form bilayers.

Other properties of the bilayer can be calculated such as elasticity and bending rigidity, which reflects the molecular components present in the membrane. More details can be found in literature [44,89,90].

## 4.6 Plasma membrane in the context of DEP separation of mammalian cells

Until now, the main characteristics of the plasma membrane and its components have been decribed. In the context of this thesis, the characteristics of the plasma membrane are important to support the results obtained by DEP separation of cells having similar size/volume in suspension. In addition, visual confirmation of the difference in morphology between cell types will be presented in the form of Transmission Electron Microscopy (TEM) and Scanning Electron Microscopy (SEM).

For a particular field frequency, the DEP response of a cell depends on whether its intrinsic dielectric polarisability is less or greater than that of its surrounding suspending medium. For the range of field frequencies and experimental conditions used in this study, the observed dynamic response is characterised either by the cell moving up a field gradient towards an electrode (positive DEP) or down a field gradient away from an electrode (negative DEP). The transition between these types of DEP response corresponds to where the effective polarisability of the cell equals that of the surrounding medium and occurs at the so-called DEP cross over frequency fxo. For a spherical cell of radius r, this frequency is given to good approximation by *Equation 2-22*. In this equation *Cm* is the specific capacitance (capacitance per unit area) of the cell membrane, $\sigma_m$ is the conductivity of the suspending medium, and the assumption is made that the high resistance to passive ion flow across the membrane has not been impaired due to the onset of cell death or physical damage, for example [14].

The protocols for obtaining the cell separations reported here relied on the different cell types (C2C12 myoblasts, myotubes and MRC-5 fibroblasts) exhibiting different

$f_{xo}$ values. This can reflect differences in either or both their average cell size or membrane capacitance. A cell's plasma membrane acts as a capacitor because it is constructed like one, namely, a thin dielectric shell situated between two conductors (the outer and inner electrolytes). It is customary to employ the low frequency (DC) approximation [26] to analyse the dielectric and conductive properties of a cell, so that for a spherical cell of measured radius r the effective permittivity $\varepsilon_{eff}$ of a cell is given by

$$\varepsilon_{eff} = \left(\frac{\varepsilon_0 \varepsilon_m r}{\delta}\right) \phi_m = r C_m \qquad \textit{Equation 4-11}$$

where $\delta$ is the membrane thickness, $\varepsilon_0$ is the permittivity of free space, and $\varepsilon_m$ is the mean relative permittivity of the material forming the membrane structure.

The factor $\phi_m$ in *Equation 4-11* is termed the membrane-folding factor to take into account cell surface features such as folds, microvilli, ruffles, and blebs [24].

For a perfectly smooth spherical cell $\phi_m = 1$. The DEP measurements reported here did not extend above 700 kHz, a suspending medium conductivity of 120 mS/m was used, and high cell viabilities were maintained during their DEP separations. Under these conditions, the low-frequency approximation used in *Equation 4-11* leads to an accurate measurement of the membrane capacitance [91].

A study recently reported that the neurogenic potential of human neural stem/progenitor cell populations can be characterised and potentially separated by their $f_{xo}$ and derived capacitance values [92].

On the basis of the efficient DEP-based cell separations reported here, the same conclusion may be reached regarding discrimination between stages of C2C12 myoblast cell differentiation.

In the DEP literature [8,14,24] it has been assumed that the value of $C_m$ primarily depends on the extent of membrane folding as given by $\phi_m$. One of the objectives of

this work was to investigate to what extent the chemical composition of the membrane might also influence its specific capacitance value. Raman spectroscopy has previously been used to investigate the chemical changes associated with the differentiation of stem cells, [93,94,95] as well as an on-chip detection method for monitoring the DEP separation of bacteria [96]. In this work, we have used Raman spectroscopy to determine how differences in the molecular composition of the membranes of two cell types of similar size, namely, C2C12 myoblasts and GFP-fibroblasts, might correlate with their observed DEP responses and derived $C_m$ values.

As described in this chapter different chemical and physical characteristics are present in the plasma membrane of cells. An exact quantification and characterisation of these properties remain difficult, however DEP may be sensitive enough to detect such differences and be able to separate cells as in the case of myoblasts C2C12 used here.

Although DEP may not give an exact description of the chemistry of the cell but it may be used in sorting cell population for further biochemical assays to elucidate the possible differences and characteristics. This was the main idea behind the implementation of a chemical, non-invasive spectroscopic technique as Raman in order to elucidate possible differences in plasma membranes of different cell type that may be responsible for the high level of separation by DEP.

In the next chapter, an analytical chemical technique in the form of Raman spectroscopy will be discussed in order to investigate the main properties responsible for the DEP results.

# Chapter 5 Raman Spectroscopy

## 5.1 Introduction

In this chapter, we analyse the basic of Raman spectroscopy as a chemical analytical technique. Although this chapter will examine the Raman technique in detail suitable for an analytical chemical perspective, exhaustive explanation of the physic behind Raman spectroscopy are beyond the scope of this thesis. Comprehensive explanations can be found in the references included in this chapter.

The basic description of the spectral regions in the electromagnetic spectrum will first be briefly reviewed. The theory behind diatomic molecules vibration and the theory for emission and scattering will then be discussed, followed by discussion of the three types of optical spectra in the form of vibrational, rotational and electronic.

The anharmonic oscillator will be introduced with descriptions of the scattering, intensity and polyatomic molecules.

Finally Raman spectra and the Fermi resonance and overtones will be addressed.

## 5.2 The Spectral regions

In the spectrum of electromagnetic radiation different types of physical phenomena take place as depicted in *Figure 5-1* The boundaries between different regions of the spectrum are not exactly defined, different techniques and instrumentations are used to determine the different regions [97]. The lowest part of the spectrum is concerned with radiowaves and is associated with nuclear magnetic resonance transition of the electrons spin [97]. Microwave spectroscopy is associated with electronic spin/rotational change of orientation and overlaps with the upper region of the infra-red [97].

The Raman/infra-red region concerns molecular excitation of rotational and vibrational modes of the spectra relevant to this chapter. The UV/visible spectral region relates to electronic excitations into higher energy levels, with elements of the rotational and vibrational transitions [97]. The x-ray region is associated with transition states of the electrons from the inner atomic energy shells [97]. Finally, the γ-radiation region involves the nuclear rearrangements of the atoms [97].

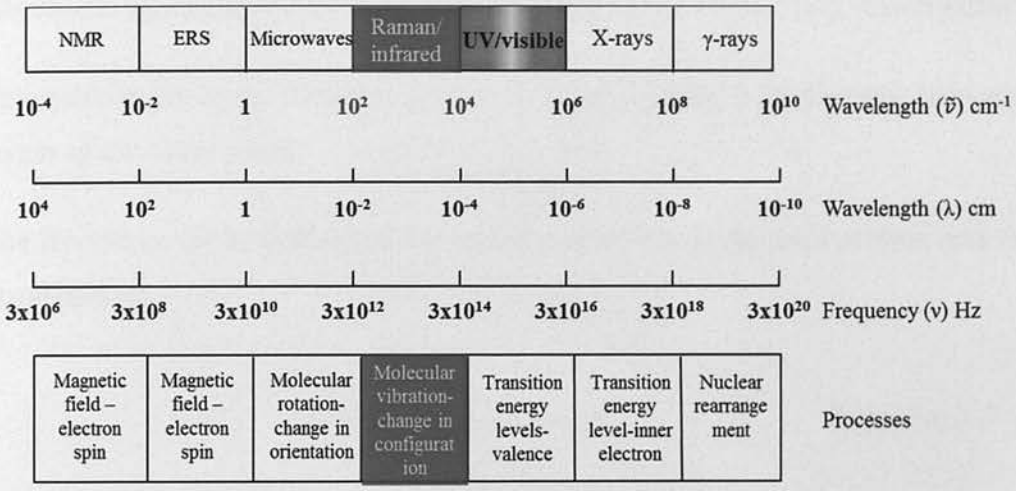


*Figure 5-1 Spectrum of electromagnetic radiations with associated wavelengths, frequencies and physical process related to the specific regions. Note that the values refers for pure vibrational frequencies.*

## 5.3 Basic theory on electromagnetic radiation

An incident electromagnetic (EM) wave hitting matter will produce scattering of light. This is generated by the EM wave perturbation of the electrons clouds surrounding the atoms/ molecules constituting matter. This perturbation has the same frequency as the electrical field of the incident wave.

The magnetic component of the EM wave will be ignored in this discussion since is not relevant for Raman spectroscopy [98]. The strength of an electric field can be expressed as:

$$E = E_{amp} cos 2\pi\nu t \qquad \textit{Equation 5-1}$$

with $E_{amp}$ as the vibrational amplitude, ν as the frequency and $t$ the unit time as illustrated in *Figure 5-2*. We can start to define some main parameters used for vibrational spectroscopy such as wavelength (λ), frequency (ν) and wavenumber($\tilde{\nu}$).

The wavelength is illustrated in *Figure 5-2* and is defined by distance between two points of the same phase.

The frequency (ν) is defined as the number of waves in the unit of time and can be expressed as:

$$\nu = \frac{c}{\lambda} \quad \text{Units Hz} \rightarrow \frac{\frac{cm}{s}}{cm} = \frac{1}{s} = Hz \qquad \textit{Equation 5-2}$$

with $c$ as the velocity of light (~$3x10^{10}$cm/s).

The wavenumber is defined by:

$$\tilde{\nu} = \frac{\nu}{c} \rightarrow \tilde{\nu} = \frac{\frac{c}{\lambda}}{c} \rightarrow \tilde{\nu} = \frac{1}{\lambda} Units\ in\ cm^{-1} \rightarrow \frac{\frac{1}{s}}{\frac{cm}{s}} = \frac{1}{cm} = cm^{-1} \qquad \textit{Equation 5-3}$$

Considering a molecule or a chemical compound, subjected to an electromagnetic field, transfer of energy to the molecule will be possible if Planck relation is satisfied as:

$$\Delta E = h\nu \rightarrow \Delta E = h\frac{c}{\lambda} \rightarrow \Delta E = hc\tilde{\nu} \qquad \textit{Equation 5-4}$$

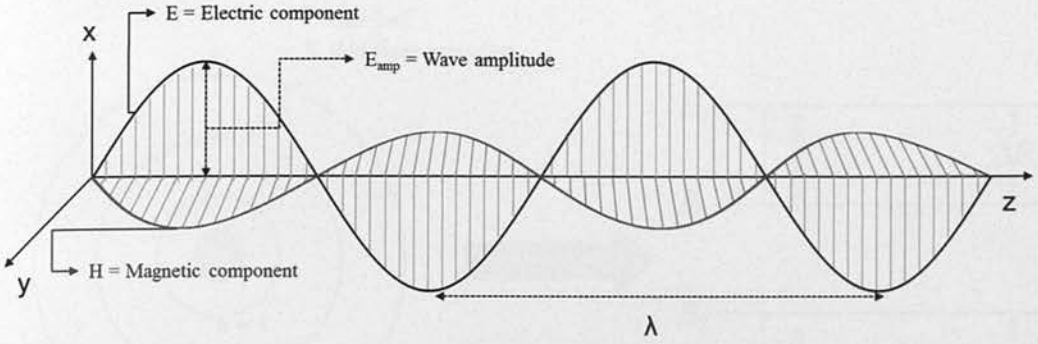


*Figure 5-2 Electromagnetic radiation with electric and magnetic components. Lambda (λ) indicates wavelength, which is the distance between two points having same phase. The electrical component of the electromagnetic wave is displayed on the x axes; the Magnetic component (H) is on the y-axes. Both components are perpendicular to each other[98]*

with $\Delta E$ as the difference in energy between two energy states, $h$ is the Planck's constant that is 6.62x $10^{-34}$ Js. As illustrated in *Figure 5-3* if $\Delta E$ is the difference between *E2* (excited state) and *E1* (as a ground state). *Equation 5-4* can be re-written as:

$$\Delta E = hc\tilde{\nu} = E_2 - E_1 \qquad \textit{Equation 5-5}$$

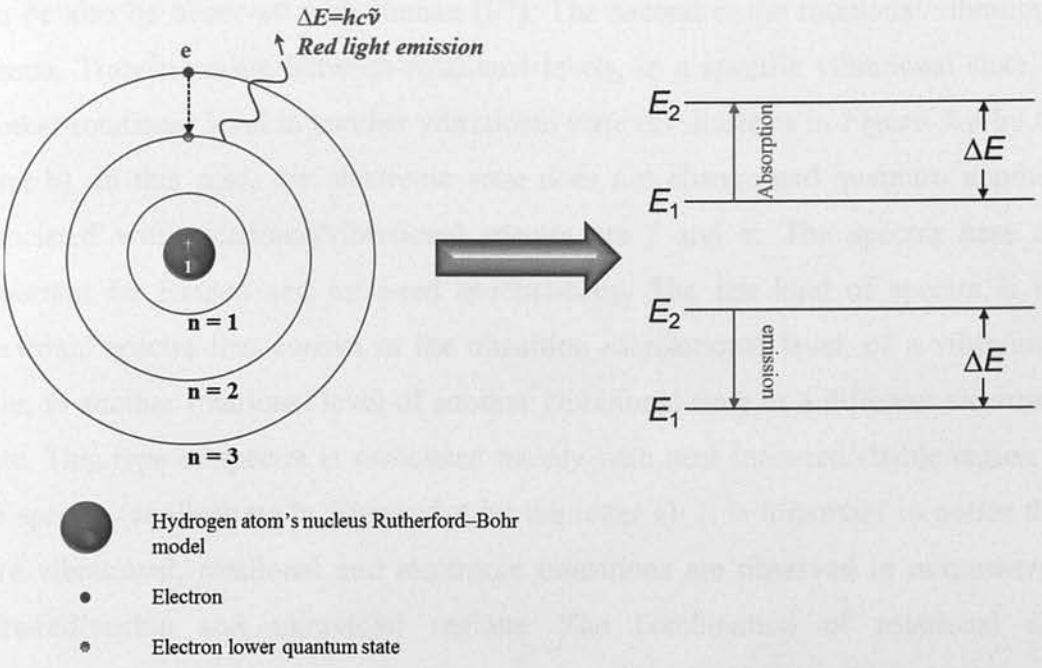


*Figure 5-3 Rutherford-Bohr model of hydrogen atom with emission and absorption of energy between a ground state $E_1$ and an excited state $E_2$.*

### 5.3.1 Types of optical spectra

The approximation of the total energy in a molecule is the sum of the three types of excitations for rotational, vibrational and electronic levels as:

$$E_{tot} = E_{elec} + E_{vib} + E_{rot} \qquad \textit{Equation 5-6}$$

with $E_{elec}$, $E_{vib}$ and $E_{rot}$ as the electronic, vibrational and rotational excitations respectively, as illustrate in *Figure 5-4* for two putative electronic states ($v'$ and $v''$). From these three excitation states, we can define the type of optical spectra that they produce. The first type is the rotational spectra that describes the transition between levels that are defined by the quantum number[22] $j$ as illustrated in *Figure 5-4* . These types of spectra are associated with microwaves/far-infra red region, although they

[22] Quantum numbers are discrete numbers, in this case integer; they provide solutions for the Schrodinger equation in term of quantized energies for the wavefunction.

can be also be observed with Raman [97]. The second is the rotational/vibrational spectra. Transitions are between rotational levels, in a specific vibrational state, to another rotational level in another vibrational state (as illustrate in *Figure 5-4* by the letter b). In this case, the electronic state does not change and quantum numbers associated with rotational/vibrational spectra are $j$ and $v$. The spectra here are important for Raman and infra-red spectroscopy. The last kind of spectra is the electronic spectra that consist in the transition of rotational level, of a vibrational state, to another rotational level of another vibrational state in a different electronic state. This type of spectra is associated mainly with near infra-red/visible region of the spectra (as illustrate in *Figure 5-4* by the letter a). It is important to notice that pure vibrational, rotational and electronic transitions are observed in microwaves, infra-red/visible and ultraviolet regions. The combination of rotational and vibrational transitions can be detected by Raman [99,100,101]. In *Figure 5-4* not all the transition are allowed between levels - the symmetry of the molecule determine the "selection rule[23]" which determine the allowable transitions.

In *Equation 5-5*, the difference between two states was described. We can now extend this to the rotational, vibrational and electronic energy by:

$$\tilde{\nu}hc = (E'_{elec} - E''_{elec}) + (E'_{vib} - E''_{vib}) + (E'_{rot} - E''_{rot}) =$$

$$= \Delta E_{elec} + \Delta E_{vib} + \Delta E_{rot} \quad \text{with } \Delta E_{elec} \gg \Delta E_{vib} \gg \Delta E_{rot} \qquad \textit{Equation 5-7}$$

For the purpose of this thesis, vibrational energy will be considered and higher energy levels such electronic transitions and lower rotational transitions are not important in this discussion. Also for the gas states, Raman measurements include vibrational and rotational transition. However in the case of the experiments detailed here non-gas samples were used.

[23] The selection rule or transition rule is a constrain regarding the available transition (rotational, vibrational and electronic). This is determined by quantum mechanics calculations based on the symmetry of the structure if the value of the integral is equal to zero the transition is not possible.

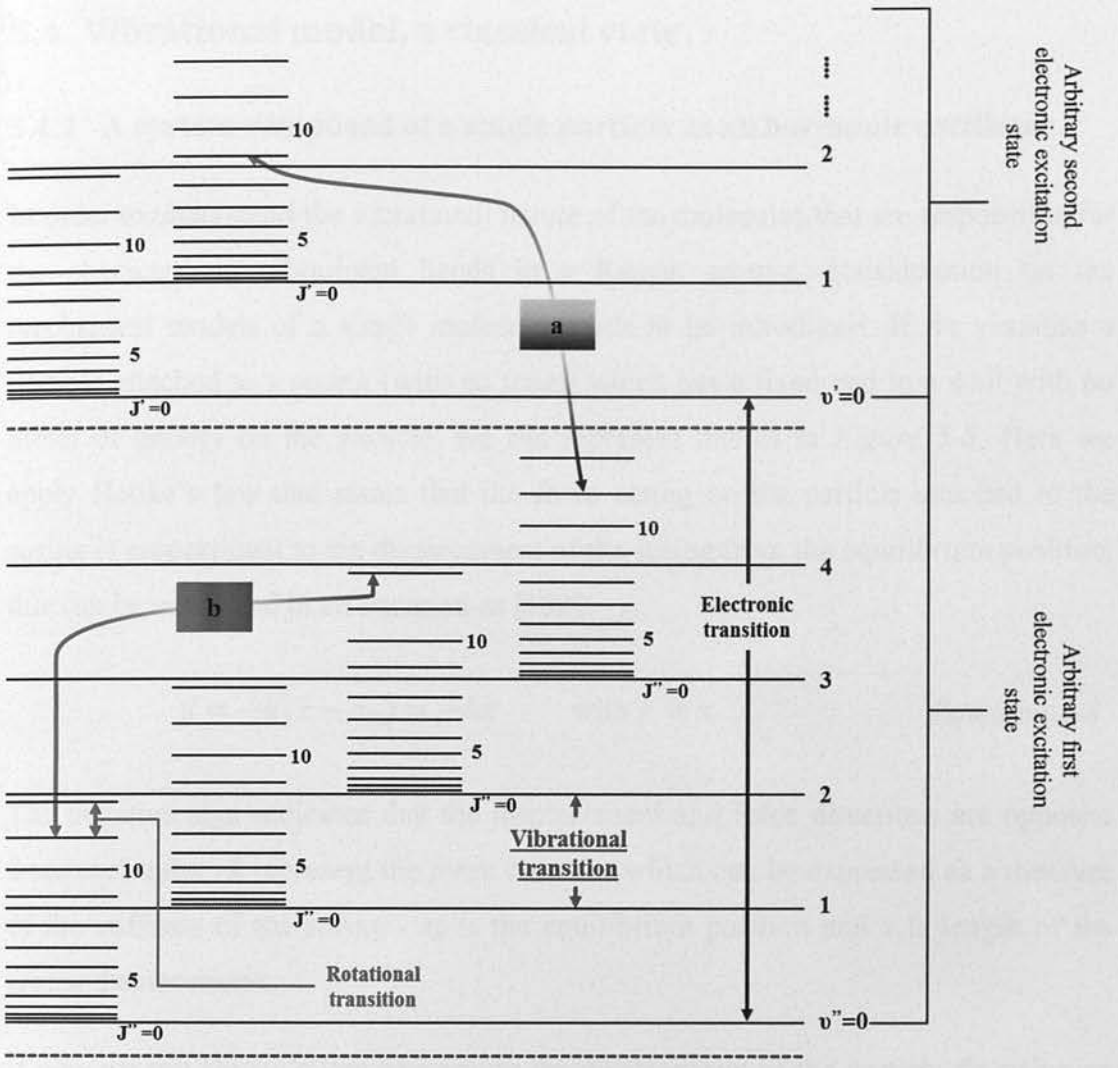


*Figure 5-4 Rotational and vibrational levels with quantum number" j" and "υ" for the two levels in a diatomic molecule. Here these two levels are depicted in for two electronic states as indicated by the brackets on the right hand side. The straight blue, red and black double arrows indicate pure rotational, vibrational and electronic transitions respectively. The box "a", with double colour curved arrow, indicates an electronic transition from rotational levels of different vibrational states to a different rotational and vibrational state in another electronic level. Box "b" indicates rotational/vibrational transition from a rotational state of a specific vibrational state to another vibrational state inside the same electronic state. Note that the spacing in the levels and in between is not accurate to describe the real differencence. Here it has been illustrated to clarify the concepts. The red dotted lines indicate the intrinsic vibration of the atoms due to nuclear vibrations for the two electronic levels.*

## 5.4 Vibrational model, a classical view

### 5.4.1 A system composed of a single particle as an harmonic oscillator

In order to understand the vibrational nature of the molecules that are responsible for the characteristic vibrational bands in a Raman spectra, consideration on the mechanical models of a single molecule needs to be introduced. If we visualise a particle attached to a spring (with no mass) which has a fixed end to a wall with no effect of gravity on the particle, we can represent this as in *Figure 5-5*. Here we apply Hooke's law that states that the force acting on the particle attached to the spring is proportional to the displacement of the spring from the equilibrium position, this can be expressed in an equation as [102]:

$$f = -k(x - x_0) = -kx \qquad \text{with } f \propto x \qquad \textit{Equation 5-8}$$

The negative sign indicates that the displacement and force directions are opposite from each other. $k$ represent the *force constant* which can be expressed as a measure of the stiffness of the spring - $x_0$ is the equilibrium position and $x$ is length of the spring displacement.

If now we use Hooke's law concerning the displacement of the particle $dx$, using an applied force $f_a$ the potential energy $U$ can be expressed as:

$$dU = f_a dx \qquad \textit{Equation 5-9}$$

with $f_a = -f$ due to the displacement in opposite direction of the force.

Now,

$$dU = -f dx \rightarrow \frac{dU}{dx} = -f \qquad \textit{Equation 5-10}$$

By inserting *Equation 5-1* and *Equation 5-10* we have:

$\frac{dU}{dx} = kx$ Note that the negative sign changes by the mathematical substitution.

From the above equation at equilibrium, we have potential energy as:

$$U = \frac{1}{2}kx^2 \qquad \textit{Equation 5-11}$$

In *Equation 5-11* can be illustrated as a parabolic function of the potential energy, which increases at both sides of the point of equilibrium as depicted in *Figure 5-5*.

Generally, the phrase *harmonic oscillator* is used to describe the parabolic function to define the chemical bond potential between atoms, as will be described in the next is a system composed of two masses using the principals explained above.

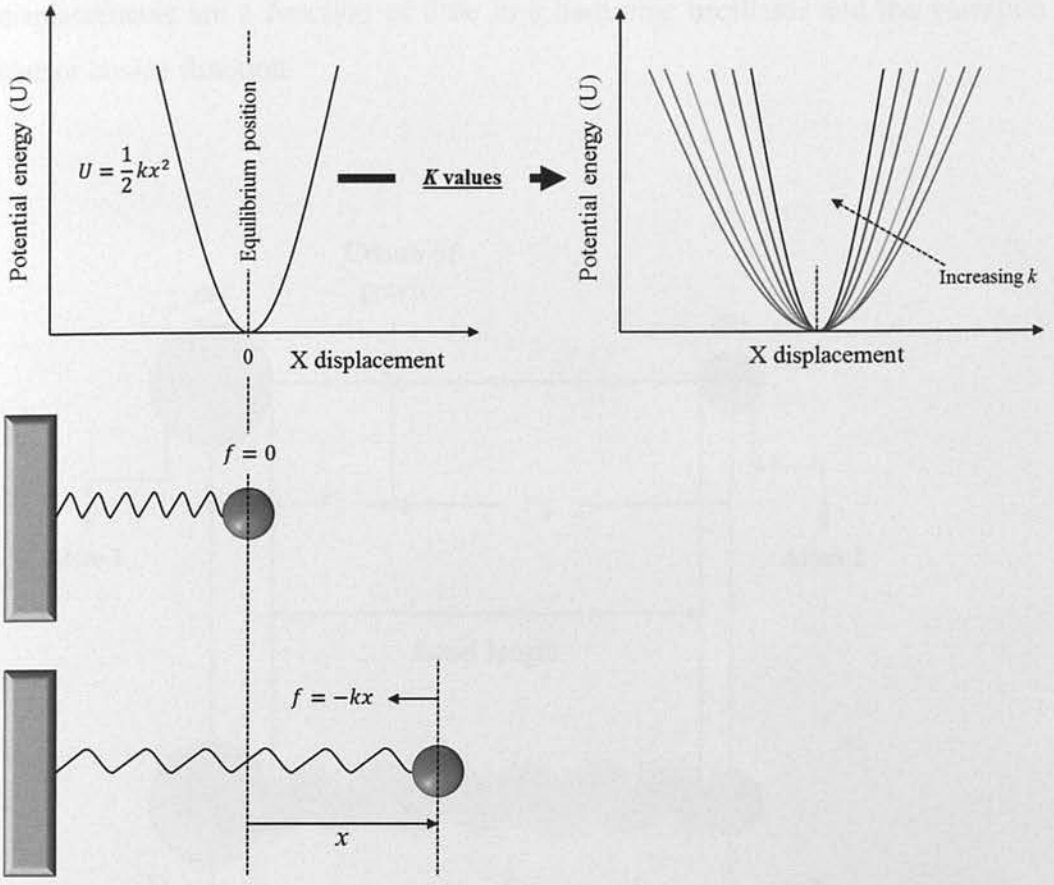


*Figure 5-5 Molecular vibration model of a harmonic oscillator with the potential energy is approximated by the parabolic equation of U. The force constant k represents the stiffness of the bond. On the top right graph, the steeper the curve walls the grater the force constant k. The equilibrium position is represented by dotted line at zero displacement. The expression of the potential energy U is indicated on the left graph. The two illustrations below represent the forces acting on a mass considering harmonic oscillations with the related displacements*

### 5.4.2 A diatomic molecule

If we take two masses $m_1$ and $m_2$ that are connected by a spring (chemical bond) to model a diatomic molecule, the basics of bands observed in Raman spectra can be explained by classical mechanical physic [103,104]. As illustrated in *Figure 5-6* considering two masses, $m_1$ and $m_2$, connected by a spring (massless) with displacements ($x_1$ and $x_2$) from equilibrium along the spring axis. These

displacements are a function of time in a harmonic oscillator and the variation is a sine or cosine function.

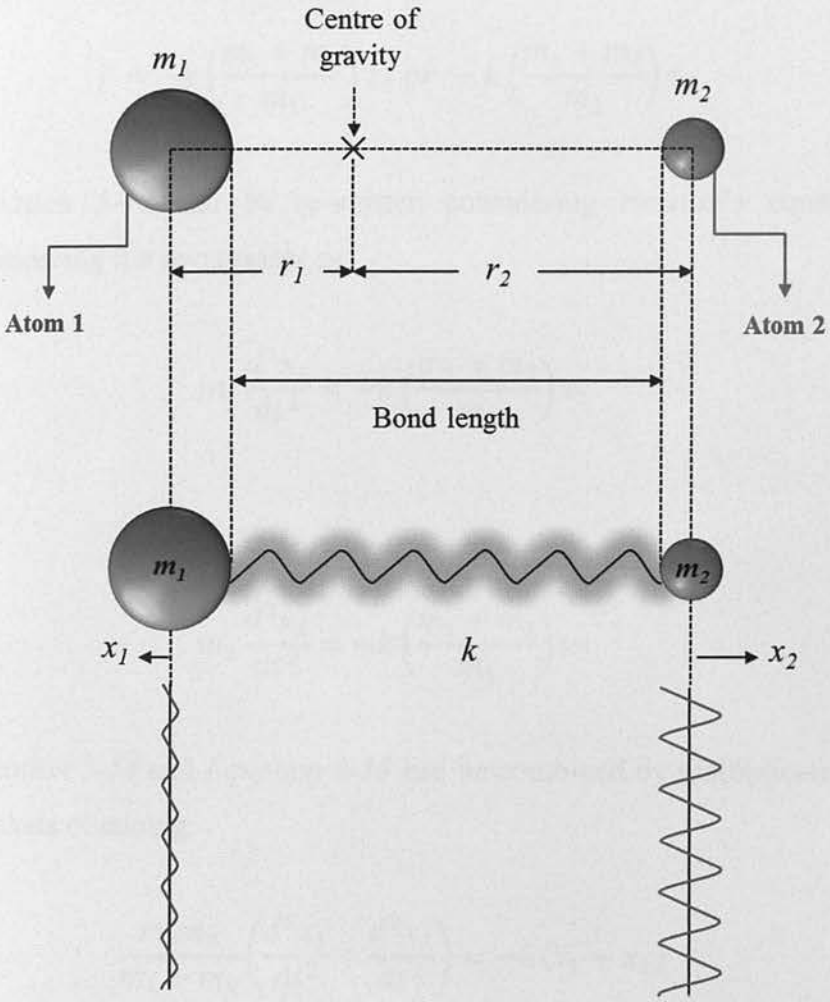


*Figure 5-6 Harmonic oscillator comprise of $m_1$ and $m_2$ masses. The displacement for the two masses is indicated by x1 and x2. The r1 and r2 distances are from the centre of gravity of the system. The amplitudes of the vibrations are represented by the two vertical red and blue waves. K is the force constant related to the bound/spring between the two masses.*

As described by *Equation 5-8* the restoring force here can be expressed by using the two equilibrium positions $x_1$ and $x_2$ as illustrated in *Figure 5-6* by:

$$f = -k(x_1 + x_2) \qquad \textit{Equation 5-12}$$

The above expression can be re-arranged to account for the masses and displacements as[98]:

$$f = -k\left(\frac{m_1 + m_2}{m_1}\right)x_2 \; or \; -k\left(\frac{m_1 + m_2}{m_2}\right)x_1 \qquad \textit{Equation 5-13}$$

*Equation 5-13* can be re-written considering Newton's equation of $f = ma$ considering the two masses as:

$$m_1\frac{d^2x_1}{dt^2} = -k\left(\frac{m_1 + m_2}{m_2}\right)x_1 \qquad \textit{Equation 5-14}$$

and

$$m_2\frac{d^2x_2}{dt^2} = -k\left(\frac{m_1 + m_2}{m_1}\right)x_2 \qquad \textit{Equation 5-15}$$

*Equation 5-14* and *Equation 5-15* can be combined by multiplication of the terms in brackets obtaining:

$$\frac{m_1 m_2}{m_1 + m_2}\left(\frac{d^2x_1}{dt^2} + \frac{d^2x_2}{dt^2}\right) = -k(x_1 + x_2) \qquad \textit{Equation 5-16}$$

The reduced mass $\mu$ can be described as:

$$\mu = \frac{m_1 m_2}{m_1 + m_2} \qquad \textit{Equation 5-17}$$

*Equation 5-17* can be re-written accounting for the reduced mass and displacement $q$ (related to the reduced mass) as:

$$\mu \frac{d^2q}{dt^2} = -kq \qquad \textit{Equation 5-18}$$

*Equation 5-18* is the differential equation for the harmonic with solution given by sine or cosine functions such that for sine is:

$$q = q_0 \sin(2\pi\nu_0 t + \varphi) \qquad \textit{Equation 5-19}$$

with $q_0$ as the maximum displacement and $\varphi$ the phase. $\nu_o$ can be expressed as:

$$\nu_0 = \frac{1}{2\pi}\sqrt{\frac{k}{\mu}} \qquad \textit{Equation 5-20}$$

*Equation 5-20* can also be expressed in wavenumber units $\bar{\nu}$ as waves per unit length ($cm^{-1}$) as:

$$\bar{\nu} = \frac{1}{2\pi c}\sqrt{\frac{k}{\mu}} \text{ with c as the speed of light in cm/s} \qquad \textit{Equation 5-21}$$

In the above equation, the masses ($\mu$) are expressed in unified atomic units and $k$ generally is expressed in millidynes/Ångström (the dyne[24] is not an SI unit of force).

The force constant $k$ for single, double and triple bond is between 3 to 6, 10 to 12 and 15 to 18 millidynes/Ångström respectively [104].

The potential and kinetic energy U and T respectively can be written as:

$$U = \frac{1}{2}kq^2 \qquad \textit{Equation 5-22}$$

[24] One dyne is equal to $1g\frac{cm}{s^2} = 10^{-5}N$(SI system)

$$T = \frac{1}{2}m_1\left(\frac{dx_1}{dt}\right)^2 + \frac{1}{2}m_2\left(\frac{dx_2}{dt}\right)^2 \qquad \textit{Equation 5-23}$$

The total energy E is:

$$E = U + T \qquad \textit{Equation 5-24}$$

## 5.5 Anharmonic oscillator: a quantum mechanics prospective

Until now, we have considered a classical harmonic oscillator from the point of view of classical mechanics. However, a quantum mechanics approach can be also used. Here we will only describe a brief review of the theory - more detailed explanations can be found elsewhere in the literature [99,101,104,105].

The potential energy U, as described in *Equation 5-22* can be plotted considering the distance between the two masses $m_1$ and $m_2$, such as a parabolic curve as illustrated by *Figure 5-7*. However in quantum mechanics the molecule has quantised energy states[25]. This implies that the vibrational energy of the molecule can only take discrete values so that this transition between energy states can be examine by Raman spectroscopy. As illustrated by *Figure 5-8* the levels of potential energy are shown for a harmonic oscillator. It is important to note that the potential states are equally separated and have energy $E$ as:

$$E = \left(v_i + \frac{1}{2}\right)h\nu \qquad \textit{Equation 5-25}$$

with $v_i$ as the quantum numbers[26] which can change by ±1 and ν the vibrational frequency. When $v_i = 0$ the energy $E$ is equal to $\frac{1}{2}h\nu$ and this can be considered as the intrinsic energy of the molecule. This can be illustrated by the so called

[25] In quantum mechanics quantized energy states refers to discrete values of energy that the system or molecule can take.
[26] These numbers can be only integer changing by only ±1(Δν)

*"potential wells"* that reflect the probability of finding the particle at a certain position (this is called the Heisenberg's principle of uncertainty[27]). Illustrated in *Figure 5-7* is the potential well with the probability function (*Figure 5-7 a*) and the corresponding wave function for the harmonic oscillator (*Figure 5-7 b*).

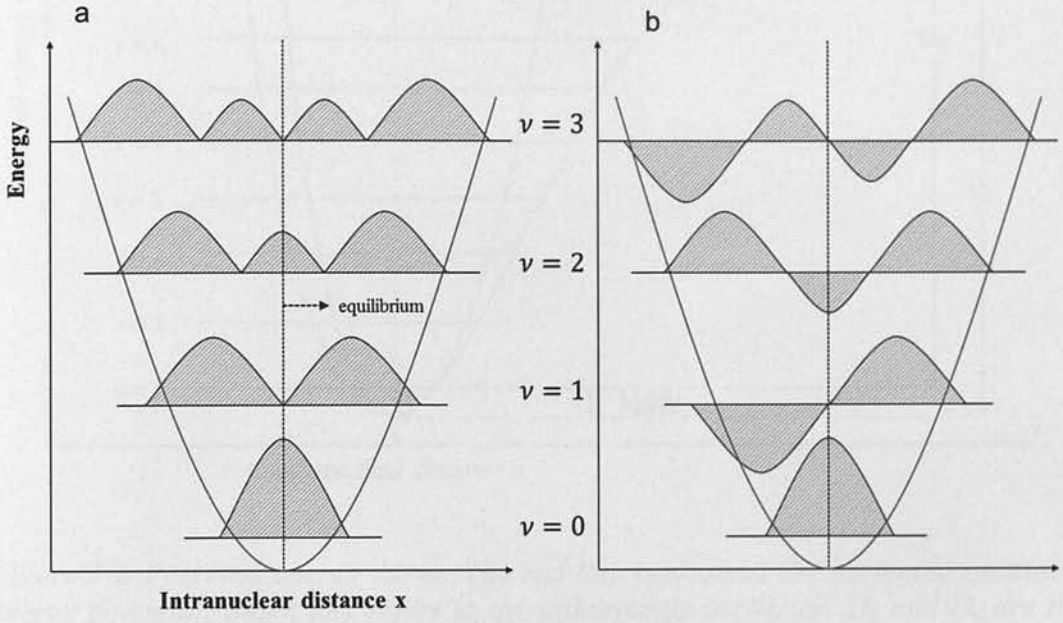


*Figure 5-7 Potential well and wave function. a) is the potential well for harmonic oscillator which describes the probability distribution. b) represents the wave function associated with the corresponding probability for* $v_n$

[27] In quantum mechanics, the exact position of the mass cannot be determined, so a probabilistic method needs to be used.

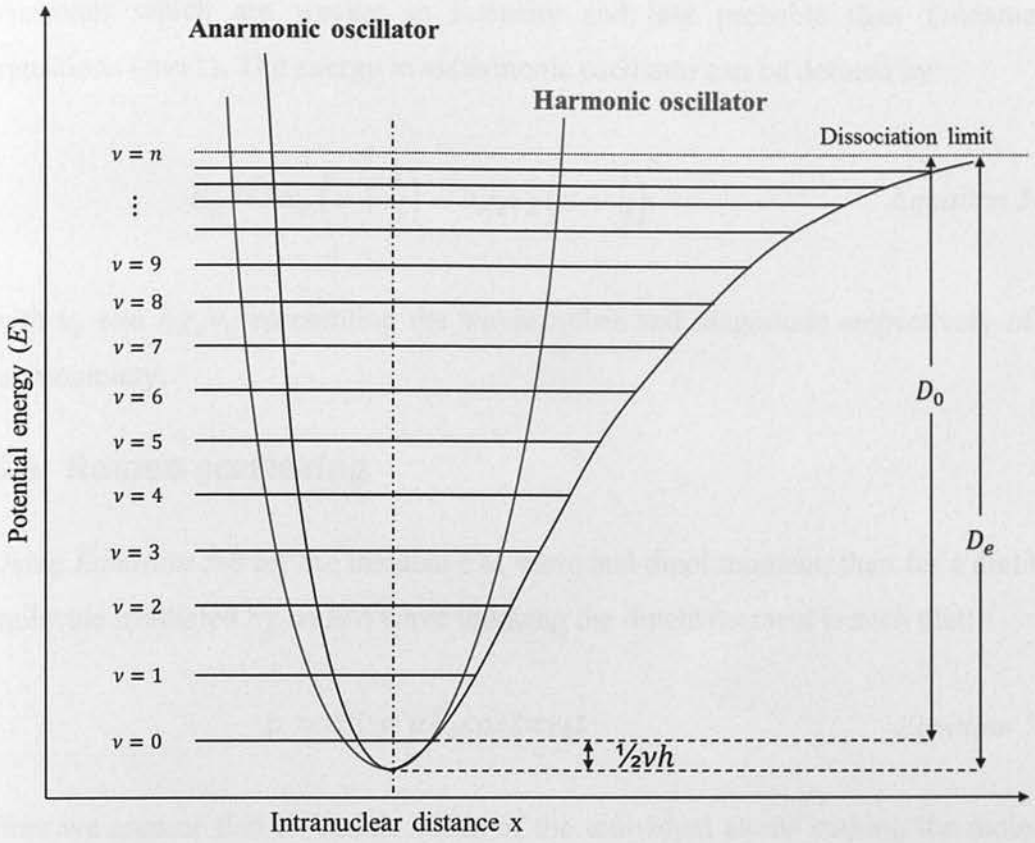


*Figure 5-8 Potential energy curve. The red line represenst the harmonic oscillator energy potential. Black line refers to the anharmonic oscillator. $D_0$ and $D_e$ are the actual and theoretical dissociation energies respectively. Dissociation is responsible for the breakage of the bond.*

Although until now the harmonic oscillator has been described, a more realistic model is in the form of an anharmonic oscillator. Here in this model we account for the change in dipole moment when it is not directly proportional to the coordinate of the nuclear displacement[104]. This is illustrated in *Figure 5-8*. The anharmonic model shows that the level separations decrease with higher quantum values for the vibrational levels moving toward the dissociation limit. In an harmonic oscillator only transitions with $\Delta v \pm 1$ are allowed (this is called selection rule). In anharmonic oscillator transitions by the selection rule $\Delta v \pm 2, 3, \ldots$is allowed, these are called

overtones which are weaker in intensity and less probable than fundamental transitions ($\Delta v \pm 1$). The energy in anharmonic oscillator can be defined by:

$$E_v = h\nu_e\left(v + \frac{1}{2}\right) - h\chi_e\nu_e\left(v + \frac{1}{2}\right)^2 \qquad \textit{Equation 5-26}$$

with $\nu_e$ and $h\chi_e\nu_e$representing the wavenumber and magnitude respectively of the harmonicicty.

## 5.6 Raman scattering

Using *Equation 5-8* for the incident EM wave and dipol moment, then for a diatomic molecule irradiated by an EM wave inducing the dipole moment is such that:

$$p = \alpha E = \alpha E_0 cos 2\pi\nu_0 t \qquad \textit{Equation 5-27}$$

Here we assume that electronic shells of the individual atoms making the molecule vibrate with the same frequency $\nu_p$ of the vector $E$ of the striking light. Here we assume that the molecule is not vibrating at any characteristic vibrational frequency. However, if the molecule is vibrating at one specific frequency the oscillations of the dipole moment will be modulated in amplitude at frequency $\nu_{vib.}$ The position of the individual atoms is responsible for the perturbation of the electrons cloud so the polarisability will change as a function of the distances $q$ between vibrating nuclei by:

$$q = q_0 \cos(2\pi\nu_{vib}t) \qquad \textit{Equation 5-28}$$

with $q$ as the equilibrium position and $q_0$ as the vibrational amplitude. In the case of small amplitude variations[28] the polarisability $\alpha$ is a linear function of $q$ as:

[28] For example $N_2$ the maximum displacement of the bond length is 10% of the total.

$$\alpha = \alpha_0 + \left(\frac{\partial \alpha}{\partial q}\right)_0 q_0 + \cdots \qquad \textit{Equation 5-29}$$

with $\alpha_0$ as the polarisability at equilibrium regarding the position, $(\partial\alpha/\partial d)$ indicate the rate of change of $\alpha$ due to changes in $q$ at equilibrium position.

Combining *Equation 5-27*, *Equation 5-28* and *Equation 5-29* we have:

$$p = \alpha E_0 cos\,(2\pi \nu_0 t)$$

$$= \alpha_0 E_0 cos\,(2\pi \nu_0 t) + \left(\frac{\partial \alpha}{\partial q}\right)_0 q E_0 cos\,(2\pi \nu_0 t)$$

$$= \alpha_0 E_0 cos\,(2\pi \nu_0 t) + \left(\frac{\partial \alpha}{\partial q}\right)_0 q E_0 cos\,(2\pi \nu_0 t)\, cos\,(2\pi \nu_{vib} t)$$

$$= \alpha_0 E_0 cos\,(2\pi \nu_0 t) + \frac{1}{2}\left(\frac{\partial \alpha}{\partial q}\right)_0 q E_0 \{cos\,[2\pi(\nu_0 + \nu_{vib})t] + cos[2\pi(\nu_0 - \nu_{vib})t]\}$$

*Equation 5-30*

In the above expression, the first term is the oscillating dipole that scatters light at frequency of $\nu_0$ (Rayleight scattering), the second term is the Raman scattering at frequency of $\nu_0 + \nu_{vib}$ (anti-Stokes) and the last term for the Stokes at frequency of $\nu_0 - \nu_{vib}$. This represents the first order Raman effect and with decreasing intensity the Raman effect changes in the form of the second order ($\nu_0 \pm 2\nu_{vib}$), third order ($\nu_0 \pm 3\nu_{vib}$) and so on (the term is added to *Equation 5-29* ). It is important to notice that necessary conditions reside in the term $\left(\frac{\partial \alpha}{\partial q}\right)$ that must be non-zero,.so that the change in polarisibility rate of α associated with the vibration must be not zero. We can interpret this as the displacement of the atoms at a specific vibrational mode that produce changes in polarisability. For example, for a diatomic molecule, the displacement (bond length) can be at equilibrium at minimum length or at maximum length. The perturbation of the electrons cloud by the incident light is dependent on the position of the atom (bond length). At minimum length, the two atoms will be

closer affecting each other regarding electrons cloud interactions. On the other hand, at maximum bond length the electron clouds will not affect each other much so the electrons will be more affected by electric field, increasing the polarisability at this maximum. Considering that $\left(\frac{\partial \alpha}{\partial q}\right)$ will be non-zero, at equilibrium, the diatomic molecules, here consider, will be Raman active with the generation of inelastic scattering at $\nu_0 - \nu_{vib}$ and $\nu_0 + \nu_{vib}$ as illustrated in *Figure 5-9*

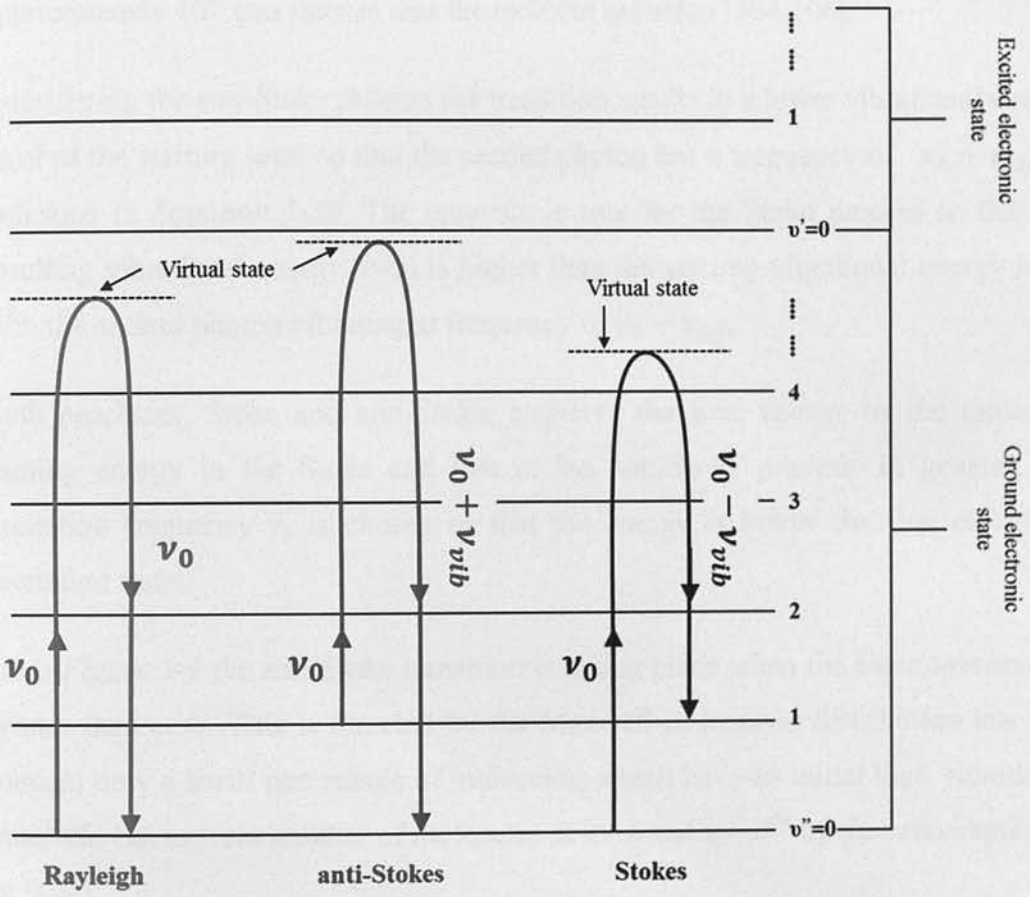


*Figure 5-9* Raman scattering. The vibrational quantum numbers are indicated by ν and ν''

depicts the scattering of a diatomic molecule, here the upward arrow depicts the transition of a photon and molecule to higher energy state which is described as virtual state (different from the excited state of the molecule). The downward arrow indicate the release of a second photon (after very short time in order of $10^{-11}$sec [102]).

Considering the Rayleigh scattering[29] both upward and downward transitions have the same energy (same length in *Figure 5-9*) but different sign (opposite direction); so here, there is not a change in photon frequency. The Rayleigh scattering is approximately $10^{-3}$ less intense that the incident radiation [104,106].

Considering the anti-Stoke process the transition results in a lower vibrational energy level of the starting level so that the second photon has a frequency of $\nu_0 + \nu_{vib}$ as indicated in *Equation 5-30*. The opposite is true for the Stoke process so that the resulting vibrational energy level is higher than the starting vibrational energy level with the second photon vibrating at frequency of $\nu_0 - \nu_{vib}$.

Both processes, Stoke and anti-Stoke, conserve the total energy by the molecule gaining energy in the Stoke and lost in the anti-Stoke process. In general, the excitation frequency $\nu_0$ is chosen so that the energy is below the first electronic excitation state.

From *Figure 5-9* the anti-Stoke transition is taking place when the electronic state is greater than zero. This is directed by the Maxwell-Boltzmann distribution law that concern only a small percentage of molecules, which have an initial high vibrational state. We can express number of molecules at $v = 1$ and $v = 0$[30] by the ratio expressed by [102]:

[29] Typically the sample will absorbed 90% (in a cm) of the incident light and only 1 on a $10^{10}$ photons will produce Raman scattering [106] R.L. McCreery, Raman Spectroscopy for Chemical Analysis, Wiley, 2005.

[30] The number of molecules at $v=0$ is larger than molecules at $v=1$ [98] J.R. Ferraro, K. Nakamoto, Introductory Raman Spectroscopy, Elsevier Science, 1994.

$$\frac{N_1}{N_0} = e^{-\frac{h\nu_{vib}}{kT}}$$ *Equation 5-31*

with $N_1$ and $N_0$ as the ratio of molecules at $v = 1$ and $v = 0$ respectively, $h$ as the Planck's constant, $k$ the Boltzmann's constant[31] and $T$ the absolute temperature.

The exponential form of *Equation 5-31* shows that the anti-Stokes lines will be significantly less strong than the Stoke in a Raman spectrum. Since both Stoke and anti-Stoke convey the same information, the Stoke is normally measured in Raman spectra. An example of Rayleigh, Stoke and anti-Stoke Raman spectra is provided in *Figure 5-10* for carbon tetrachloride ($CCl_4$). Notice that this is only a representation of the Raman spectrum for the molecule of $CCl_4$ to visually clarify the three components of Rayleigh, Stoke and anti-Stoke. The real acquired spectrum may present small differences in peaks conformation from the illustration in *Figure 5-10* . In the same figure, a simplified version of the setup used for Raman spectroscopy in this thesis is illustrated.

[31] Boltzmann's constant is equal to 1.3807 x $10^{-16}$ erg/degree

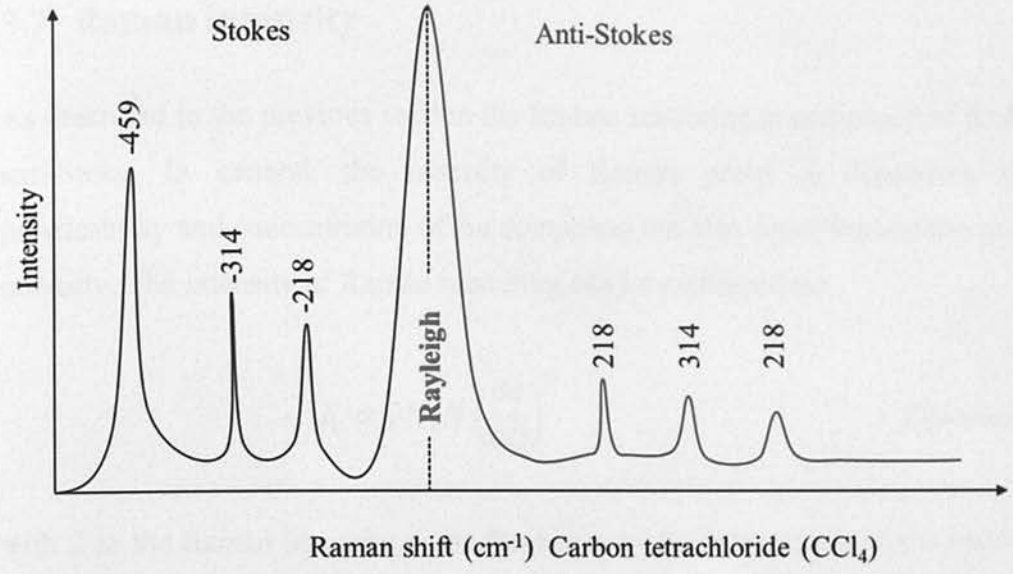


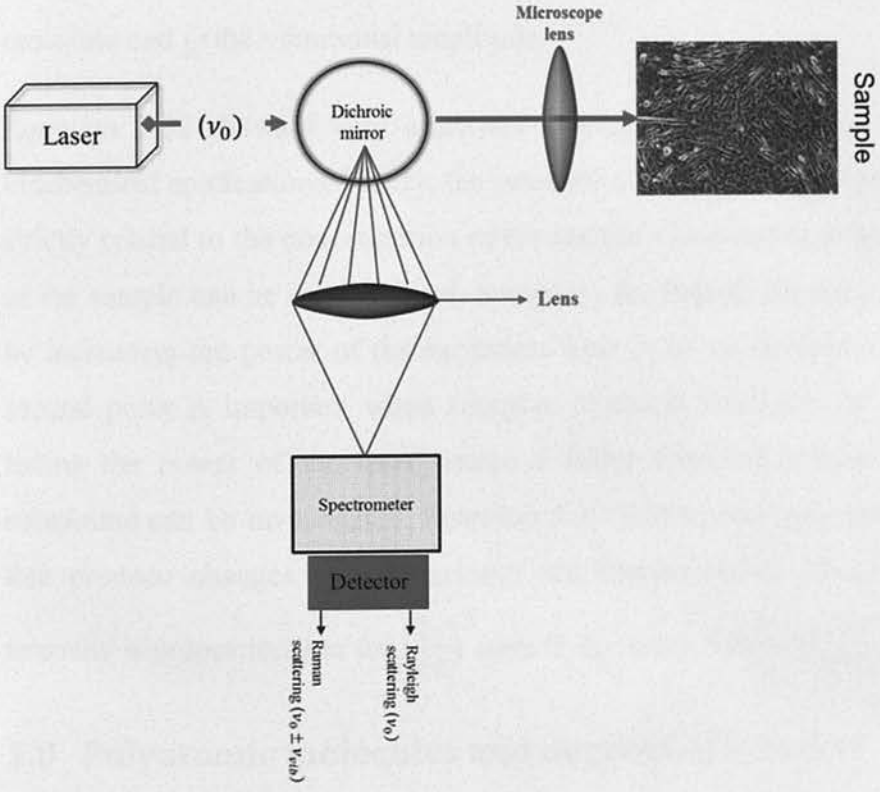


*Figure 5-10 Raman spectra of carbon tetrachloride with associated set-up for spectrum acquisition. Note that the spectrum is for clarify the concepts only it is not an actual spectrum*

## 5.7 Raman intensity

As described in the previous section the Raman scattering is composed of Stoke and anti-Stoke. In general, the intensity of Raman peaks is dependent on the polarisability and concentration of the compound but also dependent on the source of intensity. The intensity of Raman scattering can be expressed as:

$$I_r \propto \nu^4 I_0 N \left(\frac{\partial \alpha}{\partial Q}\right)^2 \qquad \textit{Equation 5-32}$$

with $I_r$ as the Raman intensity, $\nu$ the frequency of the laser source, $I_o$ the intensity of the laser source, $N$ the number of molecules scattered, $\alpha$ polarisability of the molecule and $Q$ the vibrational amplitude.

*Equation 5-32* shows a very important characteristics of Raman spectroscopy for biochemical applications. Firstly, the intensity of the peaks in a Raman spectrum are strictly related to the concentration of the sample - so quantification and comparison of the sample can be implemented. Secondly, the Raman intensity can be increased by increasing the power of the excitation laser or by using short wavelengths. This second point is important when complex chemical structures are analysed, so by tuning the power of the laser source a better chemical picture of the analysed compound can be investigated. *Equation 5-32* tells us that only molecule vibrations that produce changes in polarisability are Raman active. Therefore, the Raman intensity is proportional to the $\left(\frac{\partial \alpha}{\partial Q}\right)^2$ term in *Equation 5-32* with $\left(\frac{\partial \alpha}{\partial Q}\right) \neq 0$.

## 5.8 Polyatomic molecules and degrees of freedom

Molecular vibration results from a degree of freedom of the atoms present in the molecule. A rule of thumb is known as $3n$-5 and $3n$-6 for linear and non-linear molecules respectively. The term $n$ represents the number of atom present in the

molecule which has 3 degree of freedom of motion in the $x$, $y$ and $z$-axis. For example in water (non-linear) the degrees of freedom of three is obtain by 3(3)-6=3, in oxygen ($O_2$-linear) is 3(2)-5=1 degree of freedom. The vibration term is used to describe deformation/bending, stretching, in and out of plane vibrations of the atoms/bonds in the molecule as illustrated in *Table 5-1* for carbon dioxide ($CO_2$). In this example it is assumed that the displacement change with the same frequency without rotation of the molecule and maintaining the same centre of mass. Considering a harmonic oscillator the atomic displacement can be represented as a sinusoidal wave as function of time as illustrated in *Figure 5-7*.

| **Stretching/Out of plane** | **Stretching/In plane** | **Deformation/Bending** | **Deformation** |
|---|---|---|---|
| 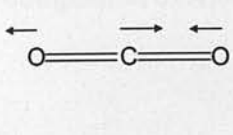 | 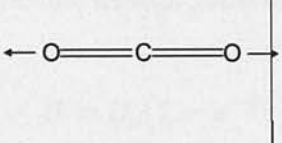 | 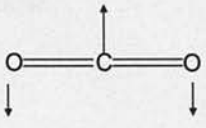 | 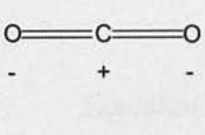 |
| 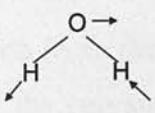 | 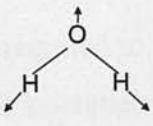 | 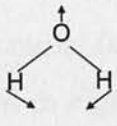 | |

*Table 5-1 Degrees of freedom of polyatomic carbon dioxide and water. The plus and minus indicates that the nuclei move upwards and downwards perpendicularly to the paper.*

In diatomic molecules as we discussed previously the vibration occurred only on the chemical bond between nuclei. In the polyatomic situation, the complexity increases because each nucleus produces its own harmonic oscillation. However, the complexity in polyatomic molecules can be broken down by considering the superimposition of the all vibrations present in the system, which are independent from one to another. Detailed information on the subject regarding the physic of

vibrational motion of polyatomic molecules is contained in the references related to this chapter.

## 5.9 Raman spectra, overtones and Fermi resonance: practical examples

The analysis of a Raman spectrum shows the presence of bands that are produced by anharmonic oscillation as described previously. We can say that the approximation of harmonicity, where the potential energy ($U$) is proportional to displacement squared as expressed by *Equation 5-11* does not fully reflect the vibrational nature of the system. In order to express a more realistic situation regarding the potential energy the Morse equation needs to be introduced. The equation describes the vibrational motions of a particular system and accounts for the anharmonicity component of the molecule as expressed below.

$$U = D_e\left(1 - e^{-\beta q}\right)^2 \qquad \textit{Equation 5-33}$$

with $D_e$ as the energy required to separate the nuclei (see *Figure 5-8*) $\beta$ is a measure of the curvature of the potential well depicted in *Figure 5-8* and $q$ account for the distance between nuclei.

In *Equation 5-33* when the value of $q$ is large we need to account for anharmonicity of the nuclei motion. Therefore, the vibrational transitions (overtones) can occur when $\Delta v > \pm 1$ although less probable. This is represented in Raman spectra by peaks less intense around the fundamental transitions ($\Delta v = \pm 1$). The molecule of β-carotene illustrates an example in *Figure 5-11*. Here Raman spectrum have been taken from the literature [107] to demonstrate some of the concepts before mentioned. The stretching of the carbon double bond produces an intense peak (in a Raman spectrum) at ~1520 $cm^{-1}$ (Raman shift in *Figure 5-11* indicated by $v_1$ ) due to transitions from $v = 0$ to $v = 1$. In addition, the stretching of single bond carbon (C-C) is present at ~1150 $cm^{-1}$ (*Figure 5-11* indicated by $v_2$) and C-H in plane bending

at ~1000 $cm^{-1}$ (*Figure 5-11* indicated by $v_3$). Here we can notice also an overtones transitions from $v = 0$ to $v = 2$ that produce a peaks at 3040 $cm^{-1}$ (*Figure 5-11* indicated by $2v_1$) and ~2300 $cm^{-1}$ (*Figure 5-11* indicated by $2v_2$). Anharmonicity can also produce weak "*combination bands*" that reflect the sum of fundamental bands, in the case of β-carotene this arise by the sum of $v_1 + v_2$ and $v_1 + v_3$ in the Raman shift region of 2674 and 2525 $cm^{-1}$ respectively as indicated in Figure 5-11. The anharmonicity of a molecule can also be responsible for the occurence of the so-called "*Fermi resonance*". In this case, the overtones and/or combination bands have very similar frequencies of the fundamental bands producing two intense peaks where a fundamental peak was supposed to be seen. An example is the side chain of the amino acid tyrosine comprise of an aromatic ring with attached a methyl group ($CH_3$) and a hydroxyl group that can be protonated[32] .This forms a "*Fermi doublet*" peak at around 830 and 850 $cm^{-1}$.

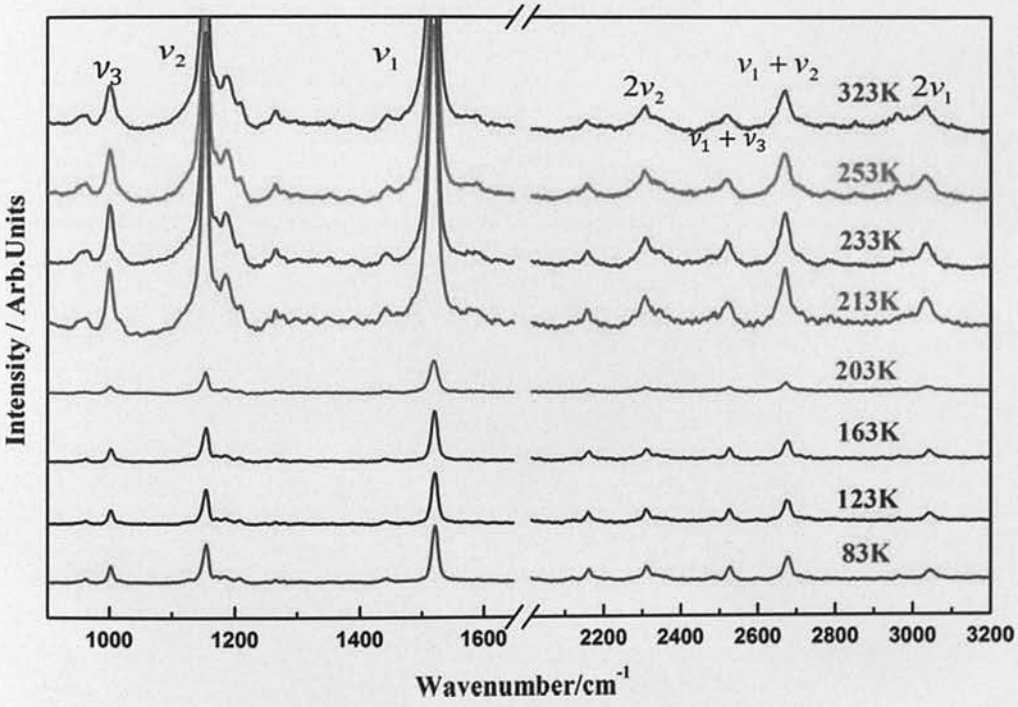


*Figure 5-11 Raman spectrum of β-carotene at different temperatures. The fundamental bands are indicated by $v_1$, $v_2$ and $v_3$. The overtones are at $2v_1$ and $2v_2$ with the combination bands indicated by $v_1 + v_2$ and $v_1 + v_3$. The number in different*

[32] Changes in the hydroxyl group (OH) determine the shape of the Fermi doublet at ~850 $cm^{-1}$

*colours on the right hand side indicate the absolute temperature at the time of acquisition of the spectra. Picture from [107].*

# Chapter 6 Materials and Methods

## 6.1 Introduction

This chapter describes the biochemical, biological and microfabrication methods and materials used for the experiments presented in this thesis. In the microfabrication section, the prototypes implemented for the final cell separation device will be presented.

Initially, the culture conditions used to grow the different cell types are presented. Secondly, the biochemical techniques to process the cells are explained. These techniques were implemented not only to process the cells but more importantly to validate the results from the DEP experiments and Raman analysis.

Thirdly, the statistical analysis of Raman data in the form of Principal Component Analysis (PCA) and Partial Least Squares (PLS) are explained.

The last section regards the engineering techniques in the form of microfabrication for the design and manufacture of the dielectrophoretic device for cell sorting and analysis

## 6.2 Biochemical/biological method

All chemical and reagents were purchased from Sigma Aldrich (Poole UK) unless otherwise stated.

### 6.2.1 Cell culture

#### *6.2.1.1 Mouse myoblast cell line*

Dr. Vlastimil Srsen donated C2C12 cell line. Cells at high passage number (>70) were seeded at a starting density of 3000 cells/cm$^2$ and grown in high glucose

DMEM growth medium (GM) supplemented with 10% FBS (HyClone), 2 mM of L-glutamine, 100 units/ml of penicillin and 100 µg/ml streptomycin sulphate (Invitrogen Carlsbad, CA, USA). Cells were passaged while at low confluence and induced to myogenic differentiation when above 90% confluence. The differentiation medium (DM), changed every other day, comprised high glucose DMEM, 0.1% FBS (Hyclone), 100 units/ml of penicillin and 100 µg/ml streptomycin sulphate (Invitrogen Carlsbad, CA, USA), 5 µg/ml transferrin and 10 µg/ml insulin. All cultures were maintained at 37°C with 5% CO2. Competency of differentiation was assessed by the visual presence of myotubes or adipocytes (Oil red O staining) by light microscopy.

#### *6.2.1.2 MRC-5 (GFP-fibroblast cell line)*

The cells were cultured in the same GM as C2C12 and were further supplemented with 2 µg/ml puromycin to maintain selection pressure, as well as green fluorescent protein (GFP) expression. The cells were passaged every two days at a ratio of 1:4 all cultures were maintained at 37°C with 5% CO2. No alterations in phenotype, morphology or anomalies in expression of embryonic myosin were seen in the C2C12 cultures exposed to this concentration of puromycin.

#### *6.2.1.3 Co-culture of C2C12 and GFP-fibroblast*

To characterise the DEP properties of cells of a similar size, MRC-5-GFP fibroblasts were used as a feeder layer for co-culturing C2C12 myoblasts. The medium for both cell types was GM supplemented with 2 lg/ml of puromycin (to select for GFP expression) and cultured for a week before analysis.

Because of the GFP (green fluorescent protein) expression, the MRC-5-GFP fibroblasts and C2C12 myoblasts could readily be identified by flow cytometry.

#### *6.2.1.4 Human primary fibroblasts cell culture*

Primary human fibroblasts were obtained from Coriell Cell repository, the Huntington's Disease (HD) fibroblasts were GM04281 from a 20 years old female

and the control fibroblasts (90011801,1BR3) were from ECACC collection. HD fibroblasts were maintained in Eagle's Minimum Essential Medium (EMEM) with Earle's salts and non-essential amino acids (NEAA) with 15% Fetal Bovine Serum (FBS-Perbio Science UK Ltd.) supplemented with 2 mM l-glutamine. For Raman spectra acquisition and membrane extractions, the passage number was kept below 15. Control fibroblasts were maintained in EMEM with Earle's salts and NEAA with2 mM l-glutamine with 15% FBS (Perbio Science UK Ltd.). All the cultures were kept in an incubator at 37° C with 5% $CO_2$.

## 6.3 Biochemical techniques

### 6.3.1 Western blot

Myoblasts and myotubes were mixed populations prior to sorting. Using the DEP device the separated cell fractions were collected for Western blot analysis. Cells were centrifuged at 250 g and re-suspended in cold PBS. The suspension was centrifuged at 350 g for three min and the pellet was re-suspended in three parts of distilled water and one part of 4XNuPAGE-SDS sample buffer (Invitrogen Carlsbad, CA, USA) supplemented with 10% of b-Mercaptoethanol. The samples were denatured by boiling for 6 min. Proteins were resolved by 6% SDS-PAGE and transferred to a nitrocellulose membrane (LI-COR Bioscience). The membrane was blocked in 5% milk in Tris-buffered saline (TBS) containing 0.1% Tween 20 overnight.

The blocking procedure was followed by 1 h incubation with antibodies against embryonic myosin (EMHC, clone F1.652, developed by Helen Blau, University of Iowa) diluted 1:1000 and anti-a tubulin antibody diluted 1:5000 (clone B-5-1-2 Sigma). The primary antibody was detected with secondary IR800 conjugated goat anti-mouse antibody (LI-COR Bioscience) at room temperature for 2 h. Visualisation of the signal was performed using a LI-COR Odyssey near-infrared scanner and ODYSSEY 3.0,16 software with median background subtraction.

### 6.3.2 Immunofluorescence spectroscopy for cell cycle analysis

Cells were fixed in 3.7% formaldehyde. Then washed three times for five minutes each in TBS washing solution composed of Tris 50mM, NaCl 150mM and 0.1% Tween 20 at pH 7.4. Ki-67 (BDbiosciences) were added in blocking solution composed of TBS, 0.1% Tween-20 and 0.9% Fish gelatine. After incubation at room temperature (RT) for an hour, cells were washed in TBS solution three times for five minutes each. Secondary antibodies diluted in blocking buffer were added for one hour at RT. Secondary antibodies used were: for C2C12 and myotubes Alexa Fluor 488 was used and Alexa Fluor 568 for GFP+ Fibroblasts. Cells were washed twice for five minutes each in washing solution before addition of DAPI or Hoechst nuclear dye for ten minutes at 37° C. Finally, cells were washed in PBS twice for five minutes each and the slides were mounted using Vectashield mounting medium. Cover slips were sealed and imaged with fluorescent microscope.

### 6.3.3 Oil red O staining

*Adipocytes inducing medium composition:*

Cells at ~70% confluence were cultured with DMEM supplemented with 10% FBS, 0.5 mM isobutyl-methylxanthine , 1 µM dexamethasone, and 10 µg/ml insulin.

*Oil red O stock solution:*

I. 300mg of Oil Red O powder and adding this to 100 mL of 99% isopropanol. In the fume hood, mix three parts of Oil Red O stock solution with two parts DI water. Incubate 10 minutes at room temperature. This working solution is only stable for 2 hours.

II. Place a piece of Whatman filter paper in a funnel above a vessel. Filter the Oil Red O working solution completely through the filter funnel. The collected solution is used for cell staining.

Cells were cultured in six well plates. Each well was washed in PBS (Phosphate Buffer Solution) for 5 minutes and 2ml 10% formalin solution was added in each well and incubated for 40 minutes at RT. Formalin was removed and cells gently rinsed with 2ml of DI water per well. A solution of 60% isopropanol was added in each well for 5 minutes.

The 60% isopropanol solution was removed and 2 mL Oil Red O working solution was added to each well and incubated for 5 minutes at room temperature.

Oil Red O solution was removed and cells rinsed under tap water at room temperature until the water rinsed off clear. Cells were analysed under light microscope for red straining of lipids droplets in the cytoplasmic portion of the cells.

### 6.3.4 Cell membrane extractions I

Twelve samples (six for each cell type) of Huntington's disease (HD) and control fibroblasts were used to extract cell membranes with approximately 15 million cells per sample. All the procedures were performed at 4°C and on ice. The cells were washed and harvested prior to centrifugation at 259 g for 5min. The pellet was suspended in extraction buffer composed of 1mM EDTA, 20mM tricine and 0.25M sucrose equilibrated at pH of 7.8. The mixture was centrifuged at 1400 g for 5min and re-suspended in extraction buffer. Homogenization was performed by a pre-chilled dounce and pestle with approximately 20 strokes and cell breakage was estimated by analysing aliquots under a light microscope.

The subsequent suspension was centrifuged at 1000 g for 10min and the supernatant was stored on ice. The pellet was homogenized and centrifuged again as previously described and the combined supernatants were layered on a 30% Percoll solution of the extraction buffer before centrifugation at 85,000 *g* for 30 min. The membranes were collected and the Percoll removed by two subsequent centrifugations at 100,000 *g* for 90 min. Raman analysis was performed immediately after extraction to minimize any possible degradation. The membranes were all analyzed the same day

of the extraction and from the time of extraction to the time of the Raman analysis, the membranes were kept under liquid nitrogen.

### 6.3.5 Cell membrane extractions II

The protocol relies on the two-phase partition process [108,109]. Briefly, the cell populations were collected and centrifuged at 405g for 7 min at 4°C. Cells were re-suspended in 0.2 m*M* EDTA in 1 mM $NaHCO_3$ with incubation on ice for 30 min to swell the cells. Homogenization was carried out with a dounce and pestle pre-chilled at -20° C. Cell breakage was estimated by analysing aliquots under a light microscope, counting the nuclei and unbroken cells ratio. Approximately 90% cell breakage was determined. Unbroken cells and nuclei were extracted from homogenate with centrifugation at 175g at 4°C for ten minutes. The resulting supernatant was further centrifuged at 25 000 g for 30 minutes at 4°C. The resulting pellet was re-suspended in 0.2 *M* potassium phosphate buffer (pH 7.2). The suspension was loaded on the two phase system composed of 6.6% Dextran T500, 6.6% (w/w) poly-ethylene glycol (PEG) 3350, 0.2 M potassium phosphate, pH 7.2 and 0.25 M sucrose. The phases were mixed by 40 inversions at 4°C. Separation of the upper phases was achieved by centrifugation at 1200 g for 5 minutes at 4°C. The upper phase was diluted in 1mM bicarbonate and collected by centrifugation.

### 6.3.6 Flow cytometry analysis

#### *6.3.6.1 DEP sorting validation*

Samples were analysed using a LSRII flow cytometer (Beckton Dickinson Immunocytome-try Systems, UK) running BD FACSDIVA v6 Software. An electronic acquisition gate was applied to the forward/side scatter (FSC/SSC) plot to exclude debris from intact material and typically more than 50 000 events were acquired in this gate. GFP or Alexa Fluor® 488-conjugated secondary antibody binding was detected using 488 nm laser excitation and a recording of fluorescence

in the range 500-550 nm. Analysis was performed using FLOWJO software (Tree Star,USA). Debris was excluded through FSC/SSC profile gating before applying electronic gates to assess green fluorescence. Sort purity was calculated through gating based on profiles from each cell type as controls. For analysis of myotubes, cells were collected separately from the central and outer exit ports of the DEP chamber and washed in phosphate buffered saline (PBS) ($Mg^{2+}$, $Ca^{2+}$ free) supplemented with 0.1% bovine serum albumin (BSA) fraction V and 0.1% $NaN_3$. The cells were centrifuged at 350 g for 5 min and the pellet was re-suspended and fixed in 2% formaldehyde solution for 10 min at room temperature. The fixed cells were washed in permeabilisation buffer (PB) composed of PBS ($Mg^{2+}$, $Ca^{2+}$-free) supplemented with 0.1% BSA V, 0.1% $NaN_3$ and 0.1% saponin (S-7900). Primary antibodies for embryonic myosin (specific for myotubes) were diluted in 100 µl of PB for incubation with the cell samples for 90 min at 4°C. After primary antibody incubation cells were centrifuged and washed in a single large volume (3 ml) of PB. Secondary antibodies, conjugated with Alexa Fluor 488, were added to cells suspended in PB and incubated for another 90 min at 4°C. Finally, cells were re-suspended in 400 µl of F-PBS and flow cytometry analysis performed.

For C2C12 myoblasts co-cultured with MRC-5-GFP fibroblasts, the separation performance by DEP was assessed by flow cytometry.

The cells were collected separately from the two exit ports of the DEP chamber and washed in Flow-PBS (F-PBS) composed of PBS ($Mg^{2+}$, $Ca^{2+}$ free) supplemented with 0.1% $NaN_3$ and 0.2% BSA V prior to acquisition.

Propidium iodide (PI), which is membrane impermeable and excluded from viable cells, was used as a fluorescent DNA stain to evaluate cell viability after DEP separation. Immediately prior to cell acquisition for viability, 10 µl PI solution (50 µg/ml PI +100 µg/ml RNase in PBS) was added directly to sample tubes and staining detected using 488 nm laser excitation and recording of fluorescence in the range 633-677 nm. Viability was calculated through gating based on profiles from unstained samples. The DEP separation and analysis by flow cytometry was

performed for 13 separate samples of each paired combination of the three cell types, with the results expressed as percentages of cells that were determined by flow cytometry to be positive for GFP or Alexa Fluor 488, or fluorescence negative.

#### *6.3.6.2 Flow cytometry for cell cycle*

For cell cycle analysis cells sorted by DEP were washed in Flow permeabilisation buffer (F-PBS) composed of phosphate buffer solution (PBS $Mg^{2+}$-, $Ca^{2+}$-free) supplemented with 0.1% BSA V and 0.1% $NaN_3$ azide. Cells were permeabilised by addition of an equal volume of cold 70% ethanol solution followed vortexing. After overnight incubation at -20° C, cells were pelleted and then washed twice by centrifugation at 2000 rpm for 5 minutes, before the addition of RNase (100µg/ml). Cells were incubated for one hour at room temperature and finally Propidium Iodine (PI) was added at concentration of 50µl/ml.

Samples were analysed using a LSRII flow cytometer (Beckton Dickinson Immunocytometry Systems, UK) running BD FACSDiva v6 Software. An electronic acquisition gate was applied to the forward/side scatter (FSC/SSC) plot to exclude debris from intact material and typically more than 50,000 events were acquired in this gate. Analysis was performed using FlowJo software (Tree Star, USA). Debris was excluded through FSC/SSC profile gating before applying electronic gates to assess green fluorescence. Sort purity was calculated by application of gates generated using profiles from each cell type alone as controls.

### 6.3.7 Microscopy techniques

#### *6.3.7.1 Immunoflurescent staining for cell suspensions count*

Cells were collected by trypsin and washed three times in PBS (by centrifugation) before adding CellTracker™ Green CMFDA (Invitrogen Carlsbad, CA, USA) at concentration of 5µM for 30 minutes with a further addition of Hoechst nuclear dye (Invitrogen Carlsbad, CA, USA) for 20 minutes. Cells were washed in PBS and re-suspended in 3.7% formaldehyde. The suspension was lightly smeared on

microscope slides and mounted using Vectashield (Vectorlabs) medium for fluorescence microscopy.

#### *6.3.7.2 Scanning electron microscopy (SEM)*

Samples of individual cell types were fixed in a solution of 3% glutaraldehyde in 0.1 M sodium cacodylate buffer (pH 7.3) for 2 hours before washing in three changes of 0.1 M sodium cacodylate buffer, each for 10 minutes. Samples were then postfixed in 1% osmium tetroxide in 0.1 M sodium cacodylate buffer for 45 minutes. A further 3 x 10 minute washes were performed in 0.1 M sodium Cacodylate buffer. Dehydration in graded concentrations of acetone (50%, 70%, 90%, and 3 x 100%) for 10 minutes each was followed by critical point drying using liquid carbon dioxide. After mounting on aluminium stubs with carbon tabs attached, the specimens were sputter coated with 20 nm gold palladium and viewed using a Hitachi S-4700 scanning electron microscope. Images were colour-enhanced to highlight differences in the microvilli structure between cell types.

#### *6.3.7.3 Transmission electron microscopy (TEM)*

For Transmission Electron Microscopy (TEM), all samples were fixed in 3% glutaraldehyde in 0.1M Sodium Cacodylate buffer, pH 7.3, for 2 hours then washed in three 10 minute changes of 0.1M Sodium Cacodylate. Specimens were then post-fixed in 1% Osmium Tetroxide in 0.1M Sodium Cacodylate for 45 minutes, then washed in three 10 minute changes of 0.1M Sodium Cacodylate buffer.

These samples were then dehydrated in 50%, 70%, 90% and 100% normal grade acetones for 10 minutes each, then for a further two 10-minute changes in acetone analaR. Samples were then embedded in Araldite resin. Sections, 1µm thick were cut on a Reichert OMU4 ultramicrotome, stained with Toluidine Blue, and viewed in a light microscope to select suitable areas for investigation. Ultrathin sections, 60nm thick were cut from selected areas, stained in Uranyl Acetate and Lead Citrate then viewed in a Philips CM120 Transmission electron microscope. Images were taken on a Gatan Orius CCD camera.

## 6.4 Chemical methods

### 6.4.1 Raman spectroscopy

#### *6.4.1.1 Raman spectroscopy data acquisition*

Raman spectra acquisition was obtained by a Renishaw in Via Raman microscope (785 nm near-IR laser excitation, 40 mW at sample) with a 40× objective lens and 0.75 numerical aperture. The membranes were dried under a stream of nitrogen and deposited onto a quartz substrate (SPI Supplies). The quartz was positioned on the inverted stage of the microscope and each spectrum was acquired over approximately 2 min for six samples obtained from the membranes of the C2C12 myoblasts, myotubes and MRC-5-GFP fibroblasts (as described in section 2.2.2.4). Principal component analyses (PCA) were performed for six separate spectra obtained from the membranes of each of the three cell types (C2C12 myoblasts, myotubes and MRC-5-GFP fibroblasts). For HD fibroblasts and controls 12 samples (six for each cell type) were used to extract cell membranes (as described in section 2.2.2.5) with approximately 15 million cells per sample. Partial Least Squares (PLS) analysis was performed on the spectral data. Spectra were acquired in the 200–3200 $cm^{-1}$ range with 1.9 $cm^{-1}$ spectral resolution.

#### *6.4.1.2 Spectra pre-analysis processes*

Cubic spline curves were chosen by trial and error for baseline subtraction. For the HD fibroblasts and controls, the nodes numbers were 12 for low wavenumber region (400–1800 cm−1) and six for high wavenumber region (2700–3200 cm−1). For myoblast, myotubes and GFP-fibroblast the nodes numbers were 12 for low wavenumber region (200–1800 cm−1) and six for high wavenumber region (2700–3200 cm−1). The data were filtered by smoothing at 9 points with polynomial of five by Savitzky–Golay function to decrease the signal-to-noise ratio. Spectra were mean and centered for PLS analysis. Statistical analysis was performed using JMP software (JMP, SAS Institute Inc., Cary, NC). Additional graphs are presented here using Origin software (OriginLab, Northampton, MA).

#### *6.4.1.3 Principal component analysis (PCA)*

Principal component analysis is a way to identify pattern in data sets in order to find similarity or/and differences. This technique not also is used to recognised data but it compressed it to, reduce the dimensions, without losing the intrinsic information that the data has. More information about the details of this mathematical technique can be found in literature [110,111,112,113].

In general, the process behind principal component analysis can be simply performed by steps such that:

- In a data set of $n$ dimensions, the mean across each dimension is subtracted from each dimension producing an average of zero.

- The covariance matrix of the data is calculated and the eigenvalue and eigenvector are extrapolated from the covariant. By plotting the data and the eigenvectors visually can be shown the possible correlations between the data and each eigenvectors (as the eigenvectors as lines of best fit of the data with each eigenvector perpendicular to each other). This correlation between eigenvectors and data point is important because the eigenvectors (different "lines of fit") characterise the data sets.

- Now the data can be compressed by analysing the eigenvalues. Each eigenvalue of the corresponding eigenvector has a "component value" that is ranked from the highest to the lower. This determines the Principal Component "level of significance" for each specific eigenvalue. Therefore, the highest component carries more information about the data and the lowest the least amount of information about the data.

- By choosing the amount of information to retain (how many components to use to describe the data), we can construct a new matrix (often called feature matrix) with only the most important.

The final process is to combine the original data sets with the feature matrix in order to derive a new data set based of the eigenvector that have more significance. The data set in not anymore expressed in terms of the $x$ and $y$ axis but by the eigenvectors. In addition, the dimensionality of the original data is reduced by using only the most significant eigenvectors to compose the new data set.

In general, we have started with sets of data and we have mathematically extrapolated patterns that correspond to lines that describe the relationships between the data.

PCA can be used to visualise correlations between variables and data whereas PLS is used to model regression for X and Y matrixes so that X can be predicted from Y, as illustrate in *Figure 6-1*.

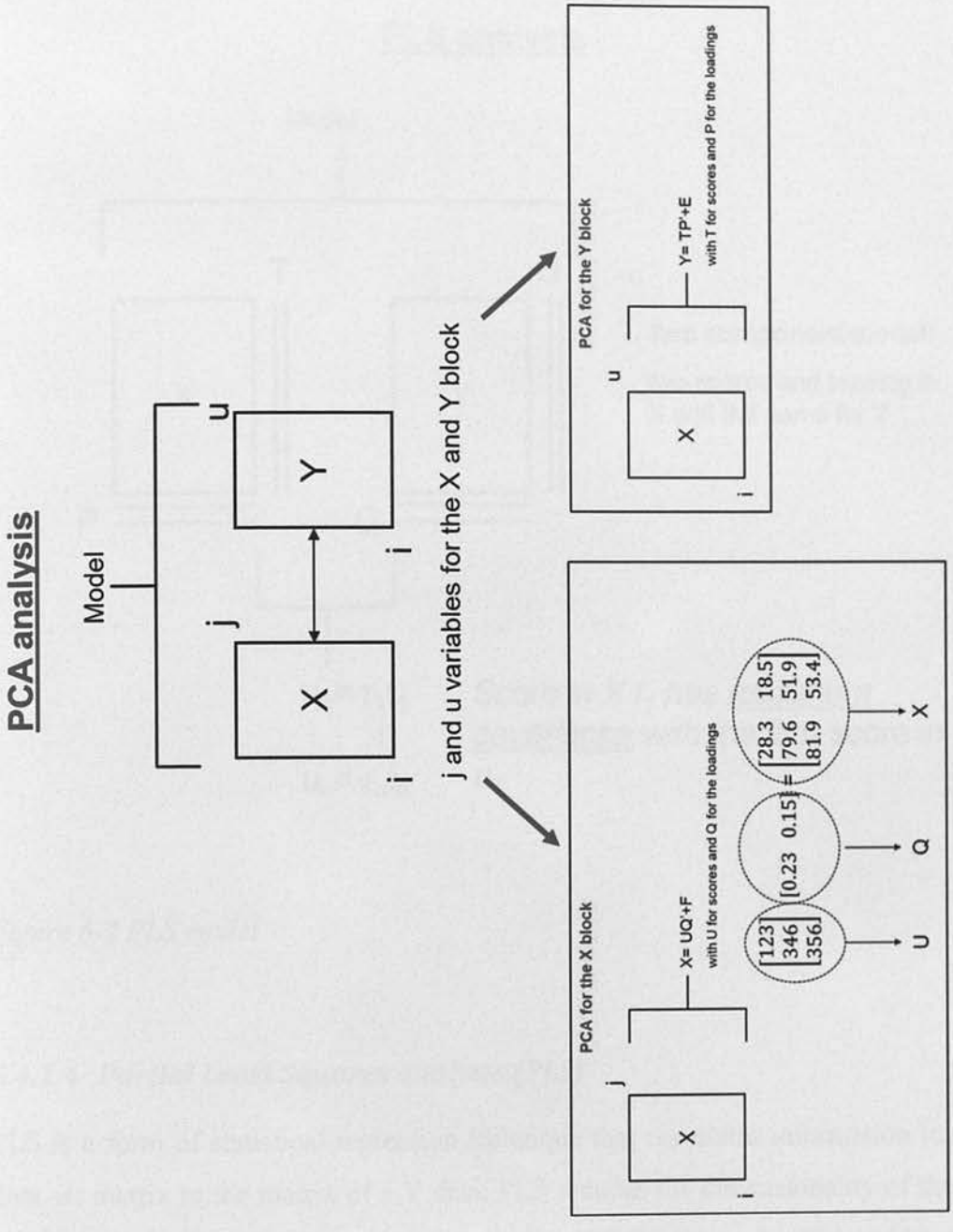


*Figure 6-1 PCA model*

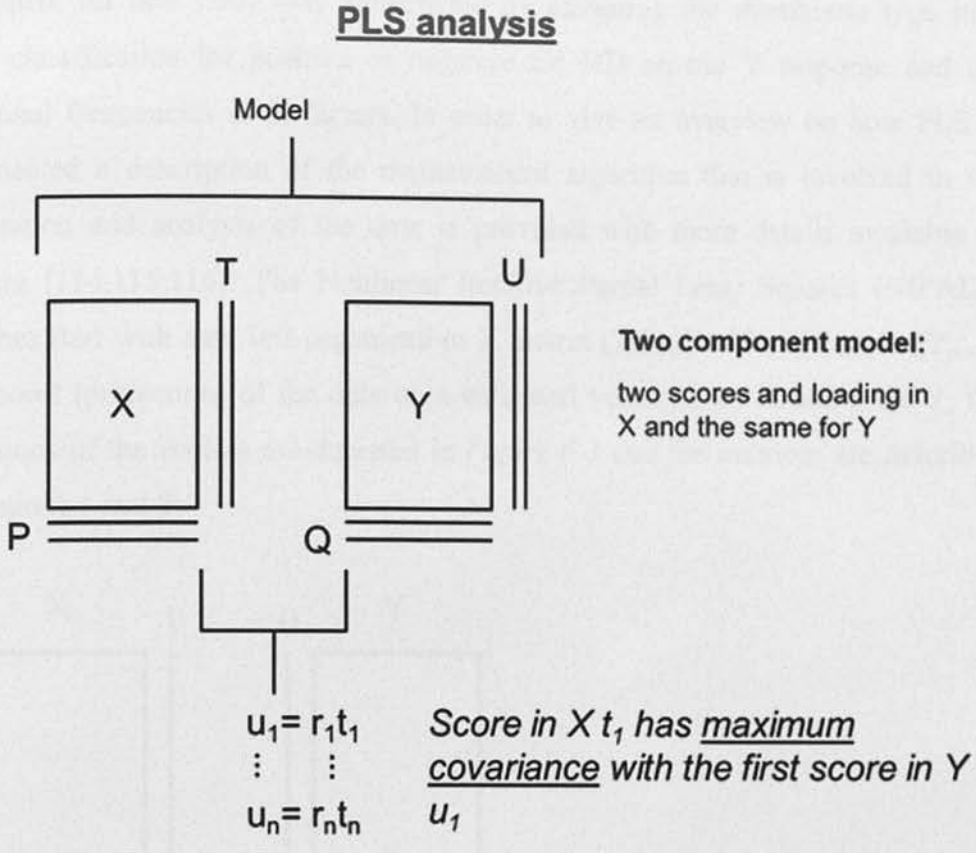


*Figure 6-2 PLS model*

#### *6.4.1.4 Partial Least Squares analysis (PLS)*

PLS is a form of statistical regression technique that correlates information in an X data set matrix to the matrix of a Y data. PLS reduces the dimensionality of the data similarly to Principal Component Analysis (PCA) although PCA address the information contained in a single X data matrix. PLS is also designed to deal with multicollinearity[33] amongst the data and in conditions where there are a small number of samples. The PLS model for analysis is illustrated in *Figure 6-2*.

[33] This is a phenomenon where two or more variables are highly correlated. This is a problem when the study needs to establish the contribution of the independent variable to dependent variable.

The matrix for this study was constructed by assigning the membrane type in a binary classification for positive or negative for HD on the Y response and the vibrational frequencies as X factors. In order to give an overview on how PLS is implemented a description of the mathematical algorithm that is involved in the computation and analysis of the data is provided with more details available in literature [114,115,116]. The Nonlinear Iterative Partial Least Squares (NIPALS) algorithm start with data sets organized in X matrix ($X_{n \times m}$) and a Y matrix ($Y_{n \times k}$) with scores (projections of the data on a weighted vector) t for X and u for Y, the dimensions of the vectors are depicted in *Figure 6-3* and the matrices are described in equations 1 and 2:

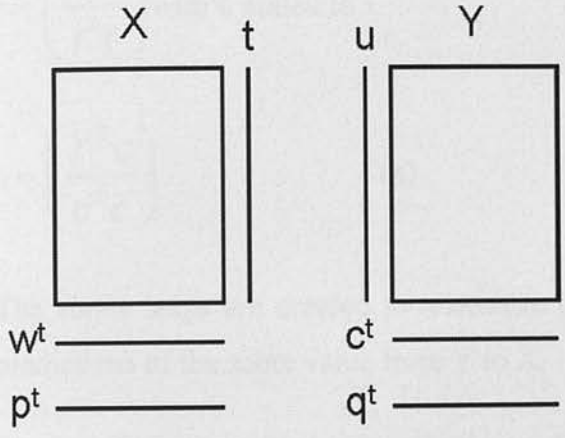


*Figure 6-3* Vector depiction for PLS

$$X = TP^t + E \quad (1)$$

$$Y = UQ^t + F \quad (2)$$

The T and U are the matrices of the scores, P and Q are expressive of the loading (a measure of contribution of T and U to X and Y) of the matrices and E and F the residuals matrix. Considering the mean centered block variable matrices $X_{n \times m}$ and

$Y_{n \times k}$ the Nonlinear Iterative Partial Least Squares (NIPALS) algorithm is used in decomposition of the matrices for X and Y as follows:

Initially the algorithm finds the u score (Y matrix) and projects it onto the w vector to produce the score vector t, c and u in steps described in equation 1 to 4:

$$w = \left( \frac{X^T u}{u^T u} \right) \text{ with w scaled to 1} \qquad (1)$$

$$t = Xw \qquad (2)$$

$$c = \left( \frac{Y^T t}{t^T t} \right) \text{with c scaled to 1} \qquad (3)$$

$$u = \left( \frac{Y^T c}{c^T c} \right) \qquad (4)$$

The above steps are created to maximize covariance between t and u; this allows predictions of the score value from Y to X.

The algorithm proceeds by creating the loading for X and Y by equations 5 and 6:

$$p = \left( \frac{X^T t}{t^T t} \right) \text{ X-loading} \qquad (5)$$

$$q = \left( \frac{Y^T u}{u^T u} \right) \text{ Y-loading} \qquad (6)$$

Consequently the regression factor b of u on t is created by equation 7:

$$b = \left( \frac{u^T t}{t^T t} \right) \qquad (7)$$

Finally X is deflated by $tp^T$ and Y by $btc^T$, from here a new w is generated to continue the process.

***Variables Importance in the Projection (VIP)***

VIP can be described as a measure of the contribution for each variable to the projections of the PLS model.

VIP was used in this study to define the most important vibrational band associated with the separation between the two types of membranes: HD and control.

The formula for VIP is described in equation 8.

$$VIP_j = \sqrt{p \frac{\sum_{m=1}^{M} w_{jm}^2 \left[SS(b_m t_m)\right]}{\sum_{m=1}^{M} SS\,(b_m t_m)}} \qquad (8)$$

With p as the variables number, M the latent variables and $W_{jm}$ as the weight of the $j^{th}$ variable for the $m^{th}$ variable X. SS ($b_m t_m$) is the proportion of y explained by the $m^{th}$ latent variable. Wold [116,117] suggested a VIP value greater than 0.8 as a relevant indicator and important predictor. In this study VIP values >0.8 were used as indicators.

## 6.5 Microfabrication methods

### 6.5.1 Device manufacture

The device was fabricated by standard microfabrication methods for MEMS using three main steps:

1. Deposition of the electrodes on glass substrate.
2. Polyimide channel fabrication on glass substrate.

3. Bonding of the two glass substrates.

More detailed steps for manufacture the DEP device are illustrated schematically in *Figure 6-4* . Top and bottom electrodes were patterned on top of 4" glass wafers by e-beam deposition of 10 nm titanium (Ti) as bonding layer and 200 nm platinum (Pt).

Polyimide was spun on top of the glass substrates and the microchannel was defined by photolithographic processes. Polyimide layer was subsequently developed and vias for the fluidic inlets and outlets were micro drilled as well as dicing the two glass wafers to measure. The two glass substrates were aligned and the polyimide was cured at 350° C for 30 minutes and bonded at 350° C for 10 minutes in $N_2$ environment.

The microcahannel was mounted on a holder that contained all the fluidics and electric connections as illustrated in *Figure 6-5* and *Figure 6-6* with the sorting set-up using DEP is illustrated in *Figure 6-7*.

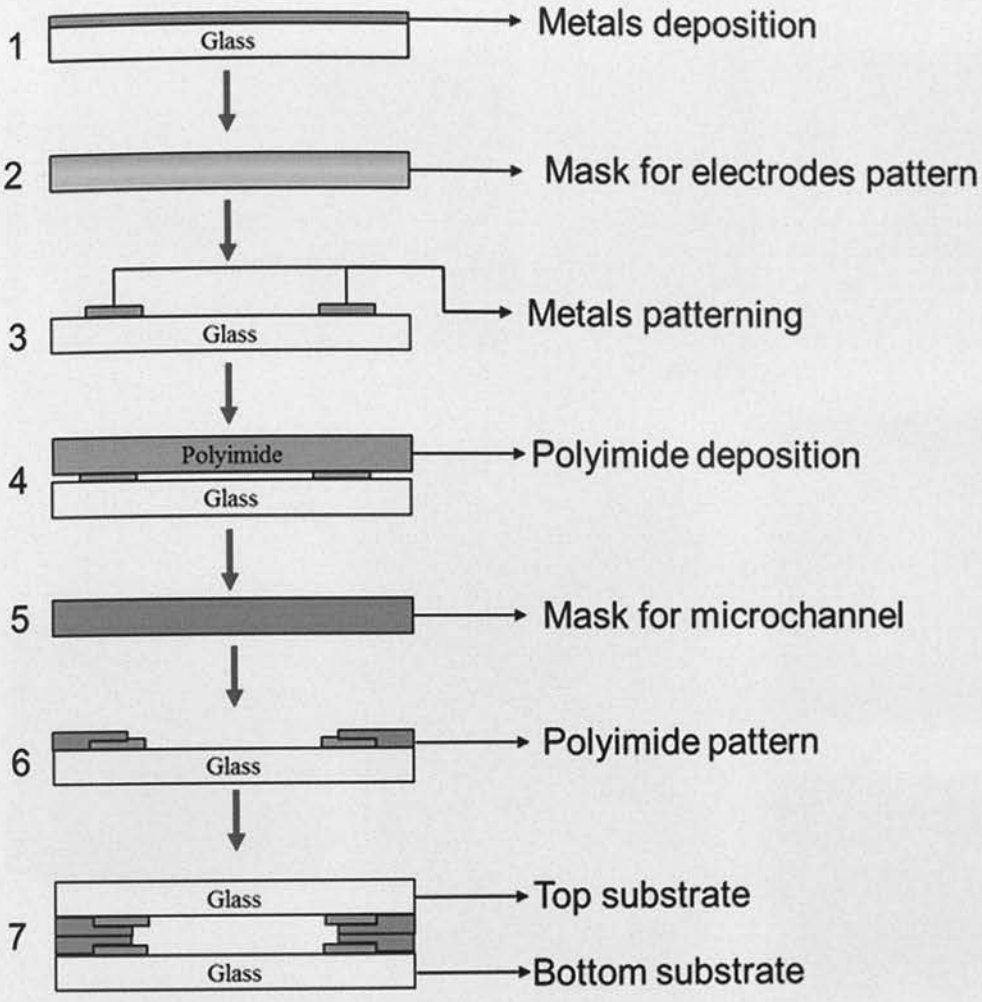


*Figure 6-4 Micro fabrication steps.*

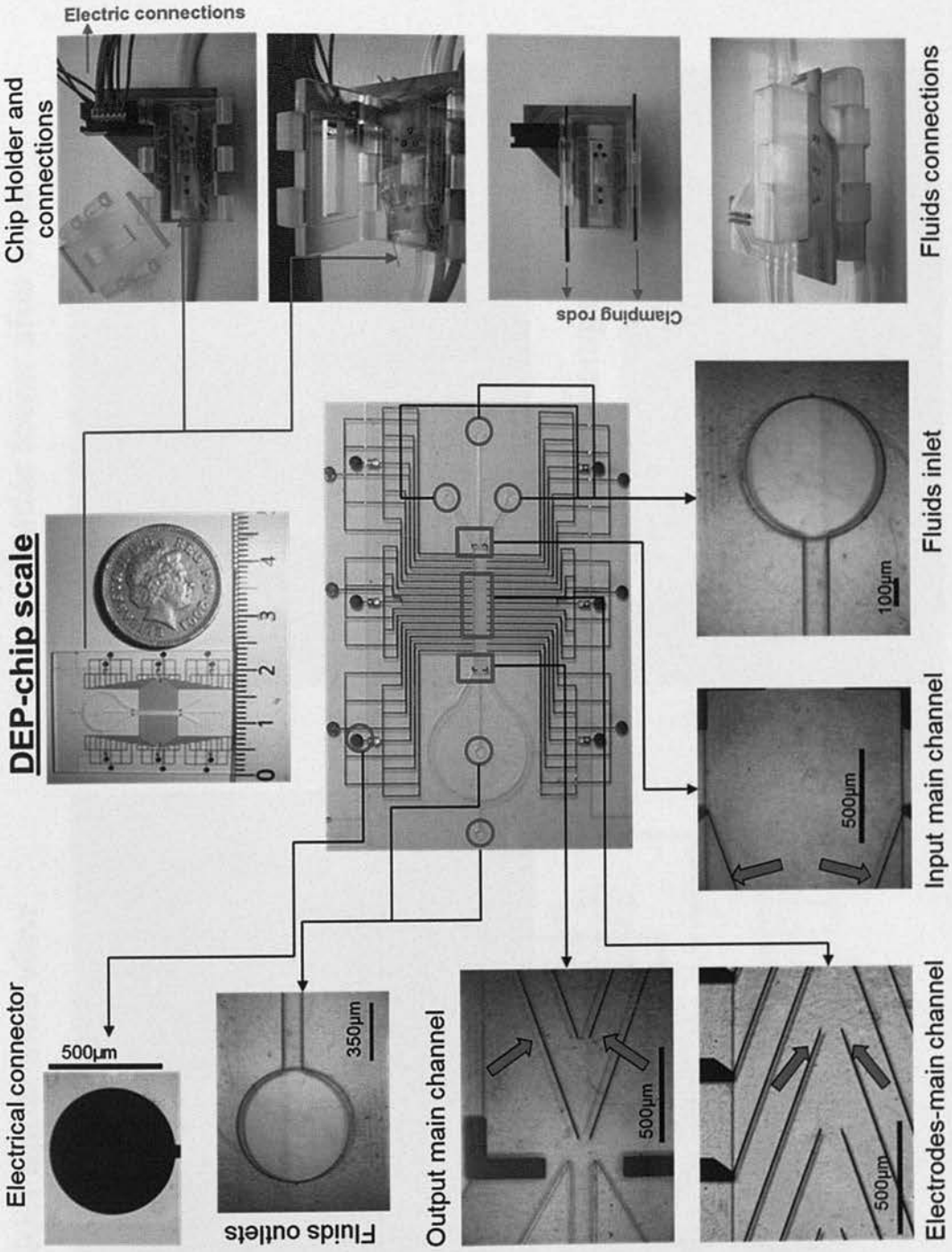


*Figure 6-5 Details of the device and main features. Large red arrows indicate the electrodes. The electrical connections are indicated on top on the right hand side. The clamping mechanism is indicated on the right hand side bottom part*

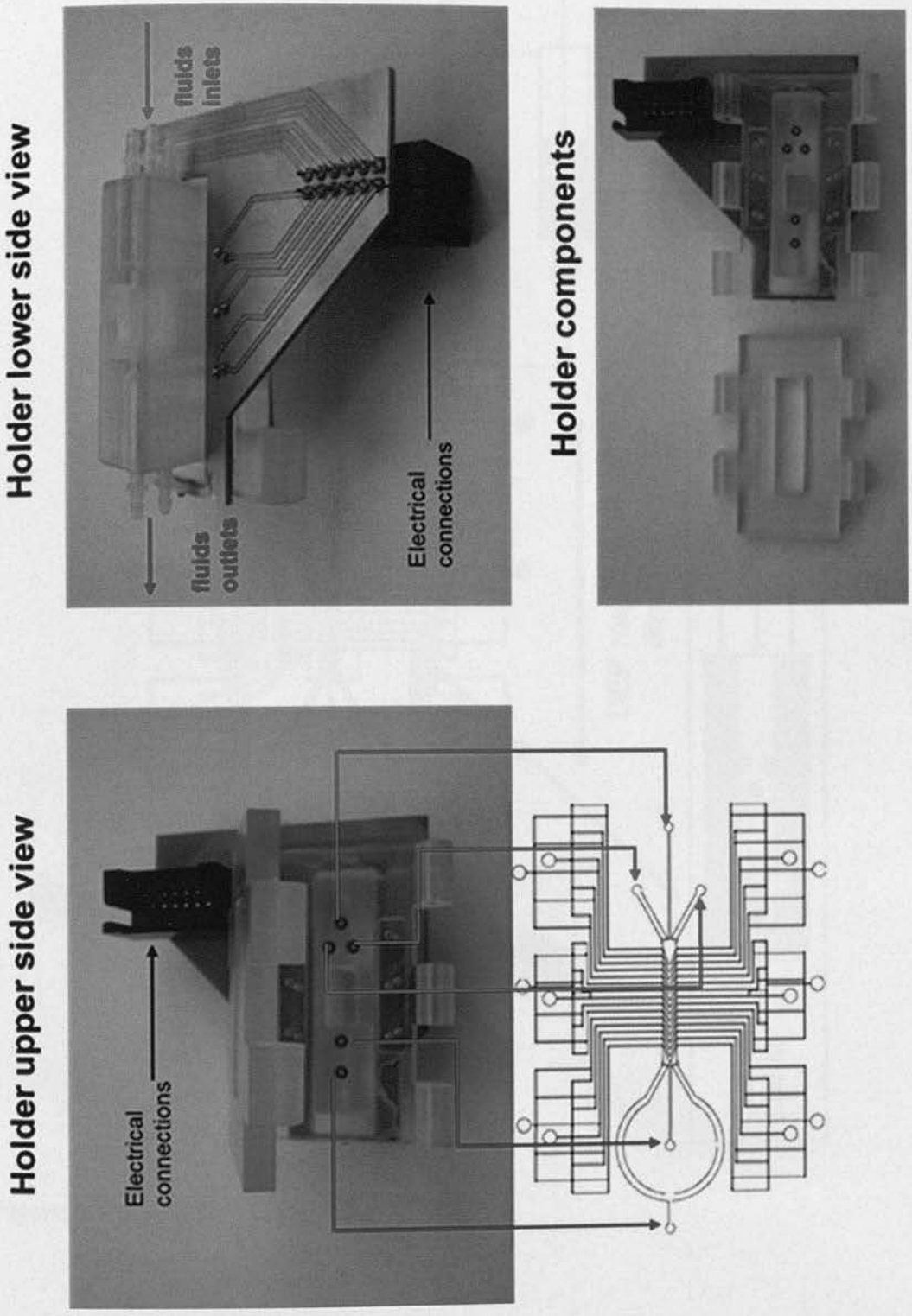


*Figure 6-6 Details of the holder for electric and fluid connections*

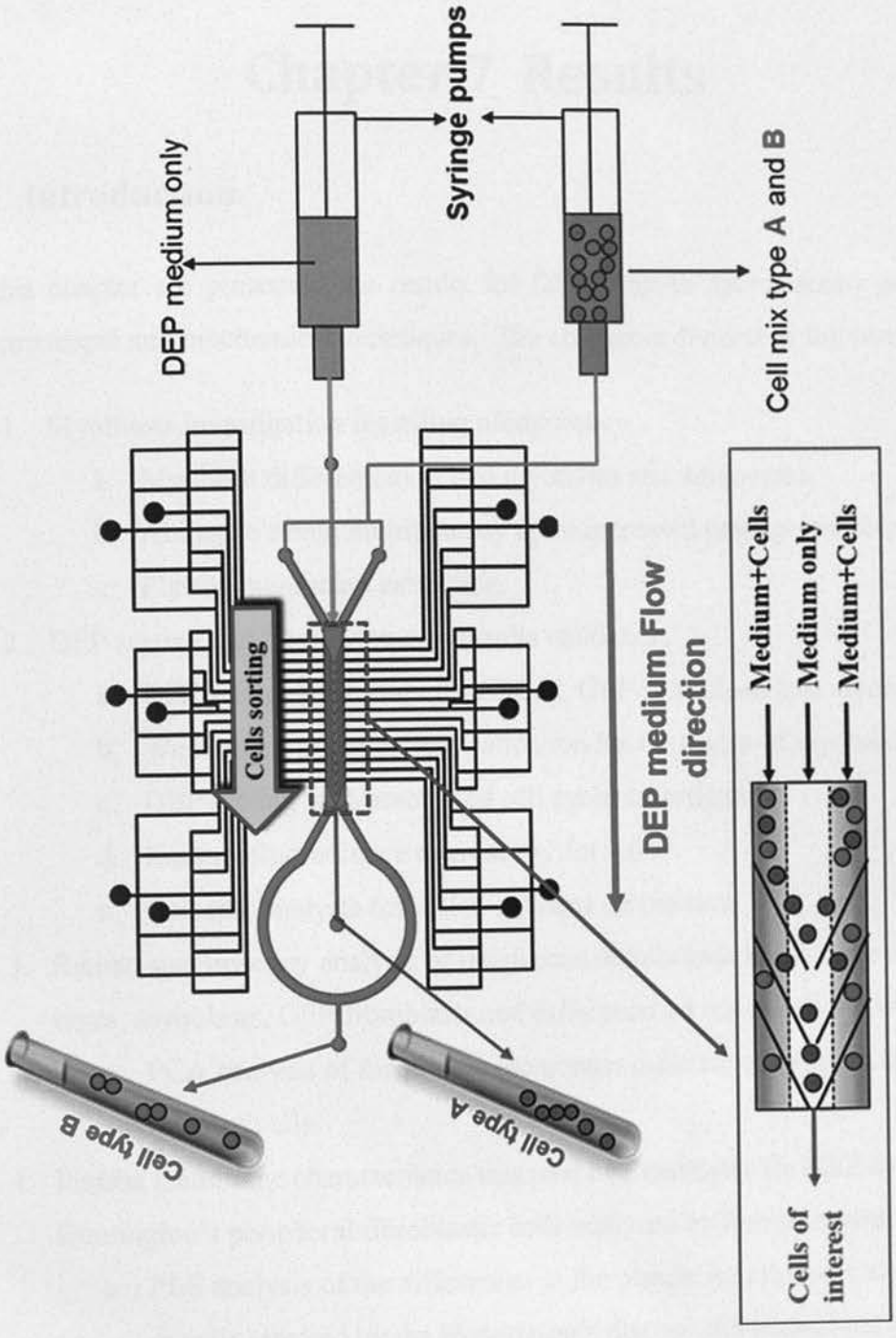


*Figure 6-7 Set-up for DEP sorting of cells*

# Chapter 7 Results

## 7.1 Introduction

In this chapter are presented the results for DEP, Raman spectroscopy and other spectroscopic and biochemical techniques. The chapter is divided as follows:

1. Myoblasts investigation regarding pluripotency:
    a. Myoblast differentiation into myotubes and adipocytes.
    b. Ability to retain multipotency upon increased passage number.
    c. Plasma membrane extraction.
2. DEP sorting and flow cytometry results validation.
    a. DEP sorting efficiency for C2C12, GFP-fibroblasts and myotubes.
    b. Western blots and further validation for the purity of myotubes.
    c. DEP sorting with associated cell cycle investigation.
    d. Immunofluorescence microscopy for Ki-67.
    e. Cell size analysis for cell in aqueous suspension.
3. Raman spectroscopy analysis of the plasma membranes in the three cell types: myoblasts, GFP-fibroblasts and differentiated myoblastic myotubes.
    a. PCA analysis of the plasma membrane differences between the three types of cells.
4. Plasma membrane characteristics that could be amenable for DEP sorting in Huntington's peripheral fibroblastic cells analysed by Raman spectroscopy.
    a. PLS analysis of the differences in the plasma membrane composition in cells affected by the Huntington's disease and normal peripheral fibroblastic controls.

5. Microscopy analysis in the form of SEM and TEM to address the overall plasma membrane characteristics of the three types of cells used for DEP sorting.

## 7.2 Myoblasts pluripotency

### 7.2.1 Myoblast differentiation in myotubes and adipocytes

Myoblasts C2C12 (donated by Dr Vlastimil Sresn) were plated at density between 3000/6000 cell/cm$^2$ approximately. The passage number of cells used in these experiments was above 50 and the rate of conversion was between 40/50% from the initial population number. The process of differentiation is briefly illustrated in *Figure 7-1*. Samples of the phenotype of C2C12 are shown in *Figure 7-2*.

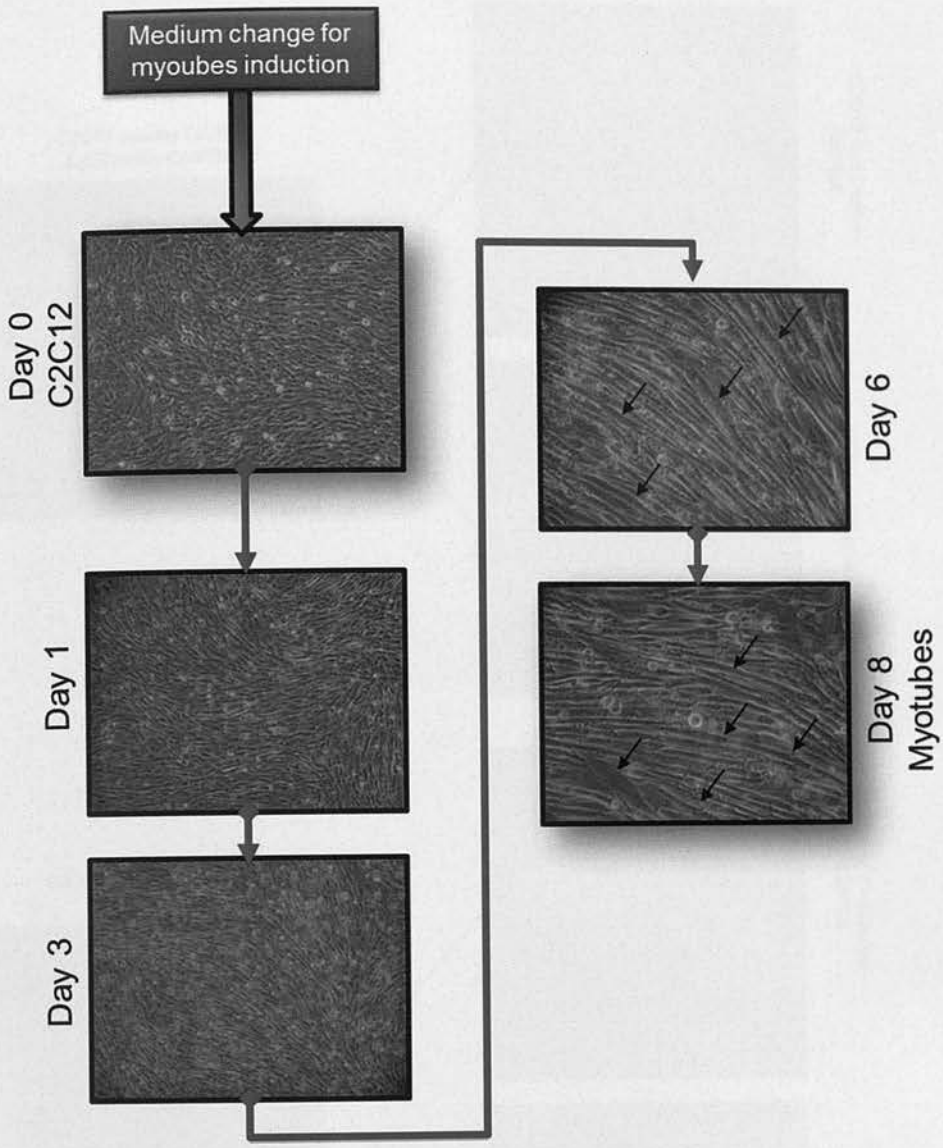


*Figure 7-1 C2C12 differentiation process.Black arrows points at myotubes*

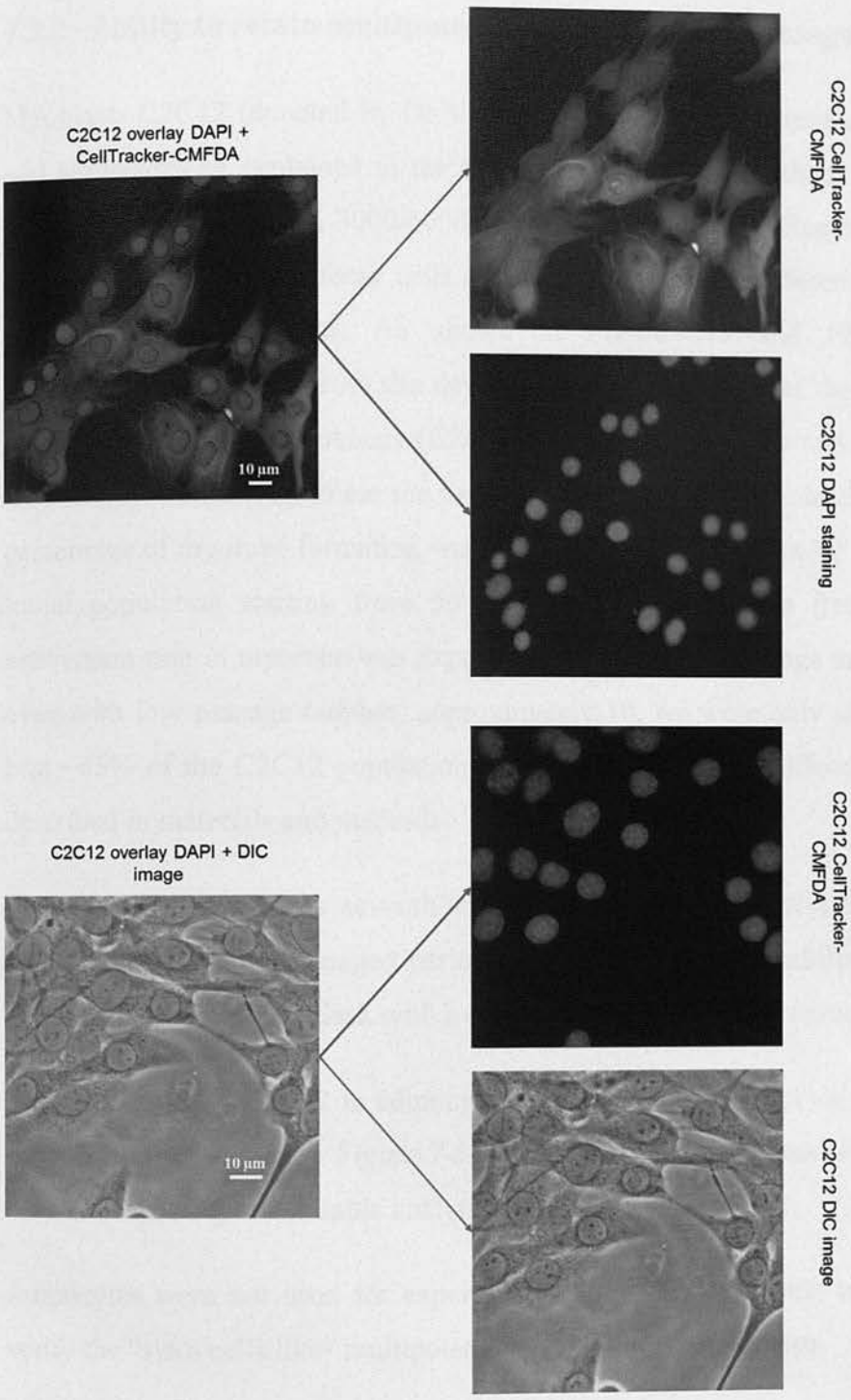


*Figure 7-2 C2C12 cultures before induction to differentiate. Top cells were stained with Cell-tracker to delimit the cell boundaries and nucleus was stained with DAPI as reference point for the viewer. Bottom another example of C2C12 using Differential Interference Contrast (DIC) and DAPI to highlight the shape and nuclear positioning in the cell*

### 7.2.2 Ability to retain multipotency upon increased passage number

Myoblasts C2C12 (donated by Dr Vlastimil Sresn) were differentiated in myotubes and adipocytes as explained in the section Materials and Methods. The cells were plated at density between 3000/6000 cell/cm$^2$ approximately. Regarding conversion into different cell types, these cells showed capabilities to differentiate and display pluripotent characteristics. As shown in *Figure 7-3* and *Figure 7-4* after approximately ten days from the day of induction to myotubes the cultures have a mixed population of myoblasts (C2C12) and myotubes. This was the case for all C2C12 populations regardless the time that they been left in inducing medium. The percentage of myotube formation was in approximately between 40 to 50% from the initial population starting from 50 as passage number. The trend of decreased conversion rate in myotube was dependent on myoblasts passage number. However even with low passage number, approximately 10, we were only able to convert at best ~65% of the C2C12 population in myotubes using the differentiation medium described in materials and methods.

The myotubes formed by seventh/tenth day were able to survive for an additional week. However, for prolonged periods above 12 days, the undifferentiated C2C12 overcrowded the culture flask with a corresponding decrease in myotubes viability.

The conversion of C2C12 in adipocytes was also undertaken to verify multipotency of these cells as shown in *Figure 7-5*. The method for adipocytes assessment was by Oil red O staining as a reliable analytical technique [118,119].

Adipocytes were not used for experiments with DEP or Raman analysis rather to verify the "stem cells like" multipotent capability of the myoblasts.

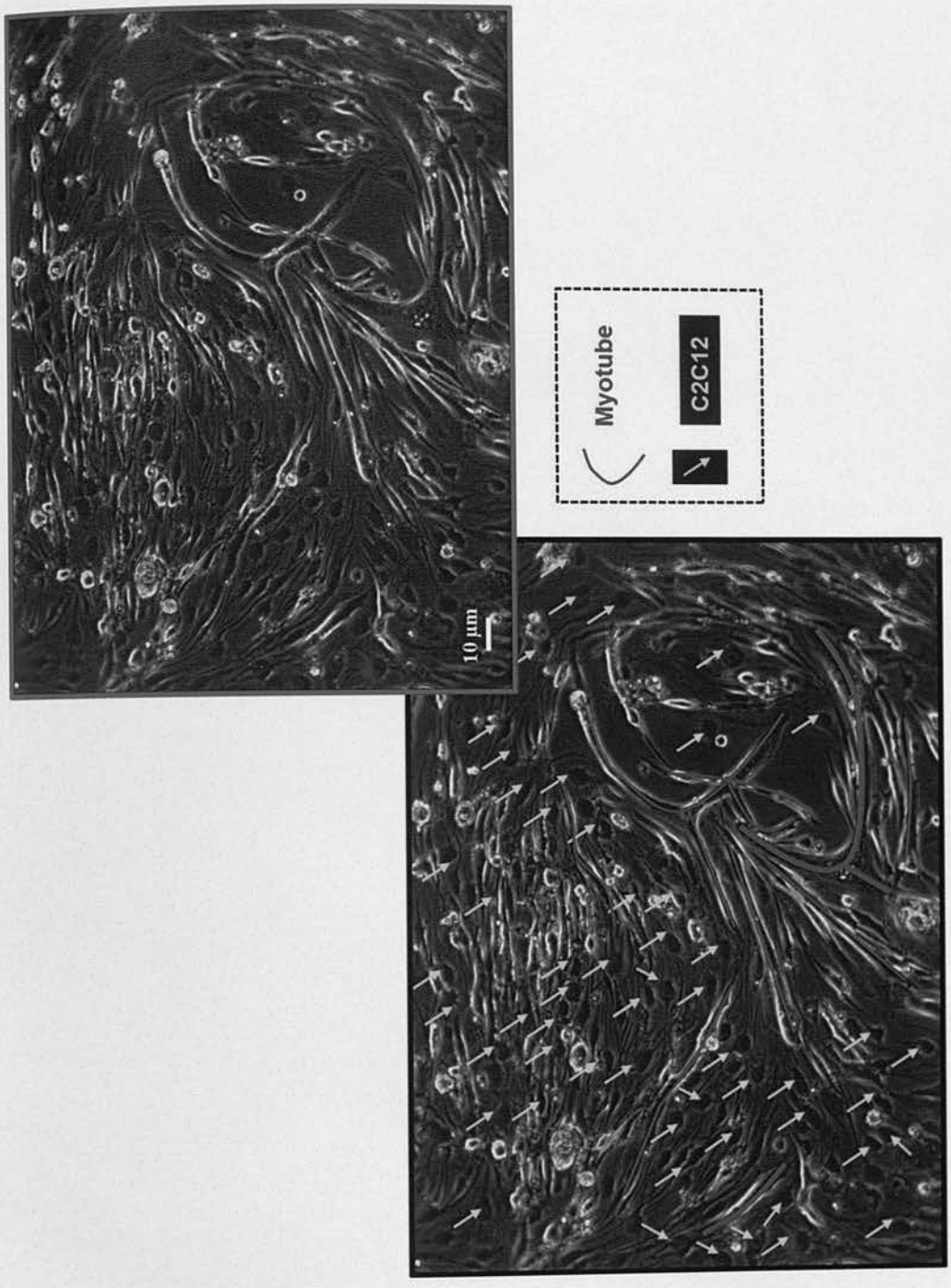


*Figure 7-3 C2C12 differentiation in myotubes. The yellow arrow shows the C2C12 and the red line the myotubes.*


*Figure 7-4 Another example of C2C12 differentiation in myotubes as previously described in Figure 7-3.*

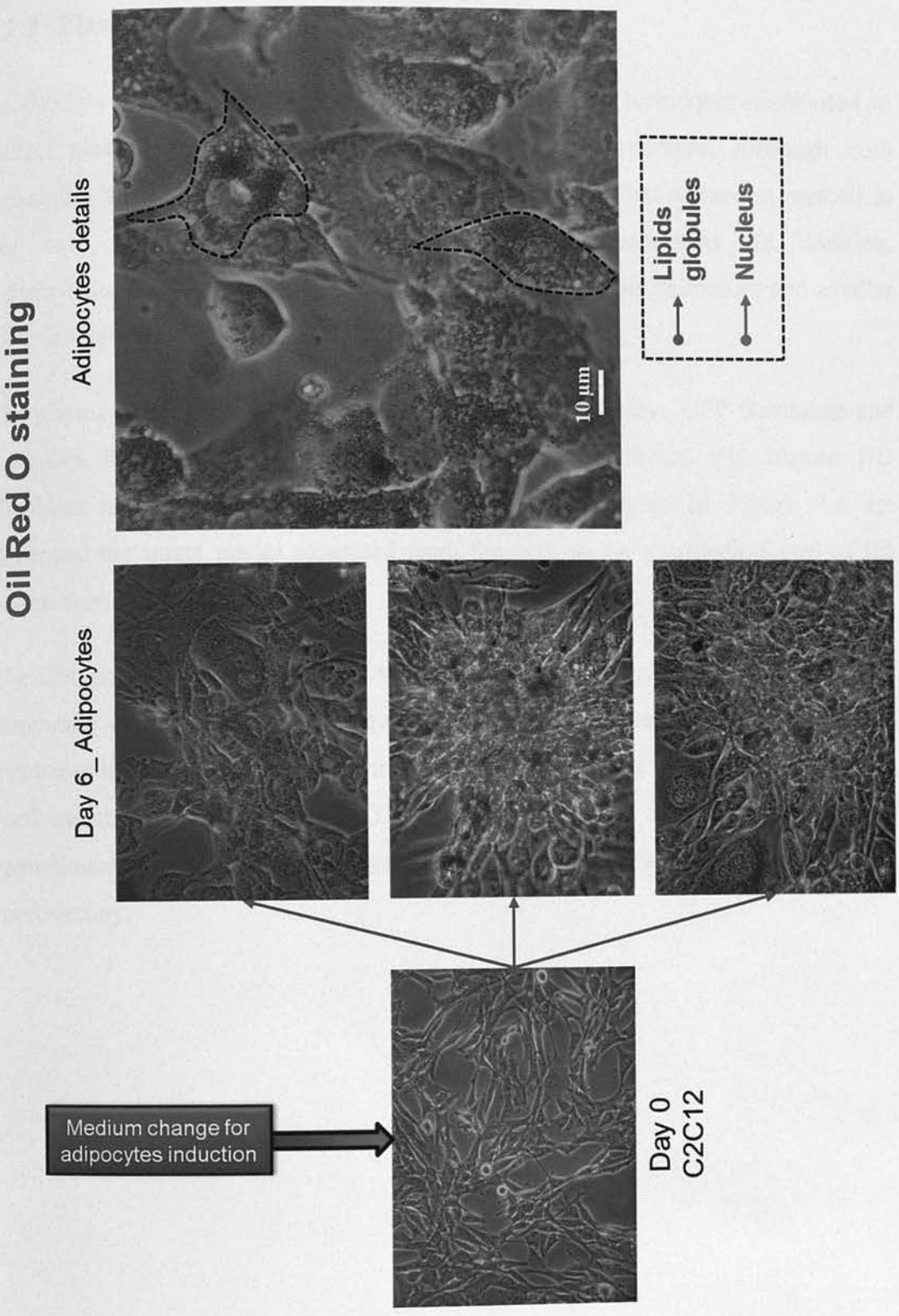


*Figure 7-5 C2C12 differentiation in adipocytes. The red arrow shows the lipids globules stained by Oil red.*

### 7.2.3 Plasma membrane extraction

As described in the Materials and Methods section two techniques were used to extract plasma membranes and associated biological structure. Although both techniques are established and reported in literature, the first extraction method in our case has produced results that are more consistent. In addition, ultracentrifugation extraction was tried but the length of the procedure and smaller yield favoured the use of the two methods before mention.

The plasma membranes were extracted from C2C12 myoblats, GFP-fibroblasts and myotubes for the DEP experiments. The Human fibroblasts and Human HD fibroblast membranes were used only for Raman analysis. In *Figure 7-6* are illustrated the intact nuclei separated from the cells as an intermediate step of the plasma membrane purification.

The cell populations were sorted by DEP and the resultant cells were used for membrane extraction. The technique using Percoll was easier to implement and number of intact nuclei was higher than the second technique (materials and methods "cell membrane extraction II"). The calculated number of cell disruption was approximately around 90%. The membrane were harvested and analysed by Raman spectroscopy.

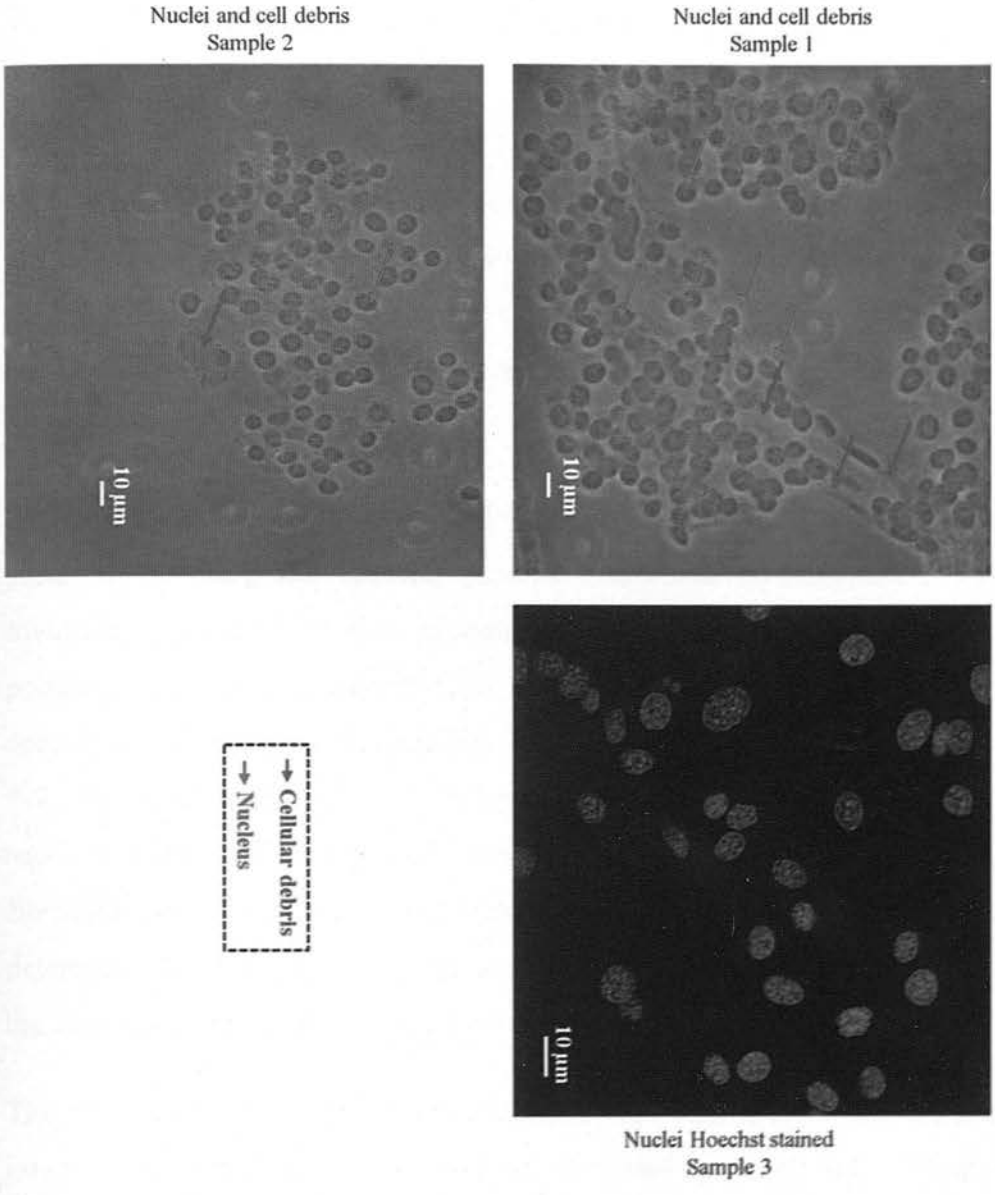


*Figure 7-6 Plasma membrane extraction. Nuclei shown by light microscope images and by Hoechst staining (blue on the bottom). The cellular debris corresponds to the cytoplasmic part of the cell.*

## 7.3 DEP sorting and flow cytometry results validation.

### 7.3.1 DEP sorting efficiency in C2C12, GFP-fibroblasts and myotubes

Cells were re-suspended in DEP medium with conductivity of approximately 120 mS/m and osmolarity of ~330 mOsm/kg. The cells were subsequently introduced in the DEP device for separation and collection with a flow rate of ~120µl/h. Purity of cells sub-population was assessed by the use of positive GFP expression in fibroblasts cells.

This was the starting point to determine the experimental cross-over frequency of the cells. In addition, the specific protein embryonic myosin, only expressed in myotubes, was used for flow cytometry to validate the DEP results in myotubes populations. In these populations, the secondary antibody with Alexa fluor 488 was conjugated to embryonic myosin for cytometric assessments as illustrated in *Figure 7-7*. The DEP separation was performed and analysed by flow cytometry on 13 separate samples of each paired combination of the three cell types (C2C12, GFP-fibroblasts and myotubes). The results expressed the percentage of cell that were determined by flow cytometry positive for the markers GFP or Alexa fluor 488 and the counterpart negativity for these two markers.

The mix population of cells was introduced in the microdevice by the two external inlets. The central inlet was reserved for fluid medium only. When the cells experience nDEP they were moved towards the central fluidic stream and collected in the central outlet. For cells experiencing pDEP, that were kept in outer fluidic stream and collected in outer outlets by the opposite mechanisms.

As illustrated in *Figure 7-7* the results validated the sorting capability of DEP for these three cells types. In absence of DEP the cells populations have almost an equal percentage distribution at the three outlets as indicated by the control on the bottom of *Figure 7-7*.

The average purity of the cell sub-population was between C2C12 and myotubes approximately 96% and 98% between C2C12 and GFP-fibroblasts. The frequency related to the Clausius-Mossotti function *Re(CM)* for the three cell types was derived based on the estimation DEP cross-over ($f_{x0}$) values. The *Re(CM)* modelling was performed using MATLAB (The Maths Works Inc.) as illustrated in *Figure 7-8*.

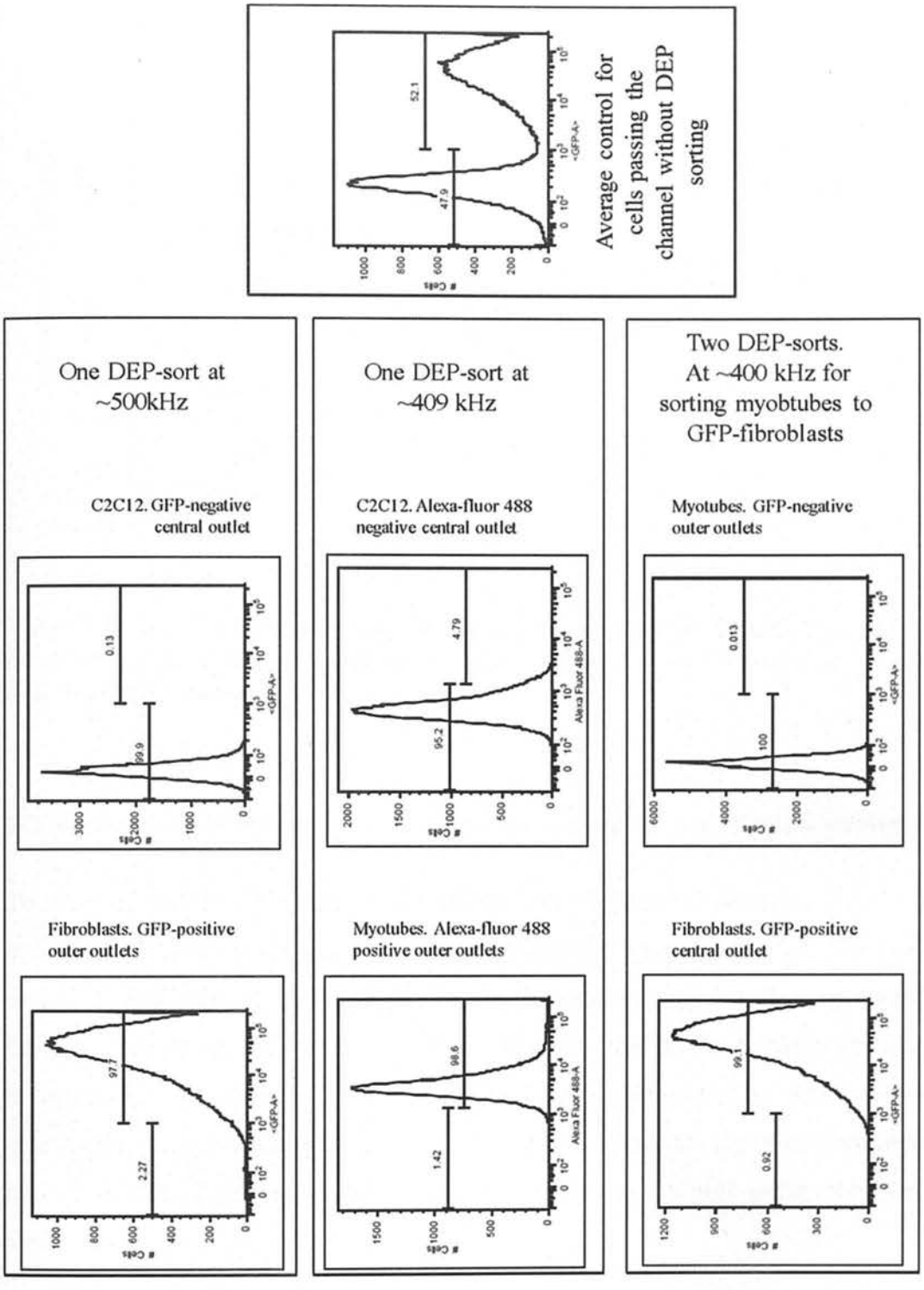


*Figure 7-7 DEP sorting validate by flow cytometry analysis. The cells were collected at the three outlets to determine the presence of the two markers GFP and Alexa fluor 488 in the three types of cells.*

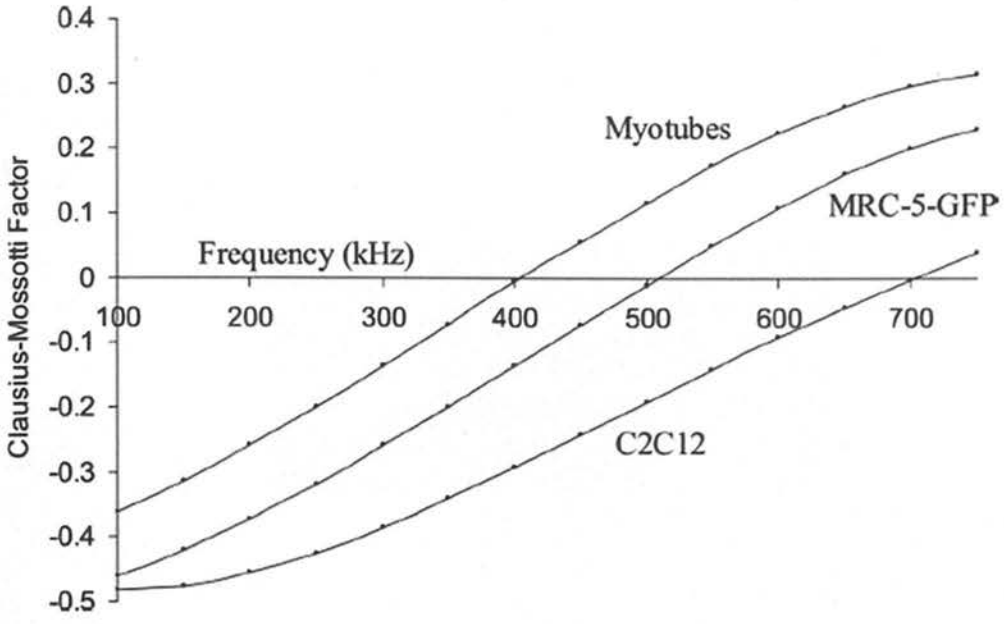


*Figure 7-8 MATLAB modelling of the Cross-over frequencies for the three cell types based on the modelling estimations. Note that this is a possible model of the cross-over frequency values.*

### 7.3.2 Western blot further validation for myotubes population purity.

To further, validate the results regarding DEP separation between C2C12 and myotubes, Western blotting for the marker embryonic myosin was used. The mixture of C2C12 and induced myotubes (present in the same culture vessel) were sorted by DEP to determine the presence of the specific marker embryonic myosin in myotubes (as illustrate in *Figure 7-9*). In *Figure 7-9* α-tubulin was used as a reference for embryonic myosin. *Figure 7-9* shows clearly the absence of embryonic myosin in C2C12 (left hand side upper part) validating the high purity achieved by DEP sorting.

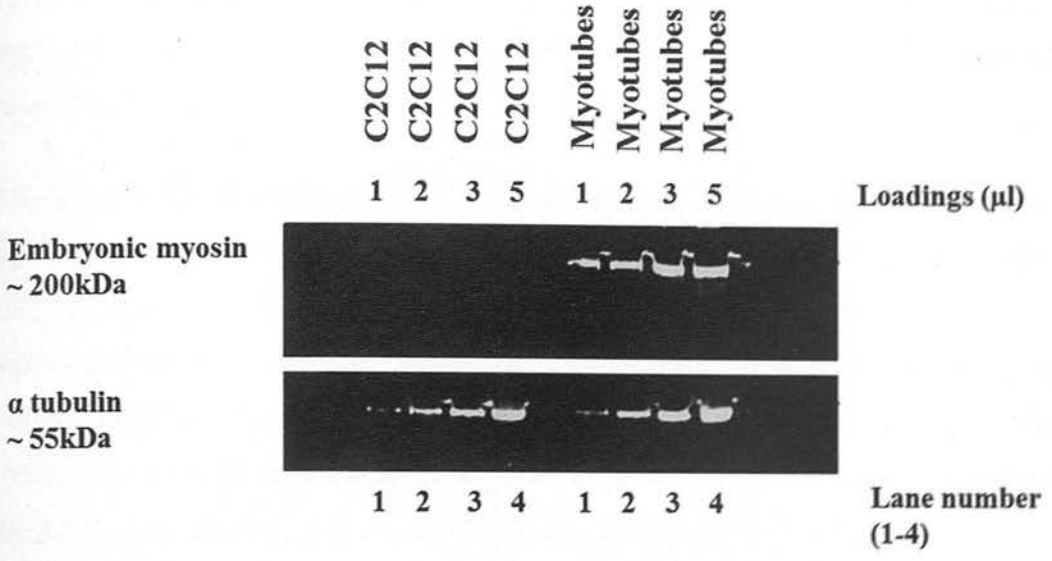


*Figure 7-9 Western blot for embryonic myosin in C2C12 and myotubes populations sorted by DEP.*

### 7.3.3 DEP sorting with associated cell cycle investigation

A second set of results is here presented. After the cells were harvested they were re-suspended in DEP-medium and loaded into the syringe pump for DEP-sorting. Purity and identity of the recovered sub-populations was assessed by flow cytometry, based on GFP-positivity (fibroblasts), the presence of embryonic myosin (C2C12 differentiated myotubes: secondary Alexa-Fluor 488) or non-fluorescence (C2C12 undifferentiated myoblasts). Representative results are shown in *Figure 7-10.* Cytometry plots in column one illustrate separation at 98% purity, following one round of DEP-sorting, of co-cultured GFP-positive fibroblasts from undifferentiated C2C12 myoblasts. At high passage number (>50) only a small percentage of C2C12 myoblasts will differentiate to myotubes. Following induction of C2C12 into myotubes the cells were DEP-sorted. The purity of the sorted myotubes from C2C12 was ~96% as illustrated by flow cytometry results in the second column in *Figure 7-10.*

Having successfully DEP-sorted C2C12 myoblasts from both fibroblasts and myotubes to high purity, we applied DEP-sorting to separation of fibroblasts and myotubes.

Co-cultures of fibroblasts andC2C12 myoblasts or cultures of differentiated C2C12 cells (containing myoblasts and myotubes) were each subjected to a first round of DEP-sorting to separate C2C12 from other cell type. After the first collection, fibroblasts and myotubes were mixed and a second round of DEP sorting was used to collect separate cell population of myotubes (from several cultures) or fibroblasts. Purity of recovered cells was assessed using GFP to identify fibroblasts as illustrated by the flow cytometry results in third column of *Figure 7-10*.

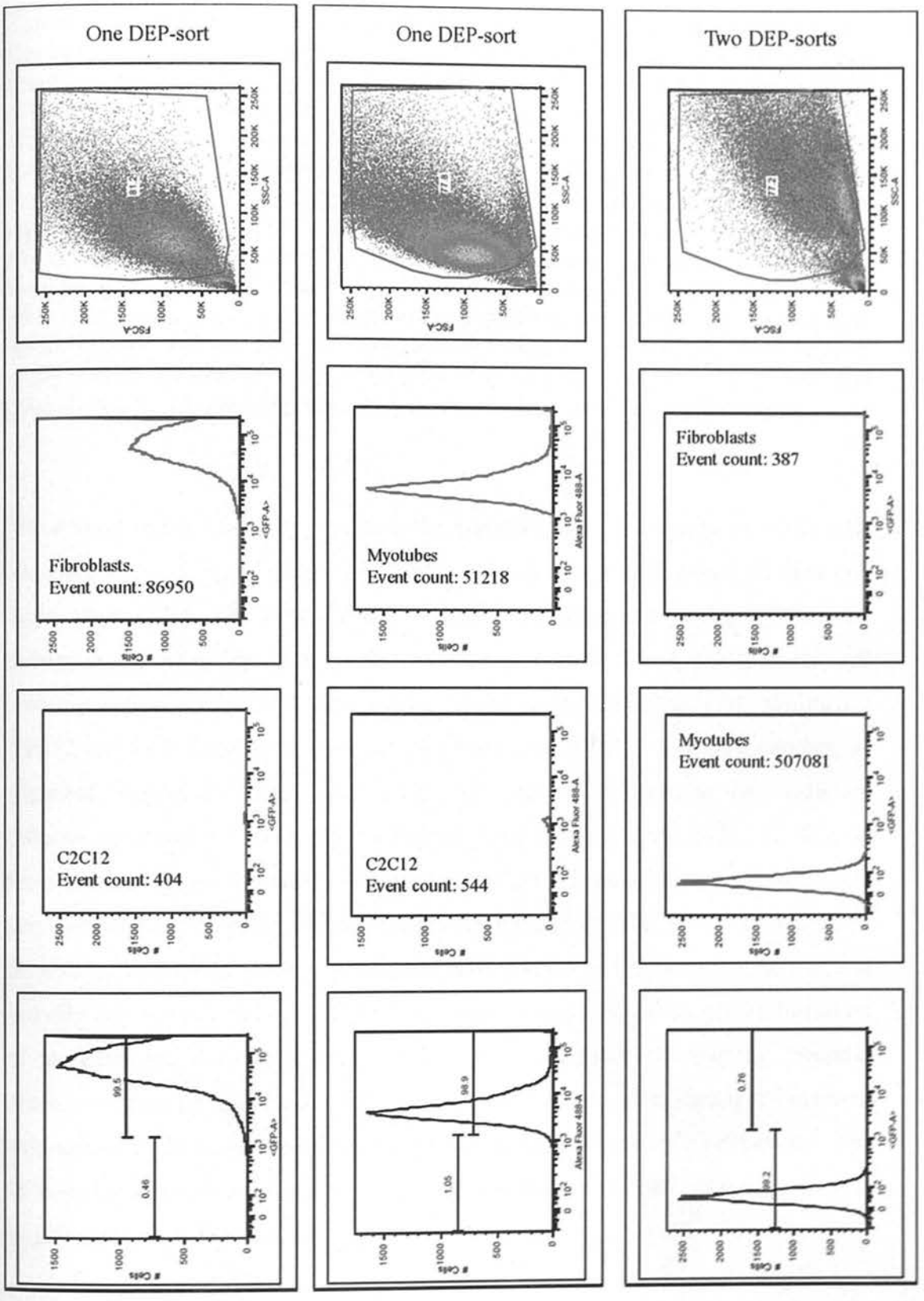
One DEP-sort
Fibroblasts.
Event count: 86950
C2C12
Event count: 404
99.5
0.46
One DEP-sort
Myotubes
Event count: 51218
C2C12
Event count: 544
98.9
1.05
Two DEP-sorts
Fibroblasts
Event count: 387
Myotubes
Event count: 507081
0.76
99.2

*Figure 7-10 Flow cytometry profiles of DEP-sorted C2C12, Fibroblasts GFP+ and myotubes. The first row (top in colors) indicates the percentage of intact cells processed by flow cytometry. The first bottom row shows the percentages of purity achieved by DEP sorting, the actual numbers of cells are shown on the second and third row from the bottom. Each vertical rectangle specifies the cell type collected at the central outlet. The left column shows an example of the level of separation between C2C12 and fibroblasts co-cultured after DEP sorting. For all the experiments (triplicates for 13 separate samples), the mean level of purity for these two cell types was ~98%. Middle column shows an example of the level of separation between C2C12 and Myotubes from a mixed (co-culture) and induced population after DEP sorting; for all the experiments (triplicates for 13 separate samples) the mean level of purity for these two cell types was ~96%. Right column shows the level of separation between myotubes and fibroblast after an initial sorting of both cell types from C2C12. The cells were sorted twice from several mixed populations.*

The second part of the study examined the possibility that the separation of the cells correlate with cell cycle, since DEP has been used to sort cells based on their cell cycle stage [120]. The flow cytometry results are illustrated in *Figure 7-11.* by histograms showing the intact cells collected in *G0/G1*, *S* and *G2/M* phase. All cultures analyzed showed a very similar profile before and after DEP sorting for C2C12 and GFP-fibroblasts as shown in *Figure 7-11.* C2C12-derived myotubes, as expected, showed a synchronicity in *G1* phase, due to the fact that these cells are differentiated and therefore they withdraw from the cell cycle [121,122,123] as shown in histograms in *Figure 7-11.* In *Figure 7-11* it is possible to see that there is very little difference in the cell cycle stages before and after DEP. C2C12 and GFP-fibroblasts showed an average profile for cells that are in the cell cycle milieu and actively developing. Note that these histograms results rely on the permeabilisation of the cells and the quantification of the DNA amount by PI staining. Specific characterization of cell cycle stage may require the use of a variety of markers although even then a precise determination of the cell stage may be debatable. For further characterization of cell cycle activity, we have used Ki-67, as the results will be presented in the next section.

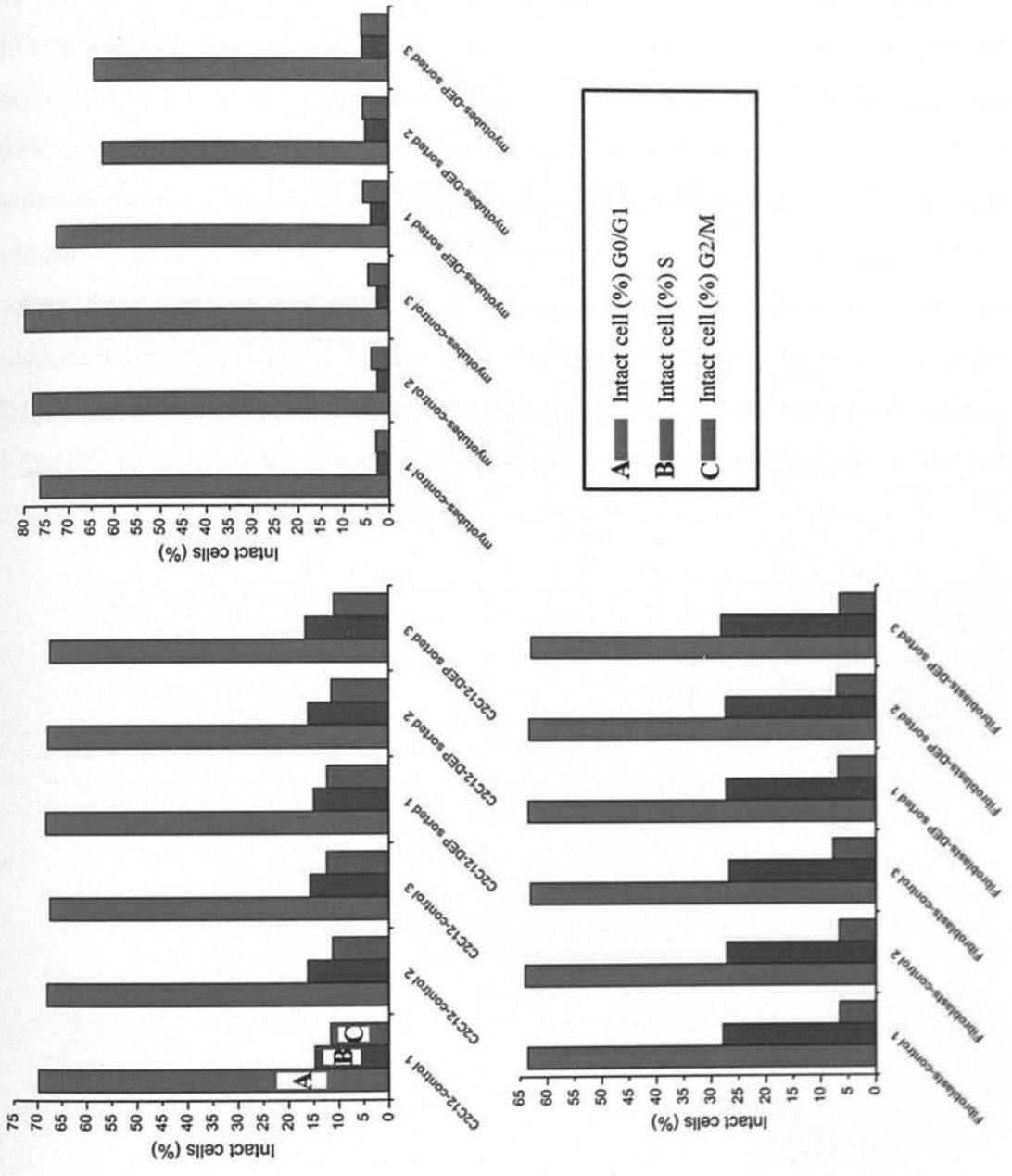


*Figure 7-11 Flow cytometry analysis of the cell cycle of the three cell types before and after DEP sorting. The three colors indicated in the legend box have been associated with letters (A, B and C) in order to avoid confusions between the three colors bars. Notice that the bars represent the percentages of cells in the three cell cycle phases (G0/G1, S and G2/M) the difference between cells sorted by DEP and control (not sorted) regarding the cell cycle is minimal.*

### 7.3.4 Immunofluorescence microscopy for Ki-67

To further validate cell cycle results by DEP cells were stained with Ki-67 to determine cell cycling activity, as illustrated in *Figure 7-12*. Both C2C12 and fibroblasts were positive for Ki-67 (*Figure 7-12* first two row from bottom) with myotubes negative as indicated in *Figure 7-12* (picture 3a). To determine size differences between the three cell types we used Hoechst nuclear dye with contrast microscopy as shown in Figure 7-14. The size validation between C2C12 and GFP-fibroblasts was important to determine if the DEP capability for sorting cells was solely dependent on cell size or if plasma membrane conformation was also responsible. It is evident in *Figure 7-14* that the C2C12-derive myotubes are much larger and are multinucleated in comparison to both C2C12 and GFP-fibroblasts. In *Figure 7-13* some C2C12 were imaged during what may be anaphase of the cell cycle.

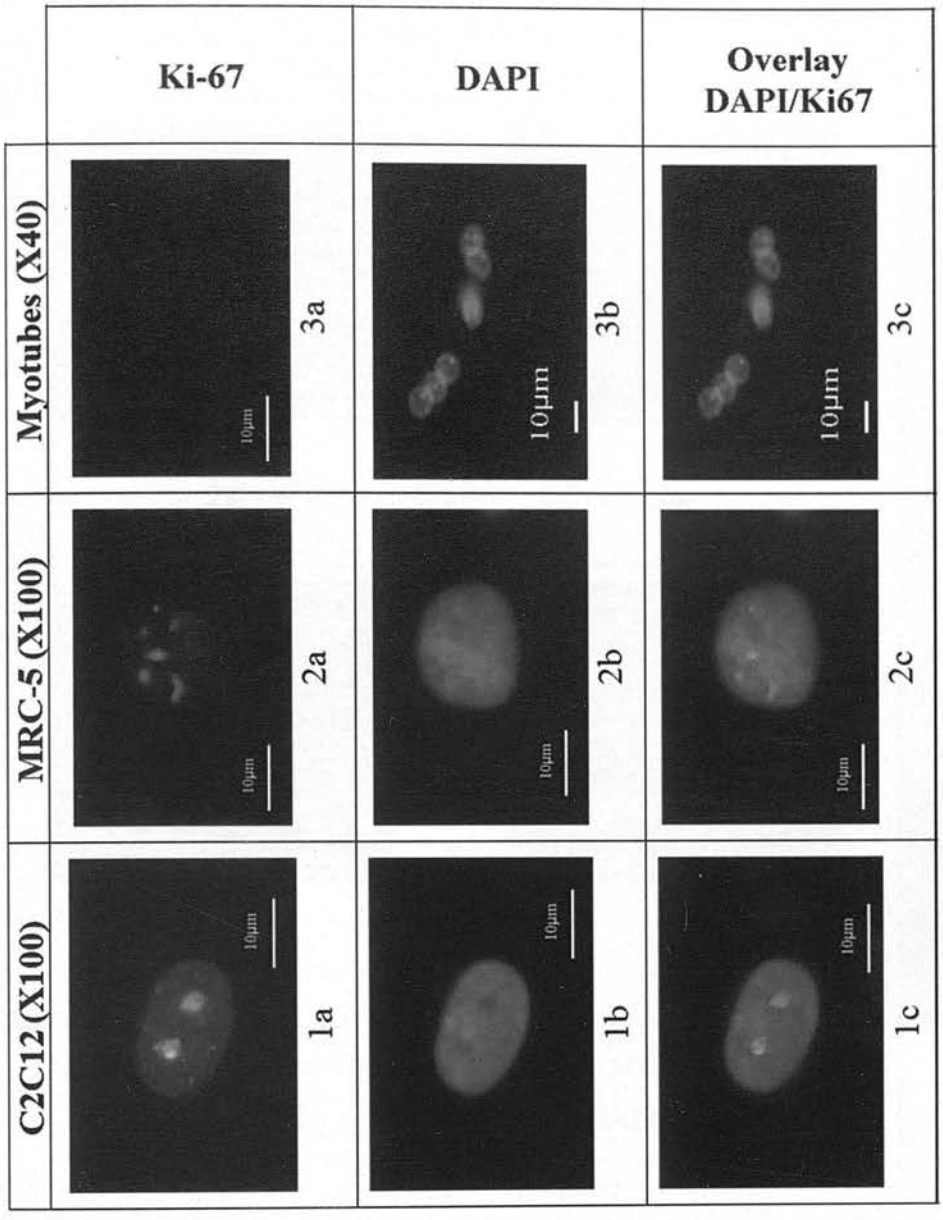


*Figure 7-12 Immunostaining for Ki-67 for cell cycling, DAPI nuclear stain was used as reference for better visualization. Both C2C12 and fibroblast are positive for Ki-67 (cell cycle active 1a and 2a) where myotubes are negative (top row 3a). Third column is an overlay of Ki-67 and DAPI staining.*

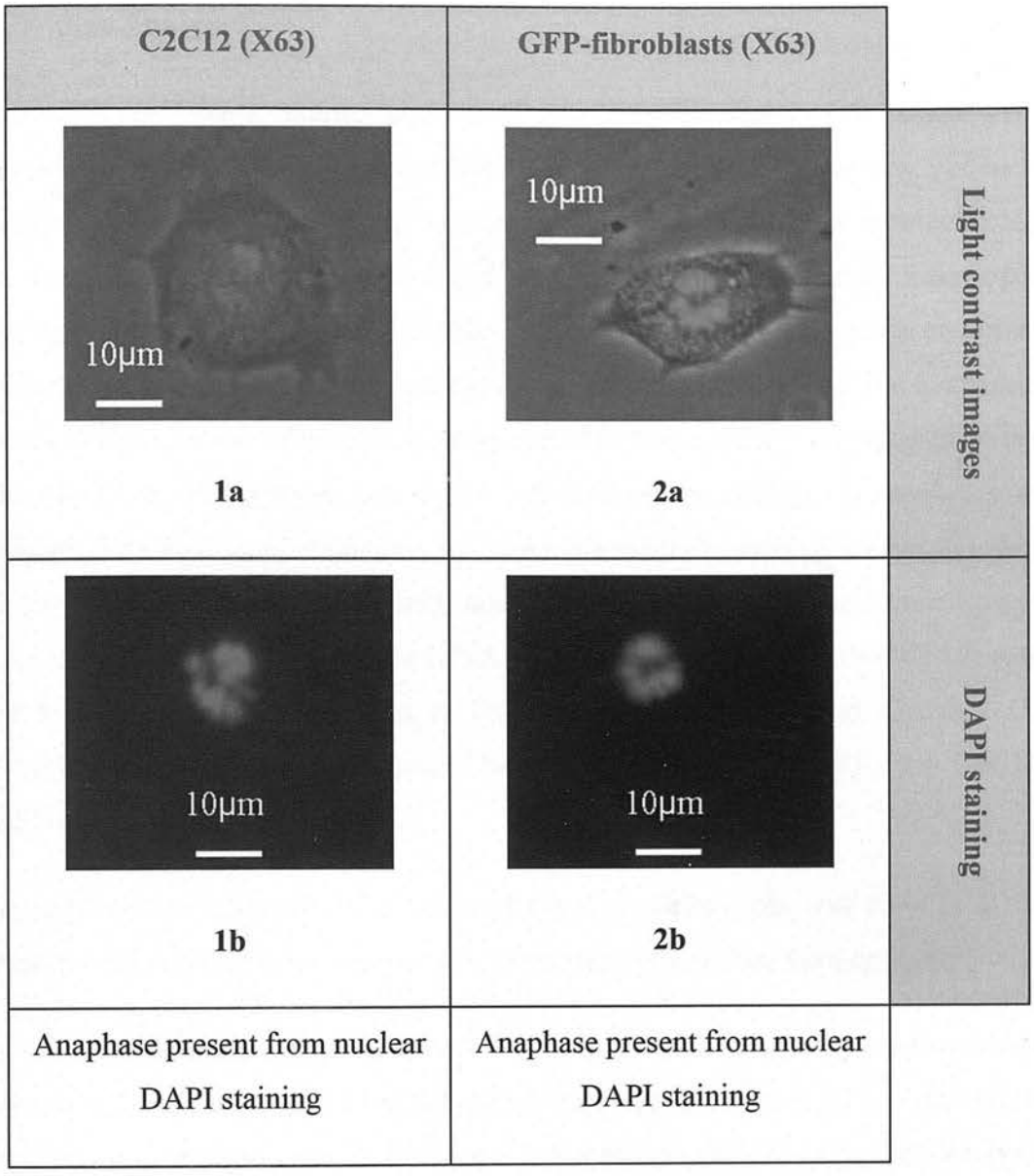


*Figure 7-13 C2C12 and GFP-fibroblast in suspension captured in possibly anaphase during mitosis. 1a and 2a) Light contrast images of C2C12 and GFP-fibroblast 1b and 2b details of the nucleus at possibly anaphase DAPI stained for better visualisation.*

### 7.3.5 Size Analysis

Fluorescent and phase contrast pictures of attached cells and in suspension were collected using an Axioscope Zeiss microscope with Photometrics camera. For each cell type in suspension 60 pictures containing an average of 30 cells were collected and repeated for 12 times. This for a total of approximately 21600 cells images per type regarding C2C12 and GFP- Fibroblast. Myotubes were not analysed at any great number (not statistically relevant in compare with the other cell types) due to the fact that the differentiation of myoblasts produced very low number of myotubes in the order of 40% by visual assessment with a light microscope of the total population of myoblats. The final number counted by immunofluorescent analysis was even lower and only 524 myotubes were counted. Images were collected of these two cell types in suspension and ImageJ software (USA, http://imagej.nih.gov/ij/, 1997-2012) was used to determine size differences as illustrated in *Figure 7-14* and *Figure 7-15*. GFP-Fibroblasts were easy to assess because they expressed GFP, for C2C12 CMFDA tracker dye was used.

It is important to notice that the count of the three cells types was done in 3.7% formalin/PBS medium therefore, osmotic pressure may have been not optimal.

The averages for C2C12 myoblast was 18.6μm ± 5.8 SD in diameter and fibroblasts 18.9 μm ± 7.4 SD in diameter (42000 cells were counted between C2C12 and GFP-fibroblasts only 500 myotubes). In *Appendix B* a sample of 1500 cells for each type and for 200 myotubes are shown.

Size was also assessed by flow cytometry using three size reference beads as indicated in *Figure 7-16*. Note that the scatter is not linear to size. The dependency is approximated to near linear in order to extract reference value for size of the cell types.

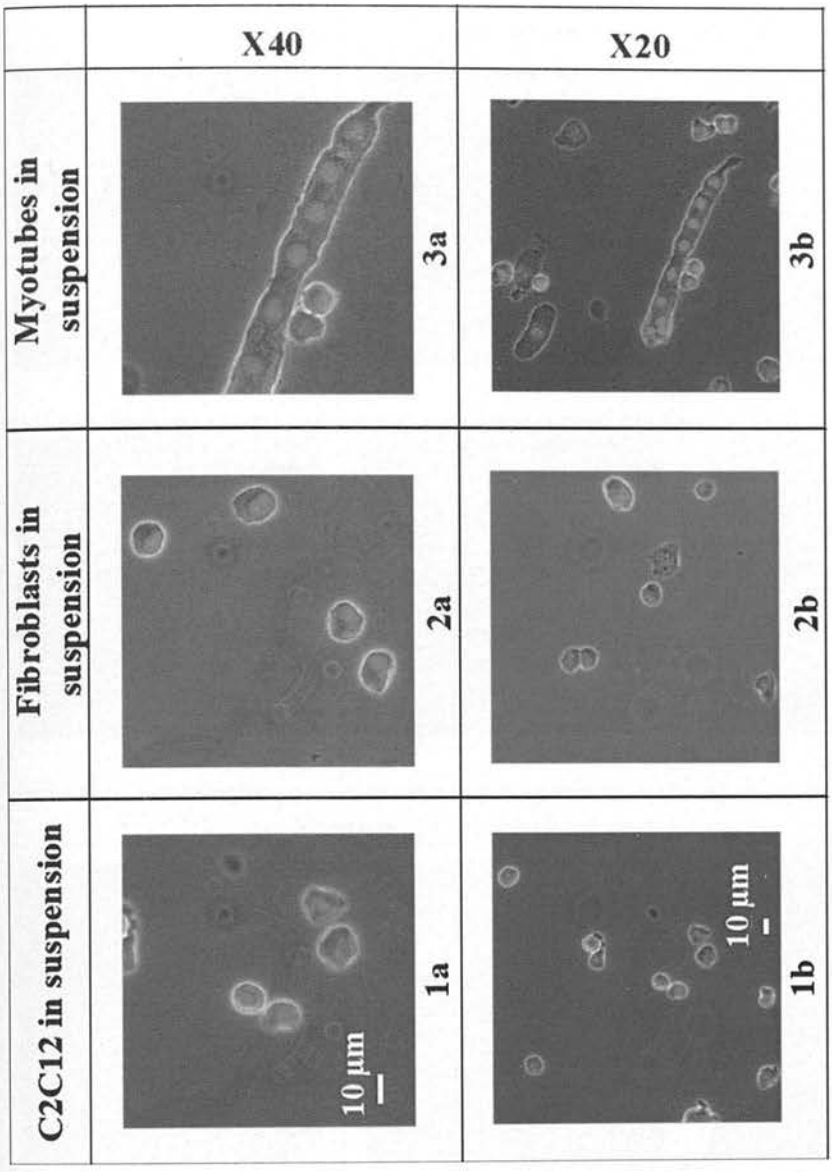


*Figure 7-14 An example of cell size when in suspension by contrast microscopy images using Hoechst nuclear dye for localization of the nucleus. Both C2C12 and fibroblasts showed similar size in suspension (first two rows from the bottom). 1a and 1b shows C2C12 in suspension at different magnification (as indicate on the top header). 2a and 2b are GFP-fibroblasts at different magnification (as indicate on the top header). Top row myotube in suspension, the polynuclear characteristic of the myotube is evident in picture 3a and 3b.*

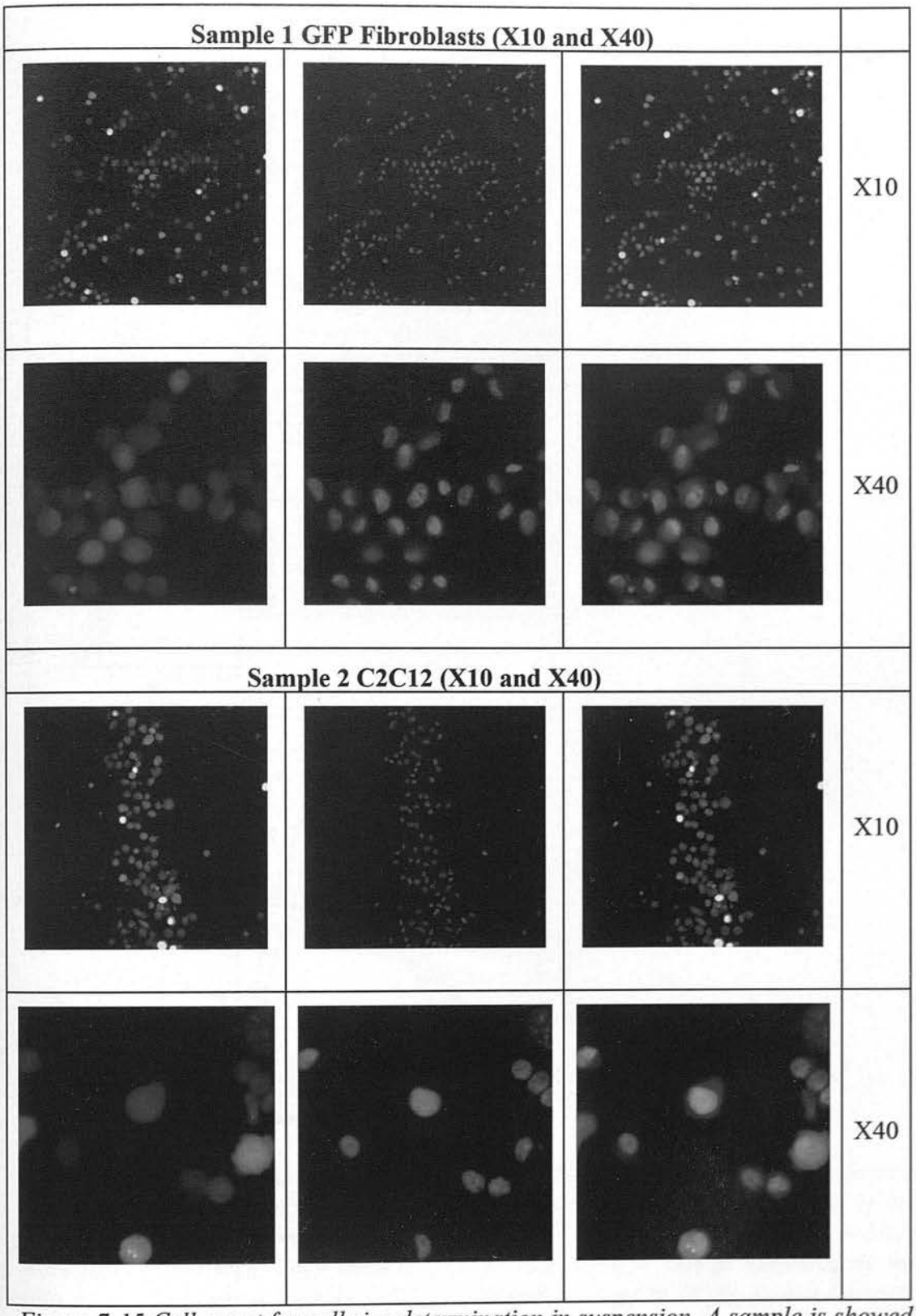


*Figure 7-15 Cell count for cell size determination in suspension. A sample is showed here for C2C12 and GFP-fibroblast*

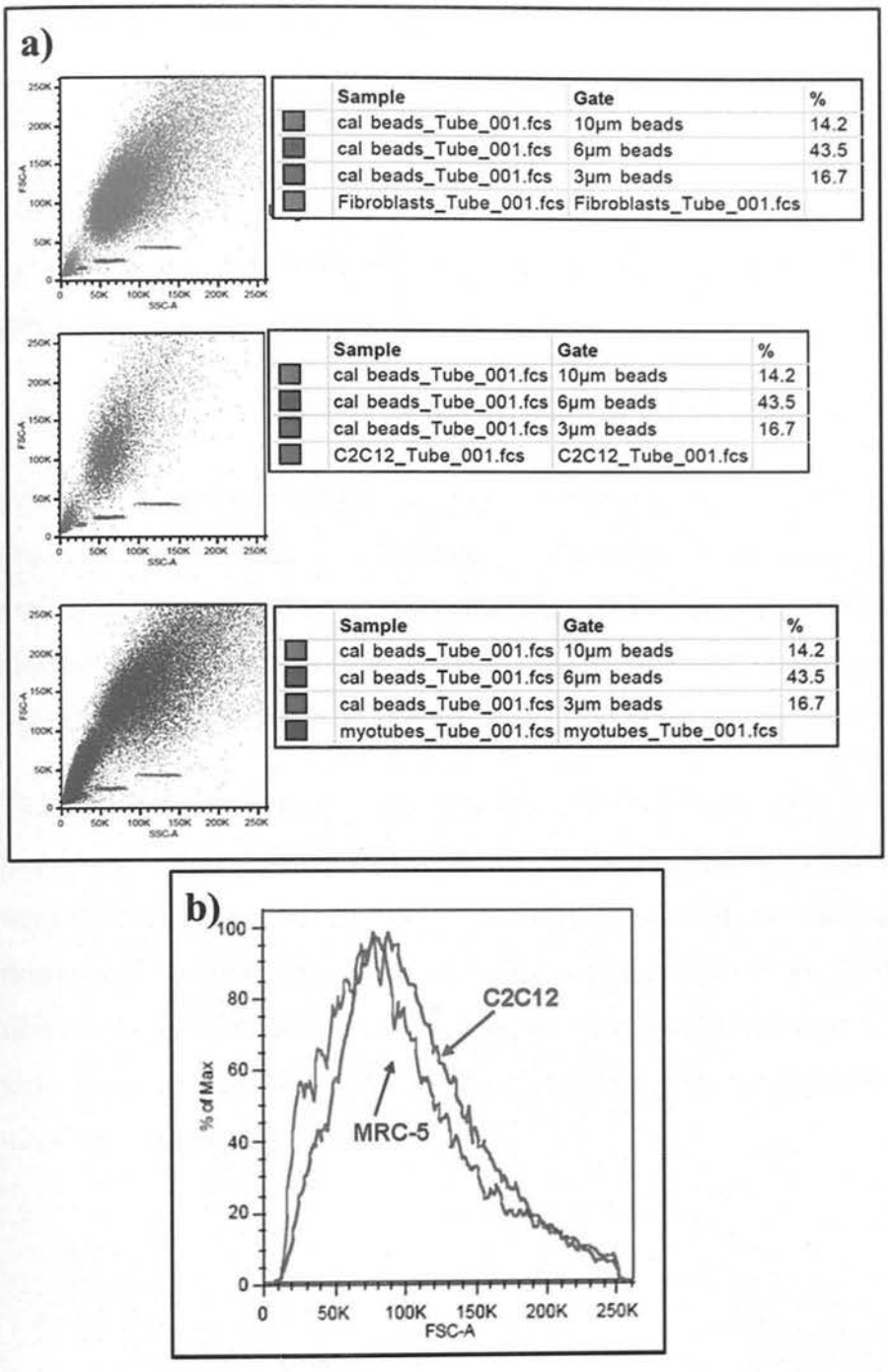


*Figure 7-16 Size analysis for the three cell types a) Cells side scatter with beads as a comparison. The diameter of the beads is indicated on the right hand side of the scatter plots. b) Due to the large difference in size, only C2C12 and GFP-fibroblast were further analysed. They show a similar distribution in size as indicated by the plot B, the two curves overlap almost completely in regard to the forward scatter (FSC-A).*

## 7.4 Raman spectroscopy

### 7.4.1 Membrane extraction

Membrane were extracted as described in Materials and Methods (Cell membrane extractions II). A sample showing the first stage of separation of the plasma membrane is shown in *Figure 7-6*.

### 7.4.2 PCA analysis of the extracted plasma membranes Raman spectra

Principal Component analysis suggested that differences from membrane types were present in these cells as illustrated in *Figure 7-17*. The method of membrane extraction was described in Materials and Method section as well as the second method for cell membrane extraction. This method was used initially as an initial quantification of possible differences in the membrane composition of these cells.

The Raman spectra may show that the GFP-fibroblasts have a different plasma membrane composition contributing for a higher membrane capacitance compared with C2C12. Myotubes difference remained difficult to assess due to the fact the these cells present very different sizes compared with the C2C12 and GFP-fibroblasts. In other words DEP sorting for myotubes is assumed to rely on the cell size only, whereas for cells of the same size the composition of the plasma membrane could play a role.

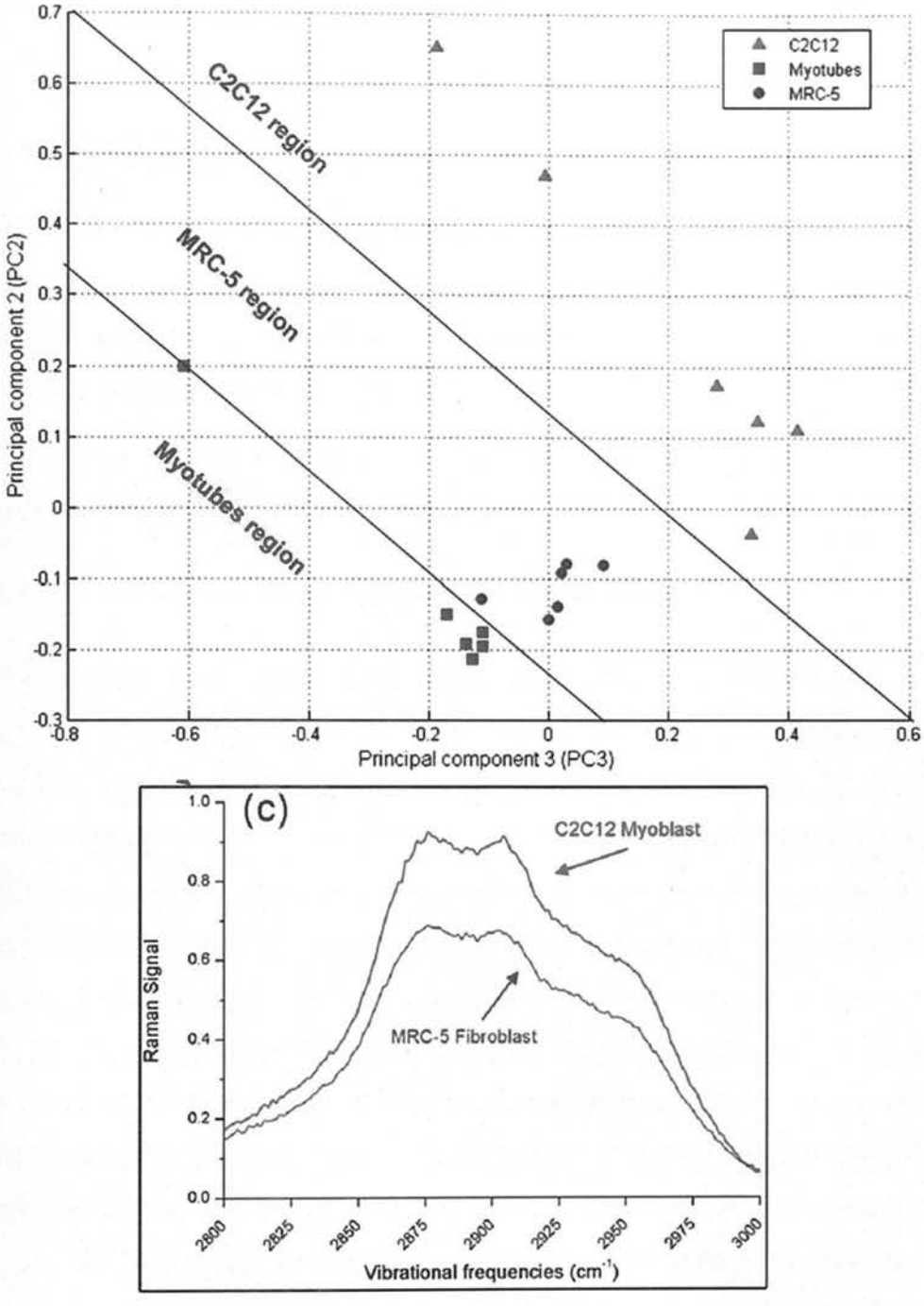


*Figure 7-17 Principal component analyses for C2C12, GFP-fibroblasts and myotubes. The total variance for PC2 and PC3 account for ~25% of the total variance between the three cell types. The region between 2800 and 3000 $cm^{-1}$ shows a possible lower level of lipids saturation in GFP-fibroblasts.*

## 7.5 Plasma membrane characteristics in Huntington's peripheral fibroblastic cells analysed by Raman spectroscopy

Membranes were extracted as described in Materials and Methods extraction I. The cells were counted by aliquots for viability before cell membrane extraction. For all the 12 experiments approximately 15 million cells per sample were used and viability was assessed prior to membrane extraction by Trypan Blue staining

The results of the first stage of extraction regarding nuclear separation from membranes are shown in *Figure 7-6*.

### 7.5.1 Low wavenumber region from 400 to 1800 cm-1

The spectral areas chosen were in the fingerprint region for biological samples between 400 and 1800 $cm^{-1}$. The results of the PLS analysis are displayed in *Figure 7-18* to demonstrate the level of discrimination for the first two factors. The PLS model reduced the number of factors to five in total with minimum root mean PRESS (Prediction Residual Sum of Squares) of 0.41. The cumulative variation explained by X and Y for the first factor was respectively ~60% and ~90%. This factor showed the most separation between membrane types as indicated in *Figure 7-19*d. The predicted model and Hotelling's (T2) plots, generated by PLS, are shown in *Figure 7-19a* and *b* as a visual mean of interpretation of how well the model fitted the actual data. All the samples fitted the model with only one Huntington's disease (HD) membrane as a borderline value shown in *Figure 7-19b* (HD-mem2). From the model the VIP values were generated as shown in *Figure 7-19c* and the threshold level was established at 0.8 as suggested by literature. Although more recently some authors [124,125,126,127] have indicated that values between 0.83 and 1.21 are more suitable indicators but we used 0.8 as a conservative approach. Note that the VIP values are associated with all the vibrational frequencies in the spectrum from 400 to 1800 $cm^{-1}$ regardless of the presence or absence of peaks in the region.

The VIP values, irrespective of the specific peak assignment, can be used as quantitative indication of specific frequency areas important to discriminate between membrane types. This was in association with a high level of variation for the first PLS factor making this type of information important for the classification of the membranes. For peak assignments, comparisons were made with the means of the two membrane types for the total of the 12 experiments. Six samples each from the two types of membranes were extracted from 12 separate cell populations with approximately 15 million cells per sample. The averages with the standard deviations are shown in *Figure 7-20a*. The differences between membranes are more evident in *Figure 7-20b*. Here differences between membranes with standard deviation are shown even though overlapping standard deviations made a visual assessment difficult. It is important to note that even if putative assignments based on available literature as shown in *Table 7-1* can be made, due to the complexity of the sample; specific identification of specific sub-cellular biochemical components remain difficult. There are also some vibrational overlapping between proteins and lipids and related molecules which further contribute to the complexity of the data. In order to quantify the possible changes between membranes the assigned peaks were integrated to determine the area under the curves as shown in *Figure 7-21a* and *Figure 7-21b*. The peaks were further compared with the respective VIP values to determine the level of contribution in discrimination of the membranes by the PLS model. As described in the experimental section only peaks above a VIP value of 0.8 were considered as shown in *Figure 7-21c*. Only the peak at 576 $cm^{-1}$ for HD membranes was below the threshold and was therefore not considered. The main membrane differences are related to the region from 428 to 701 $cm^{-1}$ which includes putative peak assignments for cholesterol and cholesterol esters. There are also peaks for phosphatidylinositol, glycogen, and C-S and C-C bonds associated with protein structures. A second region comprises peaks from 1020 to 1300 $cm^{-1}$ with the most relevant differences at 1045, 1073 and 1130 $cm^{-1}$ which include putative peaks for triglycerides, phospholipids, fatty acids, phosphate groups and proteins. The bands at 548, 1331 and 1685 $cm^{-1}$ were missing in HD membranes.

These bands are putatively associated respectively with cholesterol, phospholipids and proteins in the form of Amide type I and unsaturated fatty acids with carbon-carbon double bond. Several minor shifts were also noticed in peaks between membrane types as illustrated in the histograms in *Figure 7-21a* and *b*. These are peaks associated with the same biochemical components that were shifted in the two membrane types as shown in the first column by the annotation in brackets of *Table 7-1*. Regarding the HD overall it has a lower Raman intensity across the spectrum, the only exception was a peak at 1056 $cm^{-1}$ putatively associated with lipids which was present only for fibroblast control membranes. There are also peaks at 810 and 811 for Fibroblast and HD membranes respectively, which are reported in literature as C-C and C-O-C stretching of collagen type IV backbone as indicated in *Table 7-1*. These are very intense peaks at 810 and 811 $cm^{-1}$ that may be present due to the type of fibroblastic cells used in the study. However, there is a possibility of RNA contamination since these peaks are also strongly associated with phosphodiester Z-marker for RNA although no associated RNA peaks at ~1240 $cm^{-1}$ were present.

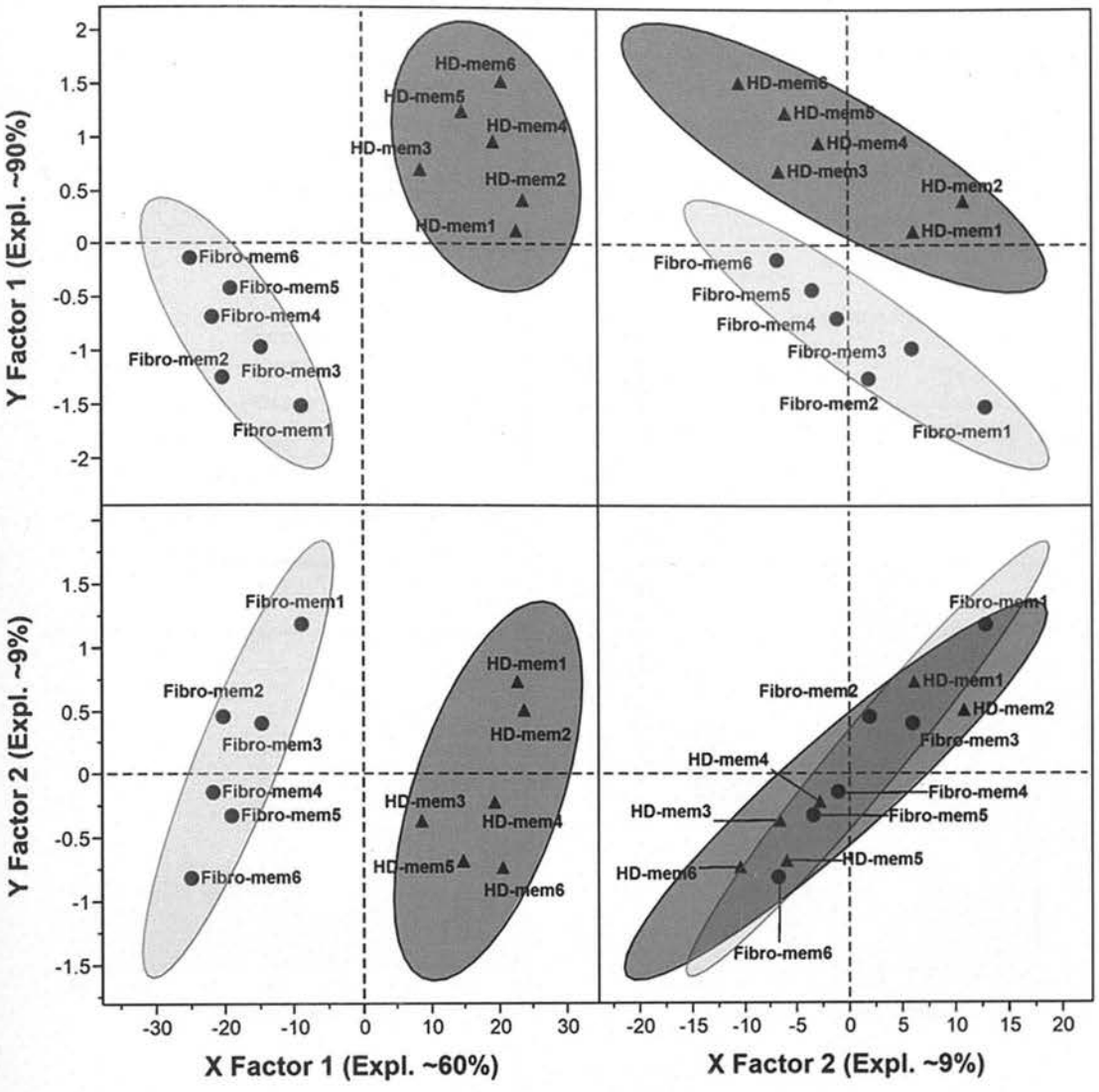


*Figure 7-18 PLS analysis scores plot for the first two factors. Fibroblast (●) and HD (▲) membranes with grouping ellipses to define the two membrane types for the low wavenumber region.*

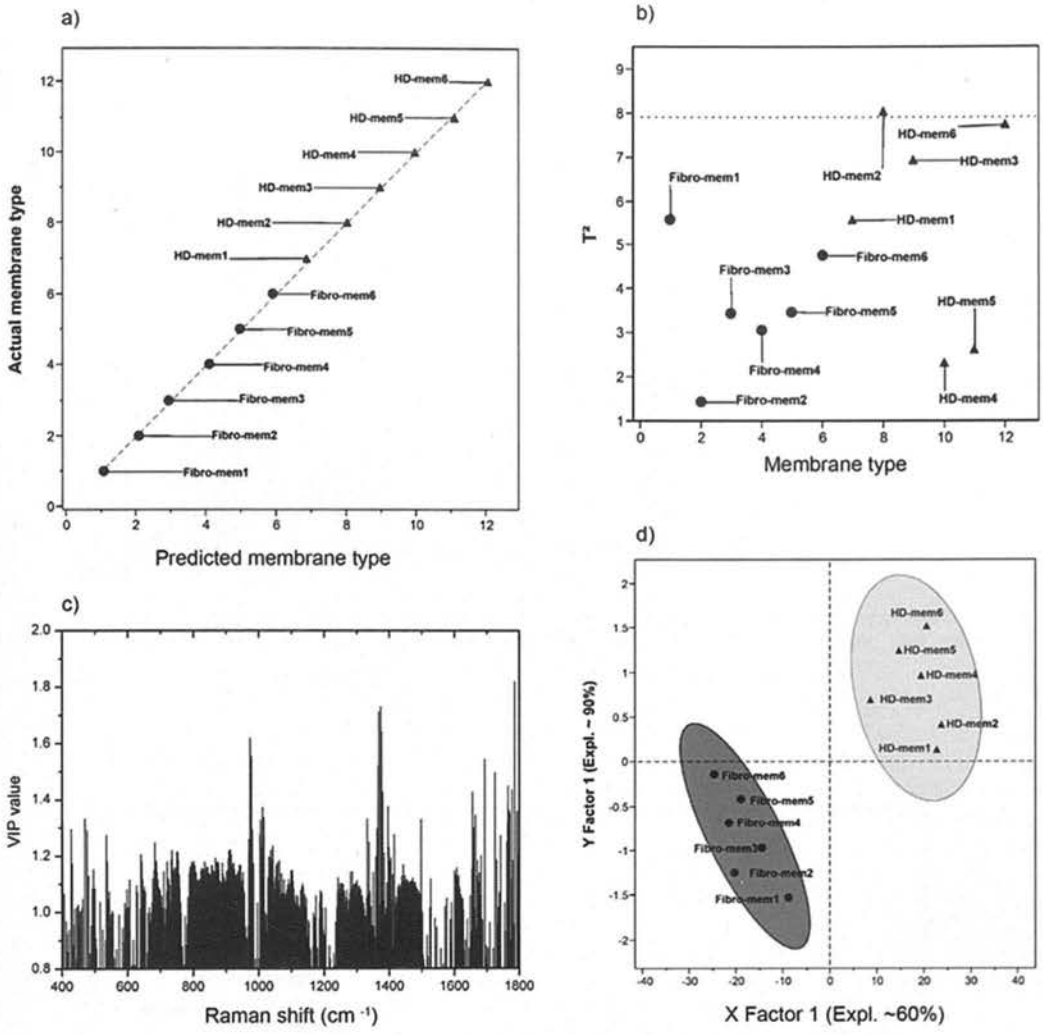


*Figure 7-19 Fibroblast (●) and HD (▲). a) Predicted versus actual graph for the PLS model. b) $T^2$ test for PLS model c) VIP values plot for the 400 to 1800 $cm^{-1}$ range with 0.8 VIP thresholds. d) First factor scores plot. The percentage of variation is illustrated in brackets. All graphs refer to the low wavenumber region.*

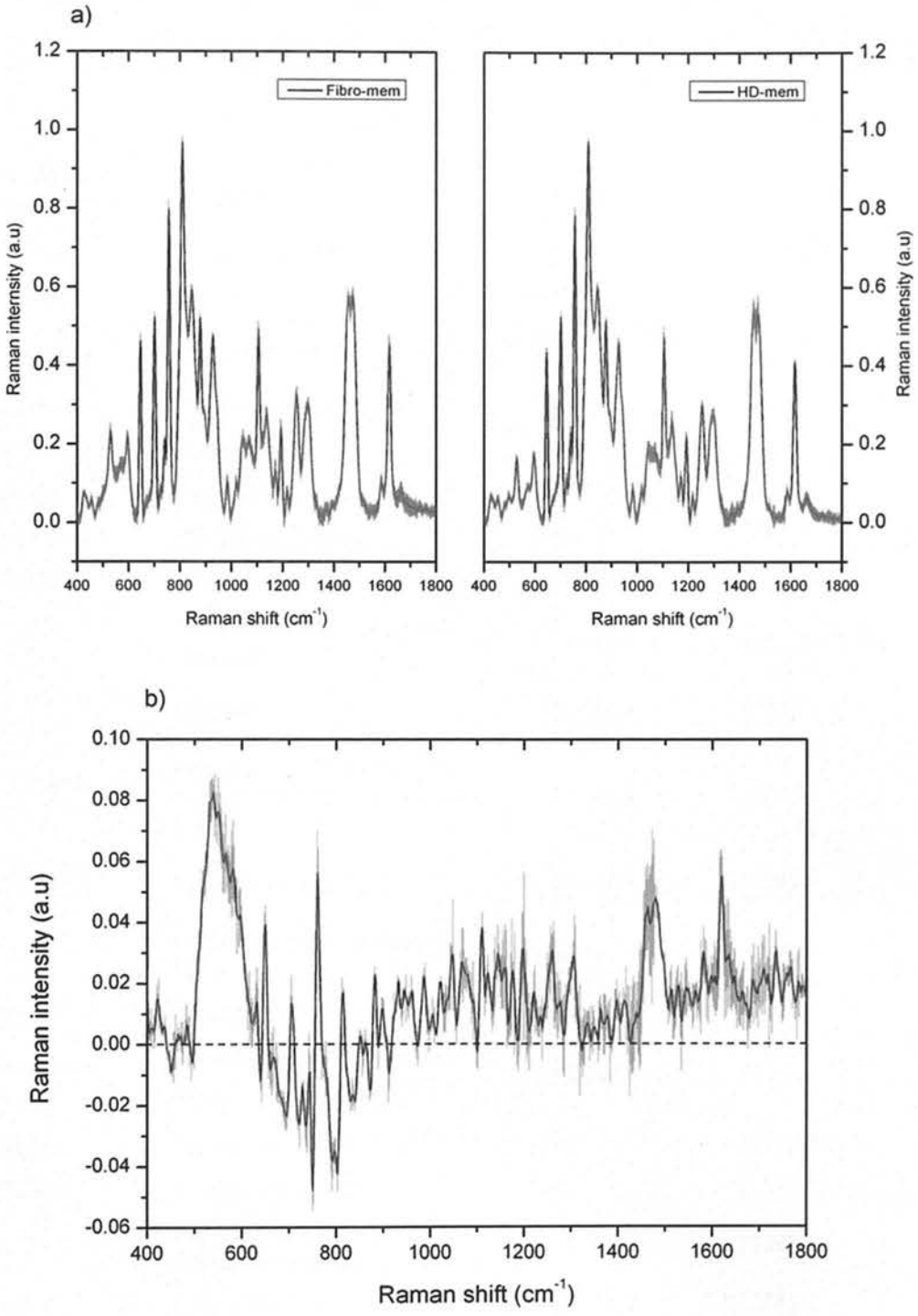


*Figure 7-20 a) Averages spectra for the two membrane types with associated standard deviations (shaded area). The graph on the left indicates the fibroblast control and graph on the right the HD. b) Difference spectra between cell membranes the shaded area indicate the standard deviation. Both graphs refer to the low wavenumber region.*

| Raman shift ($cm^{-1}$) | Assignment | VIP value | References |
|---|---|---|---|
| 428(f) and 429(HD) | Cholesterol/ cholesterol esters | 1.17 and 1.30 | [128,129] |
| 484(f) and 490(HD) | Glycogen | 0.85 and 1.08 | |
| 524(HD/f) | Phosphatidylinositol | 0.94 | [128,129] |
| 548(f) | Cholesterol | 0.99 | [128,129] |
| 574(f), 576(HD) and 595(HD/f) | Phosphatidylinositol | 0.99, ***0.61*** and 1.01 | [128,129] |
| 646(HD/f) | C-C twisting (tyrosine) | 1.08 | [129] |
| 701(HD/f) | cholesterol | 1.03 | [128] |
| 726(HD/f) | proteins C-S | 1.09 | [129] |
| 733(HD/f) | phosphatidylserine | 1.19 | [128] |
| 756(HD/f) | Tryptophane | 1.13 | |
| 810(f) and 811(HD) | ν(C-O-C) and (C-C) collagen backbone | 1.12 and 1.10 | [130,131,132] |
| 843(f) and 844(HD) | Glucose | 1.16 and 1.14 | [129] |
| 877(HD) and 878(f) | Phosphatidylcholine N+(CH3)3 and saturated lipids bonds with N+ | 1.17 and 1.15 | [128] |
| 927(HD) and 929(f) | Proteins proline valine | 1.13 and 1.13 | [129] |
| 981(HD/f) | B-sheet proteins / saturated =CH lipids | 1.05 | [129] |
| 1020(HD/f) | glycogen | 0.93 | [129] |
| 1043(HD) and 1045(f) | Carbohydrates, phosphates $PO_4^{3-}$ proline collagen I | 1.24 and 1.11 | [129] |
| 1056(HD) | Lipids, ν(C-C) and δ(COH) | 1.08 | [129,133] |
| 1073(HD/f) | Triglycerides | 1.07 | [129] |
| 1105(HD/f) | Phenylalanine ν(C-C) and C-O stretching of carbohydrates | 1.11 | [129] |
| 1130(HD/f) | fatty acids | 1.09 | [128] |
| 1170(HD) and 1172(f) | tyrosine | 0.96 and 0.98 | [134] |
| 1199(HD) and 1200(f) | Amide III | 0.82 and 0.92 | [129] |
| 1217(HD) and 1219(f) | C-N stretching/ amide III | 0.84 and 0.84 | [129] |

| Raman shift ($cm^{-1}$) | Assignment | VIP value | References |
|---|---|---|---|
| 1255(HD/f) | Lipids and amide III | 1.10 | [134,135] |
| 1300(HD/f) | fatty acids and lipids CH and $CH_2$ twisting | 1.11 | [136,137] |
| 1331(f) | Phospholipids | 1.05 | [129] |
| 1453(HD) and 1454(f) | $CH_2$ stretching and scissoring, $CH_3$ asymmetric deformation and bending associated with Phospholipids, C-H bending structural proteins | 1.10 and 1.12 | [129] |
| 1470(HD) and 1472(f) | C=N | 1.11 and 1.12 | [129] |
| 1586(HD/f) | Phenylalanine | 0.97 | [129] |
| 1616(HD) and 1618(f) | tyrosine and tryptophan | 1.08 and 1.06 | [129,134] |
| 1659(HD), 1660(f) and 1685(f) | Amide I and unsaturated (C=C) trans and cis dependent fatty acids | 1.30, 1.30 and 0.97 | [128,134,136,138,139] |
| 2715(HD/f) | CH, NH and OH for lipids and proteins | ***0.70*** | [129] |
| 2790(HD/f) | CH, NH and OH for lipids and proteins | ***0.70*** | [129] |
| 2884(HD/f) | $\nu(CH_3)$ lipids and fatty acids | 1.10 | [129] |
| 2909(HD/f) | CH lipids and proteins | 1.10 | [129] |
| 2955(HD/f) | $CH_3$ asymmetric stretches/ fatty acids | 1.10 | [129,137] |
| 3074(HD/f) | $\nu$( =CH) lipids | 1.0 | [129,130] |

*Table 7-1 Raman shift putative assignments with associated VIP values. The notation HD and f in brackets in the first column refers to HD and fibroblasts control membranes. The third column describes the VIP values for the two types of membranes, underlined bold values were below the 0.8 threshold limit. ν stretching deformation and δ vibrational deformations.*

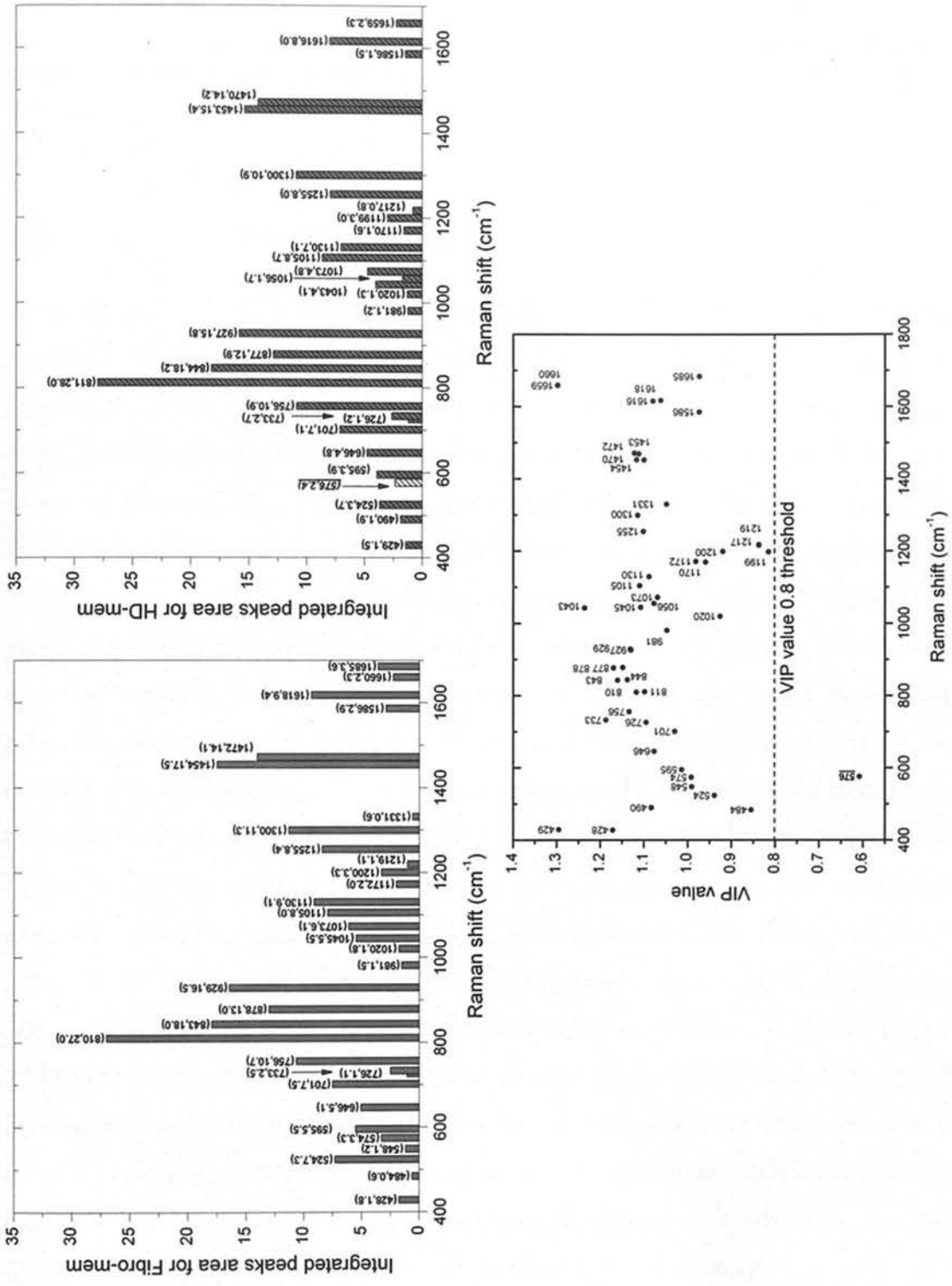


*Figure 7-21 a) Histogram for vibrational Raman shift (first number on each column) and corresponding integrated area (second number on each column) for HD. b) Histogram for vibrational Raman shift (first number on each column) and*

*corresponding integrated area (second number on each column) for fibroblasts. c) VIP values scatter plot for assigned peaks, note that only 576 $cm^{-1}$ (italic and underlined) peak was below threshold of 0.8. All graphs refer to the low wavenumber region.*

### 7.5.2 High wavenumber region from 2700 to 3200 $cm^{-1}$

Although high wavenumber regions have a less informative nature for biological samples[128] a spectral analysis was included for the 2700 to 3200 $cm^{-1}$ region for completion and to determine possible difference in lipids structures. PLS analysis was carried out as described in Materials and Methods. The first two factors are shown in *Figure 7-22a*. The PLS model in total reduced the number of factors to five with minimum root mean PRESS of 0.77. The cumulative variation explained by X and Y were lower than the low wavenumber region with ~47% and ~48% for X and Y respectively for the first factor which showed most separation. This indicated that this region is less suited in discrimination between membrane types. The predicted model is shown in *Figure 7-22b*. The fit to the predicted values by the actual data is less precise than the low wavenumber region although the Hotelling's ($T^2$) doesn't show any outliners in *Figure 7-22c*. The VIPs values are indicated in *Figure 7-22d*. The differences between the average spectra of the two membrane types are even less pronounced in this high region as illustrated by *Figure 7-23a* and *Figure 7-23b*. The peak assignments were mostly due to contributions of CH, $CH_3$, NH, and OH stretches for lipids and proteins as described in *Table 7-1*. The 2715 and 2790 $cm^{-1}$ vibrational frequencies and associated peaks presented a VIP of 0.7 indicating that these peaks have little contributions in membrane discrimination at levels indicated by the first factor in *Figure 7-22a*. The main difference between membranes in this region was the increased integrated intensity area for HD membranes of the peak at 2909 $cm^{-1}$ as shown in *Figure 7-23c* and *d*.

While the assignment is for CH stretches putatively assigned to lipid and proteins this gives very little information about specific bio-molecules that could contribute to separation between membranes. Overall this region was less informative as expected

compared with the 400 to 1800 $cm^{-1}$ lower analysis. The level of separation by PLS is also higher in the lower wavenumber region compared with the high wavenumber region.

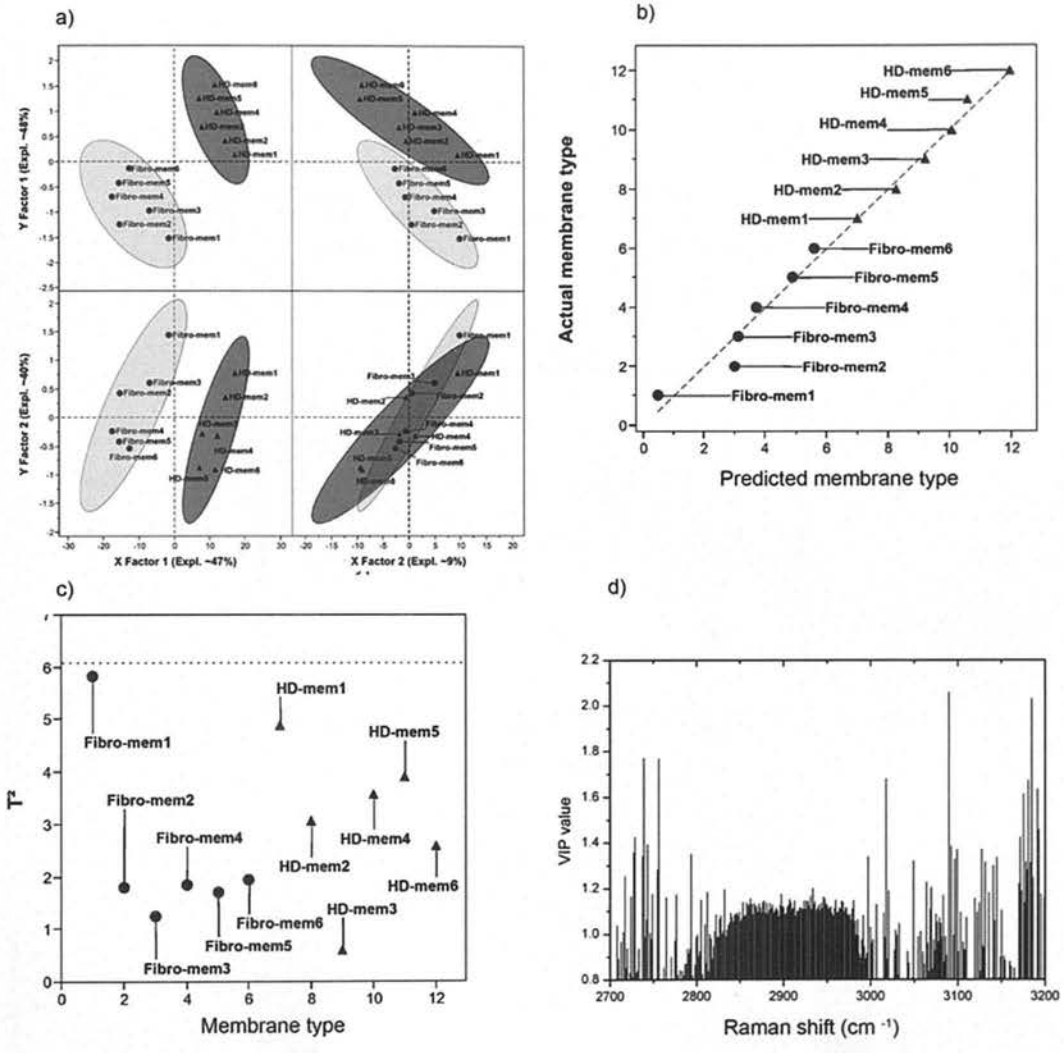


*Figure 7-22 a) High wavenumber PLS analysis scores for the first two factors. Fibroblast (●) and HD (▲) membranes with grouping ellipses to define the two membrane types for the high wavenumber region. b) Predicted versus actual for PLS model in the 2700 to 3200 $cm^{-1}$.c)$T^2$ test for PLS model. d) VIP values plot for the 2700 to 3200 $cm^{-1}$ range with 0.8 VIP thresholds.*

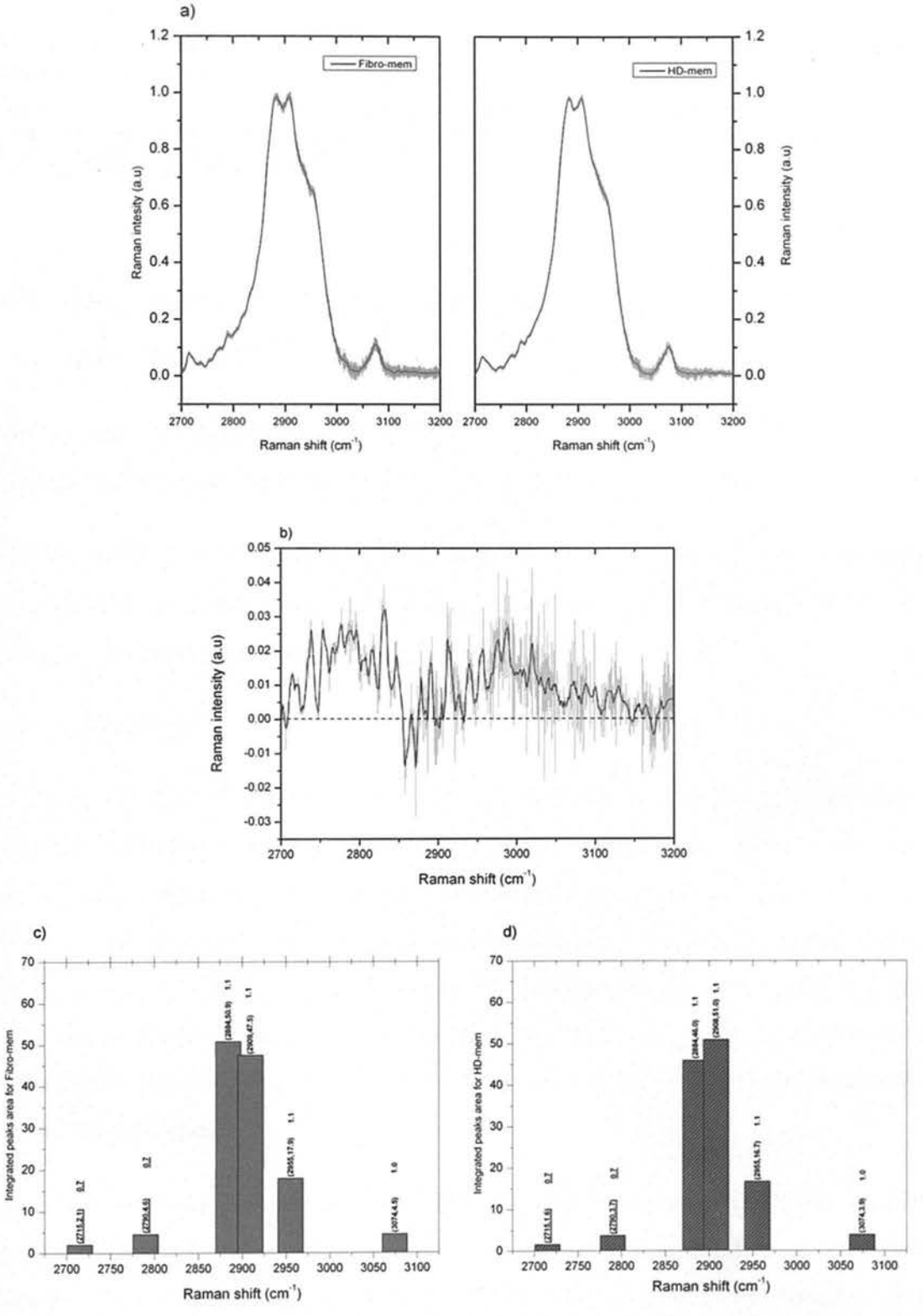


*Figure 7-23 a) Averages spectra for the two membrane types with standard deviation (shaded area). The graph on the left refers to fibroblast membranes and the graph on*

*the right refers to HD membranes. b) Difference spectra between cell membranes. Shaded area indicates the standard deviation. c) Histogram for Raman shift (first number of each column) and corresponding integrated area (second number on each column) for fibroblasts. d) Histogram for Raman shift (first number of each column) and corresponding integrated area (second number on each column) for HD. All graphs refer to the high wavenumber region*

## 7.6 Microscopy analysis for cell membrane conformation with SEM and TEM

C2C12 and GFP-fibroblast were analysed in suspension and in attached state to determine difference in plasma membrane conformation between cells.

Initially SEM pictures were taken of suspended cells to determine plasma membrane conformation/geometry. Subsequently TEM sections were analysed to determine changes in plasma membrane thickness and/or structure.

### 7.6.1 SEM results

In figure 7.4 C2C12 and GFP-fibroblasts are shown in suspension state. To verify structural differences of microvilli between cells of similar size (C2C12 myoblasts and fibroblasts) SEM microscopy was used. Results are shown in *Figure 7-24* and *Figure 7-25*. In *Figure 7-24* image of cells in suspension as they would be during DEP sorting are shown. As can be seen C2C12 myoblasts have an apparently less elaborate microvilli structure compared with fibroblast. The images have been color enhanced to highlight the differences in the quantity and conformation of microvilli in the two cell types.

To further compare the two cell types SEM images of attached cells, as they will be during culture, as shown in *Figure 7-25*. Here in low magnification images (left column *Figure 7-25*) the microvilli structure was difficult to assess although a clear difference in phenotypical shape is present in these two cell types when attached. At higher magnification, *Figure 7-25* (in suspension) right column, it is possible to see

differences in plasma membrane structure between C2C12 (bottom) and fibroblasts (top). C2C12 myoblasts are apparently smoother than fibroblasts.

As illustrated in *Figure 7-26* high magnification pictures were taken of villi structure in GFP-fibroblast (left column) to compare with the sparse presence of villi in C2C12 (right column ). Although variations existed in the two type of cells what is illustrated here is representative of what has been seen during the experiments using SEM. The overall morphology of GFP-fibroblasts plasma membrane seems on average more convoluted than the C2C12 counterpart.

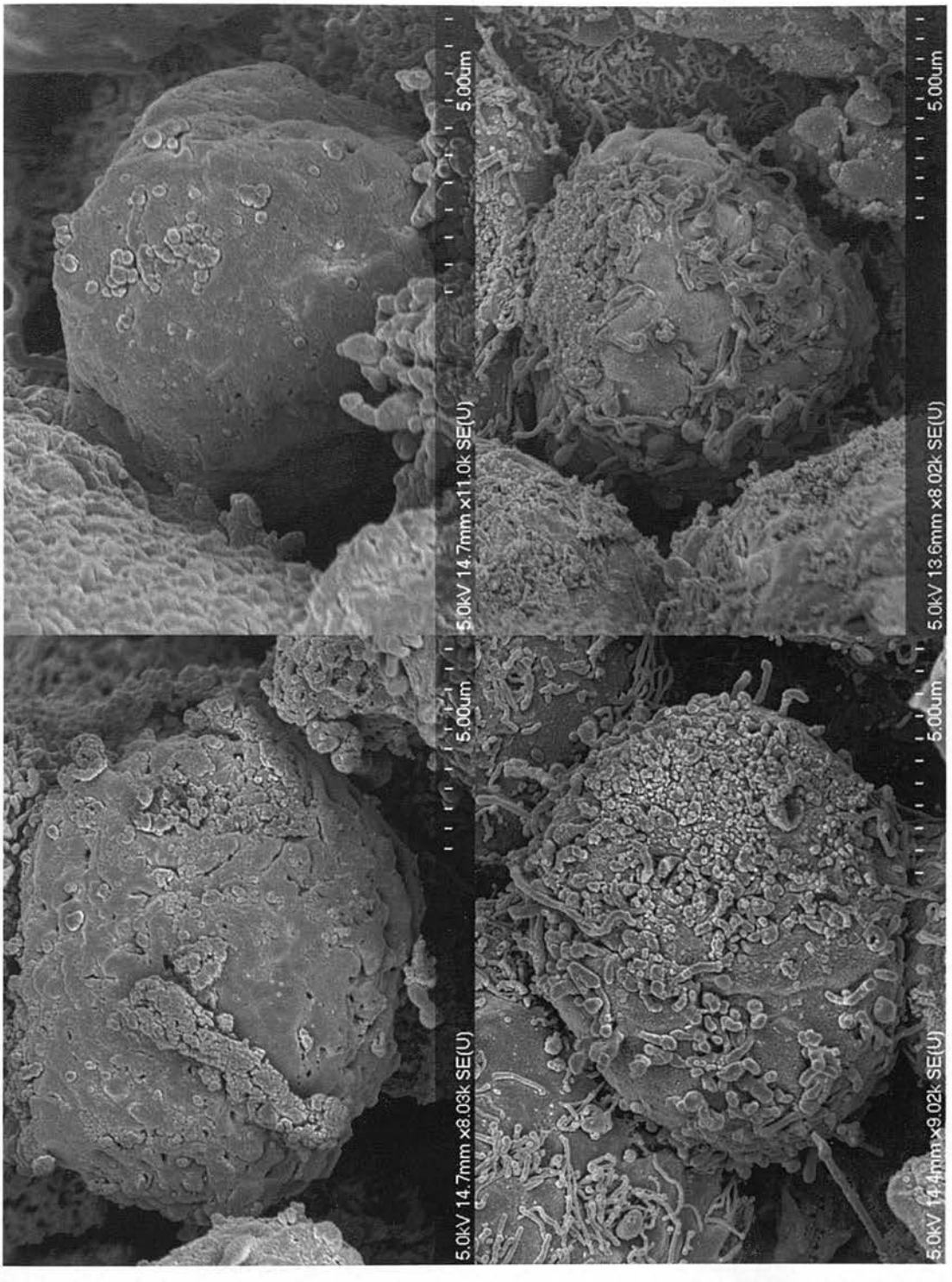


*Figure 7-24 SEM images of C2C12 (blue-red) and fibroblasts (green-red). The colors have been enhanced for better visualization. The microvilli are coloured in red and the underling surface is coloured in blue for C2C12 and green for GFP-fibroblast. The quantities and conformation of the microvilli are more pronounced on GFP-fibroblast.*

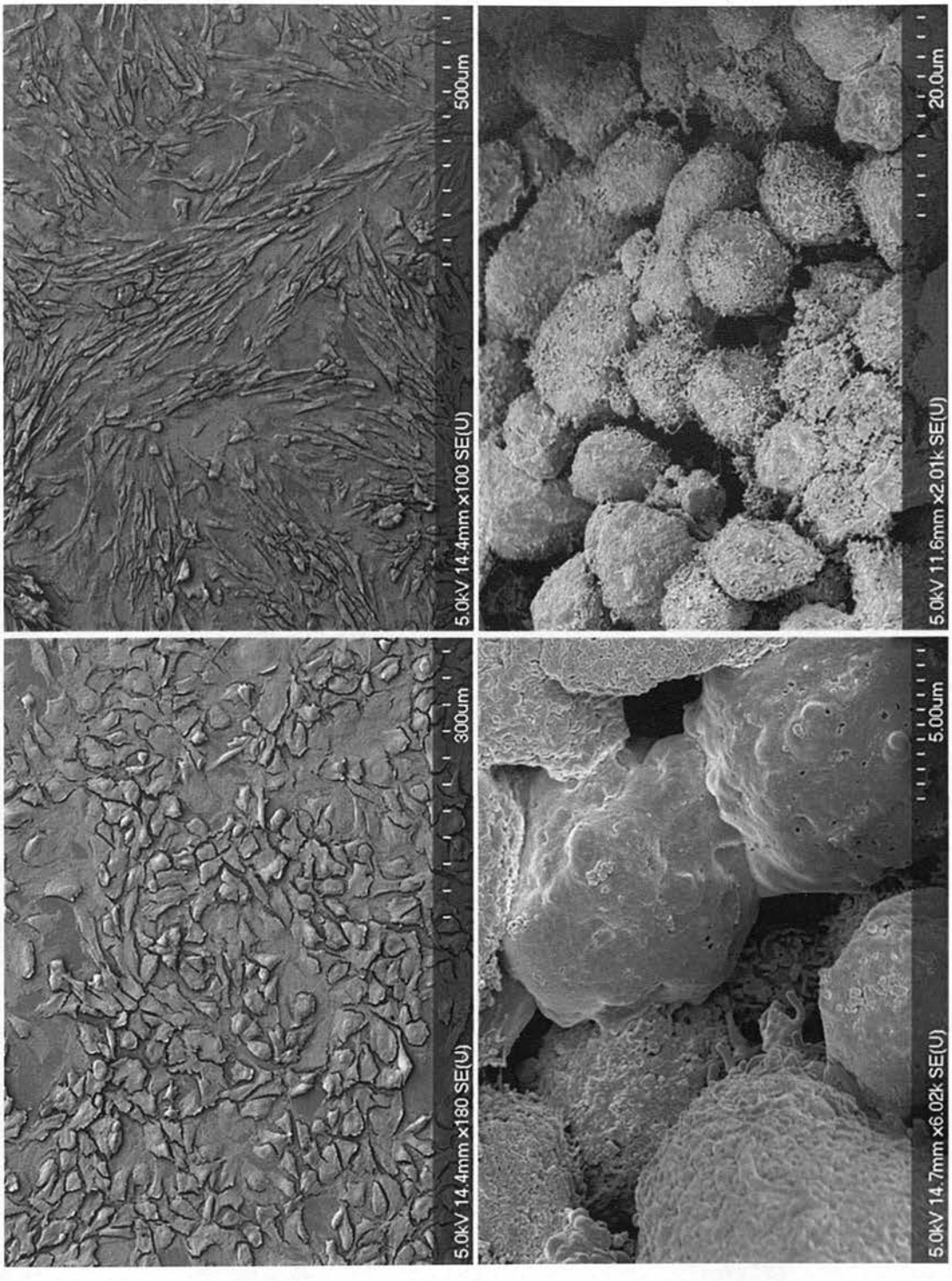


*Figure 7-25 C2C12 myoblasts (bottom row) and GFP-fibroblasts (top row) overall view of attached cells (left) and in suspension (right) by SEM microscopy. The fibroblasts on the top row show more microvilli structure compared with a less villi/more smooth morphology of C2C12 overall.*

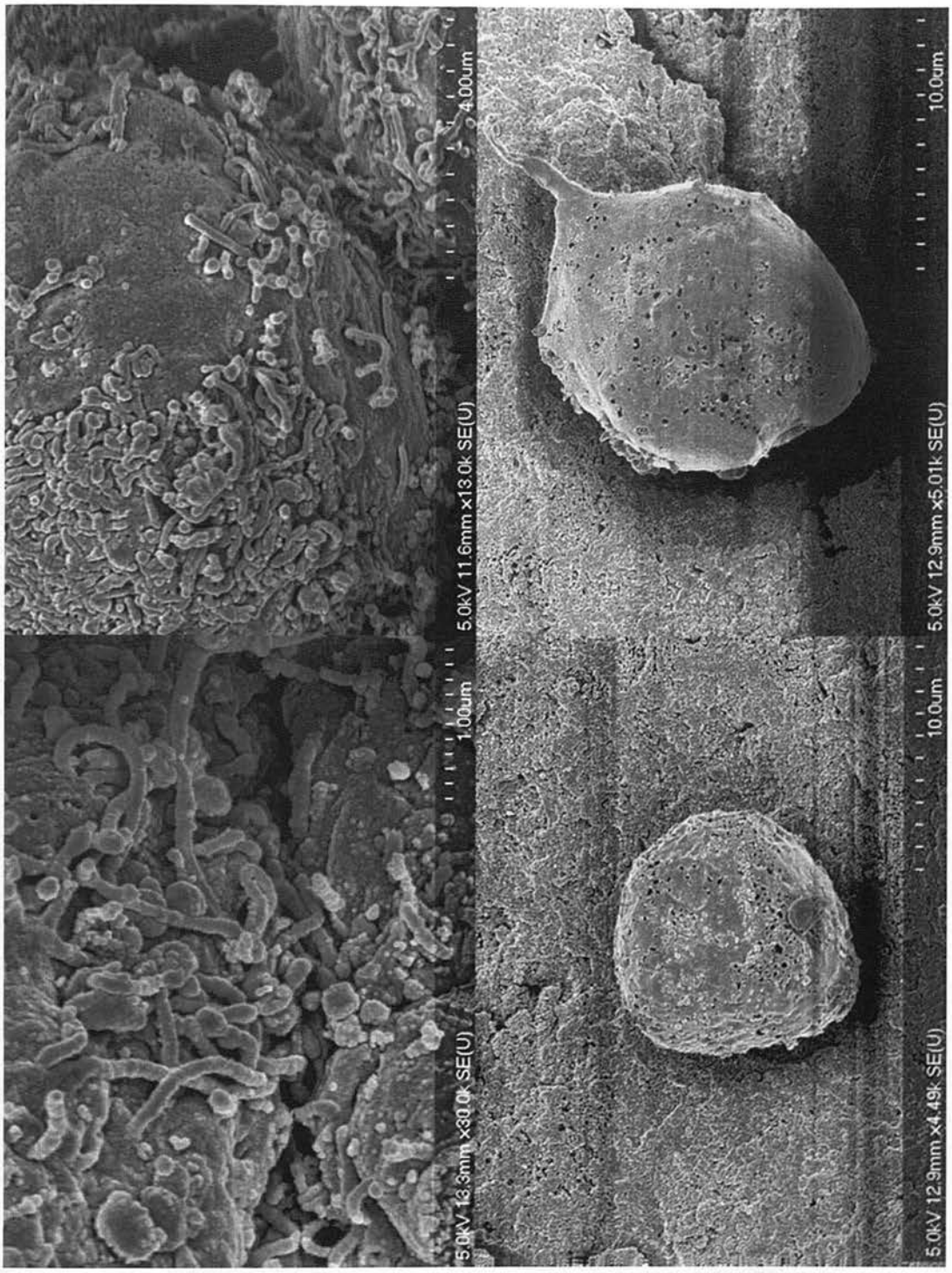


*Figure 7-26 High magnification of microvilli structure in GFP-fibroblast (left.) C2C12 myoblasts (right) pictures are taken to compare them against highly complex GFP-fibroblast structure*

### 7.6.2 TEM results

The TEM images of C2C12 plasma membranes are shown in *Figure 7-27*. This picture shows the thickness of a sample of the plasma membrane of C2C12. As illustrated the thickness has been determined by software in two random points on the plasma membrane section. A higher level of resolution may be achieved with other methods of preparation for the cell with TEM. However, for the TEM resolution capabilities and the preparation procedure described in the Materials and Methods, no major differences were not found in membrane thickness between C2C12 and GFP-fibroblasts. Although as indicated in *Figure 7-27* a local variation in thickness is present in the plasma membrane.

An important consideration about these pictures is the fact that these are 60 nm thick cut of the cell; this implies that microvilli structures may appear as detached globules outside the plasma membrane as illustrated in *Figure 7-28*. At higher resolution and by imaging a different point in the membrane the folding is evident by TEM as illustrate by *Figure 7-29*.

Images of potential myotubes are illustrated by *Figure 7-30*. The presence of two nuclei surrounded by an enclosed membrane is shown in *Figure 7-30* by red arrows.

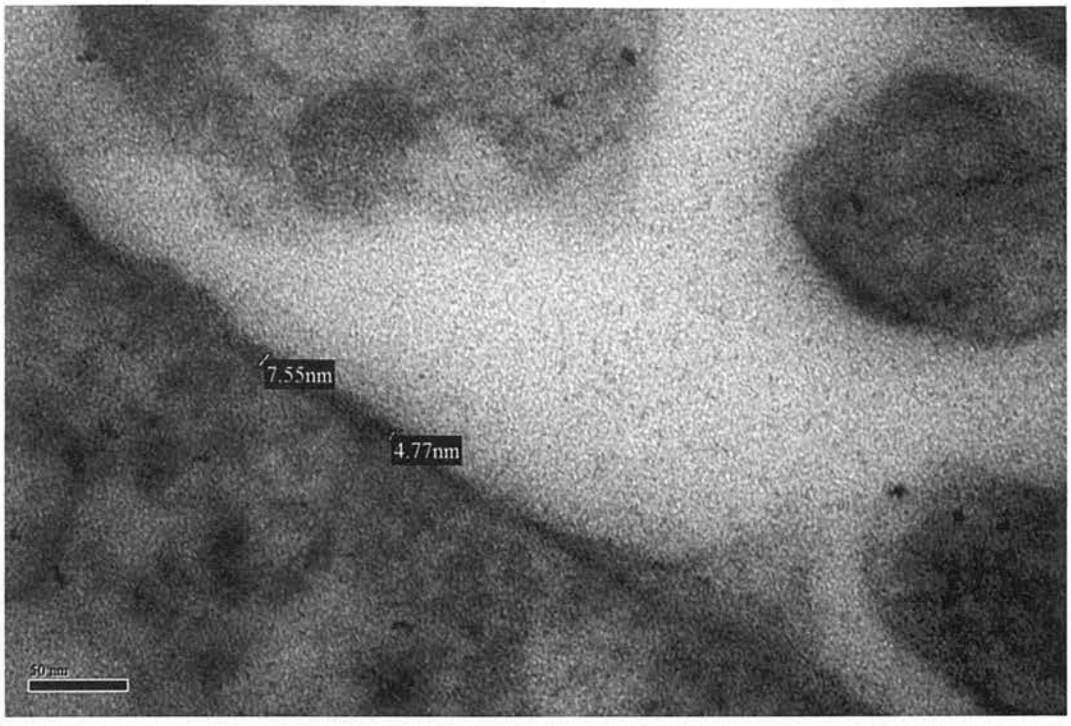


*Figure 7-27 C2C12 plasma membrane thickness by TEM (above picture)*

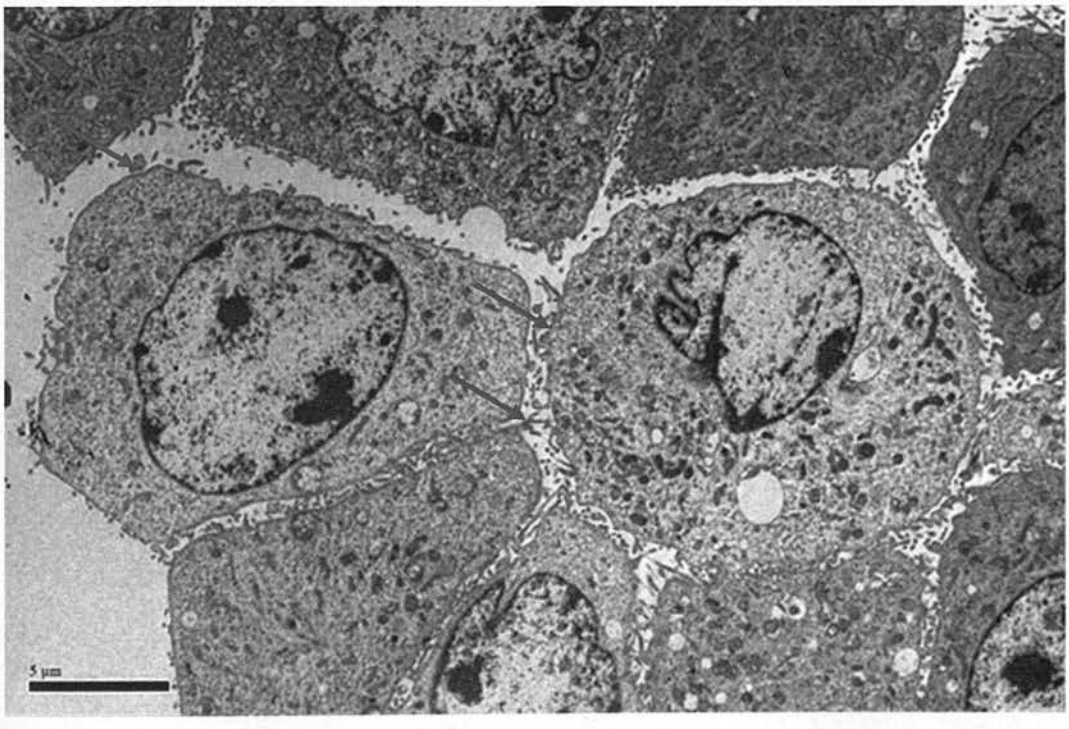


*Figure 7-28 GFP-fibroblasts section by TEM. Red arrows illustrate the microvilli structure, as detached globules due to the cut thickness need it for the preparation and imaging of the cells.*

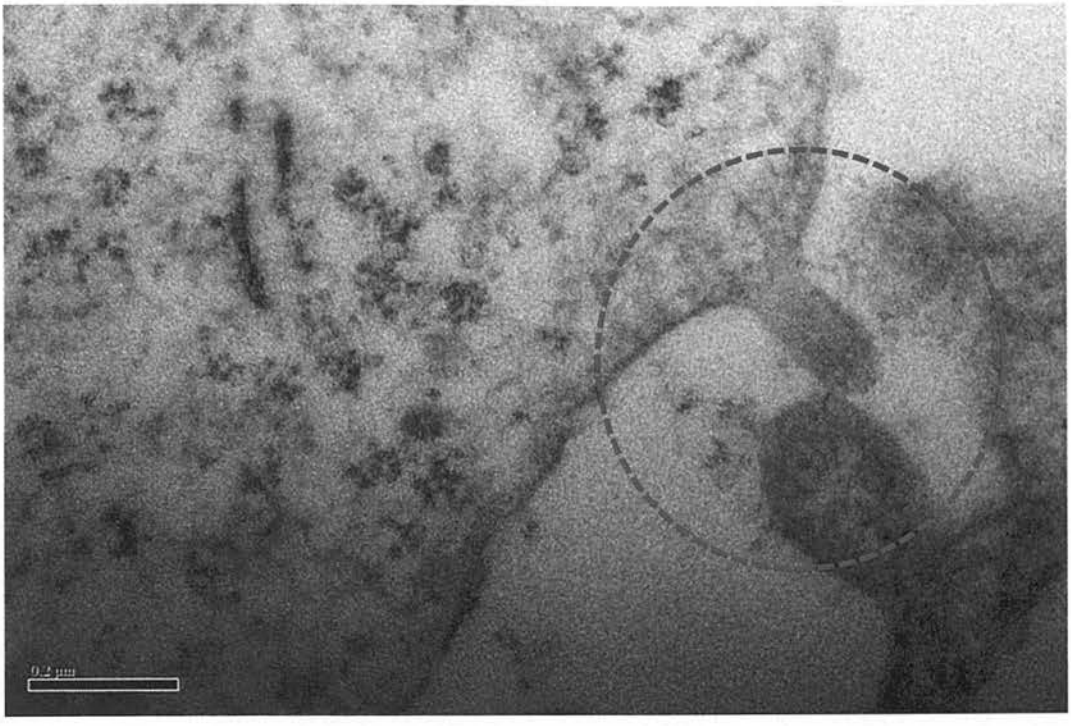

*Figure 7-29 Plasma membrane fold of GFP-fibroblasts as indicated by red circle on the TEM image.*

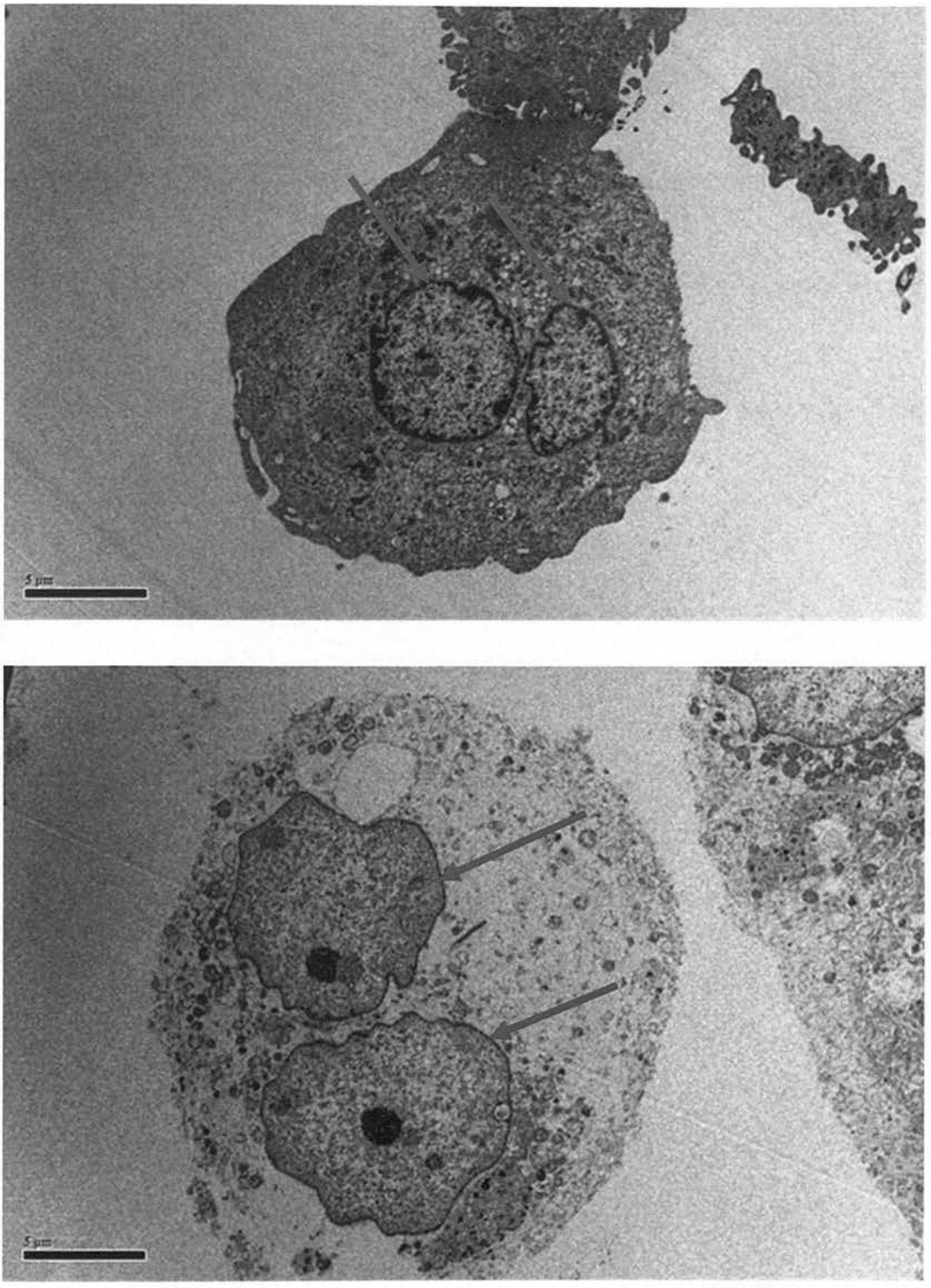

*Figure 7-30 Possible myotube section 60nm thick. The presence of two darker areas in the centre suggests the poly nuclear conformation characteristic in myotubes*

# Chapter 8 Discussions and conclusions

## 8.1 Introduction

This chapter present the conclusion and discussions of the results shown in *Chapter 7.*Results.

The results gathered from the separation by DEP, Raman spectroscopic analysis and plasma membrane characterisation are discussed in detail.

The structure of the chapter is divided in these main areas:

1) Myoblasts pluripotency.
2) DEP sorting results.
    a) The cytometric results analysis of DEP sorting.
    b) Markers for differentiation and cell cycle
        i) Embryonic myosin
        ii) Ki-67
3) Raman analysis
    a) C2C12 myoblasts and GFP-fibroblasts
    b) Huntington's fibroblastic cells
4) SEM and TEM analysis

## 8.2 Myoblast pluripotency

C2C12 myoblasts are well-studied and characterised progenitor cells used for muscle differentiation [140]. When growth factors are kept at high concentration myoblasts maintain an homogenous and proliferative state [141]. By manipulating the composition of the culture medium, C2C12 can differentiate in several cell lineages such as myotubes, adipocytes, osteoblasts and neuron like cells [141,142,143].

In addition, by using small chemical molecules such as Reversine and Neurodazine, these cells can de-differentiate from their terminal differentiated state back to their progenitor state. [118,143]. In *Appendix C*, C2C12 were first differentiated in adipocytes by chemical modification in the composition of the culture medium. Subsequently adipocytes were treated with 1μM of Reversine in order to de-differentiate them back to C2C12. In *Appendix C* notice that the morphology of the cells changed and the DNA structure seemed to be altered. From available literature the process of de-differentiation seems related to histone modifications [118] but also to the inhibition of Aurora B kinase [144].

Mesenchymal precursor cells such as C2C12 are model cells for regenerative studies due to their ability to differentiate into different cell types by means of chemical cues and/or growth factors present in the culture medium [118,145,146]. C2C12 myoblasts represent a valuable system in studies investigating stem cell plasticity [141]. Plasticity has been shown to be related to cell age (passage number/senescence) [123,147,148]. These properties were exploited for studies in animal models in cardiac grafts and cardiac cells transplantation [149,150] as well as other biomedical applications [26,141]. Altogether these results are very encouraging however the homogeneity and differentiation status of the cell population for regeneration remains problematic[151].

The dependency between the passage/senescence stage and the ability to differentiate has been noticed and verified in the experiments carried out for this thesis. The results are illustrated in *Figure 7-1*, *Figure 7-3* and *Figure 7-4* in the Results chapter.

Differentiation from C2C12 to myotubes is variable and the efficiency decrease quite significantly with the time of the cells in culture as indicated in literature [123,147,148] and in our experience working with C2C12 myoblats. With cells above 50 passages the rate of conversion in myotubes was approximately 40/45% of the total number of cells in the population by analysis with a haemocytometer. Although lower passages have been used initially to assess the level of maximal conversion no higher than 65% (from the initial C2C12 population) have been achieved with passages of ~15.

Dielectrophoresis (DEP) has been used for several biochemical and biomedical applications in order to fractionate and purify cells of interest from population of cells [24,26,152]. This technique has the advantage that it does not rely on any biological tag for cell separation and this absence of any biological manipulation is ideal for preserving the normal physiological conditions of the cells.

In the results here reported, the level of purification between C2C12 and myotubes was very high (above 96% for one cell type) using DEP. This level of purity represents an enrichment of 56% in purity in C2C12 culture of above 50 passages. Also in contrast to tag dependent techniques such as flow cytometry, the purity achieved by DEP is completely independent of any biological tag, making the implementation amenable where the end results is to purify cells that maintained a physiological homogenous state for further biomedical applications. This has very important implications in research for stem cells where the purity, viability of cells retaining certain regenerative characteristics is of primary importance in pre-clinical applications [153]. This implies a biological pure population of cells with at least phonotypical synchronicity and uniformity that more resembles the normal physiological state of the cell population.

## 8.3 DEP sorting and flow cytometry analysis

The frequency dependencies of the Clausius-Mossotti polarizability functions *Re(CM)* for the three cell types can be derived, based on their estimated DEP cross-

over ($f_{xo}$) values. Using the standard form of *Re(CM)* [8,24] modelling was performed using MATLAB (The Maths Works Inc.) and the results are shown in *Figure 7-8. Re(CM* curves*)*, limited to the region around the range of $f_{xo}$ values for the three cell types, help us understand the frequency dependencies and DEP separations shown in *Figure 7-7* and *Figure 7-10.* The difference between the average $f_{xo}$ values for the C2C12 myoblasts, myotubes and feeder GFP cells, would have been a factor leading to their efficient separation by DEP. The fact that good separations were also obtained for mixtures of myotubes and GFP fibroblasts suggests that there was a negligible overlap of their $f_{xo}$ distributions about their mean values of around 400 kHz and 500 kHz respectively.

The C2C12 myoblasts and GFP-fibroblasts were observed, using a microscope to have roughly equal diameter as indicated in *Figure 7-14*, and *Figure 7-15*. As shown in *Figure 7-16* these two cell types exhibited closely matching flow cytometry forward scatter plots, indicating that their size distributions were similar. From these results, the diameters of the C2C12 myoblasts and GFP fibroblasts can be estimated as approximately 10 ± 3.1 μm and 9.4 ± 3.3 μm, respectively. Based on a medium conductivity of 120 mS/m (see *Appendix E*) and their estimated $f_{xo}$ values of 700 kHz and 500 kHz respectively, membrane capacitance values of 7.3 ± 3.0 mF/m$^2$ and 11.5 ± 5.3 mF/m$^2$ can be estimated for the C2C12 myoblasts and GFP fibroblasts, respectively. This suggests that the DEP separation of the similar sized C2C12 and GFP fibroblasts cells was mainly associated with the difference in their membrane capacitance. The myotubes were of an elongated and convoluted shape, roughly three-times larger in volume than the C2C12 and MRC-5- GFP cells. The derivation of the membrane capacitance using *Equation 2-22* (section *2.3.5*) is only valid for spherical cells [8]. Whereas the polarizability of ellipsoids and truncated cylinders can be determined [154], the ill-defined shape of the myotubes prevents an estimation to be made of their membrane capacitance.

As shown in *Figure 7-10* (top row) there was presence of cellular debris that were excluded by the gating in the flow cytometry analysis. This can be attributed to the

manipulations associated with cell preparation for cytometric analysis; on average (for all the experiments) approximately 80/85% of the cells collected by DEP sorting were intact. Although extreme care was taken in the handling of the cells for cytometric analysis but a ~ 10/15% loss in cell number was unavoidable.

As shown in *Figure 7-14* the sphericity of the cells may be assumed for C2C12 and GFP-fibroblasts, although variation exist especially if the number of counted cells is increased to statistically relevant levels comparable to flow cytometry standards. Here cells were counted by taking pictures of cells in suspension and by analysing the pictures with ImageJ software (USA, http://imagej.nih.gov/ij/, 1997-2012) to determine the average diameter of C2C12 and fibroblasts in suspension as illustrated in *Figure 7-14* and *Figure 7-15*.

In addition, in order to better interpret the flow cytometry results (*Figure 7-16*) for cell size, the partial linear correlation between the scatter and the size of cells need to be considered. As shown in *Figure 7-16*a even the beads present a side scatter spread due to the fact that are not completely smooth on the surface. In other words, the size is not proportionally realated to the size scatter so by doubling the size of the bead there is not a double increase in side scatter although this is very close. With this taken in consideration the flow cytometry results give a good estimation of the cell size and therefore a quite accurate estimation of the membrane capacitance.

### 8.3.1 Western blot analysis

As indicated in *Figure 7-9* the embryonic myosin marker is completely absent in C2C12 cells sorted by DEP. The marker was chosen to validate the DEP sorting efficiency between C2C12 and induced myotubes from the same culture preparation. As shown in *Figure 7-9* embryonic myosin is completely absent in C2C12 but present in only myotubes cells. Since this marker is specific for myotubes these results further validate the purity of the sample.

These results further validated the level of purity of the cell population sorted by DEP. Although this was not the main goal of the Western blot analysis, an

unexpected indirect correlation between this intracellular protein and DEP can be assumed. By separating cells by DEP, assessment in expression levels of (at least embryonic myosin) intracellular markers could be made indirectly. This may be important in validating the state of differentiation of the population sorted by DEP but could also be further exploited for research in pre-clinical applications by validation of specific intracellular markers intrinsically related to differentiation.

### 8.3.2 DEP sorting associated with cell cycle investigation.

A second set of DEP experiments (*Figure 7-10*) was performed with C2C12, myotubes and GFP-fibroblasts in order to determine if there was a correlation with the sorting ability of DEP and the determination of the cell cycle stages of the cells.

This was mainly to assess if DEP sorting of C2C12 and GFP-fibroblats was due to possible changes in volume for cells in *M phase* of the cycle. Although literature has reported DEP sorting of cells based on stages of the cell cycle [120] there are certain important considerations to address.

Firstly, there is a long disputed argument about cell cycle regulation and size control in mammalian cells [155,156]. Although the association between cell cycle regulation and cell size have been elucidated in yeast [155,157,158] and Drosophila [159,160] the same is not fully clarified in mammalian cells. For mammalian cells, as used in the experiments here, there is not a clear correlation between the cell cycle stage and total increase in volume of the cell [155,156,161,162].

Secondly, based on literature consensus variation in size may exist transitorily during the cell cycle but these variations are regulated by a longer or shorter transition of the cell in a particular stages of the cell cycle [155,163]. For smaller size cell there is an increased transition time through the $G_1$ phase. The opposite situation applies to larger cells that have a shorter time transition through *G1* phase as reported in literature [155,163]. In other words, there is a certain *"conservation of mass"* with transitory variations along the cell cycle (although how long these transitory states exist has not been elucidated in literature to the best of our knowledge).

The two above mentioned points are important to consider in DEP sorting. Since the cell size seems regulated between stages of the cell cycle, the overall size/volume is constant with transitory variations during proliferation. However, considering the *M* phase of the cell cycle, where the DNA is duplicated, variation in size may occur in relation to the ratio between nucleus and cytoplasm [164] rather than the overall size of the cell. This implies that if there was a significant difference in cell's size during the cell cycle, population of cells could be sorted base on their cell cycle stage. This will produce different flow cytometry profiles for cells sorted by DEP and cell just eluted from the micro channel. Therefore, C2C12 and GFP-fibroblasts sorted by DEP will present synchronicity at a particular stage of the cell cycle with a cytometric profile similar to myotubes as shown in *Figure 7-11*and *Figure 7-12*. This was not the case in the results presented here therefore it may be assumed that the separation of similar cell size is based mainly on plasma membrane characteristics and capacitance rather than size associated with cell cycle stage. *Figure 7-11* illustrate that the cytometric profile between cells sorted by DEP and cells just eluted (no DEP) from the main channel. These do not present any significant variations associated with the cell cycle phases. In *Figure 7-13*, there are two pictures of cells captured during what is possibly anaphase among a population of cells with probably mixed cell stage. *Figure 7-11* also shows that the myotubes are mainly in the *G0/G1* phase of the cell cycle. This was expected for these differentiated cells because when terminal differentiation is achieved the cells withdraw from the cell cycle [121,122,123].

Although in the results here no correlation has been shown between the cell cycle and size of the cell with the sorting ability of DEP there are some more important details to consider. The method for assessing the cell cycle stage relies on permeabilized cells and PI staining as described in Materials and Methods (*6.3.6.2*). The cytometric gating[34] of the profile generated by the cell containing PI gives an estimation of the stage of the cell cycle based on the amount of DNA present the cell

[34] Gating refers to a selection of subsets events collected by cytometric analysis This subsets of data can be analysed statistically for data interpretation.

due to the fact that PI intercalate between DNA strands in permeabilized cells. The implications are that during the cell cycle the amount of DNA change in mitotic competent cells from *G0* to *M* phase of the cell cycle. This because, in the *M* phase, there is twice as much DNA that needs to be divided between mother and daughters cells. As before mentioned there is variation in *M* phase between the ratio of the nucleus and the cytoplasm but this variation may not be displayed significantly on the overall size of the cell. Therefore, the use of PI gives an assessment mainly of the amount of DNA present with arguable relevance regarding the cell size. More assessments of specific markers such as Ki-67, cyclins and other may be more appropriated to define the stages of the cell cycle. Since a precise estimation and correlation between the cell cycle and size of the cell is problematic with just PI staining procedure, an assessment of mitotic competence (if cells are in the cell cycle or not) has been validated by Ki-67. The marker was evaluated as illustrated in *Figure 7-12*. Ki-67 was chosen because it is widely used in assessing mitotic competence of cells [165]. As shown in *Figure 7-12* both C2C12 and GFP-fibroblats were positive for Ki-67 and as expected, myotubes were negative due to being withdraw from the cells cycle.

### 8.3.3 Cell size analysis

As described in section *8.3* the flow cytometry profiles indicated a cell diameter of approximately 10 ± 3.1 μm and 9.4 ± 3.3 μm, for C2C12 myoblasts and GFP fibroblasts respectively (as illustrate in *Figure 7-16*) . This relays on the cytometric profiles with the calibration beads. In a second set of experiments the cell sizes was estimated visually by staining the cells and count them using ImageJ software. (USA, http://imagej.nih.gov/ij/, 1997-2012) as illustrated in *Figure 7-15* and as a sample in *Figure 7-14* (see also *Appendix B*). Here the values of the diameters were higher (the averages for C2C12 myoblast was 18.6μm ±5.8 SD and fibroblasts 18.9 μm ± 7.4 SD) compared with the flow analysis against the calibration beads as shown in *Figure 7-16*a. Therefore, the value of cell membrane capacitance may be higher than what has been estimated in chapter *8.3* (DEP sorting and flow cytometry analysis).

However, similar size distribution between C2C12 and GFP-fibroblasts can be deduced by both results with flow cytometry and cell counts.

Considering the flow cytometry results more accurate in determine cell diameter a precise estimation of the diameter by cell counting has been proven difficult. This may be attributed to the procedure adopted for counting the cells as describe in Materials and Methods (*6.3.7.1*). This procedure may have produce osmotic variability because of the suspending solution, composed of PBS and formaldehyde, had been used to fix the cells. Here osmotic equilibration may have needed more time before imaging or other fixation methods may be more appropriated. However, the goal here was to validate DEP separation between similar size cells, as shown in *Figure 7-10*. If osmotic equilibrium was the problem, it was constant across all the sample and experiments. In addition, the implementation of cell counting with ImageJ software (USA, http://imagej.nih.gov/ij/, 1997-2012) has been proven a useful methodology in counting high number of cells. High number of cells could be counted quickly and accurately producing results, in terms of number of cells, comparable to the flow cytometry results. The high number count was paramount for statistical relevance.

## 8.4 Raman spectroscopic analysis of similar size cells (C2C12 and GFP-fibroblasts)

An initial evaluation of the plasma membrane characteristics to explain DEP separation of similar size cells was carried out by an analytical chemical technique in the form of Raman spectroscopy. *Figure 6-1* shows the statistical method used to evaluate statistical significant differences between cell types in the form of Principal Component Analysis (PCA). As shown in *Figure 7-17* the three cell types cover separated area of the plotted Components 2 and 3. This implies that for these two components, PC2 and PC3, there are differences in the plasma membrane chemistry. PC2 and PC3 account for approximately 30% of the differences between cell membranes. In *Figure 7-17* the region between 2800 and 3000 $cm^{-1}$ shows the higher

level of difference between C2C12 and GFP-fibroblasts. As indicated by *Table 7-1* this can be putatively attributed to saturated hydrocarbons chains and related proteins present in the plasma membrane of these two cell types. The GFP-fibroblasts contained a lower proportion of saturated hydrocarbon bonds than those of the C2C12 membranes.

Lipid bilayers formed of saturated "rigid" hydrocarbon chains will be thicker than those composed of unsaturated "kinked" chains. Several explanations of the differences found in membrane chemistry are possible but for this initial analysis we can speculated changes in permittivity of the plasma membrane due to the different level of lipids saturation[166]. If the Raman data are interpreted as the GFP-fibroblasts cells membranes having the thinner membrane, then based on *Equation 4-11* this would contribute to the finding that the GFP-fibroblasts cells possessed the larger membrane capacitance. Also, the relative permittivity of fatty acids decreases with increasing saturation [166]. This again could contribute to the GFP fibroblasts exhibiting a larger membrane capacitance compared with the C2C12 myoblasts. Therefore, membrane capacitance values derived from DEP experiments should be considered to reflect both the membrane chemistry (with interpretations regarding membrane thickness and dielectric polarizability), as well as a measure of the relative value of the membrane-folding factor $\phi_m$ in *Equation 4-11*.

## 8.5 Plasma membrane analysis by Raman spectroscopy in Huntington's disease affected cells.

In the previous section, the Raman results and DEP sorting showed that DEP could sort cells of similar size if there are differences in the plasma membrane capacitance associated with the chemical composition. This prompt the investigation in finding suitable cells associated to a pathology that reflects in the plasma membrane as a possible target for DEP sorting.

Markers for the detection and possibly early identification of the onset of HD would represent an important development in the treatment and therapy of the disease[167].

Studies have shown that the toxicity of the Htt protein affects several sub-cellular structures associated with the plasma membrane including endocytic recycling associated with Rab11 [168] and GM1 glanglioside synthesis [169] rendering cells more susceptible to apoptosis. It also produces disruptive associations with membranes phospholipids [170,171,172] although this may not only be confined to the plasma membrane but also to mitochondria membranes.

There is evidence that Htt could interact with proteins of the cysteine proteases family [173] regulating the levels of $Ca^{2+}$ ions for membranes polarization and depolarization as well as dysregulating the glutamate receptor signalling [173]. These results suggest that HD may have an effect on cell membrane biochemistry and structure making it a possible interesting sub-cellular biomarker amenable for investigation in the studies of HD pathology [174].

Although the majorities of the studies both *in vitro* and *in vivo* concern neurons and mouse models it is also important to notice that peripheral fibroblasts cells have been used extensively [169,170,175,176] as a model due to their forecasting capability in neurons. Due to this knowledge, the initial hypothesis states that the cell membrane disruption could be a possible indirect effect of the presence of the disease, which could be detected and analyzed by Raman spectroscopy.

Several studies have shown the capabilities and validity of this type of spectroscopy with associated chemometric analysis in the form of PLS, Principal Component Analysis (PCA) and other multivariate statistics in detecting, classifying, and identifying underling differences between biological and biochemical samples [177,178,179,180,181,182]. This spectrometric analysis is also well suited for this type of investigation as it gives a mean of discrimination between sample types as well as gives information of the underling characteristics on a molecular level. PLS is also useful to address the problems of multicollinearity associated with complex biological data when the number of predictors is much larger that the number of samples [183,184] in tall or wide data sets.

This study faced a similar situation where the number of samples was limited, due to the membrane extraction procedure that required large amounts of cells, in comparison to the number of predictive vibrational bands measured. Considering these factors PLS was a better option to other types of multivariate analysis [183,184]. Moreover a statistical method of reduction, classification and analysis was needed to determine the most relevant vibrational bands responsible for cell discrimination, that were not readily identifiable by visual inspection of the Raman data only. PLS analysis was used to extrapolate information from the Raman spectra in order to confirm discrimination between HD positive and negative cells.

Several studies have used Raman spectroscopy with chemometric multivariate statistical analysis for biological samples to detect diseases such as cancer [178,179,185], both *in vitro* and *ex vivo* [185,186], for forensic science in detection of body fluids[187,188], to examine components and attributes of biological relevance[128,189,190] and to determine changes and status of mammalian cells [180,191] of the whole cell and nuclei. However, the plasma membrane has not been investigated as a specific sub-cellular biomarker and its potential discriminatory attributes for detection of a specific disease. Moreover, a marker that could identify the presence of the disease will be a valuable tool for further *in vitro* research with possible applications for *in vivo* studies on animal models.

This study has used peripheral fibroblastic cells that have the advantage of being easily accessible and easy to culture compared with neurons or mouse models. The study presented here showed that extracted plasma membranes could be a useful biomarker, in conjunction with spectroscopic Raman analysis, for HD discrimination in peripheral cells as illustrated *Figure 7-18*. The implementation of PLS analysis was well suited for this study due to its intrinsic ability to discriminate small number of samples with a relative assessment of the percentage of variances between membrane types. This is important in evaluating the robustness of the model and in future predictivity. The implementation of the VIP values allowed further refinement and confidence in selecting the most suitable components, in this case vibrational

frequencies that most contributed to membrane discrimination by the PLS model. Within the VIP parameters the peaks were assigned on available literature. The PLS model showed clear separation between HD and control fibroblast as depicted in *Figure 7-19*, *Figure 7-20* and *Figure 7-21* for the low wavenumber region and in a lesser extent in *Figure 7-22* and *Figure 7-23* for the high wavenumber region. Also the PLS model fit very well the actual data as shown by *Figure 7-19*a (low wavenumber region) validating Raman spectroscopy as a suitable technique in HD discrimination based on cell membrane biochemical changes. The main biochemical differences were mainly present between 400 and 1800 $cm^{-1}$ with related putatively assigned peaks as described in *Table 7-1* based on the VIP values. Control fibroblasts presented an overall higher Raman intensity in the 400 to 1800 $cm^{-1}$ region and peaks were putatively assigned to characterize the differences between membranes. These differences were putatively associated for this initial investigation to cholesterol, phophatidylinositol and phospholipids with possible contributions of proteins containing tyrosine. The peak at 548 $cm^{-1}$ was only present in control membranes and overall the region from 428 to 701 $cm^{-1}$ presented a higher Raman intensity for control fibroblast. The peak at ~810 $cm^{-1}$ was very strong in intensity for both membrane types, this may be due to the fact that fibroblastic cells were used. These cells produce collagen between 5 to 10% of the total amount of protein[192] and the presence of such strong peaks may be justified. Furthermore, in the case of RNA contamination a distinctive peak at 1240 $cm^{-1}$ should be present and this was not the case here. Nevertheless, a contamination of cytoplasmatic residues during the extraction process by phosphate group from RNA and RNA itself can be possible. While this seems unlikely the use of RNase, a ribonuclease inhibitor, as an aggregating compound for precipitation in the extraction procedure may solve these peaks and/or extraction solely based on differential centrifugation without Percoll could be tried to fully resolve the assignments. Differential centrifugation will however significantly increase the required time for extraction and possibly not yield very highly purified membranes. The other main differences between membranes for the low wavenumber region were putatively assigned to triglycerides with a peak at

1073 $cm^{-1}$ and fatty acids at 1130 $cm^{-1}$ with an increased Raman intensity for control membranes. The peak at 1331 $cm^{-1}$ associated to phospholipids was missing in HD membranes with an increased intensity at 1454 $cm^{-1}$ for the control possibly corroborating the hypothesis of phospholipids dysregulation in HD membranes. Regarding protein bands there was not a very pronounced difference in amides type III, but for amide type I the overall intensity in the 1610 to 1690 $cm^{-1}$ region was increased for control fibroblast. There was also a peak for type I at 1685 $cm^{-1}$ in control membranes and this peak was not present in HD membranes. Overall in this low wavenumber region the control fibroblast membranes present higher Raman intensity across the spectrum with peaks putatively associated to cholesterol, phospholipids and proteins in the form of amide type I with a possible triglycerides contribution. The higher wavenumber region, from 2700 to 3200 $cm^{-1}$, was less informative in terms of discrimination between the two membranes. The PLS model presented a low percentage of discrimination between membrane types and the assignment of the peaks was less elucidating in determining attributes specifically related to sub-cellular structures related to two membranes.

## 8.6 Microscopy analysis of C2C12 and GFP-fibroblast plasma membrane.

### 8.6.1 SEM analysis of plasma membranes

In order to explain the dielectric separation between cells of similar size C2C12 and GFP-fibroblasts were analysed by SEM microscopy. The analysis by SEM microscopy revealed a quite significant difference between the plasma membrane structure and microvillation between C2C12 and GFP-fibroblasts.

The images were taken as described in Materials and Methods and they were post processed to enhance the colour of the microvilli. C2C12 were colourised in blue and GFP-fibroblast in green with red microvilli structures for both cell types. In *Figure 7-24* C2C12 and GFP-fibroblasts are shown with the same reference scale of 5μm in order to present the visible difference in the microvilli landscape between these two

cell types. In *Figure 7-25* (left hand side) SEM pictures were taken of C2C12 and GFP-fibroblast in attached state on coverslips glass in order to appreciate differences in phenotype between the two cells types. More details about the microvilli in GFP-fibroblast and C2C12 are shown in *Figure 7-26* at a higher magnification.

Regarding the cell size the SEM pictures confirmed the results shown by flow cytometry as indicated in section *8.3*. The diameter was determined to be on average very similar between C2C12 and GFP-fibroblast in suspension. This was an important confirmation of cell size and plasma membrane landscape due to the microvilli present on the cell. In contrast, cells measured in aqueous suspension have larger diameter as reported in section *8.3.3*. This presents an important point regarding careful consideration of the osmolarity of the suspending medium for not only counting cells but also more importantly for DEP sorting.

On average, the microvilli structures were more pronounced in GFP-fibroblasts than in C2C12 by visual analysis of the SEM pictures collected for this analysis. This implies that the folding factor $\phi_m$ in *Equation 4-11* will be different between the two cells types with correlated differences in permittivity of the plasma membrane. This visual assessment of the smoothness of the cells could be used tentatively to assign values of $\phi_m$. As shown in *Figure 7-26* the microvilli are more elongated in GFP-fibroblasts than in C2C12, with the plasma membrane smoother with few spherical protrusionsin C2C12. Although a precise estimate of the folding factor, $\phi_m$, remains difficult, a variation in the surface area to volume ratio is apparent. GFP-fibroblasts present more surface area of C2C12 due their microvilli landscape. A more precise simulation regarding the presence of microvilli on the cell plasma membrane is provided by Asami [18]. These results in conjunction with the Raman results further validate the hypothesis of changes in membrane capacitance due to the folding factor and permittivity. These probably are the major causative factors for differences in cross-over frequencies between C2C12 and GFP-fibroblats as indicated by MATLAB modelling *Figure 7-8*.

### 8.6.2 TEM analysis of plasma membranes

*Figure 7-27* shows a representative image of the thickness of the plasma membrane in C2C12, with a range between approximately 5 to 8 nm. The resolution may be improved with a more powerful microscope and different staining procedure however, this range thickness was present in all the batches of C2C12 and GFP-fibroblasts examined.

As describe in section *2.3.5* and *4.6*, the thickness of the plasma membrane may vary due to the presence of cholesterol and proteins but this variation maybe too small to by microscopically analysed by TEM. Although differences are present on an atomic level due to saturation of the lipids content, as indicated by the Raman results, an exact quantification of the thickness remain difficult by TEM analysis.

Microvilli presence and structure are further confirmed in *Figure 7-28* (red arrows) by detached entities/structures due to the cutting procedure for imaging as describe in Materials and Methods. Folding is also evident in the plasma membrane in *Figure 7-29* by the red dotted circle in GFP-fibroblasts.

The last cell type examined were myotubes as indicated in *Figure 7-30*. Here it is noticeable that a double nuclear envelop is present and this is due to the polynuclear nature of the myotubes and the 60nm cutting of the sample. The plasma membrane thickness in this cell type, for the all experiment was very similar to the range thickness of the C2C12 and GFP-fibroblasts.

From the results here presented, it can be hypothesised that variations of plasma membrane thickness exist due to the levels of lipids saturation, which relate to the permittivity ($\varepsilon_m$) of the plasma membrane. TEM analysis enable to further verify the microvilli structure of the cell's plasma membrane however, visual assessment of the membrane thickness has been proven difficult (see *Appendix D*) for other experiments).

## 8.7 Final conclusions and further work

This thesis has presented a novel application of a dielectrophoretic micro system and the implementations of a chemical analytical technique in the form of Raman spectroscopy for biomedical and biochemical cell based applications. The implementation of these technology and techniques involves the solving of several technical and biochemical issues. As results, the work here presented, has used a multidisciplinary approach in studying and applying DEP and Raman spectroscopy within the field of biochemistry and regenerative medicine.

The results showed high levels of separation in mixed cultures of C2C12 myoblast and terminal differentiated myotubes. The same high levels of purity were achieved by DEP separation in similar sized cells such as C2C12 and GFP-fibroblasts when co-cultured. In order to further investigate the reasons for DEP separation of similar size cells chemical analysis of the plasma membrane was performed in extracted plasma membranes from C2C12 and GFP-fibroblasts. This showed a difference in the level of lipids saturation between the two cell types. These results have implications regarding the thickness and permittivity of the plasma membrane that determine differences in membrane capacitance between C2C12 and GFP-fibroblats.

The chemical analysis of the plasma membrane prompted the investigation of the membrane characteristics in other cells types that could be amenable for DEP sorting. This led to the chemical Raman analysis of the plasma membrane in Huntington affected peripheral fibroblastic cells. The results from this investigation showed that the plasma membrane of peripheral fibroblastic cells is a novel biomarker for the disease. However, for the time allocated for this work, DEP experiments could not be carried out with fibroblasts affected by Huntington's disease but the possibility to separate these cells by DEP is feasible.

The work here presented may set a starting point for possible further research in the characterisation of amenable cell properties that could be further exploited using DEP with important implication in several fields of biological research.

Due to their non-invasive and tag free nature, DEP and Raman spectroscopy present interesting capabilities in exploring biological and biochemical problems. By combining DEP and Raman analysis, as forms of biophysical techniques in characterisation and purification of cells affected by Huntington's disease or other neuropathology, is possible to envisage further work within the field of neurobiology and medicine.

Specifically is the author interest to develop a Lab-on-chip system for neuronal micropatterning to gather electrophysiological response of neurons affected by neurodegenerative diseases. Preliminary results has been already gather (not presented in the thesis) in pheochromocytoma cells regarding clues about the electrical signal carrying mechanisms due to possible changes in biochemical characteristics between normal and cells affected by neurodegeneration. DEP is here envisage as a biophysical tool to purify mix populations of cells that present variations in there dielectric response due to change in polarisability and chemical conformation. Purification of cells, from a mixed population, that present very similar characteristics, may be very advantageous in addressing biochemical and chemical characteristics of the cells that can give more clues about the physiology of cells affected by neurodegeneration. This in conjunction with a spectroscopic Raman analysis may produce some new founding on the biochemistry of neurodegeneration.

In conclusion, the application of DEP with the increase accessibility and cost efficiency of Lab-on-chip device represent a very interesting technology with a multitude of possible applications in biology and medicine.

# Appendixes

## Appendix A Publications

1. **M. Muratore**, V. Srsen, M. Waterfall, A. Downes and R. Pethig, *Biomarker-free dielectrophoretic sorting of differentiating myoblast multipotent cells and their membrane analysis by Raman spectroscopy*. Biomicrofluidics 6 (3), 034113 (2012)

2. **M.Muratore**, *Raman spectroscopy and partial least squares analysis in discrimination of peripheral cells affected by Huntington's disease,* Analytica Chimica Acta Volume 793, 2 September 2013, Pages 1-10, ISSN 0003-2670.The paper has been selected as the a feature article of the journal for the September 2013 front cover.

3. **M.Muratore**, S. Mitchell and M.Waterfall. *Plasma membrane characterization, by scanning electron microscopy, of multipotent myoblasts-derived populations sorted using dielectrophoresis*. Volume 438, Issue 4, 6 September 2013, Pages 666-672, ISSN 0006-291X

4. **M.Muratore**, V Bertola, M,D Haw, *Drop impact of a concentrated colloidal suspension*, Proceedings of the DIPSI Workshop 2011. Droplet Impact Phenomena & Spray Investigations (pp.46-50).

5. R. Mouras ; P. Bagnaninchi ; A. Downes ; **M. Muratore** ; A. Elfick; *Nonlinear optical microscopy of adipose-derived stem cells induced towards osteoblasts and adipocytes.* Proc. SPIE 8086, Advanced Microscopy Techniques II, 80860Q (June 08, 2011); doi:10.1117/12.889780.

# Appendix B Cell counts

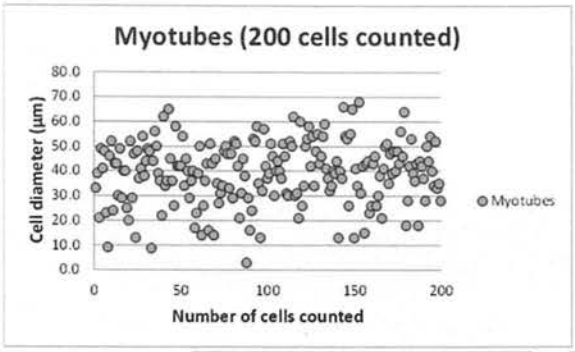


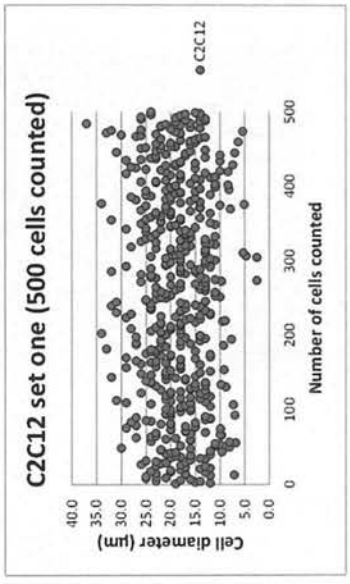


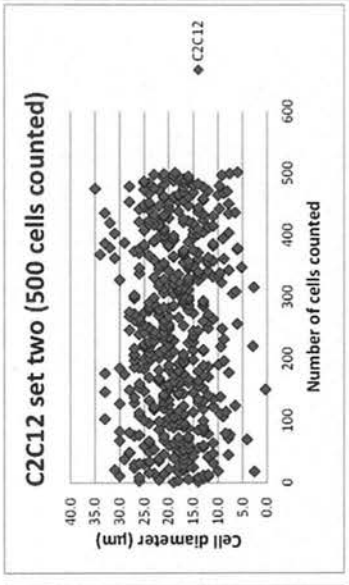


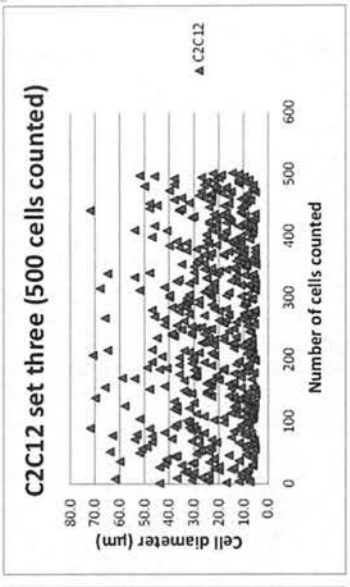


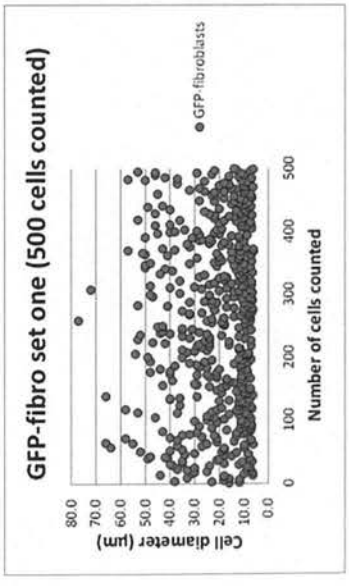


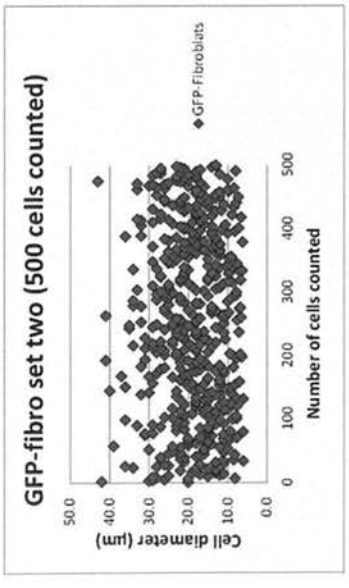


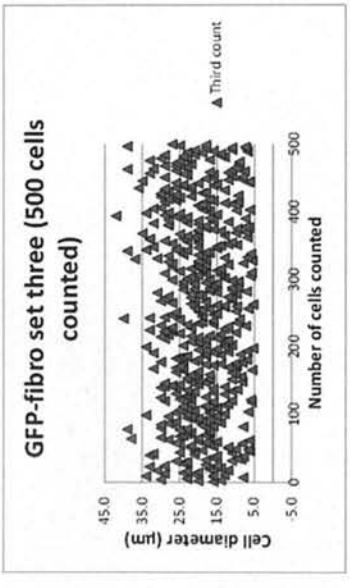

*Appendix B Cell counts. Representative counts for C2C12 GFP-fibroblasts and myotubes. The average and standard deviations are shown in table below*

| Cell count for suspensions | Set 1 | | Set 2 | | Set 3 | |
|---|---|---|---|---|---|---|
| | Average | SD | Average | SD | Average | SD |
| C2C12 | 18.5 | 5.8 | 18.7 | 6.0 | 22.5 | 14.6 |
| GFP-fibroblasts | 21.7 | 14.0 | 18.9 | 7.4 | 19.6 | 7.6 |
| Myotubes | 39.3 | 12.6 | | | | |

## Appendix C Reversine traetments

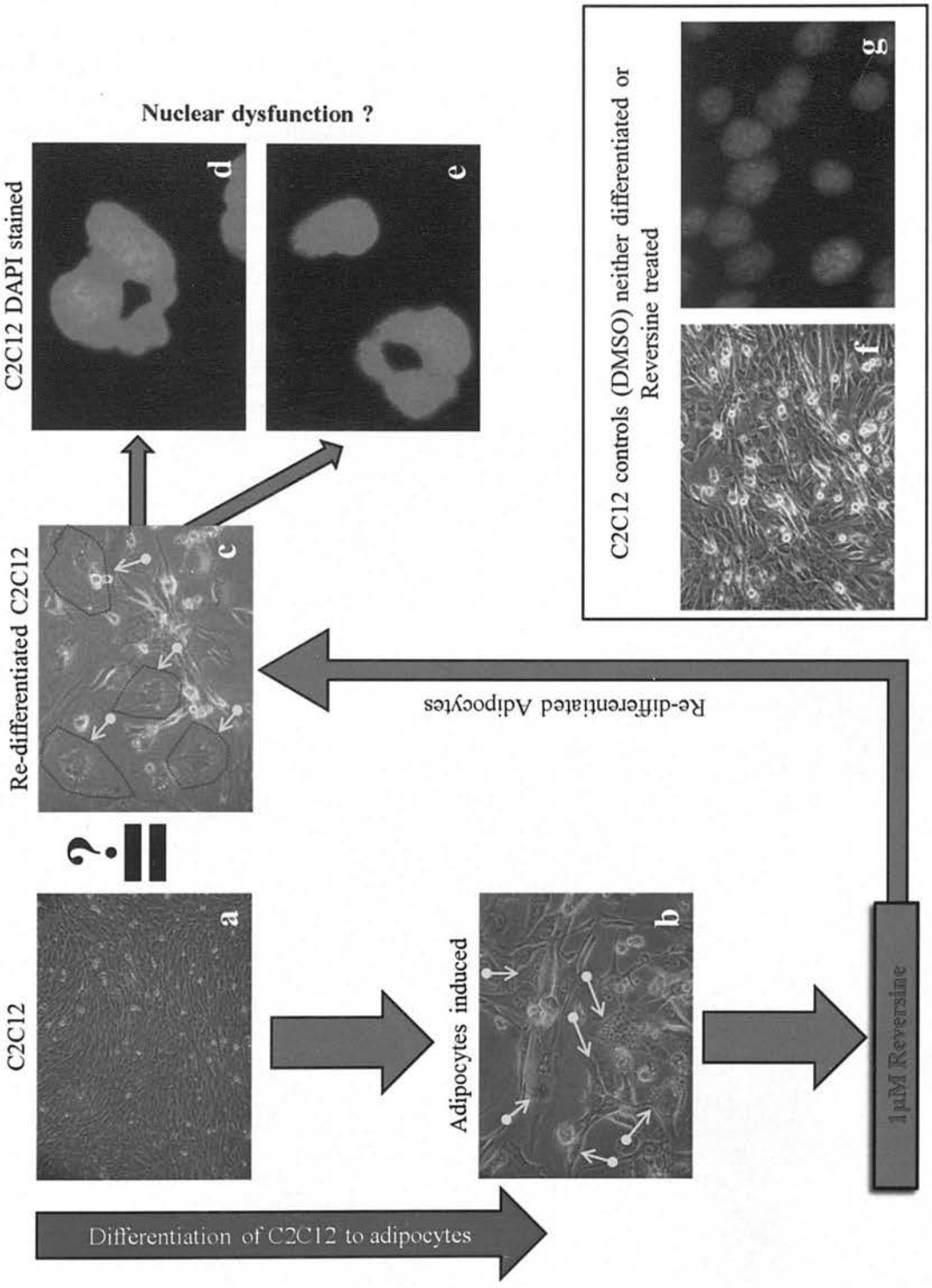


*Appendix C. C2C12 differentiation and de-differentiation using 1μM Reversine. a) indicate the C2C12 culture before induction in adipocytes (as described in Materials*

*and Methods ) b) The induced adipocytes with lipids vesicles/droplets inside cytoplasm indicated by yellow arrows. c) Adipocytes after treatment with 1μM Reversine (7 days treatment) the morphology of the cells is indicated by red dotted shapes and yellow arrows indicate the position of the cell. The phenotype is changed in a wide spread shapes d) Nuclear morphology changed in de-differentiated C2C12 also indicated in figure e. f) C2C12 controls treated with DMSO instead of 1μM Reverine the shape is characteristic of C2C12 and the nucleus present normal morphology (picture g).*

## Appendix D Freeze fracture

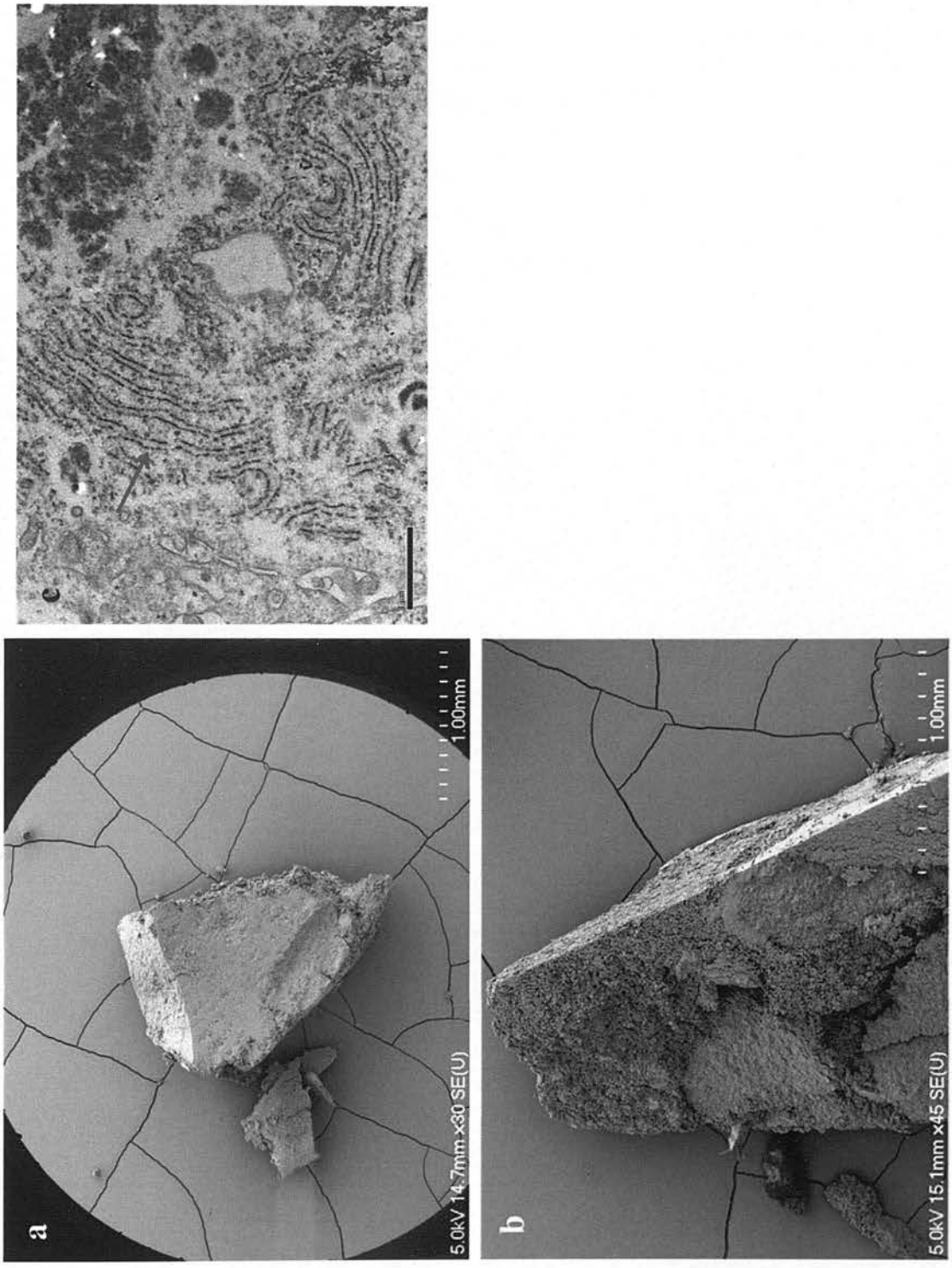


*Appendix D Several attempt in verify membrane thickness were made in particular SEM freeze fracture was tried in two occasions but in both instances there was not*

*clear breakage that could be image by SEM as shown in picture a and b. The pellet containing cells is shown in a and b at low magnification with the cutting planes exposed. Picture c shows the endoplasmic reticulum (indicated by red arrows) of GFP-fibroblasts using TEM. Although was possible to visualise the endoplasmic reticulum with the staining procedure described in Materials and Methods the thickness of the plasma membrane remained difficult to evaluate.*

## Appendix E Cell viability

Customised DEP medium was formulated to account for 330 mOsm/kg in osmolarity and 120 mS/m conductivity. To verify viability of cells in the DEP medium cell were cultured for three days. The initial number of cells was verified by haemocytometer and aliquots were counted every approximately six hours for viability over three days period The total lost in three days period was, from the initial population, of 21.5% and 16.0% for C2C12 and GFP-fibroblasts respectively as indicated in graph below.

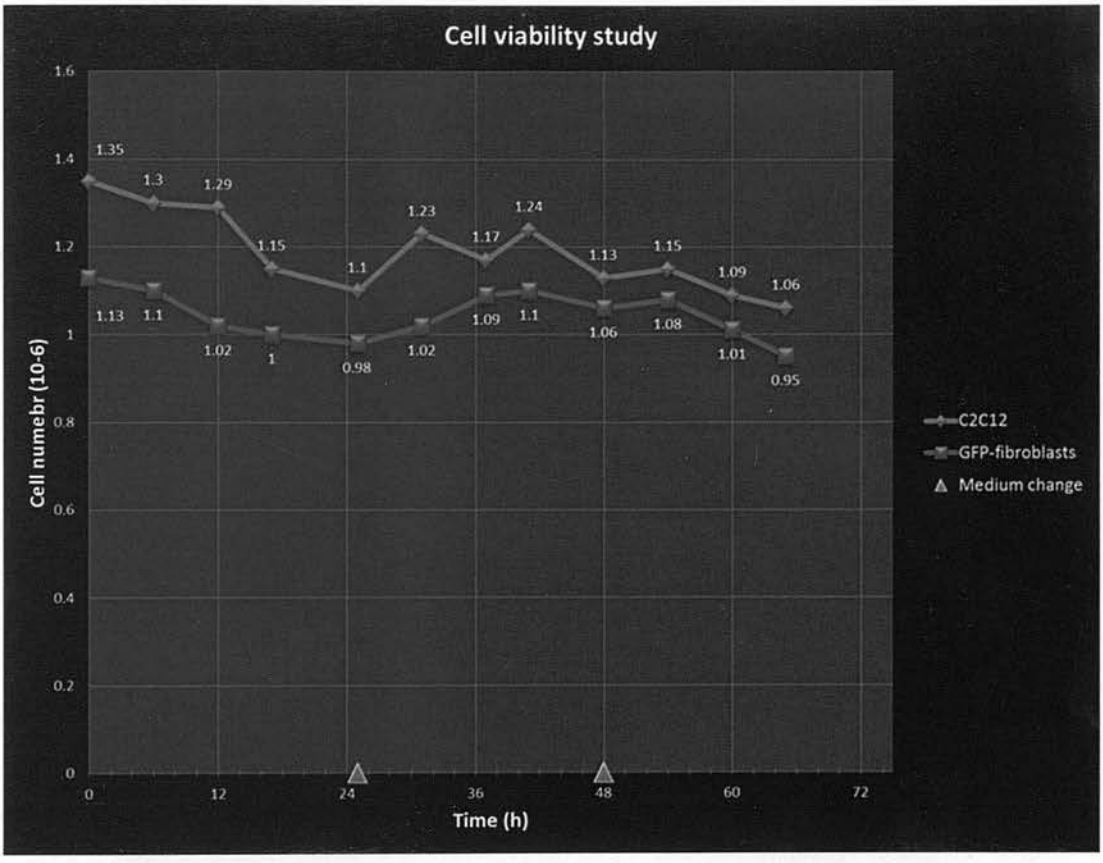


*Appendix E Cell count for viability in DEP medium over 72 hours (three days period)*

# References

[1] A. Ramos, Electrokinetics and electrohydrodynamics in microsystems, SpringerWienNewYork, Vienna ; New York, 2011.

[2] M.P. Hughes, Nanoelectromechanics in engineering and biology, CRC Press, Boca Raton, Fla.; London, 2003.

[3] D. Griffiths, Introduction to Electrodynamics (3rd Edition), Benjamin Cummings, 1998.

[4] T.B. Jones, Electromechanics of Particles, Cambridge University Press, 1995.

[5] R. Hunter, Foundations of colloid science, Oxford University Press, 2001.

[6] J. Voldman, Electrical Forces For Microscale Cell Manipulation, Annual Review of Biomedical Engineering 8 (2006) 425-454.

[7] L.D. Landau, L.P. Pitaevskii, E.M. Lifshitz, Electrodynamics of Continuous Media, Second Edition: Volume 8 (Course of Theoretical Physics), Butterworth-Heinemann, 1984.

[8] R. Pethig, Review Article---Dielectrophoresis: Status of the theory, technology, and applications, Biomicrofluidics 4 (2010) 022811.

[9] M. Washizu, T.B. Jones, Multipolar dielectrophoretic force calculation, Journal of Electrostatics 33 (1994) 187-198.

[10] W.B. Russel, D.A. Saville, W.R. Schowalter, Colloidal Dispersions (Cambridge Monographs on Mechanics), Cambridge University Press, 1992.

[11] P.R.C. Gascoyne, J. Vykoukal, Particle separation by dielectrophoresis, ELECTROPHORESIS 23 (2002) 1973-1983.

[12] H. Morgan, N.G. Green, AC electrokinetics: colloids and nanoparticles, Research Studies Press, 2003.

[13] Y. Huang, R. Holzel, R. Pethig, B.W. Xiao, Differences in the AC electrodynamics of viable and non-viable yeast cells determined through

combined dielectrophoresis and electrorotation studies, Physics in Medicine and Biology 37 (1992) 1499.

[14] R. Pethig, L.M. Jakubek, R.H. Sanger, E. Heart, E.D. Corson, P.J. Smith, Electrokinetic measurements of membrane capacitance and conductance for pancreatic beta-cells, IEE proceedings. Nanobiotechnology 152 (2005) 189-193.

[15] Y. Huang, X.-B. Wang, F.F. Becker, P.R.C. Gascoyne, Membrane changes associated with the temperature-sensitive P85gag-mos-dependent transformation of rat kidney cells as determined by dielectrophoresis and electrorotation, Biochimica et Biophysica Acta (BBA) - Biomembranes 1282 (1996) 76-84.

[16] X. Wang, F.F. Becker, P.R.C. Gascoyne, Membrane dielectric changes indicate induced apoptosis in HL-60 cells more sensitively than surface phosphatidylserine expression or DNA fragmentation, Biochimica et Biophysica Acta (BBA) - Biomembranes 1564 (2002) 412-420.

[17] R. Pethig, M.S. Talary, Dielectrophoretic detection of membrane morphology changes in Jurkat T-cells undergoing etoposide-induced apoptosis, IET Nanobiotechnology 1 (2007) 2-9.

[18] K. Asami, Dielectric properties of microvillous cells simulated by the three-dimensional finite-element method, Bioelectrochemistry 81 (2011) 28-33.

[19] K. Asami, Y. Takahashi, S. Takashima, Dielectric properties of mouse lymphocytes and erythrocytes, Biochimica et Biophysica Acta (BBA) - Molecular Cell Research 1010 (1989) 49-55.

[20] S. Takashima, K. Asami, Y. Takahashi, Frequency domain studies of impedance characteristics of biological cells using micropipet technique. I. Erythrocyte, Biophysical Journal 54 (1988) 995-1000.

[21] H. Yoshihito, O. Ikuya, K. Yoichi, O. Shinji, Y. Akio, A. Koji, Dielectric inspection of erythrocyte morphology, Physics in Medicine and Biology 53 (2008) 2553.

[22] A. Irimajiri, K. Asami, T. Ichinowatari, Y. Kinoshita, Passive electrical properties of the membrane and cytoplasm of cultured rat basophil leukemia cells. II. Effects of osmotic perturbation, Biochimica et Biophysica Acta (BBA) - Biomembranes 896 (1987) 214-223.

[23] F.H. Labeed, H.M. Coley, M.P. Hughes, Differences in the biophysical properties of membrane and cytoplasm of apoptotic cells revealed using dielectrophoresis, Biochimica et Biophysica Acta (BBA) - General Subjects 1760 (2006) 922-929.

[24] X.-B. Wang, Y. Huang, P.R.C. Gascoyne, F.F. Becker, R. Hölzel, R. Pethig, Changes in Friend murine erythroleukaemia cell membranes during induced differentiation determined by electrorotation, Biochimica et Biophysica Acta (BBA) - Biomembranes 1193 (1994) 330-344.

[25] C. Huang, A. Chen, L. Wang, M. Guo, J. Yu, Electrokinetic measurements of dielectric properties of membrane for apoptotic HL-60 cells on chip-based device, Biomedical Microdevices 9 (2007) 335-343.

[26] M. Muratore, V. Srsen, M. Waterfall, A. Downes, R. Pethig, Biomarker-free dielectrophoretic sorting of differentiating myoblast multipotent progenitor cells and their membrane analysis by Raman spectroscopy, Biomicrofluidics 6 (2012) 034113.

[27] D. Zimmermann, A. Zhou, M. Kiesel, K. Feldbauer, U. Terpitz, W. Haase, T. Schneider-Hohendorf, E. Bamberg, V.L. Sukhorukov, Effects on capacitance by overexpression of membrane proteins, Biochemical and Biophysical Research Communications 369 (2008) 1022-1026.

[28] K. Park, J. Jang, D. Irimia, J. Sturgis, J. Lee, J.P. Robinson, M. Toner, R. Bashir, 'Living cantilever arrays' for characterization of mass of single live cells in fluids, Lab on a Chip 8 (2008) 1034-1041.

[29] M. Dürr, J. Kentsch, T. Müller, T. Schnelle, M. Stelzle, Microdevices for manipulation and accumulation of micro- and nanoparticles by dielectrophoresis, ELECTROPHORESIS 24 (2003) 722-731.

[30] H. Suzuki, H. Chih-Ming, N. Kasagi, A chaotic mixer for magnetic bead-based micro cell sorter, Microelectromechanical Systems, Journal of 13 (2004) 779-790.

[31] K.H. Kang, X. Xuan, Y. Kang, D. Li, Effects of dc-dielectrophoretic force on particle trajectories in microchannels, Journal of Applied Physics 99 (2006) 064702.

[32] K.H. Kang, Y. Kang, X. Xuan, D. Li, Continuous separation of microparticles by size with Direct current-dielectrophoresis, ELECTROPHORESIS 27 (2006) 694-702.

[33] S. Burgarella, S. Merlo, B. Dell'Anna, G. Zarola, M. Bianchessi, A modular micro-fluidic platform for cells handling by dielectrophoresis, Microelectronic Engineering 87 (2010) 2124-2133.

[34] I.-F. Cheng, H.-C. Chang, D. Hou, H.-C. Chang, An integrated dielectrophoretic chip for continuous bioparticle filtering, focusing, sorting, trapping, and detecting, Biomicrofluidics 1 (2007) 021503.

[35] S. Fiedler, S.G. Shirley, T. Schnelle, G. Fuhr, Dielectrophoretic Sorting of Particles and Cells in a Microsystem, Analytical Chemistry 70 (1998) 1909-1915.

[36] X. Hu, P.H. Bessette, J. Qian, C.D. Meinhart, P.S. Daugherty, H.T. Soh, Marker-specific sorting of rare cells using dielectrophoresis, Proceedings of the National Academy of Sciences of the United States of America 102 (2005) 15757-15761.

[37] U. Kim, J. Qian, S.A. Kenrick, P.S. Daugherty, H.T. Soh, Multitarget Dielectrophoresis Activated Cell Sorter, Analytical Chemistry 80 (2008) 8656-8661.

[38] T. Müller, G. Gradl, S. Howitz, S. Shirley, T. Schnelle, G. Fuhr, A 3-D microelectrode system for handling and caging single cells and particles, Biosensors and Bioelectronics 14 (1999) 247-256.

[39] A.J. Goldman, R.G. Cox, H. Brenner, Slow viscous motion of a sphere parallel to a plane wall—II Couette flow, Chemical Engineering Science 22 (1967) 653-660.

[40] H. Li, R. Bashir, On the Design and Optimization of Micro-Fluidic Dielectrophoretic Devices: A Dynamic Simulation Study, Biomedical Microdevices 6 (2004) 289-295.

[41] Y. Huang, X.B. Wang, F.F. Becker, P.R. Gascoyne, Introducing dielectrophoresis as a new force field for field-flow fractionation, Biophysical Journal 73 (1997) 1118-1129.

[42] P. Stephen Williams, S. Lee, J. Calvin Giddings, Characterization of hydrodynamic lift forces by field-flow fractionation inertial and near-wall lift forces, Chemical Engineering Communications 130 (1994) 143-166.

[43] X.-B. Wang, J. Vykoukal, F.F. Becker, P.R.C. Gascoyne, Separation of Polystyrene Microbeads Using Dielectrophoretic/Gravitational Field-Flow-Fractionation, Biophysical Journal 74 (1998) 2689-2701.

[44] D.H. Boal, Mechanics of the cell, Cambridge University Press, Cambridge [ETC.], 2012.

[45] B. Alberts, A. Johnson, J. Lewis, M. Raff, K. Roberts, P. Walter, Molecular Biology of the Cell, fourth edition, Garland Science, 2002.

[46] J.M. Berg, J.L. Tymoczko, L. Stryer, Biochemistry, W. H. Freeman & Co Ltd, 2007.

[47] H. Lodish, A. Berk, C. Kaiser, M. Krieger, M. Scott, A. Bretscher, H. Ploegh, P. Matsudaira, Molecular Cell Biology (Lodish, Molecular Cell Biology), W. H. Freeman, 2007.

[48] D.E. Vance, J.E. Vance, Biochemistry of lipids, lipoproteins, and membranes, Elsevier, Amsterdam ; Boston, 2002.

[49] E. Fahy, S. Subramaniam, H.A. Brown, C.K. Glass, A.H. Merrill Jr, R.C. Murphy, C.R.H. Raetz, D.W. Russell, Y. Seyama, W. Shaw, T. Shimizu, F. Spener, G. Van Meer, M.S. VanNieuwenhze, S.H. White, J.L. Witztum, E.A. Dennis, A comprehensive classification system for lipids, Journal of Lipid Research 46 (2005) 839-861.

[50] N.E. Braverman, A.B. Moser, Functions of plasmalogen lipids in health and disease, Biochimica et Biophysica Acta (BBA) - Molecular Basis of Disease 1822 (2012) 1442-1452.

[51] N. Nagan, R.A. Zoeller, Plasmalogens: biosynthesis and functions, Progress in Lipid Research 40 (2001) 199-229.

[52] P. Brites, H.R. Waterham, R.J.A. Wanders, Functions and biosynthesis of plasmalogens in health and disease, Biochimica et Biophysica Acta (BBA) - Molecular and Cell Biology of Lipids 1636 (2004) 219-231.

[53] X. Han, D.M. Holtzman, D.W. McKeel Jr, Plasmalogen deficiency in early Alzheimer's disease subjects and in animal models: Molecular characterization using electrospray ionization mass spectrometry, Journal of Neurochemistry 77 (2001) 1168-1180.

[54] B. Maggio, M.L. Fanani, C.M. Rosetti, N. Wilke, Biophysics of sphingolipids II. Glycosphingolipids: An assortment of multiple structural information transducers at the membrane surface, Biochimica et Biophysica Acta (BBA) - Biomembranes 1758 (2006) 1922-1944.

[55] C.J. Clarke, C.F. Snook, M. Tani, N. Matmati, N. Marchesini, Y.A. Hannun, The Extended Family of Neutral Sphingomyelinases, Biochemistry 45 (2006) 11247-11256.

[56] K. Simons, D. Toomre, Lipid rafts and signal transduction, Nat Rev Mol Cell Biol 1 (2000) 31-39.

[57] R.G. Parton, Caveolae and caveolins, Current Opinion in Cell Biology 8 (1996) 542-548.

[58] E.J. Smart, G.A. Graf, M.A. McNiven, W.C. Sessa, J.A. Engelman, P.E. Scherer, T. Okamoto, M.P. Lisanti, Caveolins, Liquid-Ordered Domains, and Signal Transduction, Molecular and Cellular Biology 19 (1999) 7289-7304.

[59] J.E. Darnell, H.F. Lodish, Molecular cell biology, Scientific American Books : Distributed by W.H. Freeman and Co., New York, 1995.

[60] S.J. Singer, G.L. Nicolson, The Fluid Mosaic Model of the Structure of Cell Membranes, Science 175 (1972) 720-731.

[61] D.A. Brown, E. London, Function of lipids rafts in biological membranes, Annual Review of Cell and Developmental Biology 14 (1998) 111-136.

[62] M.B. Sankaram, T.E. Thompson, Interaction of cholesterol with various glycerophospholipids and sphingomyelin, Biochemistry 29 (1990) 10670-10675.

[63] J. Malinsky, M. Opekarová, G. Grossmann, W. Tanner, Membrane Microdomains, Rafts, and Detergent-Resistant Membranes in Plants and Fungi, Annual Review of Plant Biology 64 (2013) 501-529.

[64] A.D. Dupuy, D.M. Engelman, Protein area occupancy at the center of the red blood cell membrane, Proceedings of the National Academy of Sciences 105 (2008) 2848-2852.

[65] D.A. Brown, J.K. Rose, Sorting of GPI-anchored proteins to glycolipid-enriched membrane subdomains during transport to the apical cell surface, Cell 68 (1992) 533-544.

[66] K. Simons, E. Ikonen, Functional rafts in cell membranes, Nature 387 (1997) 569-572.

[67] K. Simons, G. van Meer, Lipid sorting in epithelial cells, Biochemistry 27 (1988) 6197-6202.

[68] E.K. Fridriksson, P.A. Shipkova, E.D. Sheets, D. Holowka, B. Baird, F.W. McLafferty, Quantitative Analysis of Phospholipids in Functionally Important Membrane Domains from RBL-2H3 Mast Cells Using Tandem High-Resolution Mass Spectrometry†, Biochemistry 38 (1999) 8056-8063.

[69] R. Schroeder, E. London, D. Brown, Interactions between saturated acyl chains confer detergent resistance on lipids and glycosylphosphatidylinositol (GPI)-anchored proteins: GPI-anchored proteins in liposomes and cells show similar behavior, Proceedings of the National Academy of Sciences 91 (1994) 12130-12134.

[70] A. Pralle, P. Keller, E.-L. Florin, K. Simons, J.K.H. Hörber, Sphingolipid–Cholesterol Rafts Diffuse as Small Entities in the Plasma Membrane of Mammalian Cells, The Journal of Cell Biology 148 (2000) 997-1008.

[71] T. Friedrichson, T.V. Kurzchalia, Microdomains of GPI-anchored proteins in living cells revealed by crosslinking, Nature 394 (1998) 802-805.

[72] C. Eggeling, C. Ringemann, R. Medda, G. Schwarzmann, K. Sandhoff, S. Polyakova, V.N. Belov, B. Hein, C. von Middendorff, A. Schonle, S.W. Hell, Direct observation of the nanoscale dynamics of membrane lipids in a living cell, Nature 457 (2009) 1159-1162.

[73] A. Kusumi, C. Nakada, K. Ritchie, K. Murase, K. Suzuki, H. Murakoshi, R.S. Kasai, J. Kondo, T. Fujiwara, Paradigm shift of the plasma membrane concept from the two-dimensional continuum fluid to the partitioned fluid: High-Speed Single-Molecule Tracking of Membrane Molecules, Annual Review of Biophysics and Biomolecular Structure 34 (2005) 351-378.

[74] T. Harder, P. Scheiffele, P. Verkade, K. Simons, Lipid Domain Structure of the Plasma Membrane Revealed by Patching of Membrane Components, The Journal of Cell Biology 141 (1998) 929-942.

[75] B.S. Wilson, J.R. Pfeiffer, J.M. Oliver, Observing Fcεri Signaling from the Inside of the Mast Cell Membrane, The Journal of Cell Biology 149 (2000) 1131-1142.

[76] K. Jacobson, O.G. Mouritsen, R.G.W. Anderson, Lipid rafts: at a crossroad between cell biology and physics, Nat Cell Biol 9 (2007) 7-14.

[77] M. Leslie, Do Lipid Rafts Exist?, Science 334 (2011) 1046-1047.

[78] N.M. Hooper, Detergent-insoluble glycosphingolipid/cholesterol-rich membrane domains, lipid rafts and caveolae (review), Mol Membr Biol 16 (1999) 145-156.

[79] M.D. Resh, Fatty acylation of proteins: new insights into membrane targeting of myristoylated and palmitoylated proteins, Biochimica et Biophysica Acta (BBA) - Molecular Cell Research 1451 (1999) 1-16.

[80] A. Rietveld, S. Neutz, K. Simons, S. Eaton, Association of Sterol- and Glycosylphosphatidylinositol-linked Proteins with Drosophila Raft Lipid Microdomains, Journal of Biological Chemistry 274 (1999) 12049-12054.

[81] U. Vogel, K. Sandvig, B. van Deurs, Expression of caveolin-1 and polarized formation of invaginated caveolae in Caco-2 and MDCK II cells, Journal of Cell Science 111 (1998) 825-832.

[82] R.G. Parton, M. Way, N. Zorzi, E. Stang, Caveolin-3 Associates with Developing T-tubules during Muscle Differentiation, The Journal of Cell Biology 136 (1997) 137-154.

[83] T.V. Kurzchalia, R.G. Partan, Membrane microdomains and caveolae, Current Opinion in Cell Biology 11 (1999) 424-431.

[84] A. Kusumi, Y. Sako, M. Yamamoto, Confined lateral diffusion of membrane receptors as studied by single particle tracking (nanovid microscopy). Effects of calcium-induced differentiation in cultured epithelial cells, Biophysical Journal 65 (1993) 2021-2040.

[85] J.F. Nagle, S. Tristram-Nagle, Structure of lipid bilayers, Biochimica et Biophysica Acta (BBA) - Reviews on Biomembranes 1469 (2000) 159-195.

[86] T.J. McIntosh, A. Vidal, S.A. Simon, Sorting of Lipids and Transmembrane Peptides Between Detergent-Soluble Bilayers and Detergent-Resistant Rafts, Biophysical Journal 85 (2003) 1656-1666.

[87] B.A. Lewis, D.M. Engelman, Lipid bilayer thickness varies linearly with acyl chain length in fluid phosphatidylcholine vesicles, Journal of Molecular Biology 166 (1983) 211-217.

[88] C. Tanford, The Hydrophobic Effect: Formation of Micelles and Biological Membranes, Wiley, 1980.

[89] R. Goetz, G. Gompper, R. Lipowsky, Mobility and Elasticity of Self-Assembled Membranes, Physical Review Letters 82 (1999) 221-224.

[90] R. Goetz, R. Lipowsky, Computer simulations of bilayer membranes: Self-assembly and interfacial tension, The Journal of Chemical Physics 108 (1998) 7397-7409.

[91] U. Lei, P.-H. Sun, R. Pethig, Refinement of the theory for extracting cell dielectric properties from dielectrophoresis and electrorotation experiments, Biomicrofluidics 5 (2011) 044109, doi:http://dx.doi.org/10.1063/1.3659282 .

[92] F.H. Labeed, J. Lu, H.J. Mulhall, S.A. Marchenko, K.F. Hoettges, L.C. Estrada, A.P. Lee, M.P. Hughes, L.A. Flanagan, Biophysical Characteristics Reveal Neural Stem Cell Differentiation Potential, PLoS ONE 6 (2011) e25458.

[93] A. Downes, R. Mouras, P. Bagnaninchi, A. Elfick, Raman spectroscopy and CARS microscopy of stem cells and their derivatives, Journal of Raman Spectroscopy 42 (2011) 1864-1870.

[94] I. Notingher, I. Bisson, A.E. Bishop, W.L. Randle, J.M.P. Polak, L.L. Hench, In Situ Spectral Monitoring of mRNA Translation in Embryonic Stem Cells during Differentiation in Vitro, Analytical Chemistry 76 (2004) 3185-3193.

[95] J.W. Chan, D.K. Lieu, T. Huser, R.A. Li, Label-Free Separation of Human Embryonic Stem Cells and Their Cardiac Derivatives Using Raman Spectroscopy, Analytical Chemistry 81 (2009) 1324-1331.

[96] I.-F. Cheng, H.-C. Chang, D. Hou, H.-C. Chang, An integrated dielectrophoretic chip for continuous bioparticle filtering, focusing, sorting, trapping, and detecting, Biomicrofluidics 1 (2007) -.

[97] H. Haken, H.C. Wolf, Molecular Physics and Elements of Quantum Chemistry: Introduction to Experiments and Theory, Springer, 2004.

[98] J.R. Ferraro, K. Nakamoto, Introductory Raman Spectroscopy, Elsevier Science, 1994.

[99] D.A. Long, Raman spectroscopy, McGraw-Hill International Book Company, 1977.

[100] J.M. Hollas, Modern Spectroscopy, Wiley, 2004.

[101] M. Diem, Introduction to modern vibrational spectroscopy, Wiley, 1993.

[102] P.R. Carey, Biochemical applications of Raman and resonance Raman spectroscopies, Academic Press, 1982.

[103] G.M. Barrow, Introduction to Molecular Spectroscopy, McGraw-Hill, 1988.

[104] P. Larkin, Infrared and Raman Spectroscopy; Principles and Spectral Interpretation, Elsevier Science, 2011.

[105] L. Pauling, E.B. Wilson, Introduction to Quantum Mechanics: With Applications to Chemistry, Dover Publications, 1985.

[106] R.L. McCreery, Raman Spectroscopy for Chemical Analysis, Wiley, 2005.

[107] G. Qu, M. Sun, S. Li, C. Sun, T. Liu, S. Xu, Z. Men, Z. Li, Phase-transition induced changes in the electron–phonon coupling of all-trans-β-carotene, Spectrochimica Acta Part A: Molecular and Biomolecular Spectroscopy 104 (2013) 92-96.

[108] D.M. Morré, D.J. Morre, Aqueous two-phase partition applied to the isolation of plasma membranes and Golgi apparatus from cultured mammalian cells, Journal of Chromatography B: Biomedical Sciences and Applications 743 (2000) 377-387.

[109] P. Navas, D.D. Nowack, D.J. Morré, Isolation of Purified Plasma Membranes from Cultured Cells and Hepatomas by Two-Phase Partition and Preparative Free-Flow Electrophoresis, Cancer Research 49 (1989) 2147-2156.

[110] I.T. Jolliffe, Principal Component Analysis, Springer, 2002.

[111] S. Wold, K. Esbensen, P. Geladi, Principal component analysis, Chemometrics and Intelligent Laboratory Systems 2 (1987) 37-52.

[112] H. Hotelling, Analysis of a complex of statistical variables into principal components, 4, Warwick & York, US, 1933, pp. 417-441.

[113] H. Abdi, L.J. Williams, Principal component analysis, Wiley Interdisciplinary Reviews: Computational Statistics 2 (2010) 433-459.

[114] J.P.M. Andries, Y.V. Heyden, L.M.C. Buydens, Predictive-property-ranked variable reduction with final complexity adapted models in partial least squares modeling for multiple responses, Analytical Chemistry 85 (2013) 5444-5453.

[115] A. Höskuldsson, PLS regression methods, Journal of Chemometrics 2 (1988) 211-228.

[116] S. Wold, PLS for Multivariate Linear Modeling, QSAR: Chemometric Methods in Molecular Design; Methods and Principles in Medicinal Chemistry, Weinheim, Germany: Verlag-Chemie. (1994).

[117] S. Wold, A. Johansson, M. Cochi, ESCOM Lieden (1993) 523-550.

[118] S. Chen, S. Takanashi, Q. Zhang, W. Xiong, S. Zhu, E.C. Peters, S. Ding, P.G. Schultz, Reversine increases the plasticity of lineage-committed mammalian cells, Proceedings of the National Academy of Sciences 104 (2007) 10482-10487.

[119] D.F. Pisani, C. Cabane, B. Derijard, C.A. Dechesne, The topoisomerase 1-interacting protein BTBD1 is essential for muscle cell differentiation, Cell Death Differ 11 (2004) 1157-1165.

[120] U. Kim, C.-W. Shu, K.Y. Dane, P.S. Daugherty, J.Y.J. Wang, H.T. Soh, Selection of mammalian cells based on their cell-cycle phase using dielectrophoresis, Proceedings of the National Academy of Sciences 104 (2007) 20708-20712.

[121] X. Shen, J.M. Collier, M. Hlaing, L. Zhang, E.H. Delshad, J. Bristow, H.S. Bernstein, Genome-wide examination of myoblast cell cycle withdrawal during differentiation, Developmental Dynamics 226 (2003) 128-138.

[122] V. Andrés, K. Walsh, Myogenin expression, cell cycle withdrawal, and phenotypic differentiation are temporally separable events that precede cell fusion upon myogenesis, The Journal of Cell Biology 132 (1996) 657-666.

[123] A.P. Sharples, N. Al-Shanti, M.P. Lewis, C.E. Stewart, Reduction of myoblast differentiation following multiple population doublings in mouse C2C12 cells: A model to investigate ageing?, Journal of Cellular Biochemistry 112 (2011) 3773-3785.

[124] T. Mehmood, H. Martens, S. Saebo, J. Warringer, L. Snipen, A Partial Least Squares based algorithm for parsimonious variable selection, Algorithms for Molecular Biology 6 (2011) 27.

[125] M.A. Nemeth, Multi- and Megavariate Data Analysis, Technometrics 45 (2003) 362-362.

[126] I.-G. Chong, C.-H. Jun, Performance of some variable selection methods when multicollinearity is present, Chemometrics and Intelligent Laboratory Systems 78 (2005) 103-112.

[127] J.P.M. Andries, Y.V. Heyden, L.M.C. Buydens, Predictive-property-ranked variable reduction in partial least squares modelling with final complexity adapted models: Comparison of properties for ranking, Analytica Chimica Acta 760 (2013) 34-45.

[128] C. Krafft, L. Neudert, T. Simat, R. Salzer, Near infrared Raman spectra of human brain lipids, Spectrochimica Acta Part A: Molecular and Biomolecular Spectroscopy 61 (2005) 1529-1535.

[129] Z. Movasaghi, S. Rehman, I.U. Rehman, Raman Spectroscopy of Biological Tissues, Applied Spectroscopy Reviews 42 (2007) 493-541.

[130] S. Le Blond, E. Guilminot, G. Lemoine, N. Huet, J.Y. Mevellec, FT-Raman spectroscopy: A positive means of evaluating the impact of whale bone preservation treatment, Vibrational Spectroscopy 51 (2009) 156-161.

[131] T. Ikoma, H. Kobayashi, J. Tanaka, D. Walsh, S. Mann, Physical properties of type I collagen extracted from fish scales of Pagrus major and Oreochromis niloticas, International Journal of Biological Macromolecules 32 (2003) 199-204.

[132] V.A. Iconomidou, M.E. Georgaka, G.D. Chryssikos, V. Gionis, P. Megalofonou, S.J. Hamodrakas, Dogfish egg case structural studies by ATR FT-IR and FT-Raman spectroscopy, International Journal of Biological Macromolecules 41 (2007) 102-108.

[133] U. Bocker, R. Ofstad, Z. Wu, H.C. Bertram, G.D. Sockalingum, M. Manfait, B. Egelandsdal, rg, A. Kohler, Revealing Covariance Structures in Fourier Transform Infrared and Raman Microspectroscopy Spectra: A Study on Pork Muscle Fiber Tissue Subjected to Different Processing Parameters, Applied Spectroscopy 61 (2007) 1032-1039.

[134] K. Sowoidnich, H.-D. Kronfeldt, Fluorescence Rejection by Shifted Excitation Raman Difference Spectroscopy at Multiple Wavelengths for the Investigation of Biological Samples, ISRN Spectroscopy 2012 (2012) 11.

[135] N.C. Maiti, M.M. Apetri, M.G. Zagorski, P.R. Carey, V.E. Anderson, Raman Spectroscopic Characterization of Secondary Structure in Natively Unfolded Proteins: α-Synuclein, Journal of the American Chemical Society 126 (2004) 2399-2408.

[136] C.J. Frank, D.C.B. Redd, T.S. Gansler, R.L. McCreery, Characterization of human breast biopsy specimens with near-IR Raman spectroscopy, Analytical Chemistry 66 (1994) 319-326.

[137] D. Naumann, FT-INFRARED AND FT-RAMAN SPECTROSCOPY IN BIOMEDICAL RESEARCH, Applied Spectroscopy Reviews 36 (2001) 239-298.

[138] A. Tfayli, O. Piot, F. Draux, F. Pitre, M. Manfait, Molecular characterization of reconstructed skin model by Raman microspectroscopy: Comparison with excised human skin, Biopolymers 87 (2007) 261-274.

[139] B.G. Frushour, J.L. Koenig, Raman scattering of collagen, gelatin, and elastin, Biopolymers 14 (1975) 379-391.

[140] K. Walsh, H. Perlman, Cell cycle exit upon myogenic differentiation, Current Opinion in Genetics & Development 7 (1997) 597-602.

[141] Y. Watanabe, S. Kameoka, V. Gopalakrishnan, K.D. Aldape, Z.Z. Pan, F.F. Lang, S. Majumder, Conversion of myoblasts to physiologically active neuronal phenotype, Genes & Development 18 (2004) 889-900.

[142] L. Teboul, D. Gaillard, L. Staccini, H. Inadera, E.-Z. Amri, P.A. Grimaldi, Thiazolidinediones and Fatty Acids Convert Myogenic Cells into Adipose-like Cells, Journal of Biological Chemistry 270 (1995) 28183-28187.

[143] D.R. Williams, M.-R. Lee, Y.-A. Song, S.-K. Ko, G.-H. Kim, I. Shin, Synthetic Small Molecules that Induce Neurogenesis in Skeletal Muscle, Journal of the American Chemical Society 129 (2007) 9258-9259.

[144] G. Amabile, A.M. D'Alise, M. Iovino, P. Jones, S. Santaguida, A. Musacchio, S. Taylor, R. Cortese, The Aurora B kinase activity is required for the maintenance of the differentiated state of murine myoblasts, Cell Death Differ 16 (2008) 321-330.

[145] Y. Xu, Y. Shi, S. Ding, A chemical approach to stem-cell biology and regenerative medicine, Nature 453 (2008) 338-344.

[146] Y. Yoshiko, K. Hirao, N. Maeda, Differentiation in C2C12 myoblasts depends on the expression of endogenous IGFs and not serum depletion, American Journal of Physiology - Cell Physiology 283 (2002) C1278-C1286.

[147] E. Schultz, B.H. Lipton, Skeletal muscle satellite cells: Changes in proliferation potential as a function of age, Mechanisms of Ageing and Development 20 (1982) 377-383.

[148] M.C. Gibson, E. Schultz, Age-related differences in absolute numbers of skeletal muscle satellite cells, Muscle & Nerve 6 (1983) 574-580.

[149] G.Y. Koh, M.G. Klug, M.H. Soonpaa, L.J. Field, Differentiation and long-term survival of C2C12 myoblast grafts in heart, The Journal of Clinical Investigation 92 (1993) 1548-1554.

[150] R.B. Thompson, S.M. Emani, B.H. Davis, E.J. van den Bos, Y. Morimoto, D. Craig, D. Glower, D.A. Taylor, Comparison of Intracardiac Cell Transplantation: Autologous Skeletal Myoblasts Versus Bone Marrow Cells, Circulation 108 (2003) II-264-II-271.

[151] X.L. Aranguren, J.D. McCue, B. Hendrickx, X.-H. Zhu, F. Du, E. Chen, B. Pelacho, Pe, xF, I. uelas, G. Abizanda, M. Uriz, S.A. Frommer, J.J. Ross, B.A. Schroeder, M.S. Seaborn, J.R. Adney, J. Hagenbrock, N.H. Harris, Y. Zhang, X. Zhang, M.H. Nelson-Holte, Y. Jiang, A.D. Billiau, W. Chen, Pr, F. sper, C.M. Verfaillie, A. Luttun, Multipotent adult progenitor cells sustain function of ischemic limbs in mice, The Journal of Clinical Investigation 118 (2008) 505-514.

[152] Z.R. Gagnon, Cellular dielectrophoresis: Applications to the characterization, manipulation, separation and patterning of cells, ELECTROPHORESIS 32 (2011) 2466-2487.

[153] J.M. Gimble, A.J. Katz, B.A. Bunnell, Adipose-Derived Stem Cells for Regenerative Medicine, Circulation Research 100 (2007) 1249-1260.

[154] G.G. Nicolas, B.J. Thomas, Numerical determination of the effective moments of non-spherical particles, Journal of Physics D: Applied Physics 40 (2007) 78.

[155] H. Dolznig, F. Grebien, T. Sauer, H. Beug, E.W. Mullner, Evidence for a size-sensing mechanism in animal cells, Nat Cell Biol 6 (2004) 899-905.

[156] D. Killander, A. Zetterberg, A quantitative cytochemical investigation of the relationship between cell mass and initiation of DNA synthesis in mouse fibroblasts in vitro, Experimental Cell Research 40 (1965) 12-20.

[157] P. Jorgensen, J.L. Nishikawa, B.-J. Breitkreutz, M. Tyers, Systematic Identification of Pathways That Couple Cell Growth and Division in Yeast, Science 297 (2002) 395-400.

[158] I. Rupeš, Checking cell size in yeast, Trends in Genetics 18 (2002) 479-485.

[159] L.J. Saucedo, B.A. Edgar, Why size matters: altering cell size, Current Opinion in Genetics & Development 12 (2002) 565-571.

[160] H. Stocker, E. Hafen, Genetic control of cell size, Current Opinion in Genetics & Development 10 (2000) 529-535.

[161] T.W. Holstein, C.N. David, Cell cycle length, cell size, and proliferation rate in hydra stem cells, Developmental Biology 142 (1990) 392-400.

[162] H. Shima, M. Pende, Y. Chen, S. Fumagalli, G. Thomas, S.C. Kozma, Disruption of the p70s6k/p85s6k gene reveals a small mouse phenotype and a new functional S6 kinase, EMBO J 17 (1998) 6649-6659.

[163] M. Barberis, E. Klipp, M. Vanoni, L. Alberghina, Cell Size at S Phase Initiation: An Emergent Property of the G<sub>1</sub>/S Network, PLoS Comput Biol 3 (2007) e64.

[164] B. Novak, J.J. Tyson, Modeling the Cell Division Cycle: M-phase Trigger, Oscillations, and Size Control, Journal of Theoretical Biology 165 (1993) 101-134.

[165] T. Scholzen, J. Gerdes, The Ki-67 protein: From the known and the unknown, Journal of Cellular Physiology 182 (2000) 311-322.

[166] H. Lizhi, K. Toyoda, I. Ihara, Dielectric properties of edible oils and fatty acids as a function of frequency, temperature, moisture and composition, Journal of Food Engineering 88 (2008) 151-158.

[167] B.R. Underwood, D. Broadhurst, W.B. Dunn, D.I. Ellis, A.W. Michell, C. Vacher, D.E. Mosedale, D.B. Kell, R.A. Barker, D.J. Grainger, D.C. Rubinsztein, Huntington disease patients and transgenic mice have similar pro-catabolic serum metabolite profiles, Brain 129 (2006) 877-886.

[168] X. Li, C. Standley, E. Sapp, A. Valencia, Z.-H. Qin, K.B. Kegel, J. Yoder, L.A. Comer-Tierney, M. Esteves, K. Chase, J. Alexander, N. Masso, L. Sobin, K. Bellve, R. Tuft, L. Lifshitz, K. Fogarty, N. Aronin, M. DiFiglia, Mutant Huntingtin Impairs Vesicle Formation from Recycling Endosomes by Interfering with Rab11 Activity, Molecular and Cellular Biology 29 (2009) 6106-6116.

[169] V. Maglione, P. Marchi, A. Di Pardo, S. Lingrell, M. Horkey, E. Tidmarsh, S. Sipione, Impaired ganglioside metabolism in Huntington's disease and neuroprotective role of GM1, Journal of Neuroscience 30 (2010) 4072-4080.

[170] K.B. Kegel, E. Sapp, J. Yoder, B. Cuiffo, L. Sobin, Y.J. Kim, Z.H. Qin, M.R. Hayden, N. Aronin, D.L. Scott, G. Isenberg, W.H. Goldmann, M. DiFiglia, Huntingtin associates with acidic phospholipids at the plasma membrane, Journal of Biological Chemistry 280 (2005) 36464-36473.

[171] K.B. Kegel, V. Schewkunow, E. Sapp, N. Masso, E.E. Wanker, M. DiFiglia, W.H. Goldmann, Polyglutamine expansion in huntingtin increases its insertion into lipid bilayers, Biochemical and Biophysical Research Communications 387 (2009) 472-475.

[172] B.L. Kagan, Y. Hirakura, R. Azimov, R. Azimova, The channel hypothesis of Huntington's disease, Brain Research Bulletin 56 (2001) 281-284.

[173] D. Bano, F. Zanetti, Y. Mende, P. Nicotera, Neurodegenerative processes in Huntington's disease, Cell Death and Dis 2 (2011) e228.

[174] M. Muratore, Raman spectroscopy and partial least squares analysis in discrimination of peripheral cells affected by Huntington's disease, Analytica Chimica Acta 793 (2013) 1-10.

[175] P. Hoyo, A. García-Redondo, F. Bustos, J. Molina, Y. Sayed, H. Alonso-Navarro, L. Caballero, J. Arenas, F. Jiménez-Jiménez, Oxidative Stress in Skin Fibroblasts Cultures of Patients with Huntington's Disease, Neurochemical Research 31 (2006) 1103-1109.

[176] K.E. De Rooij, J.C. Dorsman, M.A. Smoor, J.T. Den Dunnen, G.-J.B. Van Ommen, Subcellular Localization of the Huntington's Disease Gene Product in Cell Lines by Immunofluorescence and Biochemical Subcellular Fractionation, Human Molecular Genetics 5 (1996) 1093-1099.

[177] A. Abbas, M. Josefson, G.M. Nylund, H. Pavia, K. Abrahamsson, Chemical images of marine bio-active compounds by surface enhanced Raman spectroscopy and transposed orthogonal partial least squares (T-OPLS), Analytica Chimica Acta 737 (2012) 37-44.

[178] C. Kendall, N. Stone, N. Shepherd, K. Geboes, B. Warren, R. Bennett, H. Barr, Raman spectroscopy, a potential tool for the objective identification and classification of neoplasia in Barrett's oesophagus, The Journal of Pathology 200 (2003) 602-609.

[179] C. Krafft, S.B. Sobottka, G. Schackert, R. Salzer, Near infrared Raman spectroscopic mapping of native brain tissue and intracranial tumors, Analyst 130 (2005) 1070-1077.

[180] K.W. Short, S. Carpenter, J.P. Freyer, J.R. Mourant, Raman Spectroscopy Detects Biochemical Changes Due to Proliferation in Mammalian Cell Cultures, Biophysical Journal 88 (2005) 4274-4288.

[181] A. Nijssen, T.C. Bakker Schut, F. Heule, P.J. Caspers, D.P. Hayes, M.H.A. Neumann, G.J. Puppels, Discriminating Basal Cell Carcinoma from its Surrounding Tissue by Raman Spectroscopy, 119 (2002) 64-69.

[182] R. Madsen, T. Lundstedt, J. Trygg, Chemometrics in metabolomics—A review in human disease diagnosis, Analytica Chimica Acta 659 (2010) 23-33.

[183] D.V. Nguyen, D.M. Rocke, Tumor classification by partial least squares using microarray gene expression data, Bioinformatics 18 (2002) 39-50.